

Planetary-period oscillations in Saturn's magnetosphere

Thesis submitted for the degree of

Doctor of Philosophy

at

The University of Leicester

by

David J. Andrews

Radio and Space Plasma Physics Group

Department of Physics and Astronomy

University of Leicester

August 2011

Abstract

This thesis is concerned with the study of near-planetary rotation period oscillations in Saturn's magnetic field. Similar oscillations are present in a variety of other magnetospheric phenomena, most notably kilometre-wavelength radio emissions, and together they have a substantial influence throughout the Saturnian plasma environment. However, their origin remains poorly understood, despite more than a decade of study. Surprising new discoveries have been made regarding the seasonality of these oscillatory phenomena, and their intrinsic connection to the high-latitude upper atmosphere and ionosphere of the planet, though a complete theory of their origin remains to be developed.

In this thesis, three detailed studies of this phenomenon are presented, each of which uses magnetic field data recently obtained by the Cassini spacecraft. The first consists of an extensive survey of near-equatorial field data during southern summer, from which the structure of the rotating oscillations is determined and the electrical currents flowing through the equatorial plane are calculated. The second study is prompted by the recent discovery of a north-south asymmetry in the period of related radio emissions, and consists of a survey of high-latitude magnetic field data in which evidence for a corresponding asymmetry in the magnetic field rotation period is found. Finally, the third study concerns the presence of long-term drifts between the phase of the magnetic field oscillation and the Saturn kilometric radiation (SKR) modulation, which, through construction of a simple theoretical model, is shown to arise as a consequence of 'rotational' modulations in the SKR rather than the hitherto assumed 'strobe-like' modulations. These three studies substantially further our understanding of these phenomena, and in the case of the detection of a rotational modulation in the SKR overturn three decades of previous thought. Consequently, the results presented here elucidate characteristics of these phenomena that any theoretical understanding of their origin must serve to explain, and will therefore be of central importance in further development of this topic in the future.

Before presenting these three studies, an introduction to the topics of space plasma physics and planetary magnetospheres is presented in Chapter 1. This is followed in Chapter 2 with a discussion of Saturn's magnetosphere, and the topic of near-planetary period oscillations, and in Chapter 3 by descriptions of the instruments with which data used in this thesis have been obtained.

Acknowledgements

Firstly I wish to thank Stan, for providing guidance, insight and clarity on an often complex topic. His reputation as an excellent teacher is thoroughly deserved. I also wish to thank my co-authors Andrew, Baptiste, Gabby, Laurent, Michele, and Philippe for their continued helpful discussions on the work presented here, and furthermore for provision of the data upon which this thesis relies. I wish to thank the RSPP group for providing a fantastic environment within which to work over these last three years, and the wider ‘magnetospheres of the outer planets’ community for providing lively debate. Finally, without support from Mum, Dad, Jon and Vicki, I wouldn’t be here doing this.

“For those who believe in God, most of the big questions are answered. But for those of us who can't readily accept the God formula, the big answers don't remain stone-written. We adjust to new conditions and discoveries. We are pliable. Love need not be a command nor faith a dictum. I am my own god. We are here to unlearn the teachings of the church, state, and our educational system. We are here to drink beer. We are here to kill war. We are here to laugh at the odds and live our lives so well that Death will tremble to take us.”

Bukowski

Declaration

I, David J. Andrews, hereby declare that the work contained within this thesis is my own. I acknowledge the sources of my data and reference any material which is reproduced. Sections of this thesis have been previously published in the following papers:

- Andrews, D. J., S. W. H. Cowley, M. K. Dougherty, and G. Provan (2010). Magnetic field oscillations near the planetary period in Saturn's equatorial magnetosphere: Variation of amplitude and phase with radial distance and local time, *J. Geophys. Res.*, doi:10.1029/2007JA014729.
- Andrews, D. J., A. J. Coates, S. W. H. Cowley, M. K. Dougherty, L. Lamy, G. Provan and P. Zarka (2010). Magnetospheric period oscillations at Saturn: Comparison of equatorial and high-latitude magnetic field periods with north and south SKR periods, *J. Geophys. Res.*, doi:10.1029/2010JA015666.
- Andrews, D. J., B. Cecconi, S. W. H. Cowley, M. K. Dougherty, L. Lamy, G. Provan and P. Zarka (*in press*). Planetary period oscillations at Saturn: Evidence in magnetic field phase data for rotational modulation of Saturn kilometric radiation emissions, *J. Geophys. Res.*, doi:10.1029/2011JA016636.

Contents

1	Introduction	1
1.1	Overview	1
1.2	Governing physics of space plasmas	2
1.3	The Sun and solar wind	9
1.4	Planetary magnetospheres	10
2	Saturn and its magnetosphere	17
2.1	Overview	17
2.2	Past exploration of the Saturnian system	17
2.3	Formation	18
2.4	Moons and rings	19
2.5	Interior and magnetic field	22
2.6	Atmosphere and ionosphere	25
2.7	Magnetosphere	26
2.8	Planetary period oscillations at Saturn	32
3	Instrumentation	51
3.1	Overview	51
3.2	The Cassini-Huygens mission to Saturn	51
3.3	The Cassini Magnetometer Instrument	53
3.4	The Cassini Plasma Spectrometer	57
3.5	Radio & Plasma Wave Science Instrument	58
3.6	The Cassini orbital tour	58
4	Equatorial field oscillations	63
4.1	Introduction	63
4.2	Data selection and analysis	66
4.3	Amplitude and phase of the field oscillations in the equatorial region	79
4.4	Radial and azimuthal phase speeds	88
4.5	Form of the oscillating field in the equatorial region	93
4.6	North-South currents in the equatorial plane	97

4.7 Summary of results	107
4.8 Discussion of results	115
5 High-latitude field oscillations	123
5.1 Introduction	123
5.2 Data selection, processing, and analysis	127
5.3 Magnetic oscillation phase results	138
5.4 Summary and discussion	153
6 SKR rotational modulation	162
6.1 Introduction	162
6.2 Methodology	168
6.3 Determination of Magnetic Phase Values	180
6.4 Revised Period of the Southern Hemisphere Oscillations	191
6.5 Summary	200
7 Summary and conclusions	205
A The RANSAC Algorithm	208
B Directional statistics	210
C List of Acronyms	214
References	216

List of Figures

1.1	Guiding-centre motion	3
1.2	Heliospheric current sheet	11
1.3	Closed magnetosphere	12
1.4	Open magnetosphere	14
1.5	Configuration of the magnetosphere	15
2.1	Pioneer & Voyager flyby trajectories	20
2.2	Enceladus plumes	21
2.3	Magnetic signature of Enceladus's plume	22
2.4	Saturn in eclipse	23
2.5	Saturn's zonal winds	26
2.6	Saturn's ionosphere	27
2.7	Equatorial plasma densities	29
2.8	Plasma distribution	29
2.9	Magnetosphere-ionosphere coupling currents	31
2.10	Equatorial plasma flows	31
2.11	Meridional field lines	33
2.12	Current sheet deflection	34
2.13	SKR Periodogram	37
2.14	SKR seasonal variation	38
2.15	Pioneer 11 field oscillations	39
2.16	3-D field perturbations	43
2.17	Motion of the magnetopause	43
2.18	Carbary et al. periodic ENA emission	44
2.19	Southern UV aurora vs. SKR phase	45
2.20	Gurnett et al. plasma convection	48
2.21	Southwood and Kivelson 'camshaft' model	49
2.22	Rotating partial ring current	49
3.1	Cassini schematic	52
3.2	Residual spacecraft field	54
3.3	FGM schematic	54

3.4	Cassini FGM photograph	55
3.5	CAPS schematic	59
3.6	RPWS instrument placement	59
3.7	Cassini interplanetary trajectory	60
3.8	Cassini orbital tour	61
4.1	Cassini's equatorial trajectory	69
4.2	Cassini's latitudinal coverage	70
4.3	Typical field oscillations	77
4.4	Amplitude and phase versus radial distance	80
4.4	Amplitude and phase versus LT	81
4.5	Oscillation phase	84
4.6	Phase differences	87
4.7	Radial phase velocities	90
4.7	Azimuthal phase velocities	91
4.8	Equatorial field oscillation	95
4.9	Equatorial current density	99
4.10	Integrated current density	104
4.11	Meridional field lines	114
4.12	Rotating current systems	118
5.1	Field polarisation sketches	125
5.2	Empirical northern and southern SKR phases	129
5.3	Rev 95 field and plasma data	131
5.4	Cassini orbital tour	136
5.5	Southern hemisphere open field region phases	139
5.6	Core region field phases	145
5.7	Northern hemisphere open field phases vs. southern SKR	149
5.8	Northern hemisphere open field phases vs. northern SKR	151
5.9	Oscillatory perturbation field sketches	156
6.1	Model of rotating SKR phase	170
6.2	Orbit-averaged phase deviations	173
6.3	Lamy SKR phases	181
6.4	Core and southern magnetic phases	185
6.5	Northern magnetic phases	192
6.6	Comparison of magnetic and SKR periods	194
6.7	Southern magnetic periodogram	196
6.8	Comparison of magnetic and SKR phases	199
B.1	Wrapped normal distributions	213

Chapter 1

Introduction

1.1 Overview

This thesis is concerned with the study of near-planetary rotation period oscillations in Saturn's magnetic field. Similar oscillations are present in a variety of other magnetospheric phenomena, most notably kilometre-wavelength radio emissions, and together they exert substantial influence throughout the Saturnian plasma environment. However, their origin remains uncertain, despite more than a decade of study. Surprising new results regarding the seasonality and structure of these oscillatory phenomena have shown them to be substantially more complicated than initially supposed, and they therefore provide an intriguing, if somewhat enigmatic subject to study.

In this chapter, the basic physics of space plasmas is reviewed, so as to develop a framework within which the magnetosphere of Saturn and the near-planetary rotation period oscillations that pervade it can then be introduced in Chapter 2. This chapter begins with a description of the motion of individual charged particles under the influence of electromagnetic fields, before introducing the concept of a plasma to describe the behaviour of collections of such particles. A brief discussion of the Sun and the solar wind then follows, and finally the basic physics of planetary magnetospheres are introduced. Descriptions of the various instruments from which data is used in this thesis is then provided in Chapter 3, before three separate studies of aspects of the

magnetic field oscillations and their related phenomena are presented in Chapters 4-6. The thesis is then briefly summarised and conclusions drawn in Chapter 7.

1.2 Governing physics of space plasmas

1.2.1 Single particle motion

A single particle with mass m and charge q , moving with velocity \mathbf{v} in the presence of an electric field \mathbf{E} and a magnetic field \mathbf{B} will experience a force \mathbf{F} given by

$$\mathbf{F} = q(\mathbf{E} + \mathbf{v} \times \mathbf{B}). \quad (1.1)$$

From this it is simple to show that in the case where the electric field is zero and the magnetic field is uniform, such a particle will gyrate in a circle about the magnetic lines of force ('field lines'). This will occur at an angular frequency ω_g , termed the cyclotron frequency, given by

$$\omega_g = \frac{qB}{m}, \quad (1.2)$$

with the sense of motion about the field lines being reversed for particles with opposite charge. In addition, particles will move along the field with constant speed. This gyromotion about the field line is sketched in Figure 1.1.

It is therefore generally convenient to separately consider the particle's velocity in terms of components parallel and perpendicular to the field direction, denoted by \mathbf{v}_{\parallel} and \mathbf{v}_{\perp} , respectively, with their ratio defining the 'pitch angle' α of the particle, given by

$$\alpha = \tan^{-1}\left(\frac{\mathbf{v}_{\perp}}{\mathbf{v}_{\parallel}}\right). \quad (1.3)$$

The pitch angle α thus defines the angle of the motion of a particle along a helical trajectory.

Associated with motion of a charged particle in a more general magnetic field, three adiabatic invariants of the motion can be defined. These are described here as they apply to particles moving in quasi-dipolar fields, as is often the case for magnetospheric charged particles. The first adiabatic invariant is the magnetic moment of the particle

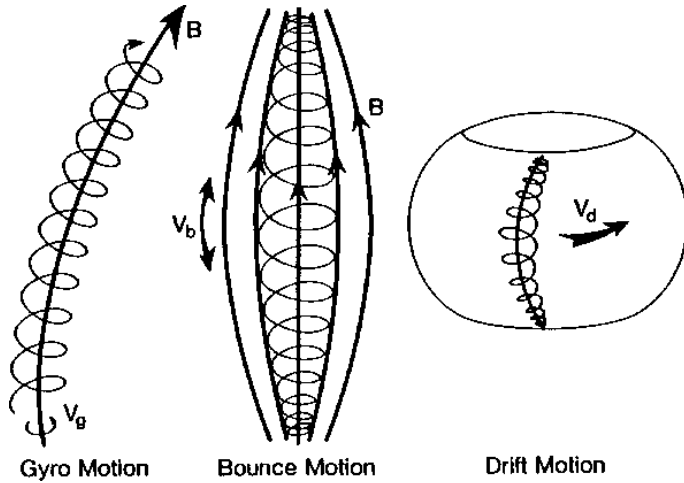


Figure 1.1: Illustration of the motion of charged particles in magnetic fields. The left-hand figure shows the gyro motion of a particle along a field line, otherwise known as ‘guiding-centre’ motion. The centre figure shows this gyromotion superimposed upon bounce motion between two regions of high field strength (magnetic mirrors). The right hand figure shows the combination of both the gyro-, bounce-, and drift-motion in a dipolar field. From *Kivelson* [1995].

μ , given by

$$\mu = \frac{mv_{\perp}^2}{2B} = \frac{W_{\perp}}{B}, \quad (1.4)$$

where W_{\perp} is the perpendicular energy of the particle,

$$W_{\perp} = \frac{mv_{\perp}^2}{2}. \quad (1.5)$$

As a consequence of the conservation of both μ and the total kinetic energy

$$W = \frac{mv^2}{2}, \quad (1.6)$$

particles will reflect or ‘mirror’ in moving from regions of low to high field strength, and can be effectively trapped between two such mirrors, as depicted in the centre sketch in Figure 1.1. This mirroring occurs as W_{\perp} increases as the particle moves into higher field strengths, such that μ remains constant. Consequently, to maintain constant W the particle’s parallel kinetic energy (and hence $v_{||}$) must fall, and reaches zero at the mirror point where $\alpha = 90^\circ$. The particle can then only leave the high-field region in the direction in which it entered, hence the term ‘magnetic mirror’.

The second adiabatic invariant, J , termed the ‘longitudinal invariant’ defines the relationship between the parallel velocity $\langle v_{||} \rangle$, as averaged during the motion between

mirror points s_1 and s_2 , and the length of the field line l (line element ds)

$$J = m \int_{s_1}^{s_2} \mathbf{v}_{||} ds. \quad (1.7)$$

Conservation of J leads to parallel acceleration as the length of the field line decreases.

Finally, the third adiabatic invariant Φ simply describes conservation of the flux of the background field threading the orbit of the particle. It is also important to note that these three adiabatic invariants, μ , J and Φ are only conserved when the field in which the particles are moving varies slowly on spatial and temporal scales compared with those of the gyro-, bounce, and drift motion, respectively. Collectively, satisfaction of these conditions indicate the validity of the ‘guiding-centre’ approximation in each case (though while μ and J are generally conserved, the significantly longer timescales involved in particle drift motion generally means that Φ is not in fact constant).

Elegantly, any force \mathbf{F} acting on a charged particle in a magnetic field will introduce a ‘drift’ motion \mathbf{v}_F given by

$$\mathbf{v}_F = \frac{1}{\omega_g} \left(\frac{\mathbf{F}}{m} \times \frac{\mathbf{B}}{B} \right), \quad (1.8)$$

provided that the guiding-centre approximation remains valid.

Typical forces acting to produce drift motion of the particles are

$$\mathbf{F}_E = q\mathbf{E} \quad \text{Coulomb, or electric field} \quad (1.9)$$

$$\mathbf{F}_V = -\mu \nabla \mathbf{B} \quad \text{magnetic gradient} \quad (1.10)$$

$$\mathbf{F}_P = -m \frac{d\mathbf{v}_{\perp}}{dt} \quad \text{polarisation} \quad (1.11)$$

$$\mathbf{F}_G = -mg \quad \text{gravity} \quad (1.12)$$

$$\mathbf{F}_C = mv_{||}^2 \frac{\mathbf{R}_C}{R_C^2} \quad \text{field curvature,} \quad (1.13)$$

in which \mathbf{g} is the gravitational acceleration (generally negligible within the context of space plasmas), and \mathbf{R}_C is the local radius of field curvature. Note that, upon substitution of these forces into equation (1.8), the velocities of all except the Coulomb ($\mathbf{E} \times \mathbf{B}$) drift depend on the sign of the particle charge, such that electrons will drift in one direction and ions in the opposite, indicating that a net current will flow. The $\mathbf{E} \times \mathbf{B}$ drift velocity is independent of both sign of the charge on the particle and its mass, and is equivalent to a frame transformation.

While the description of the interactions between charged particles and electromagnetic fields presented above will hold as long as the guiding-centre approximation remains valid, collective interactions between particles through these fields are not accounted for by this framework alone, and it is necessary to introduce the concept of a plasma.

1.2.2 Plasma physics

A plasma consists of an ensemble of interacting charged particles. Naturally occurring plasmas generally satisfy the ‘quasi-neutrality’ condition, meaning that beyond some characteristic length scale any given volume will contain an approximately equal number of positive and negative charges. Consequently, electrostatic forces are insignificant on scales larger than this. The scale in question is referred to as the Debye length λ_D , and is given by

$$\lambda_D = \sqrt{\frac{\epsilon_0 k_B T_e}{n_e e^2}}, \quad (1.14)$$

in which k_B is Boltzmann’s constant, T_e is the electron temperature and n_e the electron number density. The ‘plasma parameter’ N_D expresses the number of charged particles in a sphere of radius λ_D , and is given by

$$N_D = \frac{4}{3}\pi n_e \lambda_D^3. \quad (1.15)$$

For collective behaviour of the particles to be significant, they must be able to interact with one-another, and therefore N_D must be much greater than unity. Within the context of space plasmas, the processes of interest typically have length scales $L \gg \lambda_D$, and therefore the ion density $n_i \approx n_e$ and quasi-neutrality holds. Furthermore, while a plasma need not necessarily consist of fully-ionised material, the density of neutral particles n_n must be low enough that collisions between the charged and neutral particles do not dominate the interactions between charged particles and the field.

The properties of the electromagnetic field are described by Maxwell’s equations, which define the divergence and curl of the electric and magnetic fields. These are

given by

$$\nabla \cdot \mathbf{E} = \frac{\rho_q}{\epsilon_0} \quad (1.16)$$

$$\nabla \cdot \mathbf{B} = 0 \quad (1.17)$$

$$\nabla \times \mathbf{E} = -\frac{\partial \mathbf{B}}{\partial t} \quad (1.18)$$

$$\nabla \times \mathbf{B} = \mu_0 \mathbf{j} + \mu_0 \epsilon_0 \frac{\partial \mathbf{E}}{\partial t}, \quad (1.19)$$

where the charge density $\rho_q = e(n_i - n_e)$, \mathbf{j} is the current density and μ_0 and ϵ_0 are the permeability and permittivity of free space, respectively. Equations (1.16) and (1.17) are Gauss's laws for the electric and magnetic fields, respectively, and equations (1.18) and (1.19) are Faraday's law and the Ampère-Maxwell equation, respectively. The behaviour of a plasma is wholly governed by Maxwell's equations, the Lorentz force (equation (1.1)), and Newton's law of motion. Furthermore, when considering low-frequency phenomena, the displacement current term in equation (1.19) is negligible (thus the expression reduces to that originally formed by Ampère).

Through combining Maxwell's equations, along with a simplified Ohm's law given by

$$\mathbf{j} = \sigma_0 (\mathbf{E} + \mathbf{v} \times \mathbf{B}), \quad (1.20)$$

in which collisional terms have been neglected, and where the plasma conductivity σ_0 is given by

$$\sigma_0 = \frac{n_e e^2}{m_e v_c}, \quad (1.21)$$

in which m_e is the electron mass and v_c is the ion-electron collision frequency, it can be shown that

$$\frac{\partial \mathbf{B}}{\partial t} = \nabla \times (\mathbf{v} \times \mathbf{B}) + \frac{1}{\mu_0 \sigma_0} \nabla^2 \mathbf{B}. \quad (1.22)$$

The relative importance of the convective and diffusive terms on the right hand side of equation (1.22) can be expressed as a dimensionless "magnetic Reynold's number", given by

$$R_m = \mu_0 \sigma_0 V L_B, \quad (1.23)$$

where V is the averaged field-perpendicular velocity of the plasma and L_B is the typical length scale of the variation in the field. For large values of R_m (corresponding to

high conductivity, high velocity, and large length scales), as is typically the case for the generally collision-free magnetospheric plasmas in which $v_c \approx 0$, the right hand term in equation (1.22) can be neglected. This is equivalent to the statement that $\mathbf{E} + \mathbf{v} \times \mathbf{B} \approx 0$, such that the only field-perpendicular drift is the $\mathbf{E} \times \mathbf{B}$ drift (specified by equations (1.8) and (1.9)). This yields an expression for the joint motion of the plasma and field, otherwise referred to as Alfvén's theorem or the ‘frozen-in flux condition’, which states that if the plasma moves, the field embedded within it is advected along with the motion, and vice-versa. Conversely, in the limit of low R_m (corresponding to low conductivity, low velocity, and small length scales), equation (1.22) reduces to a diffusion equation. Diffusive processes are thus typically only of significance in the dense ionospheric plasma, where collisional interactions become important, or near the magnetopause where the length scales become small and reconnection takes place (see section 1.4).

Rather than characterise a plasma in the strictest possible sense, by determining a particle distribution function and studying how it evolves within the system of interest through Liouville’s theorem, where possible it is often sufficient to study the behaviour of the moments of the distribution function, i.e. the macroscopic variables such as mass density ρ , bulk velocity \mathbf{V} , pressure p and so on. The theory describing these macroscopic properties of a plasma is called ‘magneto-hydrodynamics’ (MHD), in reference to non-conducting fluid dynamics. In the following expressions, the plasma is treated as a single species, quasi-neutral conducting fluid, rather than considering separate ion and electron populations. MHD theory specifies a continuity equation (assuming no sources and losses of plasma),

$$\frac{\partial \rho}{\partial t} + \nabla \cdot (\rho \mathbf{V}) = 0, \quad (1.24)$$

and a momentum conservation equation,

$$\rho \frac{D\mathbf{v}}{Dt} = \rho \frac{\partial \mathbf{V}}{\partial t} + \rho(\mathbf{v} \cdot \nabla) \mathbf{v} = -\nabla p + \mathbf{j} \times \mathbf{B} + \rho \mathbf{g}. \quad (1.25)$$

The set of equations for \mathbf{E} , \mathbf{B} , \mathbf{j} , \mathbf{v} , ρ and p are then closed usually through inclusion of some equation of state, rather than including an explicit equation governing conservation of energy.

1.2.3 Waves in space plasmas

Many different wave modes can be excited in a plasma, and while it is beyond the scope of this thesis to cover them all in any great detail, it is necessary to introduce a few of them, such that some of the mechanisms by which information and energy can be communicated through a plasma are understood. The most typical oscillation that exists in a quasi-neutral plasma is known as the electron plasma oscillation, or ‘Langmuir’ oscillation. It arises as a consequence of the electrostatic forces which act to maintain quasi-neutrality. A localised departure from quasi-neutrality will produce an electrostatic field that will act on the charged particles to restore neutrality. In typical space plasmas, the electrons will respond fastest to this applied field. However, owing to their inertia, in responding to the electrostatic field the electrons will oscillate about equilibrium, at the electron plasma frequency ω_{pe} , given by

$$\omega_{pe}^2 = \frac{n_e e^2}{m_e \epsilon_0}. \quad (1.26)$$

Note that there is no dependence on the wavenumber k in equation (1.26), and consequently the group velocity of the electron plasma oscillation is zero. However, when the electron thermal pressure is included in the analysis, the dispersion equation is modified to

$$\omega_l^2 = \omega_{pe}^2 + k^2 \gamma_e \frac{k_B T_e}{m_e}, \quad (1.27)$$

which now gives rise to propagation at a finite speed, dependent on the properties of the plasma.

In a magnetised plasma additional wave modes can propagate, of which three are briefly discussed here, these being the Alfvén wave and the fast- and slow-magnetosonic wave modes. These are valid in the low-frequency MHD limit discussed in section 1.2.2, i.e. for temporal and spatial scales large compared to the gyroperiod and gyroradius, respectively.

The Alfvén wave is a dispersionless oscillation which propagates parallel to the field at a speed v_A given by

$$v_A^2 = \frac{B^2}{\mu_0 \rho}, \quad (1.28)$$

and represents the fundamental speed at which changes in the field can propagate. The Alfvén wave is often regarded as analogous to a wave on a taught string, with the restorative force in this case provided by the ‘tension’ in the magnetic field.

Meanwhile, the fast- and slow-mode magnetosonic waves have a dispersion relation given by

$$\omega_{ms}^2 = \frac{k^2}{2} \left(c_{ms}^2 \pm \left[(v_A^2 - c_s^2)^2 + 4v_A^2 c_s^2 \frac{k_\perp^2}{k^2} \right]^{1/2} \right), \quad (1.29)$$

in which the magnetosonic speed c_{ms} is given by

$$c_{ms}^2 = c_s^2 + v_A^2, \quad (1.30)$$

and the sound speed c_s by

$$c_s^2 = \frac{\gamma k_B T}{m_i}, \quad (1.31)$$

where γ is the polytropic index. The ratio $k_\perp^2/k^2 = \sin^2\theta$ defines the angle θ of propagation relative to the magnetic field direction. The ‘fast’ and ‘slow’ magnetosonic speeds are given by the solutions of equation (1.29) taking the positive and negative signs in the expression, respectively. The characteristics of both wave modes are thus strongly dependent on the field strength and plasma temperature. Finally, it is worth noting that the ‘fast’ mode is equivalent to a sound wave in the limit of $\mathbf{B} \rightarrow 0$ i.e. $v_A \rightarrow 0$ and $c_{ms} \rightarrow c_s$.

1.3 The Sun and solar wind

The Sun lies at the centre of the solar system. It is comprised principally of hydrogen (73%) and helium (25%), along with traces of heavier elements. Its mass ($\sim 2 \times 10^{30}$ kg) is sufficiently large that the Sun’s gravitational potential allows for the sustained fusion of $\sim 5 \times 10^6$ kg s⁻¹ of hydrogen into helium. This heats the core to $\sim 1.5 \times 10^7$ K, and the outward transport of this heat drives convection systems across a range of scales from hundreds to millions of km. The visible surface of the Sun is termed the photosphere, and has a temperature of ~ 5800 K. Above this, in the solar corona, the solar atmosphere becomes much more tenuous, and is heated to $\sim 2 \times 10^6$ K through mechanisms that remain poorly understood. The high temperature and pressure of the solar corona are

such that this atmosphere is no longer gravitationally bound, and continually streams off the solar surface, forming the ‘solar wind’ [Parker, 1958]. The solar wind continues to accelerate beyond the solar corona over distances of a few solar radii, and is flowing at near-constant super-magnetosonic speeds when it arrives at the planets.

The Sun possesses a magnetic field, generated in its interior through a dynamo process operating in a differentially rotating layer of metallic hydrogen, in the same manner as the gas giant planets. Relative to the planetary dynamos, the Sun’s is significantly more variable, with the resulting field reversing quasi-periodically with a characteristic timescale of ~ 11 years. Localised cool, dark sunspots are a visible manifestation of this process. As a consequence of Alfvén’s theorem, the outflowing, collisionless solar wind plasma carries with it the solar magnetic field, generally referred to as the ‘interplanetary magnetic field’ (IMF) when it impinges on the planets of the solar system. The rotation period of the Sun is ~ 25 days at the equator (though it is significantly longer at the poles), and consequently the field lines of the IMF are bent into spirals as they move outwards from the Sun. During the rising and declining phases of the solar cycle, when the solar magnetic field is generally ‘ordered’ into some quasi-dipolar configuration and the magnetic equator is typically tilted out of the rotational equator by $\sim 10^\circ$, the sense of the IMF will reverse twice per solar rotation at a planet lying in the ecliptic plane. However, when the tilt of the solar magnetic field is smallest, near solar minimum, departures in the solar field from a perfect tilted dipole will produce a higher-order structure in the IMF, as is shown in Figure 1.2 in which a four-sector structure is depicted.

1.4 Planetary magnetospheres

The magnetised planets (Mercury, Earth, Jupiter, Saturn, Uranus, Neptune) are obstacles to the passage of the solar wind and the IMF convected with it. To a first approximation, Alfvén’s theorem forbids the mixing of the solar wind plasma and IMF with the quasi-dipolar fields produced in the interior of these planets. Consequently, a cavity is formed in the solar wind, termed the ‘magnetosphere’, illustrated in Figure 1.3.

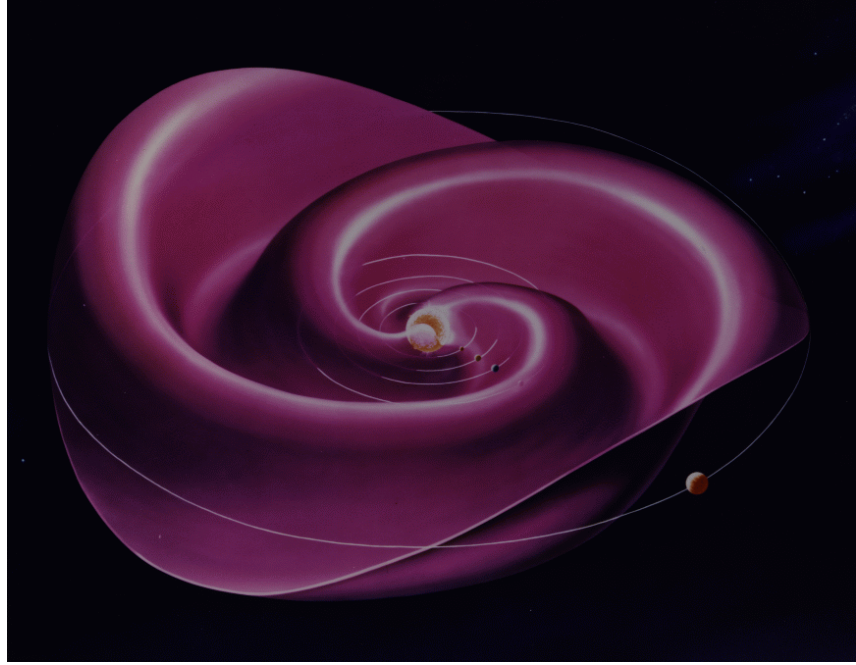


Figure 1.2: Illustration of the heliospheric current sheet, across which the sense of the IMF reverses, showing its north-south deflection due to the tilt of the solar magnetic equator, and the spiral structure which forms due to convection with the outward flowing solar wind. The orbits of the planets are indicated. Image credit: NASA/GSFC.

The ‘bow shock’ is formed upstream of the magnetosphere as the super-magnetosonic solar wind is reduced to sub-sonic speeds, and flows around the magnetosphere. Consequently, there is a layer of shock-heated sub-sonic solar wind plasma surrounding the magnetosphere, termed the magnetosheath, though this is rapidly accelerated and returns to supersonic speeds downstream from the ‘nose’ of the bow shock.

The nature of the interaction between the solar wind plasma and the planetary magnetic field was first suggested by *Chapman and Ferraro* [1930], and consists of the formation of a thin current sheet ,termed the magnetopause, between the weakly magnetised solar wind and the planetary field, in which strong electrical currents flow, termed Chapman-Ferraro currents. These currents close wholly within the magnetopause, and produce the field configuration depicted in Figure 1.3, while the $\mathbf{j} \times \mathbf{B}$ force opposes the incident shocked solar wind and deflects it. The size of the magnetosphere is then determined by the balance of pressures across the magnetopause,

$$\rho_{sw} V_{sw}^2 = \frac{B_{ms}^2}{2\mu_0}, \quad (1.32)$$

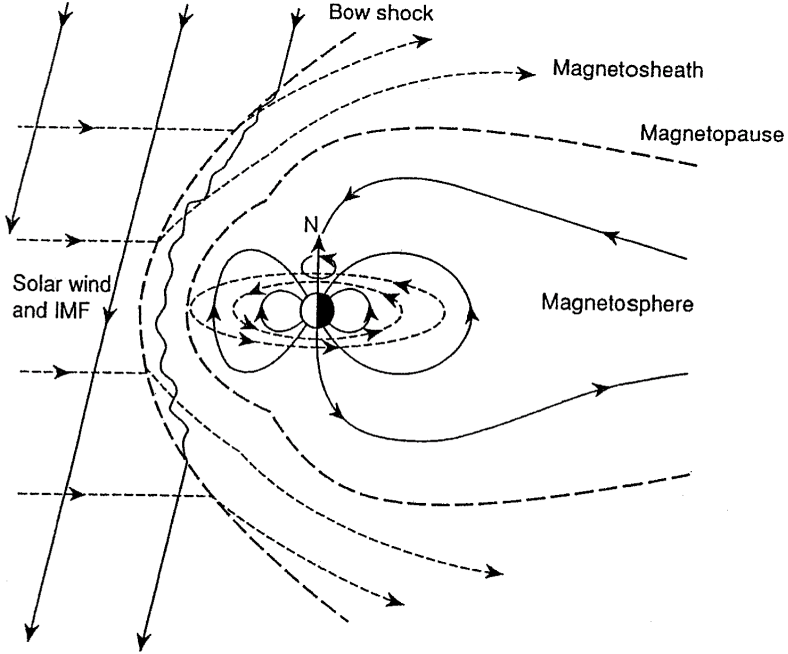


Figure 1.3: Sketch of the Earth's magnetosphere in the configuration initially proposed by *Chapman and Ferraro* [1930], in which there is no transport of material and magnetic flux across the magnetopause boundary. IMF and planetary field lines are shown by the solid lines, plasma streamlines by the short dashed lines, and the magnetopause and bow shock surfaces by the long dashed lines. From *Cowley* [1991].

in which ρ_{sw} is the solar wind dynamic pressure, V_{sw} its velocity, B_{ms} is the magnetospheric field inside the boundary, and where the contributions due to the field embedded in the IMF and the plasma in the magnetosphere have been neglected. However, in reality the situation is often more complex than that depicted in Figure 1.3. The solar wind cannot generally be considered as unmagnetised as the IMF is embedded within it, and as discussed in the previous section both the strength and orientation of the IMF are variable, and it is compressed in the sub-solar magnetosheath. Consequently, when the IMF has a significant component anti-parallel to the planetary field, the magnetic Reynolds number R_m (equation (1.23)) will become small at the magnetopause due to the reversal in field over small length scales. This signals the localised breakdown of Alfvén's theorem, and allows magnetic 'reconnection' to occur at the dayside magnetopause, in which the planetary field lines become connected to the IMF. These are then referred to as 'open' field lines, as they have only a single planetary footprint, and therefore any plasma previously confined upon them in the

original quasi-dipolar field configuration is able to escape into the solar wind.

The cyclical process by which the IMF and planetary field lines reconnect and move through the magnetosphere is named the ‘Dungey cycle’, after its initial proposal by *Dungey* [1961], and is sketched in Figure 1.4. In the Dungey cycle, reconnection occurs at the dayside magnetopause along a magnetic X-line, formed when the IMF has a component anti-parallel to the magnetospheric field. This dayside reconnection opens the magnetospheric field lines to the solar wind, and they are then convected anti-sunward with the solar wind, driving ionospheric flows at their planetary footprints.

Continued dayside reconnection and anti-sunward convection builds up magnetic flux in the magnetotail, distending it and leading to a current sheet separating the north and south lobes. This strong current leads to the formation of a second reconnection site in the tail at low latitudes, and returns the open field lines to a closed, dipolar configuration. As they continue to flow around the planet back to the dayside, the return of these field lines to a dipolar configuration from their previously stressed (tail-like) configuration leads to local heating (acceleration) of the plasma contained upon them. The process is therefore cyclical, and allows for an ‘open’ magnetosphere in which flux is continually cycled, and allows penetration of solar wind plasma into the magnetosphere. Furthermore, it also is evident that through control of the dayside reconnection rate, the solar wind and the embedded IMF is able to exert its influence on the configuration of the magnetosphere, the size of the polar cap, and ionospheric and magnetospheric plasma flows, mainly through the direction of the IMF.

Together, these processes determine the overall configuration of the magnetosphere (at least, at Earth), as illustrated in Figure 1.5. Just inside of the magnetopause, boundary layers (the plasma mantle, low-latitude boundary layer and the cusp) are formed, which typically contain mixtures of both solar wind and magnetospheric plasma. Hot plasma is present on closed field lines at low latitudes in the tail, forming the ‘plasma sheet’, in which the tail current closes. The plasma in this region is broadly flowing sunwards. A ‘ring current’ flows around the planet, carried by plasma confined on quasi-dipolar field lines undergoing magnetic gradient- and curvature-

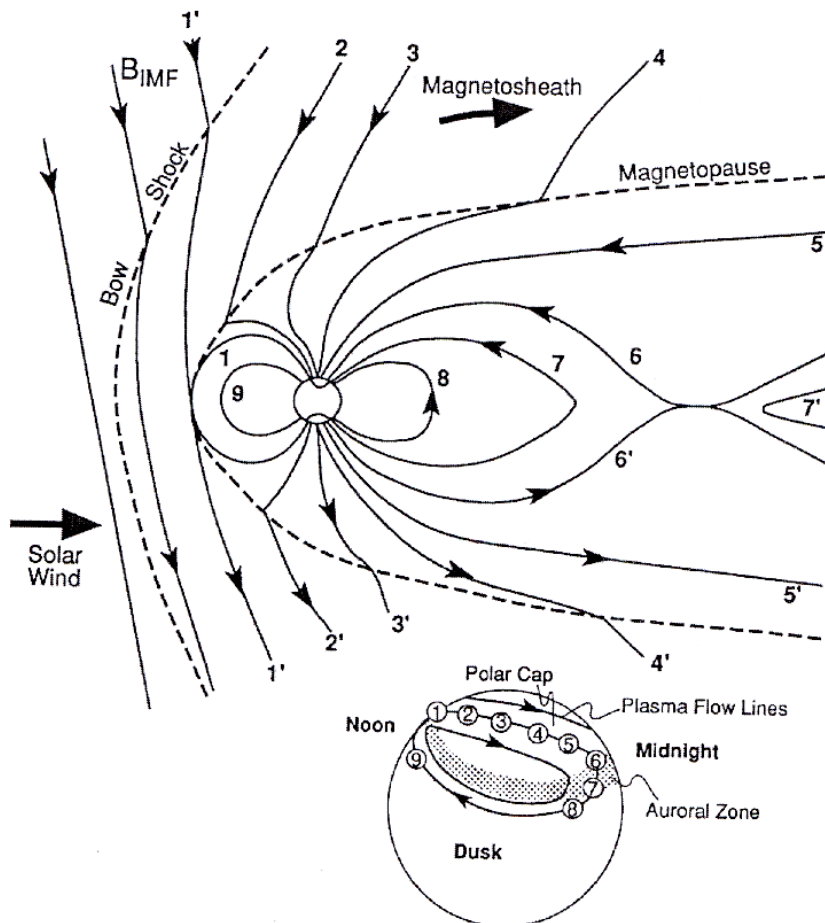


Figure 1.4: Sketch of the magnetosphere of the Earth, in which steady reconnection is occurring at both the dayside magnetopause and in the nightside plasma sheet. IMF and planetary field lines are shown by the solid lines, while the magnetopause is shown by the dashed line. Field lines are numbered sequentially illustrating the progress of the Dungey cycle, beginning with dayside reconnection of antiparallel IMF and planetary field lines at (1), antisunward convection with the IMF (2-5), tail reconnection (6), the return of closed field lines to a dipolar state along with plasmoid release (7, 8), and return to the dayside (9). The inset shows the motion of the footprints of the field lines in the ionosphere, and are similarly numbered. From *Hughes* [1995].

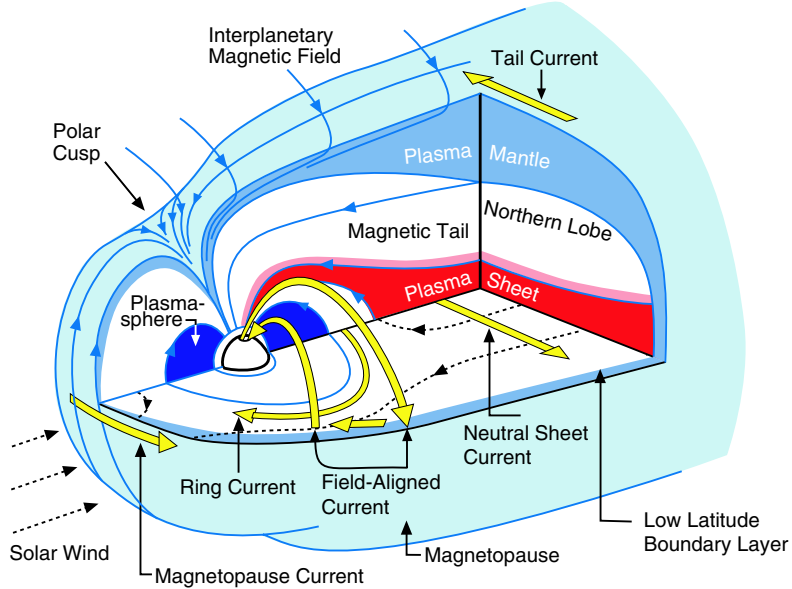


Figure 1.5: Oblique illustration of the plasma boundaries, populations and currents in the magnetosphere of Earth. Field lines are shown by the light blue lines, plasma streamlines by the dashed black lines, currents by the yellow arrows, and the plasma populations are shaded as indicated in the figure. From *de Keyser et al.* [2005], after *Hughes* [1995].

drift (equations (1.10) and (1.13)), and produces a field that opposes that of the planet inside the current loop. Finally, close to the planet on closed field lines, which map to sufficiently low latitudes that they take no part in the Dungey-cycle, there is a region of cool, dense plasma of ionospheric origin which rotates near-rigidly with the planet, termed the plasmasphere.

While generic, the description of planetary magnetospheres provided above is most representative of that of the Earth. As can be seen from the tabulated parameters given in Table 1.1, the magnetospheres of Jupiter and Saturn differ in two important respects. Firstly, both possess substantial internal sources of plasma, in the form of material ejected from geologically active moons. At Jupiter, $\sim 1 \times 10^3 \text{ kg s}^{-1}$ of neutral sulphur dioxide is ejected from the volcanically active moon Io, and ionisation of this material forms a substantial plasma torus near its orbit, extending into the ‘magnetodisk’ at larger distances. A similar process takes place at Enceladus, as will be discussed in the next chapter. Secondly, the rapid rotation periods of the giant planets, combined with weaker coupling to the solar wind, produces corotation of the magnetosphere out to much larger radial distances than is the case for the

Parameter	Earth	Jupiter	Saturn
Heliocentric distance / AU	1	5.2	9.5
Equatorial radius / km	6,371	71,492	60,268
Rotation period / h	23.94	9.925	~10.5
Magnetic moment / T m ³	7.75×10^{15}	1.55×10^{20}	4.6×10^{18}
Dipole tilt	10.5°	10 °	<0.1 °
Typical IMF $ \mathbf{B} $ / nT	4	1	0.5
Typical solar wind dynamic pressure / nPa	1.7	0.07	0.015
Typical sub-solar magnetopause distance / planetary radii	10	50-100	21
Magnetospheric plasma source rate / kg s ⁻¹	~1	~10 ³	~200

Table 1.1: Magnetospheric parameters of Earth, Jupiter and Saturn compared. Tabulated from *Gombosi et al.* [2009].

plasmasphere at Earth, corresponding to most of the closed field region in those cases.

Chapter 2

Saturn and its magnetosphere

2.1 Overview

This chapter begins with a brief history of the exploration of Saturnian system, before discussing current understanding of its formation, the composition and interior structure of the planet, and its satellites and rings. The remaining part of this chapter is reserved for a detailed discussion of the Saturnian magnetosphere, the physics of which are of central importance in the chapters that follow.

2.2 Past exploration of the Saturnian system

Saturn is routinely visible with the naked eye in the night sky. With the invention of the telescope, Galileo (1564-1642) was the first to directly image the rings of Saturn, in ~1610. Puzzled by the apparent secular variation of their form and brightness, he proposed that the features he saw were in fact two ‘moons’ of the planet. Due to Saturn’s 26.7° axial tilt relative to the ecliptic plane normal, the appearance of the rings as viewed from Earth varies significantly over the Saturnian ‘year’ (being 29.5 years). Some ~50 years after Galileo’s first observations, using more powerful telescopes, Huygens (1629-1695) first put forward the theory that the rings are a thin disc of material surrounding the planet about its rotational equator. In addition, he discovered Titan, the largest of Saturn’s many moons. Further observations over the

subsequent decades, with ever improving apparatus, lead to the discovery of multiple new moons of Saturn, by Cassini (1625-1712) and Herschel (1738-1822) among others.

Remote observations from ground-based, and more recently space-based telescopes across a broad range of wavelengths continued to further our understanding of the Saturnian system. Flybys made by Pioneer 11 and Voyagers 1 and 2 during 1979-1981, each equipped with a suite of scientific instruments afforded the first opportunity to undertake ‘in-situ’ observations. It is worth noting that Pioneer 11, the first of the trio, was launched from Earth in 1973, only \sim 16 years after the launch of the first man-made satellite. Communication was lost with Pioneer 11 in 1995, though both Voyager spacecraft still function and continue to transmit data back to Earth.

The trajectories of these three spacecraft through the Saturnian system are shown in Figure 2.1, in the Kronographic solar magnetic (KSM)¹ coordinate system, in which X is positive towards the Sun, Y is positive towards local dusk and Z completes the right-handed set. Labels along each trajectory indicate the day of year (in 1979, 1980, and 1981 for Pioneer 11, Voyager 1, and Voyager 2 respectively) along with crossings of the bow shock (S) and magnetopause (M).

Remote exploration of the Saturnian system has continued to the present day, with distant radio observations being made with the Ulysses solar orbiter from 1994 to 2008, and more recently with the Cassini-Huygens mission, details of which are discussed in Chapter 3.

2.3 Formation

Many open questions remain concerning the formation of Saturn in the early solar system. The current accepted estimate for the age of the universe is $\sim 13.7 \times 10^9$ years, with the collapse of the proto-solar nebular and the beginning of nuclear fusion in the Sun occurring some $\sim 4.6 \times 10^9$ years ago. Numerical simulations suggest that the gas giant planets formed relatively rapidly from the proto-planetary disc, typically within a few 10^6 years. It is believed likely that they reached their current orbits only after a

¹A full list of acronyms used in this thesis is provided in Appendix C.

period of inward migration, having formed further away from the Sun [Johnson and Estrada, 2009]. A connection between this inward migration and the possibility of an interval for which a 1 : 2 orbital resonance between Jupiter and Saturn was in effect and the epoch of the ‘late heavy bombardment’ some $\sim 3.9 \times 10^9$ years ago has been suggested [Gomes *et al.*, 2005]. Much less is understood about the formation of the moons and rings of Saturn.

2.4 Moons and rings

Saturn has 61 moons, most of which are only a few km in diameter. Key physical parameters are given in Table 2.1 for the innermost large moons, specifically those which orbit within the magnetosphere. However, Saturn’s largest moon, Titan, is occasionally external to the magnetosphere during its orbit through the dayside [e.g. Bertucci *et al.*, 2008], and is the only moon in the solar system known to have a significant atmosphere, composed largely of molecular nitrogen [Strobel *et al.*, 2009]. It is a differentiated ‘rocky’ body, most likely with a sub-surface layer of water ice. The Huygens descent probe, part of the Cassini-Huygens mission to Saturn outlined in Chapter 3, was the first probe to land on and return images and science data from the surface of Titan, some ~ 350 years after it was discovered by the probe’s namesake. However, as concerns the central topic of this thesis, despite its substantial size in comparison to its companions in the Saturn system, Titan has, at best, only a minor influence. Surprisingly, it is one of the smaller moons, Enceladus, that is of most significance.

Orbiting in the interior of the Saturnian system $\sim 1 R_S$ beyond the outer edge of the visible rings, Enceladus has both a layer of surface water ice and a differentiated or partially differentiated rocky core. Crucially, it is in a 2:1 orbital resonance with Dione, which imposes significant periodic tidal forces on the small moon as it orbits Saturn. These tidal forces result in a regular ‘flexing’ of Enceladus, with the heat deposited into the moon by this process expected to account for most of the ~ 6 GW excess thermal radiation observed from its surface [Spencer *et al.*, 2009]. It is believed that

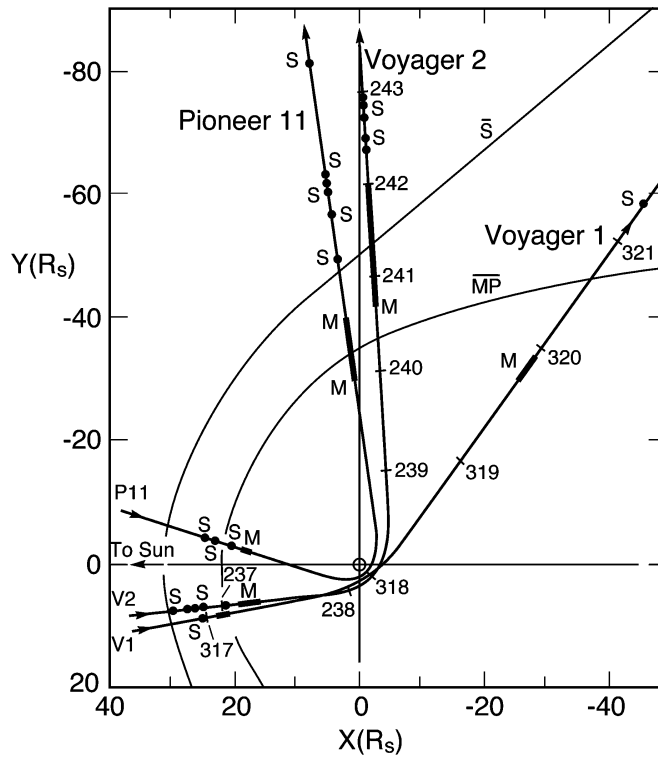


Figure 2.1: Plot showing the trajectories of the Pioneer 11, Voyager 1 and 2 flybys of Saturn, in the KSM coordinate system. Labels along each trajectory indicate the day of year in 1979, 1980 and 1981 for the three flybys, respectively, along with observed crossings of the bow shock (S) and magnetopause (M). From Dougherty *et al.* [2004].

	Mimas	Enceladus	Tethys	Dione	Rhea	Titan
Orbital radius / R_S	3.1	3.9	4.9	6.3	8.7	20.3
Orbital period / day	0.942	1.370	1.888	2.737	4.518	15.945
Mean radius / km	198	252	533	562	764	2576
Mass / 10^{20} kg	0.375	1.079	6.175	10.96	23.07	1350
Density / g cm ⁻³	1.150	1.608	0.973	1.476	1.233	1.880
Discoverer	W. Herschel	W. Herschel	G. Cassini	G. Cassini	G. Cassini	C. Huygens
Year	1789	1789	1684	1684	1672	1655

Table 2.1: Masses and orbital characteristics of some of Saturn's moons, from Jacobson *et al.* [2006].

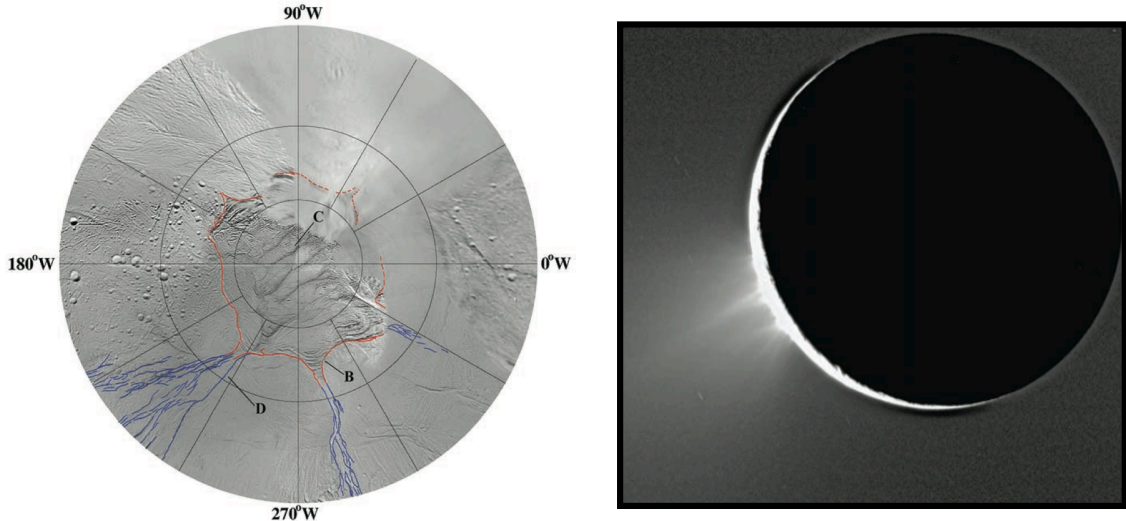


Figure 2.2: ISS images of Enceladus. Left, composite projected images showing the southern polar ‘tiger stripes’ labeled ‘C’, the surrounding circumpolar tectonic margin (red) and young tension fractures (blue). Right, image showing the water ice plume emitted from the tiger stripes. From *Porco et al.* [2006].

this tidal heating is sufficient to cause partial melting and/or evaporation of the subsurface ice in the southern polar regions of the moon. This process is thought to play a significant role in the generation of the ‘plumes’ of water-ice particles ejected into the Saturnian magnetosphere through ~ 500 km long fissures in Enceladus’s southern polar ice sheet [Dougherty *et al.*, 2006; Spencer *et al.*, 2009].

An image of these fissures, termed ‘tiger stripes’, is shown in Figure 2.2. The existence of the plume was first inferred from Cassini magnetometer data through detection of a significant deflection of the background Saturnian magnetic field over the south pole of Enceladus, caused by the presence of the outgassing conducting medium. The rate at which water ice is vented from Enceladus is $\sim 200 \text{ kg s}^{-1}$, and appears to be effectively constant over the interval studied thus far [Hansen *et al.*, 2008]. The Enceladus plume is most likely the dominant source of the material in the E-ring, along with the water-group neutral gas and plasma in the magnetosphere.

While not visible from Earth with the naked eye, Saturn’s substantial ring system can be readily seen with low-powered optics. Saturn’s ring system is shown in Figure 2.4, in which (from outermost to innermost) the diffuse E and G rings, the faint, thin F ring and the ‘main’ A, B, and C rings can be seen. The rings extend

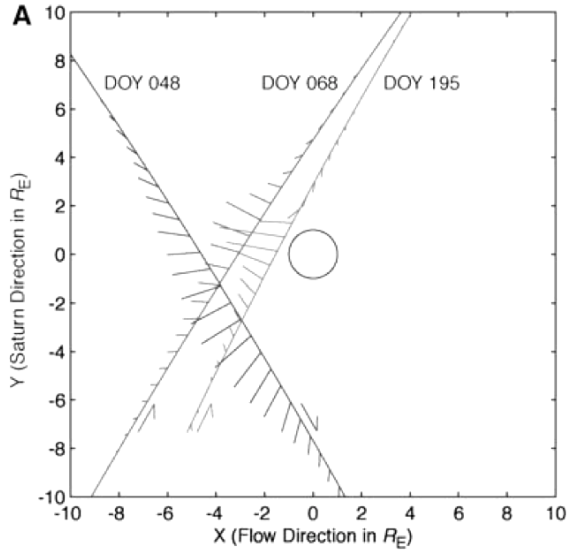


Figure 2.3: Geometry of the first three Enceladus flybys, with residual magnetic field vectors plotted along the trajectory showing the perturbing effect of the plume over the southern hemisphere of the moon. From *Dougherty et al.* [2006].

from ~ 0.1 to ~ 1.4 R_S above the 1-bar pressure ‘surface’ of Saturn, and are usually grouped into separate rings based on their characteristics (principally their optical depth) and their location. The ring system has a total mass of $\sim 3 \times 10^{19}$ kg, similar to that of one of Saturn’s small moons, e.g. Mimas, and is composed of $\sim 99.9\%$ water ice, with the observed distribution of ring particle sizes ranging over several orders of magnitude [see e.g. *Cuzzi et al.*, 2009].

2.5 Interior and magnetic field

2.5.1 *Interior composition and structure*

Saturn is comprised of $\sim 96\%$ hydrogen, $\sim 3\%$ helium, $\sim 0.4\%$ methane, and traces of heavier elements and more complex molecules [*Fouchet et al.*, 2009]. It has a mass of 5.7×10^{26} kg, ~ 95 times that of the Earth [*Jacobson et al.*, 2006]. The equatorial radius of the 1 bar pressure surface is 60,268 km = $1 R_S$ (generally taken to be the ‘reference surface’), while its radius at the poles is 54,364 km. Consequently, it is the least dense planet in the solar system, though it is still believed to possess a rocky core of perhaps $\sim 15\text{--}20$ Earth-masses [*Fouchet et al.*, 2009].

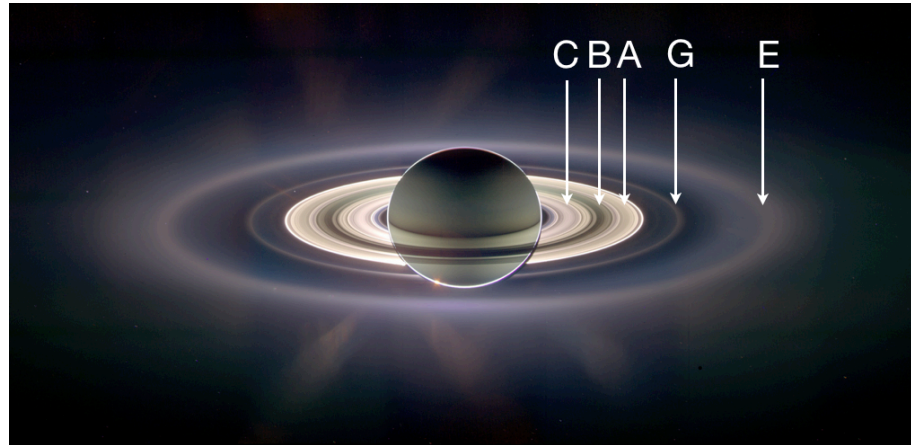


Figure 2.4: Saturn viewed from Cassini in eclipse, showing the structure of the main A, B, and C rings along with the tenuous E and G rings. Image Credit: NASA/JPL.

2.5.2 Magnetic field

Saturn's magnetic field is believed to be generated by a dynamo operating in a conducting layer of metallic hydrogen in the interior of the planet. Uniquely among the other planets of the solar system, Saturn's magnetic field is axisymmetric [Smith *et al.*, 1980; Connerney *et al.*, 1982]. Measurements made using Cassini magnetometer data give an upper limit to the tilt between the planet's spin and magnetic axis of $\sim 0.1^\circ$ [Burton *et al.*, 2010]. Furthermore, there is no evidence for secular variation in the field [Cao *et al.*, 2011].

Several models have been produced that describe Saturn's internally generated magnetic field using sets of spherical harmonics, initially using Voyager and Pioneer data [Acuña *et al.*, 1983; Connerney *et al.*, 1984]. In the absence of electric currents, the magnetic field \mathbf{B} is described by a scalar potential function V ,

$$\mathbf{B} = -\nabla V, \quad (2.1)$$

where V is given by the infinite sum

$$V = a \sum_{n=1}^{\infty} \left(\frac{a}{r}\right)^{n+1} T_n^i, \quad (2.2)$$

in which

$$T_n^i = \sum_{m=0}^n P_n^m(\cos\theta) [g_n^m \cos(m\varphi) + h_n^m \sin(m\varphi)]. \quad (2.3)$$

From	Model			
	SOI Acuña <i>et al.</i> [1983]	SPV Davis and Smith [1990]	Z3 Dougherty <i>et al.</i> [2005]	GD Burton <i>et al.</i> [2010]
g_1^0 / nT	21248	21225	21084	21136
g_2^0 / nT	1613	1566	1544	1526
g_3^0 / nT	2683	2332	2150	2219
	$g_n^m \equiv 0$ for $n > 3$ or $m \neq 0$, and $h_n^m \equiv 0$			
$\Delta Z / R_S$	0.038	0.037	0.037	0.036

Table 2.2: Saturn internal field Gauss coefficients for various models, determined from field data under the assumption of axisymmetry. Values given are adjusted such that they correspond to a planetary radius $1 R_S = 60,268$ km in each case.

In the above expressions, a is the planetary radius, r is radial distance from the centre of the planet, θ is colatitude, φ is azimuth, $P_n^m(\cos\theta)$ are Schmidt-normalised Legendre polynomials of degree n and order m , and g_n^m and h_n^m are internal and external ‘Gauss coefficients’ (to be determined from measured magnetic field data). In practice, incomplete coverage of a spacecraft’s trajectory around a planet will limit the order to which the Gauss coefficients can meaningfully be determined, and often there will be substantial ‘coupling’ between them. Values of the Gauss coefficients for various models of Saturn’s internal field are given in Table 2.2, where only the first three axisymmetric terms have been resolved to date.

The dipole tilt angle α between the spin and magnetic axis is given by

$$\alpha = \arccos \left(\frac{g_1^0}{\sqrt{(g_1^0)^2 + (g_1^1)^2 + (h_1^1)^2}} \right), \quad (2.4)$$

which is identically zero for all of the models listed in Table 2.2. In each case the non-axisymmetric Gauss coefficients are taken to be identically zero, as no statistically significant evidence has been found to suggest otherwise.

The lack of any measurable asymmetry in Saturn’s magnetic field is by far its most puzzling feature, as this apparently directly contradicts the theorem put forward by *Cowling* [1933], which forbids the generation of an axisymmetric field by a dynamo process. Possible resolutions of this paradox have been suggested which invoke a differentially rotating conducting layer between the dynamo itself and the surface of the planet, which ‘screens out’ the non-axisymmetric fields that are produced by the

dynamo [Stevenson, 1980; Stanley, 2010].

As a result of the non-zero axial g_2^0 quadrupole term, Saturn's 'magnetic equator' is displaced northward from the kronographic equator by an amount ΔZ given by

$$\Delta Z = a \frac{g_2^0}{2g_1^0}, \quad (2.5)$$

with calculated values of ΔZ shown in Table 2.2. Consequently, the field strength in the northern polar ionosphere is $\sim 17\%$ stronger than in the southern, an effect which may play a significant role in the physics of the magnetosphere.

2.6 Atmosphere and ionosphere

Saturn's atmosphere is highly dynamic, with complex long-lived storms and circulation systems embedded in alternating zonal winds which reach speeds of $\sim 500 \text{ m s}^{-1}$ at the equator, and are generally flowing eastwards as shown in Figure 2.5. The presentation in Figure 2.5 assumes the International Astronomical Union (IAU) reference rotation period for Saturn. However, for reasons that will be discussed in section 2.8, this IAU rotation period is now no-longer generally accepted as reflecting the true rotation period of the planet (it having been derived from Voyager measurements of modulations in an intense radio emission originating from several planetary radii above Saturn's polar regions, that was then believed to be related to some rotating magnetic anomaly). Employing a shorter rotation period, as postulated e.g. by *Anderson and Schubert* [2007] would result in a more balanced system of eastward and westward flowing zonal winds (though still dominated by eastward flow).

The zonal wind profile shown in Figure 2.5 relates principally to flows at the altitude of the tropospheric cloud tops. Frictional vertical coupling between the troposphere, the stratosphere and ultimately the thermosphere is the mechanism by which the rotation period of the deep interior of the planet is communicated into the magnetosphere, via the ionospheric plasma present in the thermosphere. Typical temperatures in the thermosphere are $\sim 300\text{-}500 \text{ K}$, several hundreds of K hotter than can be explained simply through solar heating [*Nagy et al.*, 2009]. The excess heating could well be

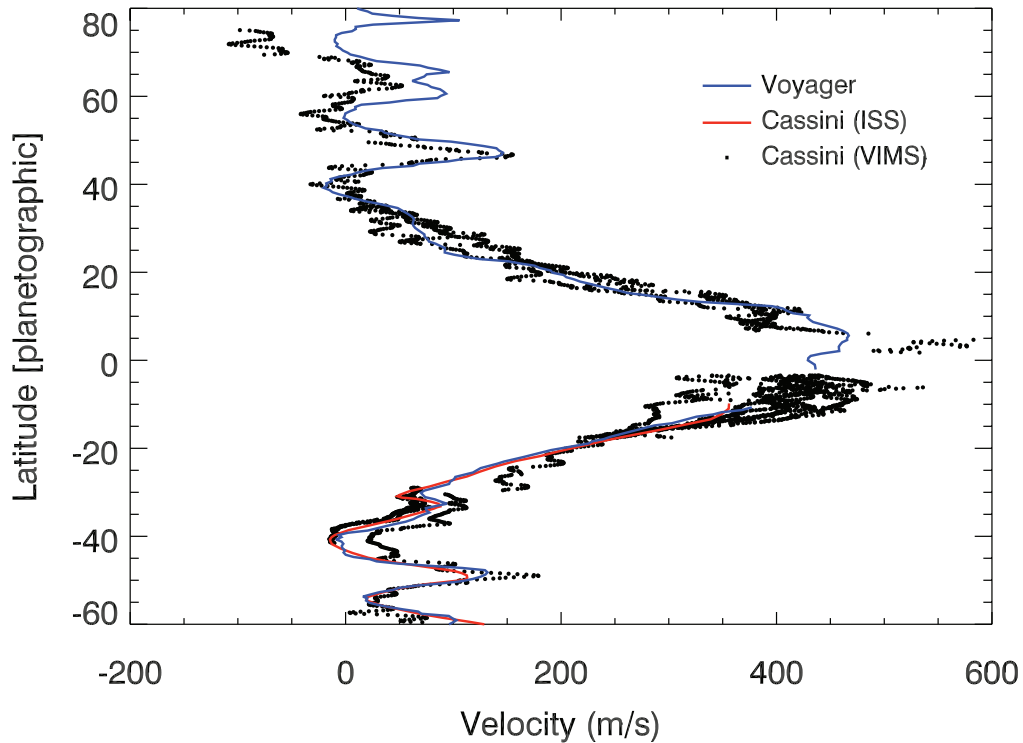


Figure 2.5: Latitudinal profile of zonal wind velocities as measured by both Voyager and Cassini. Positive velocities indicate eastward flow. From *Choi et al.* [2009].

provided by magnetospheric sources, through atmospheric Joule-heating caused by ion-neutral collisions in the ionospheric Pedersen conducting layer [e.g. *Cowley et al.*, 2004]. However, given the strong zonal wind structures observed, transporting this heat to lower latitudes remains a significant open issue.

Radio occultation performed using Voyager and Cassini readily yield vertical profiles of the ionospheric electron density. Modelling of the production, transport and destruction of ionospheric plasma can be used to estimate ion densities, as shown in Figure 2.6. H^+ is the dominant ion within the upper ionosphere, while the H_3^+ molecular ion becomes significant at lower altitudes.

2.7 Magnetosphere

2.7.1 Magnetopause and bow shock

Typically the sub-solar magnetopause boundary is located $\sim 22 R_S$ upstream of the planet, as compared to ~ 10 and $\sim 50\text{-}100$ planetary radii in the cases of Earth and

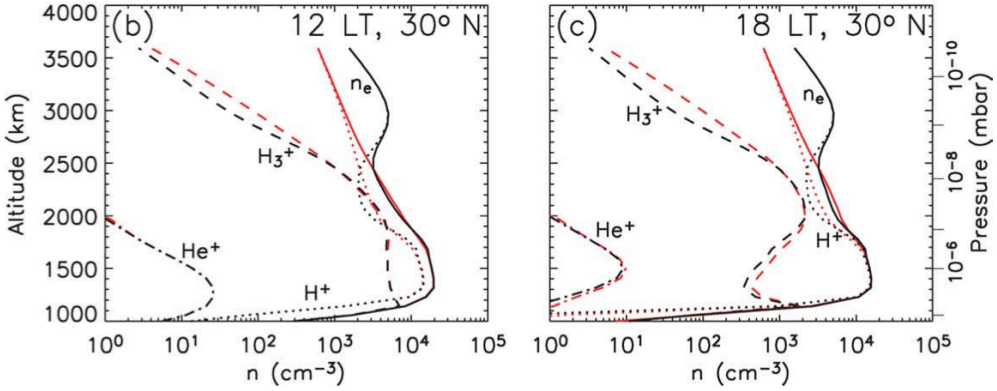


Figure 2.6: Models of Saturn’s ionosphere at 30° N latitude, computed at 12 h LT and 18 h LT respectively, in the northern hemisphere at equinox. Black curves show profiles computed using a computer code that includes only photochemical processes, while red shows the results of computations including diffusive transport of plasma. Altitudes given are relative to the 1-bar pressure surface. From *Moore et al.* [2004].

Jupiter, respectively. Empirical models of Saturn’s magnetopause and bow shock surfaces have been developed by fitting observed spacecraft crossings of these boundaries, normalised to the solar wind dynamic pressure, to conical functions. For example, *Slavin et al.* [1985] modelled the position of Saturn’s bow shock from the observed crossings in the Pioneer 11 and Voyagers 1 and 2 flyby data. More recently, *Achilleos et al.* [2006] and *Masters et al.* [2008] have used Cassini data to determine the position of the bow shock across a wider extent of the surface, finding that the sub-solar position of the bow shock, r_{BS} , lies at ~ 25 R_S for a solar wind dynamic pressure P_{SW} of ~ 0.03 nPa, and varies as $r_{BS} \propto P_{SW}^{-0.17}$. Similar modelling of the Saturnian magnetopause reveals that its sub-solar distance is typically ~ 20 R_S , again with a power-law dependence on the solar wind dynamic pressure [*Arridge et al.*, 2006]. Comparison with similar magnetopause models constructed for Jupiter and Earth suggests that at Saturn, the dependence of the distance to the sub-solar magnetopause upon the solar wind dynamic pressure is intermediate (weaker than at Jupiter, but stronger than Earth) [*Achilleos et al.*, 2008]. Evidence for a bi-modal distribution in the sub-solar magnetopause position has been presented by *Achilleos et al.* [2008], apparently the result of some internal processes rather than a similar bi-modality in the controlling solar wind parameters. Meanwhile, *Masters et al.* [2009, 2010] have presented observations of waves and wave-like structures on Saturn’s magnetopause

which they suggest are generated through the Kelvin-Helmholtz instability.

2.7.2 Plasma populations

There are many sources of plasma within Saturn's magnetosphere. The O⁺ and O²⁺ plasma that exists in the vicinity of the main ring system is most likely produced by photoionisation and magnetospheric charged particle sputtering of the icy ring material [e.g. *Young et al.*, 2005]. Outflow of ionospheric plasma from Saturn at high latitudes may provide a weak source of plasma into the magnetosphere. Somewhat unexpectedly, Titan does not appear to contribute much plasma into the magnetosphere, as evidenced by the lack of significant N⁺ densities [e.g. *Smith et al.*, 2007].

Outside of $\sim 3 R_S$, there is a significant neutral gaseous water torus, originating from the active geysers on Enceladus. Photoionisation and charge-exchange processes acting on this neutral material introduce a ‘water group’ plasma into Saturn’s inner magnetosphere, consisting principally of H⁺, O⁺, OH⁺, H₂O⁺ and H₃O⁺ (collectively referred to as ‘W⁺’, excluding the H⁺ component). Modelled ion distributions based on Cassini Plasma Spectrometer (CAPS) and Radio and Plasma Wave Science (RPWS) plasma data from the first ~ 4 years of the Cassini mission are shown in Figure 2.7, from which it is readily apparent that the heavier and denser water-group plasma is confined closer to the equatorial plane than the lighter proton plasma. The overall distribution of the magnetospheric plasma is shown schematically in Figure 2.8. The ‘cool’ plasma produced at the orbit of Enceladus slowly drifts outwards, whilst rotating in the same sense as the planet, though at sub-corotational speeds. The hotter, more tenuous plasma is most likely produced in ‘injection events’, associated with the centrifugal interchange instability [e.g. *Burch et al.*, 2005]. The influence of the plasmas in Saturn’s magnetosphere upon the configuration of the magnetic field is discussed below.

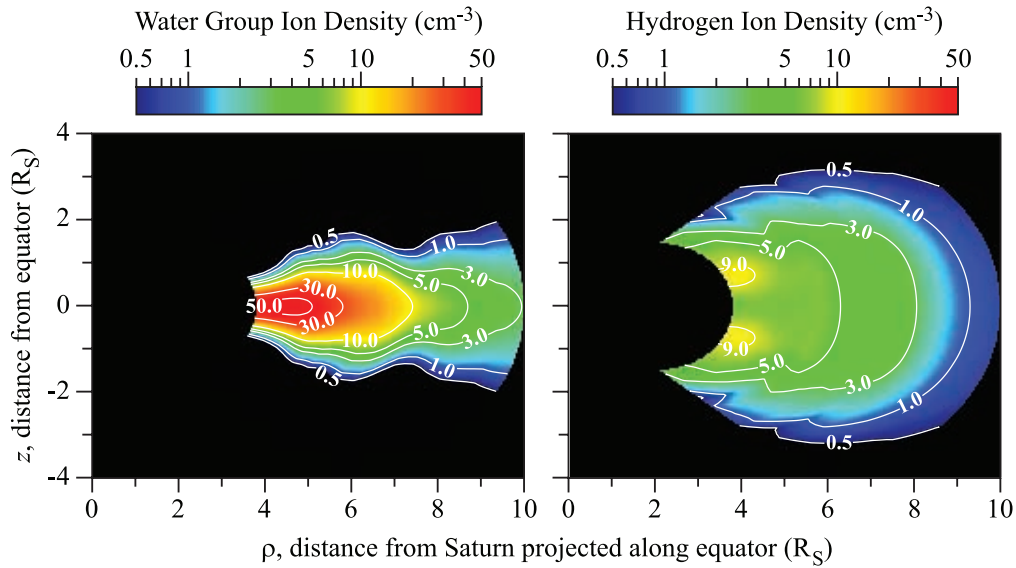


Figure 2.7: Modelled plasma densities in Saturn's inner magnetosphere, with water group and proton plasmas shown separately. From *Persoon et al.* [2009].

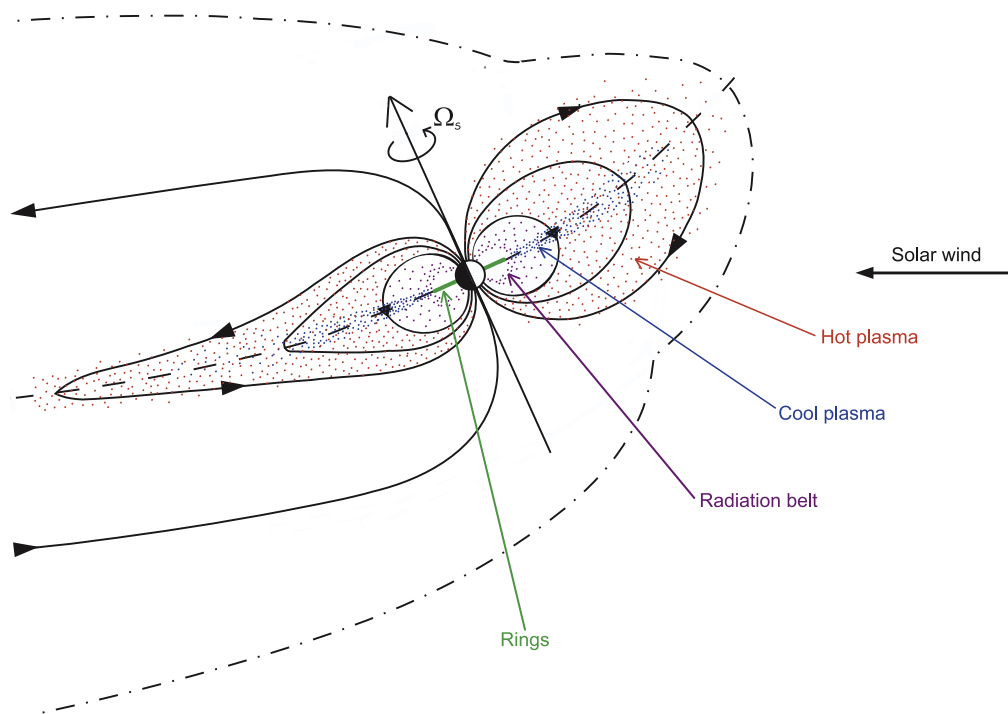


Figure 2.8: Sketch of Saturn's magnetosphere. The magnetic field is shown by the solid black lines, the plane of the plasma sheet by the dashed line, the magnetopause by the dot-dashed line, and the ring plane by the solid green line. The various plasma populations are indicated by the dotted shading. Blue shading indicates the 'cool' plasma (thermal energies less than ~ 10 eV), red the 'warm' and 'hot' (\sim keV to tens of keV), purple the trapped radiation belts (higher energies than the 'hot' plasma, up to tens of \sim MeV). From *Kellett et al.* [2009].

2.7.3 Configuration

The presence of a mass-loaded and sub-corotating plasma disc in the equatorial magnetosphere, coupled to the motion of the neutral atmosphere via the ionospheric footprints of the planetary field lines, induces a system of field aligned currents, closing through the equatorial plane in the magnetosphere and via Pedersen currents in the ionosphere, as is sketched in Figure 2.9. Theoretical models of this current system, originally developed for Jupiter by *Cowley and Bunce* [2001], employing empirical profiles of the magnetospheric plasma angular velocity data and ionospheric Pedersen conductivity have been presented [*Cowley and Bunce*, 2003; *Saur et al.*, 2004]. The relatively weak ionospheric field-aligned current densities that are required to maintain the observed sub-corotating plasma angular velocity profile are not thought to be sufficient to represent the source of the main auroral emission at Saturn. Rather, Saturn's aurora appear to be due to the strong shear in plasma velocity that occurs at the boundary between open and closed field lines [*Cowley et al.*, 2008; *Bunce et al.*, 2008].

Plasma streamlines in Saturn's equatorial plane are illustrated in Figure 2.10. The region within which the plasma is sub-corotating and slowly being transported radially outwards lies within the innermost dashed lines. Beyond this, the motion of the plasma is expected to be driven by two processes. Firstly, the rotation-driven ‘Vasyliūnas cycle’ removes plasma from the inner magnetosphere, through the formation of a magnetic ‘X-line’ in the magnetotail along which reconnection can take place, forming a plasmoid that moves down the tail [*Vasyliūnas*, 1983]. Secondly, the ‘Dungey cycle’, introduced in section 1.4, in which reconnection at the dayside magnetopause adds open flux to the system, driving plasma flow across the polar caps [*Dungey*, 1961]. The ensuing build up of flux in the magnetotail is balanced by the reconnection along another X-line in the magnetotail (not necessarily colocated with that expected from the Vasyliūnas cycle), driving equatorial plasma flows sunward, principally on the dawn side of the magnetosphere.

Azimuthal currents flowing in Saturn's equatorial magnetosphere generate a

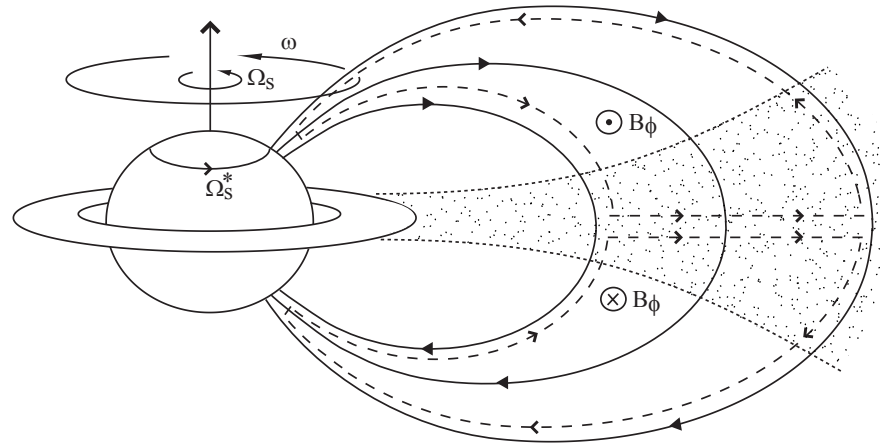


Figure 2.9: Sketch showing the ‘corotation enforcement currents’ (dashed lines) which couple the ionosphere to the equatorial magnetosphere, flowing parallel or anti-parallel the background planetary magnetic field (solid lines). Angular velocities of the planet, neutral atmosphere, and depicted field lines are indicated by the symbols Ω_S , Ω_S^* and ω , respectively, where it is assumed that $\Omega_S > \Omega_S^* > \omega$, at least on average. The sense of the azimuthal magnetic field perturbation B_ϕ implied is shown by the icons into and out of the plane of the figure, with the sense reversing between the northern and southern hemispheres. From Cowley and Bunce [2003].

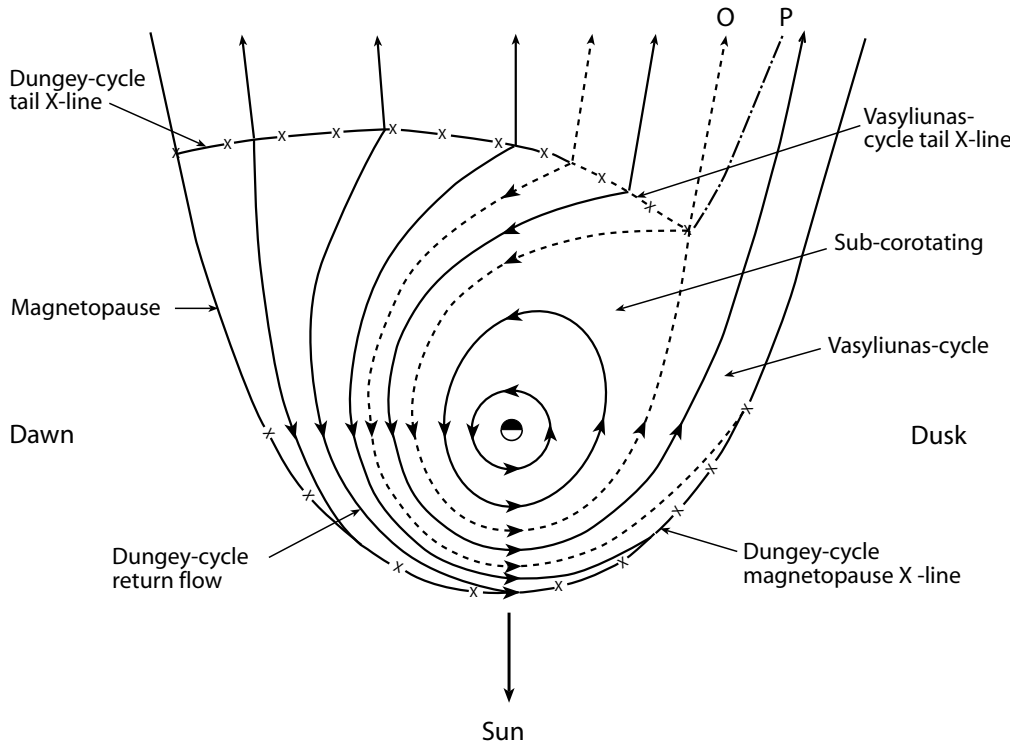


Figure 2.10: Sketch showing the motion of plasma in the equatorial magnetosphere arising as a consequence of simultaneously operating Dungey and Vasyliunas cycles. Plasma streamlines are shown solid, while boundaries between different flow regimes are otherwise indicated. From Cowley *et al.* [2004].

poloidal field which opposes that of the planet in the inner magnetosphere, displacing the field lines outward at the equator beyond their ‘dipolar’ configuration. *Connerney et al.* [1983] modelled this ring current as a cylindrically symmetric disc with inner and outer edges of 8 and 15.5 R_S , respectively, and half-thickness 3 R_S centred on the the equatorial plane. Fits to Voyager magnetometer data showed that the total azimuthal current flowing in an eastward (prograde) direction was ~ 10 MA (c.f. ~ 1 MA for Earth and ~ 300 MA for Jupiter). Using Cassini data, *Bunce et al.* [2007] have shown that the total azimuthal current is closely related to the sub-solar magnetopause distance, indicating that a more expanded magnetosphere corresponds to a stronger ring current and vice-versa. Modelled field lines, including the effect of this ring current are shown in Figure 2.11. More recently, *Kellett et al.* [2011] have shown that there is little evidence for systematic variations in ring current parameters with either time or local time (LT).

The north-south symmetry of the magnetosphere is seasonally disturbed by the action of the solar wind flowing obliquely to the planet (i.e., from the south to the north during southern summer conditions [*Arridge et al.*, 2008b] as depicted in Figure 2.12). *Arridge et al.* [2008b] modelled the vertical displacement z_{CS} of the plasma sheet from Saturn’s equatorial plane by fitting the function

$$z_{CS}(r, \theta_{Sun}) = \left[r - R_H \tanh\left(\frac{r}{R_H}\right) \right] \tan\theta_{Sun}, \quad (2.6)$$

where r is radial distance from the planet, θ_{Sun} is the latitude of the sub-solar point (referenced to the spin- and magnetic-axes). The sole free parameter in the above expression, the ‘hinging distance’ $R_H = 29 R_S$ was determined through fits to Cassini magnetic field data.

2.8 Planetary period oscillations at Saturn

2.8.1 Overview

Though initially detected in data obtained during the Pioneer and Voyager 1 and 2 flybys, the significance of near planetary rotation period oscillations in Saturn’s mag-

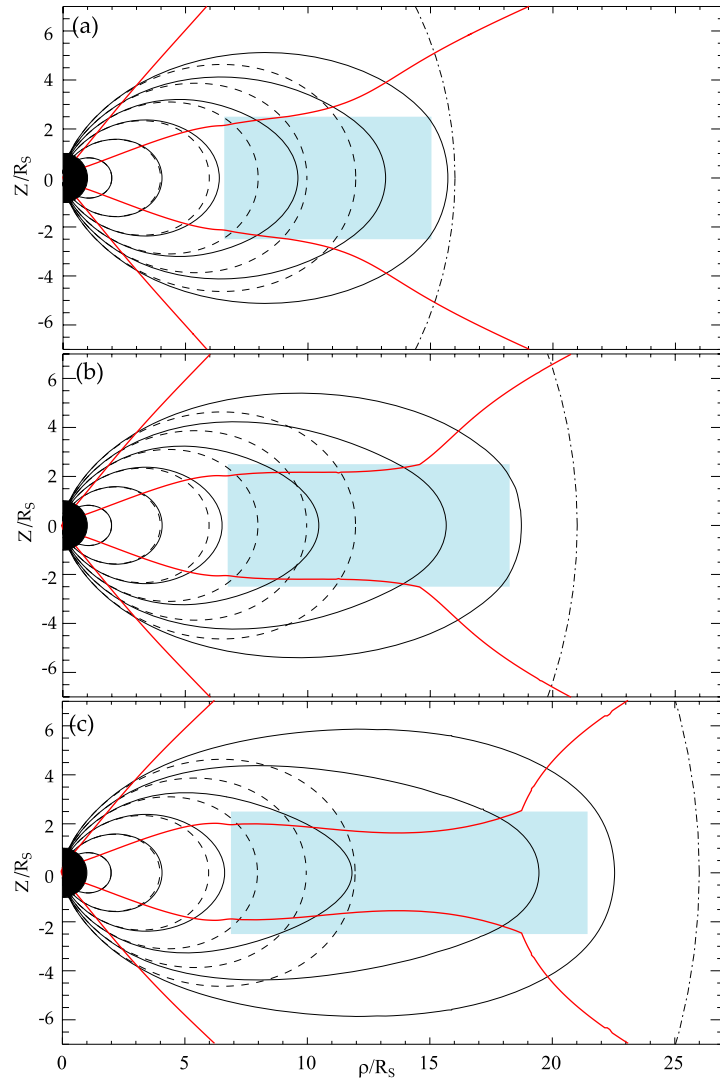


Figure 2.11: Plots of magnetic field lines shown in a meridional plane, with the distending effect of the ring current included for three different magnetopause and ring current configurations. From top to bottom, the sub-solar magnetopause is located at 16, 21 and 26 R_S , respectively, and the outer edge of the ring current correspondingly moves as modelled by *Bunce et al.* [2007]. In each case, black dashed lines show the internal planetary field lines, black solid lines include the effect of the ring current, which is flowing within the shaded blue region. Dot-dashed black lines show the position of the magnetopause, and the red lines bound the region where the inclination of the field lines to the equatorial plane is less than 30°. From *Bunce et al.* [2008].

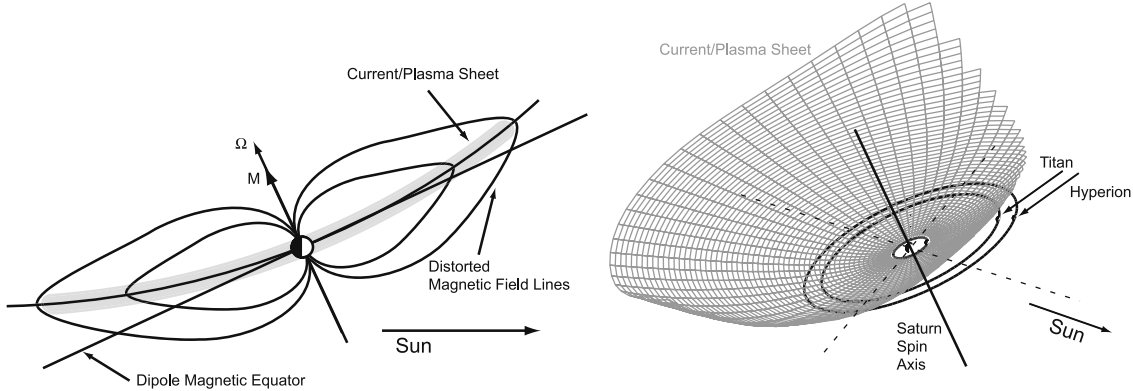


Figure 2.12: Schematic illustrating the deflection of Saturn's current sheet northwards out of the spin-equatorial plane due to the oblique flow of the solar wind during southern summer conditions. The sense of deflection is reversed during southern winter. From Arridge *et al.* [2008b].

netosphere was made fully apparent during the early portion of the Cassini orbital tour. Oscillations near the (assumed) ~ 10.5 h planetary rotation period have been detected in a multitude of phenomena, and throughout the magnetosphere. The oscillations detected in the magnetic field are the central subject of this thesis, and it is therefore necessary to review current understanding of these oscillations in some detail, as is done in this section.

2.8.2 Voyager and the SKR

None of the gas giant planets possess a visible solid surface that can be studied to discern their rotation period, and other methods must therefore be used. In the case of Jupiter, periodic variations in intense decametric radiation generated by unstable accelerated magnetospheric electrons, readily detectable even from Earth, have provided a high-accuracy determination of the planet's rotation period based on many years of continued study. The periodic modulation of the Jovian radio emission is caused directly by the $\sim 10^\circ$ tilt of the planet's magnetic axis relative to its spin axis, and the resultant periodic variation in the interaction between the planetary field and the Io plasma torus (being qualitatively similar to the Enceladus plasma torus at Saturn, mentioned above).

Qualitatively similar modulations in radio emissions originating from Saturn in

the Saturn kilometric radiation (SKR) by the Planetary Radio Astronomy (PRA) instruments on board the two Voyager spacecraft [Kaiser *et al.*, 1980], despite an apparent lack of a measurable tilt in the planet's magnetic axis (see section 2.5.2). Central to much of the analysis presented in this thesis, the SKR is a powerful ($\sim 10^9$ W) circularly polarised-emission, generated in the right-hand mode from the northern hemisphere and in the left-hand mode from the southern [Warwick *et al.*, 1981, 1982]. The dependence of the polarisation on the orientation of the local magnetic field is a consequence of the process by which the SKR is believed to be generated, namely the cyclotron maser instability [Wu and Lee, 1979; Zarka, 1998]. The SKR propagates from its source regions some $\sim 2\text{-}3 R_S$ above the planet's surface as a free-space extraordinary (X) mode wave [Warwick *et al.*, 1981, 1982]. Due to limitations of the PRA instruments, which were not able to provide measurements of the incident directions of radio waves within the SKR frequency band (centred near ~ 200 kHz), the locations of the SKR sources were inferred from the observed frequency cutoff, which, assuming generation by the above instability, is equal to the local electron gyrofrequency (equation (1.2)) [Wu and Lee, 1979; Zarka, 1998]. This places the sources at auroral latitudes ($|\lambda|$ greater than $\sim 60^\circ$), while considerations of the visibility of SKR emission along the flyby trajectories indicated that the strongest sources of SKR were present in the dawn to noon sectors (06 - 12 h LT) [Kaiser *et al.*, 1981; Kaiser and Desch, 1982; Lecacheux and Genova, 1983].

During the Voyager epoch, the period of these modulations was found to be ~ 10.7 h [Desch and Kaiser, 1981], as is shown in Figure 2.13, close to the expected value of the Saturnian rotation period based on several centuries of observations of the motion of features in Saturn's atmosphere. The phase of the modulation of the SKR was observed to be unchanged between the inbound and outbound passes of the Voyager flyby trajectories, at LTs near noon and dawn respectively (see Figure 2.1), thus indicating a 'strobe-like' (or 'clock-like') modulation independent of the position of the observer, rather than a rotating source like a lighthouse beam [Warwick *et al.*, 1981; Gurnett *et al.*, 1981]. In spite of the apparent lack of any rotational component, the SKR period determined by Desch and Kaiser [1981] was used to define a rotating coordinate

system, the Saturn longitude system (SLS), and was adopted by the IAU as the *de-facto* rotation period for Saturn [Seidelmann *et al.*, 2007].

Restating the definition of the SLS coordinate system in the framework employed throughout this thesis, the ‘longitude’ of an observer λ_{SLS} is given by

$$\lambda_{SLS}(t, \varphi) = \Phi_{SKR}(t) - \varphi + 100^\circ, \quad (2.7)$$

where the temporal phase of the SKR, Φ_{SKR} , is given by

$$\Phi_{SKR}(t) = \Omega_{SLS}(t - t_0) = 360^\circ \frac{(t - t_0)}{\tau_0}, \quad (2.8)$$

in which time t is measured in days, t_0 is the time of the SLS reference epoch (00:00 h UT, 1 January 1980), the angular rotation speed $\Omega_{SLS} = 810.76^\circ \text{ day}^{-1}$, equivalent to a period τ_0 of 10.7628 h or 0.4497 d, φ is the azimuth of the observer in degrees, measured positive towards dusk from midday (00:00 h LT is equivalent to $\varphi = 0^\circ$). The 100° introduced in equation (2.8) by Kurth *et al.* [2007] is such that the SKR power, which varies as $\cos(\Phi_{SKR}(t))$ is at a maximum when the 100° ‘longitude’ passes through the sub-solar point, $\varphi = 0^\circ$. (This arbitrary definition was adopted by Kurth *et al.* [2007] such that the peak in SKR power occurred at the same ‘longitude’ as in the Voyager era data as determined by Kaiser and Desch [1982].) The delay proportional to the ‘one way light travel time’ between the planet and the observer is negligible within the Saturnian system, and has been ignored in these and all following related expressions.

2.8.3 Subsequent discoveries regarding the SKR

Recent discoveries made since the turn of the century have extended understanding of the SKR in several important respects.

First, it has been shown, initially using Ulysses data and in more detail with Cassini, that the SKR modulation period varies slowly over time, typically by fractions of a percent over yearly intervals – much too large a rate to be associated directly with the rotation of the planet itself [Galopeau and Lecacheux, 2000; Gurnett *et al.*, 2005; Kurth *et al.*, 2007, 2008]. The revised ‘longitude’ systems presented by Kurth *et al.* [2007, 2008]

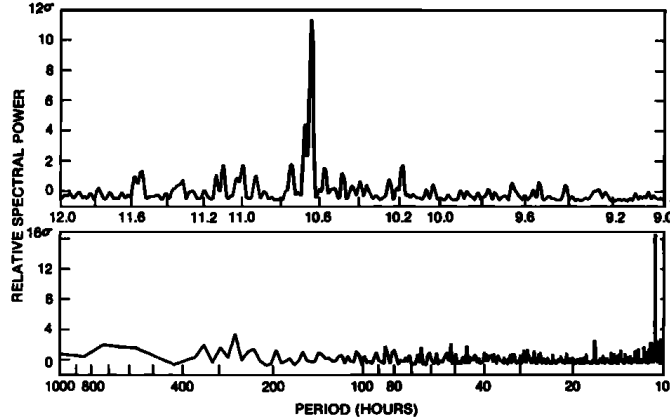


Figure 2.13: Periodogram of the SKR as measured by the Voyager-1 and -2. The peak lies at a period of ~ 10.69 h. From *Desch and Kaiser* [1981].

therefore employ a non-linear form of $\Phi(t)$ in equation (2.7) to account for the slow change in the observed SKR modulation period.

Furthermore, it has also been demonstrated that the modulation periods corresponding to emissions from the northern and southern hemispheres are distinctly different, ~ 10.6 h in the north and ~ 10.8 h in the south during the southern summer conditions that prevailed in the initial pre-equinox Cassini epoch, 2004–2009 [Gurnett *et al.*, 2009a, 2010b; Lamy, 2011]. Indeed, retrospective analysis of both the Ulysses and Voyager data suggests that secondary signals corresponding to the northern hemisphere sources were also present before its significance was understood from Cassini data [Gurnett *et al.*, 2010b]. Separated northern and southern SKR emission periods are shown in Figure 2.14, along with Saturn’s season. It has been suggested by Gurnett *et al.* [2010b] and Lamy [2011] that the periods of the northern and southern SKR sources converge and cross at a common value of ~ 10.7 h shortly after Saturn equinox, though similar such events have not yet been detected in related periodic phenomena.

Finally, it has also been demonstrated from visibility considerations and use of the direction-finding capability of the Cassini Radio and Plasma Wave Science (RPWS) experiment [Gurnett *et al.*, 2004], that SKR emission sources are not confined to the dawn-to-noon sector [Farrell *et al.*, 2005; Cecconi *et al.*, 2009]. Rather, they are broadly distributed around a circumpolar oval in each hemisphere that is coincident with the

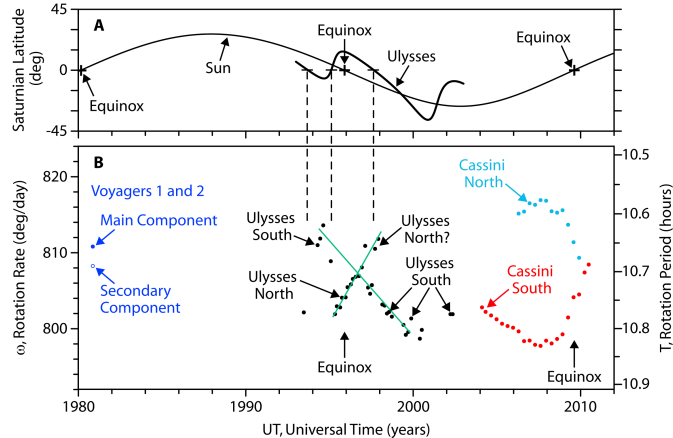


Figure 2.14: Plot of SKR period as determined from both Voyager, Ulysses and Cassini data. The top panel shows the latitudes of the Sun and Ulysses in the Saturnian system. The lower panel shows the measured SKR angular frequency on the left axis, and period (decreasing) on the right. In the case of Ulysses and Cassini measurements, the source hemisphere is inferred from the spacecraft latitude. For the Voyager data, the ‘Main component’ is assumed to relate to the southern source. From Gurnett *et al.* [2010b].

ultraviolet (UV) auroral oval [Lamy *et al.*, 2009]. However, the emitted power strongly maximises in the mid-morning sector as found from Voyager results, where ultraviolet (UV) auroral emissions are also usually brightest [Trauger *et al.*, 1998; Clarke *et al.*, 2005; Grodent *et al.*, 2005; Gérard *et al.*, 2006]. Most recently it has been shown that the UV emission power in the dawn sector is also modulated near the planetary period, in phase with the SKR emissions from the corresponding hemisphere [Nichols *et al.*, 2010a].

In view of these results, the models put forward by Kurth *et al.* [2007, 2008] and Lamy [2011] are hereinafter referred to SKR ‘phase models’ rather than ‘longitude systems’, as they more properly describe the modulation in SKR power, and cannot be said to truly reflect the rotation period of the planet, which cannot be changing by $\sim 1\%$ per year² and different north-south.

2.8.4 Magnetic field oscillations

Magnetic field oscillations at a period corresponding to the dominant SKR emission were first detected in Pioneer and Voyager data during subsequent reanalysis by Es-

²Slowing Saturn’s rotation by $\sim 1\%$ per year would require $\sim 2 \times 10^{26}$ W, or approximately half the power output of the Sun.

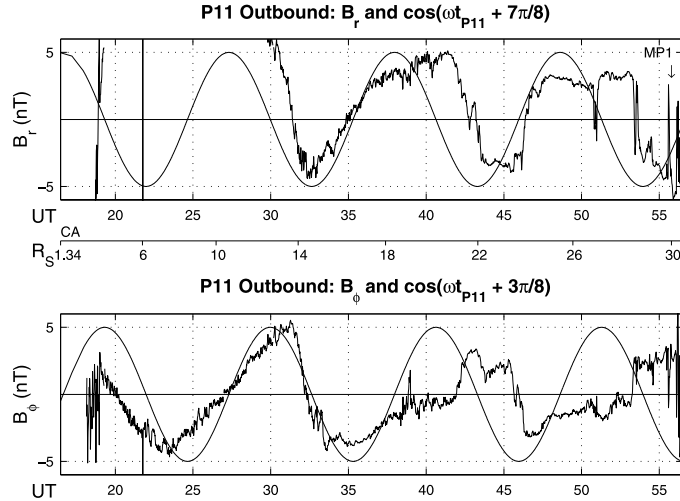


Figure 2.15: Radial and azimuthal component magnetic field oscillations as measured by Pioneer 11 during its outbound pass. The baseline shows time in hours, with the plot covering a total of ~ 40 h from CA to the first magnetopause crossing at ‘MP1’. Sinusoids at the 10h 39m 24s period deduced from SKR data by *Kaiser et al.* [1980] are overplotted, with the sinusoid in the lower panel lagging by $\pi/2$ radians (90°). From *Espinosa et al.* [2003b].

pinosa and Dougherty [2000], who showed the presence of oscillations with amplitudes of $\sim 1\text{-}2$ nT in both the radial (r) and azimuthal (φ) field components. Data from these two field components obtained on the outbound pass of Pioneer 11 are shown in Figure 2.15, along with a model sinusoidal oscillation at the SKR period overplotted. Further analysis showed that phasing of the oscillations was such that the φ field component was in lagging quadrature with the r in each case, and consequently the field was ‘quasi-uniform’, apparently everywhere pointing in a fixed direction in a frame rotating in the same sense as the planet at the SKR period [*Espinosa et al.*, 2003b].

It is noted that these oscillations cannot be due to a tilt in the planet’s internally generated magnetic field, as the amplitude of any such oscillation would decrease rapidly with increasing radial distance r from the planet (as $\sim r^{-3}$ or faster). The observed oscillations retain significant amplitudes at radial distances out to the magnetopause, as is evident in Figure 2.15. Furthermore, a rotating tilted dipole would produce field oscillations in which the φ component is in leading quadrature with r , rather than the observed lagging quadrature.

Extended study of these magnetic field oscillations began upon Cassini’s arrival.

Cowley et al. [2006] showed the presence of a significant Doppler-shifting of the rotating field oscillations due to the azimuthal motion of the spacecraft. Cassini's prograde orbit about Saturn and the prograde motion of the field oscillations (increasing azimuth φ with time t) lead to a lengthening of the observed oscillation period to ~ 15 h during closest approach. Meanwhile, *Giampieri et al.* [2006] conducted the first extended survey of the period of the magnetic oscillations, using data from the first 14 Revs. Correcting for the observed Doppler shift and using a Lomb-Scargle analysis, they determined a rotation period of 10.785 h and estimated the effective dipole tilt that would be required to produce the field signatures observed in the magnetosphere. The anomaly producing such a tilt would necessarily be very large, ~ 800 nT. Such a large anomaly is inconsistent with the independently measured axisymmetry of the internal field, given determined values of the g_1^1 coefficient of the order of $\sim 23 \pm 23$ nT [e.g. *Giampieri and Dougherty*, 2004].

Gurnett et al. [2007] showed using the *Kurth et al.* [2007] time-variable SKR phase model that an asymmetry in the electron plasma density is present inside of $\sim 5 R_S$, which rotates in phase with the φ component field oscillations, and thus is in lagging quadrature with the r and θ components. Further detailed studies of the magnetic field oscillations using the *Kurth et al.* [2007, 2008] SKR phase models by *Southwood and Kivelson* [2007], *Andrews et al.* [2008]³, and *Provan et al.* [2009a] have shown that the phase relationships between the three magnetic field components are maintained over the entire Cassini mission (to May 2007, in the *Provan et al.* [2009a] study). In each case, the oscillations in field component i were modelled by expressions of the form

$$B_i(\varphi, t) = B_{i0} \cos(\Phi_{SKR}(t) - \varphi - \psi_{Mi}(t)), \quad (2.9)$$

with one of the various SKR phase models substituted for $\Phi_{SKR}(t)$. The relative phase of the magnetic field oscillations $\psi_{Mi}(t)$ was then determined through fits to field data in each of the three components, and found to be approximately constant compared to the uncertainty, and the linear and higher-order terms in $\Phi_{SKR}(t)$. (*Southwood and Kivelson* [2007] took ψ_{Mi} to be an exact constant over the restricted interval for which

³The study published by *Andrews et al.* [2008] is the work of the author, but does not form part of this thesis, it having been completed prior to the commencement of this PhD studentship in late 2008.

Symbol	Description
t	Time, generally expressed in days since 00 h UT on 1 January 2004
φ	Azimuth, measured positive towards dusk from noon ($\varphi = 0^\circ \equiv 12$ h LT)
r, θ	Radial and colatitudinal coordinates
λ, L	Latitude and dipole L-shell
Ψ	A rotating phase, i.e. $B_r \propto \cos(\Psi(t, r, \varphi))$
Φ	A phase dependent only on time, i.e. a describing a ‘strobe-like’ modulation, e.g. $\Phi_{SKR_s}(t)$ - southern hemisphere SKR phase
ψ	A phase defined relative to some other phase model, which may depend on other coordinates (temporal or spatial)

Table 2.3: Some mathematical conventions used in this thesis.

they analysed field data.) The derivative of $\psi_{Mi}(t)$ defines the difference between the magnetic and SKR periods, and is found to be of the order of a few tens of seconds, typically. To aid the reader, symbols used throughout this thesis in the study of these rotational phenomena are outlined in Table 2.3.

Provan et al. [2009a] were the first to study magnetic field phase data from the series of orbits inclined with respect to Saturn’s equatorial plane, finding that the relative phases of the three components changes on northern and southern open field lines. Specifically, the φ component was found to be in leading quadrature with r , as is consistent with the signature of a rotating transverse dipole lying in the equatorial plane. The form of the rotating field perturbations found by *Provan et al.* [2009a] are shown in Figure 2.16. The significance of the lack of ordering of the northern open field phase data in time was not fully understood in this study, as the discovery of the differences between the northern and southern SKR periods had not yet been made by *Gurnett et al.* [2009a]. Consequently, these data are effectively re-analysed in Chapter 5 in view of this new result.

Andrews et al. [2008] also studied the quasi-random ‘jitter’ present in near-equatorial magnetic field phase data, noting strong positive correlation between the phases of the r and φ components. In view of the recent discoveries of two distinct period signals in the SKR, *Provan et al.* [2011] have subsequently investigated these phase ‘jitters’ in more detail, and showed that they are produced by the simultaneous presence of a weaker perturbation field rotating at the northern period, superimposed upon the dominant (southern) field perturbation.

2.8.5 Magnetopause and bow shock oscillations

Espinosa et al. [2003b] hypothesised that a rotating pressure modulation associated with the observed field oscillations would lead to a periodic motion of the magnetopause boundary. Such an effect was observed in Cassini data by *Clarke et al.* [2006], and the amplitude of the boundary displacement was estimated to be ~ 1 R_S. Cassini's slower speed within the Saturnian system typically leads to multiple crossings of the magnetopause, rather than single crossings of the boundary throughout its modulation.

Further investigation by *Clarke et al.* [2010a] showed that these magnetopause oscillations maintained a fixed phase relationship with the magnetic field oscillations studied by *Provan et al.* [2009a]. Moreover, the rotating phase at which the magnetopause undergoes its maximum outward displacement from its unperturbed position corresponds to the phase of the maximum plasma density observed by *Gurnett et al.* [2007] and *Burch et al.* [2009], delayed as expected from the finite radial phase propagation speed of the field oscillations, as shown schematically in Figure 2.17. Related oscillations were also found to be present in the position of the bow shock [*Clarke et al.*, 2010b].

2.8.6 Related periodic phenomena at Saturn

Similar periodic modulations to those observed in the magnetic field, SKR emissions, and magnetopause and bow shock locations have also been detected in various plasma populations within Saturn's magnetosphere. *Carbary and Krimigis* [1982] detected modulations in the count-rates of hot ($\sim 10\text{-}100$ keV) ions and electrons using data from the low energy charged particle experiments on board the Voyager 1 and 2 spacecraft, which they suggested were the result of an asymmetry in the Saturnian magnetic field.

Subsequent analysis of Cassini data has provided further evidence for such rotational modulations in Saturn's higher-energy plasma populations. Specifically, supporting evidence has been presented for periodic variations in the fluxes of hot

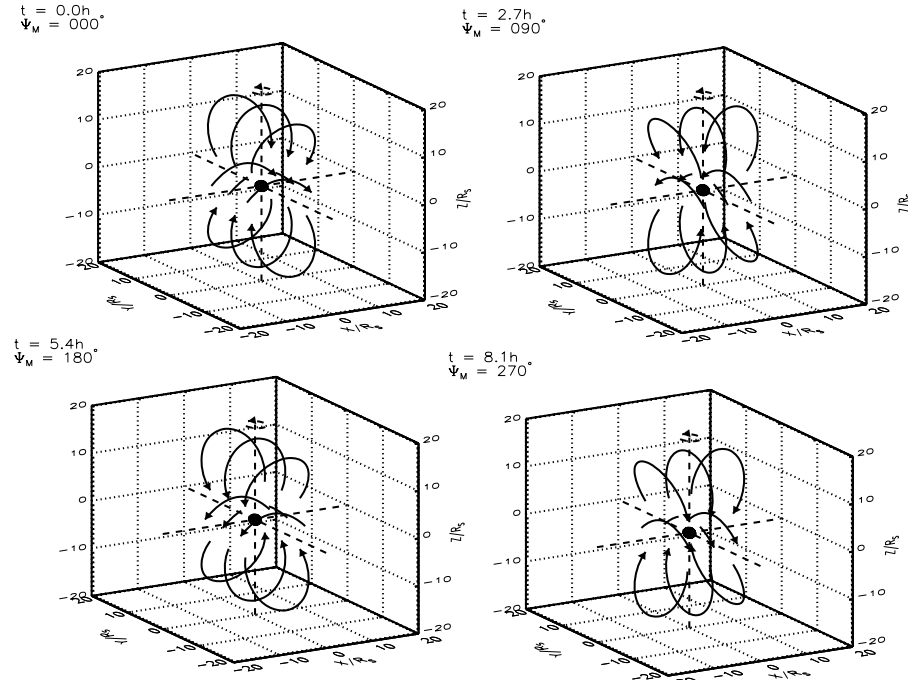


Figure 2.16: 3-D illustrations of the rotating field perturbations found from equatorial and high-southern and -northern latitude data by Provan *et al.* [2009a]. Each panel is separated by 1/4 of a cycle of the assumed rotation period, which is here taken to be equal in both hemispheres. From Provan *et al.* [2009a].

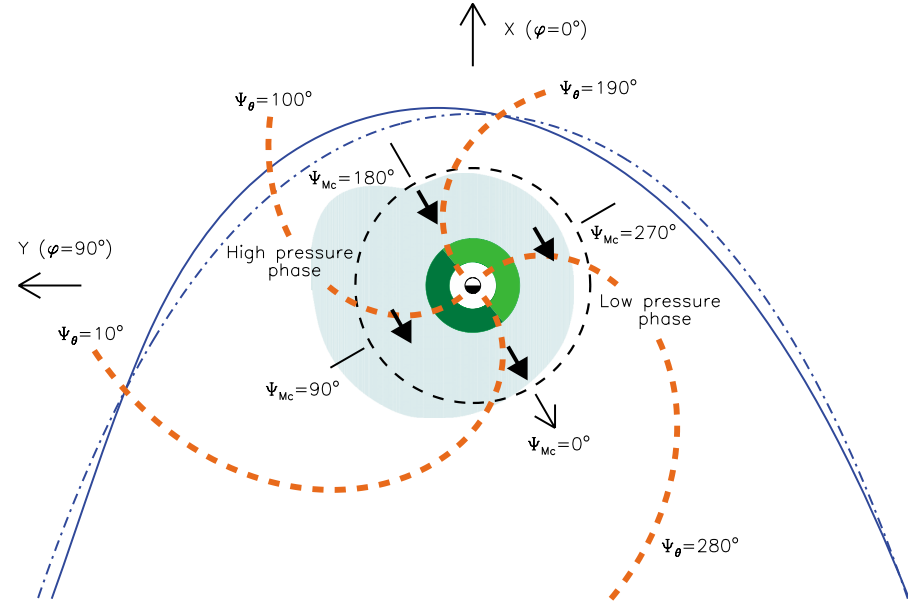


Figure 2.17: Schematic view of Saturn's magnetopause in the $X - Y$ plane, showing the spirals formed by the finite outward phase propagation speed of the θ component of the magnetic field oscillations as determined in Chapter 4. The phase of maximum outward displacement of the magnetopause thus corresponds to the maximum in magnetospheric plasma density found by Gurnett *et al.* [2007] and Burch *et al.* [2009]. From Clarke *et al.* [2010a].

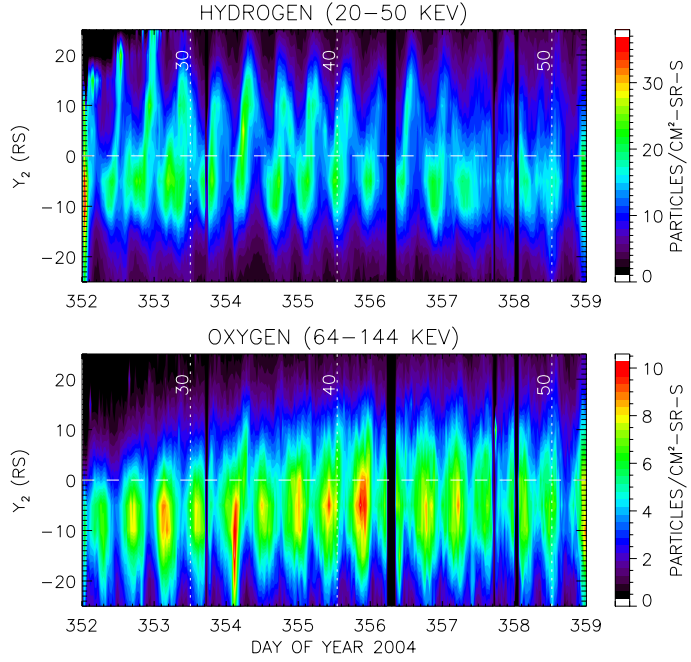


Figure 2.18: Plots showing vertically summed ENA emission projected onto the dawn-dusk meridian versus time for 7 days in late 2004. Positive and negative values of the coordinate ‘ Y_2 ’ indicate dayside and nightside sources, respectively. The colour coding indicates received fluxes of neutral H (top panel) and O (bottom panel). From *Carbary et al.* [2008a].

ions and electrons [Krupp *et al.*, 2005; *Carbary et al.*, 2007b,c, 2009a, 2010a], in cool electrons (temperatures of \sim 1eV - 20 keV) [Gurnett *et al.*, 2007, 2010a; Arridge *et al.*, 2008a; Burch *et al.*, 2009; DeJong *et al.*, 2010; Morooka *et al.*, 2009] and energetic neutral atom (ENA) emissions [*Carbary et al.*, 2008a,b, 2010b]. Figure 2.18 shows projections of ENA emission along the dawn-dusk meridian summed vertically, in which the strongest periodic modulations are observed from nightside sources of ENAs. Such observations are generally understood as rotating azimuthal asymmetries in the plasma close to the planet (within \sim 15 R_S), or as large scale modulations in the position of the plasma sheet at larger radial distances. *Carbary et al.* [2009b] have presented the detection of oscillations at two different periods in energetic electron data from the Magnetospheric Imaging Instrument (MIMI) instrument, most likely related to the separate northern and southern SKR emission periods discussed in section 2.8.3.

Periodic modulations have also been noted in the position of the UV auroral emissions, as seen in Hubble Space Telescope (HST) data [*Nichols et al.*, 2008] which

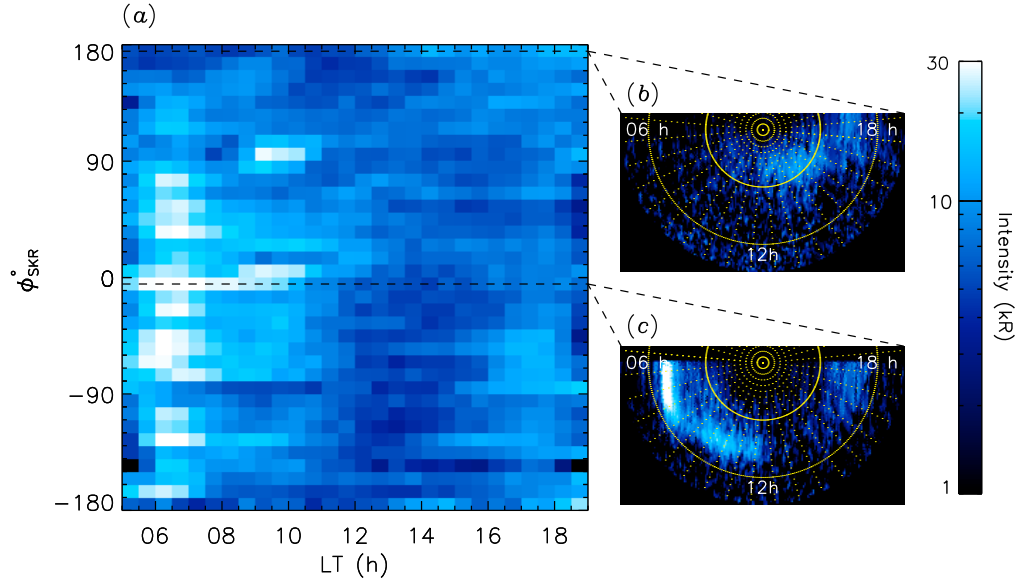


Figure 2.19: Plots of the southern UV auroral intensity from HST data, binned in planetary local time and SKR phase (left), along with two selected projected UV images corresponding to $\Phi_{SKR} \approx 180^\circ$ and $\Phi_{SKR} \approx 0^\circ$. From *Nichols et al.* [2010a].

have been directly related to the rotating magnetic field perturbations [*Provan et al.*, 2009a]. More recently, it has been shown that the modulation in emitted power from the southern UV aurora is largest in the dawn to noon sector, as is the case for the SKR emission, though weaker periodic modulations are also observed around the whole UV auroral oval [*Nichols et al.*, 2010a]. Figure 2.19 shows HST UV intensities projected onto the southern hemisphere of Saturn, binned in LT and SKR phase. It is readily seen that the modulation in UV intensity near dawn is in phase with the SKR, which is maximal when $\Phi_{SKR} = 0^\circ$ (to modulo 360°), while in the dusk sector it is apparently in anti-phase with the SKR. Furthermore, using HST data obtained near Saturn's equinox (August 2009) when it was possible to simultaneously view both the northern and southern UV ovals, it has been shown that a dawn-dusk oscillation is present in both hemispheres at the corresponding northern and southern SKR periods [*Nichols et al.*, 2010b].

2.8.7 Theoretical models of planetary period oscillations

Various theoretical models have been proposed to explain the origin of these periodic phenomena in an apparently axisymmetric system, which are briefly summarised in

Table 2.4. The models proposed by *Gurnett et al.* [2007], *Southwood and Kivelson* [2007] and *Provan et al.* [2009a] are of particular significance for the material that follows in this thesis, and are reviewed in more detail in this section.

The model proposed by *Gurnett et al.* [2007] invokes a rotating twin-cell convection pattern in the inner magnetosphere, in which plasma ‘outflow’ takes place over a restricted range of azimuth in the rotating frame, as is sketched in Figure 2.20. They suggest that the plasma disc, which rotates at an angular frequency ω less than that of the neutral atmosphere Ω , interacts with the sub-corotating Enceladus neutral torus to produce an asymmetry in the plasma density, and consequently an identical asymmetry in the magnitude of the centrifugal force acting upon the plasma. This in turn leads to preferential outflow within a restricted range of azimuth, inducing the observed azimuthal field oscillations. As noted in Table 2.4, however, it is not clear that such a model reproduces the observed colatitudinal field oscillations. Furthermore, the outflowing plasma should produce a change in the sign of the oscillating radial field on the equatorial plane, something that is not observed e.g. by *Espinosa et al.* [2003b]. Additionally, it is unclear how such an ‘equatorial’ source of these periodic phenomena could introduce two distinctly different periodicities in the northern and southern SKR emissions.

The model proposed by *Southwood and Kivelson* [2007], later somewhat refined by *Southwood and Kivelson* [2009], seeks to explain the observed magnetic field perturbations through the presence of a rotating inter-hemispheric field aligned current system. Such a system is sketched in Figure 2.21, in which the inter-hemispheric currents have an ‘ $m = 1$ ’ azimuthal structure, and flow along field lines which intersect the equator at $\sim 15 R_S$. Inside this radius the field perturbation is quasi-uniform, as observed e.g. by *Espinosa and Dougherty* [2000] and *Espinosa et al.* [2003b]. At larger distances, the field becomes more like that expected for a rotating transverse dipole, due to a change in the phase of the azimuthal component relative to the radial. The rotating current system thus produces an effective dipole tilt of $\sim 10\text{--}20^\circ$ at larger distances, it being imposed in the magnetosphere rather than within the planet itself. However, such a system with equal currents flowing through the northern and

Model	Description	Remarks
<i>Carbary et al.</i> [2007a]	Qualitatively similar to <i>Khurana et al.</i> [2009]	Inconsistent with (1, 2)
<i>Goldreich and Farmer</i> [2007]	Qualitatively similar to <i>Gurnett et al.</i> [2007]	Inconsistent with (1)
<i>Gurnett et al.</i> [2007]	Rotating twin-cell plasma convection system in the inner magnetosphere	Inconsistent with (1)
<i>Southwood and Kivelson</i> [2007]	Rotating inter-hemispheric current system	Inconsistent with (1, 2)
<i>Zarka et al.</i> [2007]	Solar-rotation period variation in solar wind speed drives variation in SKR period through the Kelvin-Helmholtz instability	Inconsistent with (4)
<i>Burch et al.</i> [2008]	Periodic release of plasmoids	(4)
<i>Khurana et al.</i> [2009]	Obliquely flowing solar wind imposes periodic vertical motion on an asymmetric plasma sheet	Inconsistent with (1, 2)
<i>Provost et al.</i> [2009a]	Rotating partial ring current	Inconsistent with (1)
<i>Andrews et al.</i> [2010] (Chapter 5)	Separate rotating partial ring currents	
<i>Smith</i> [2011]	Rotating thermospheric heat source	Inconsistent with (5)
	(1) Observations of dual-periodicities (north-south asymmetry)	
	(2) Observed polarisation of magnetic field oscillations	
	(3) Non-detection of periodic release of equatorial plasmoids	
	(4) As yet un-observed phenomena	
	(5) Sense of magnetic field phase variation	

Table 2.4: Summary of published models of planetary period oscillations.

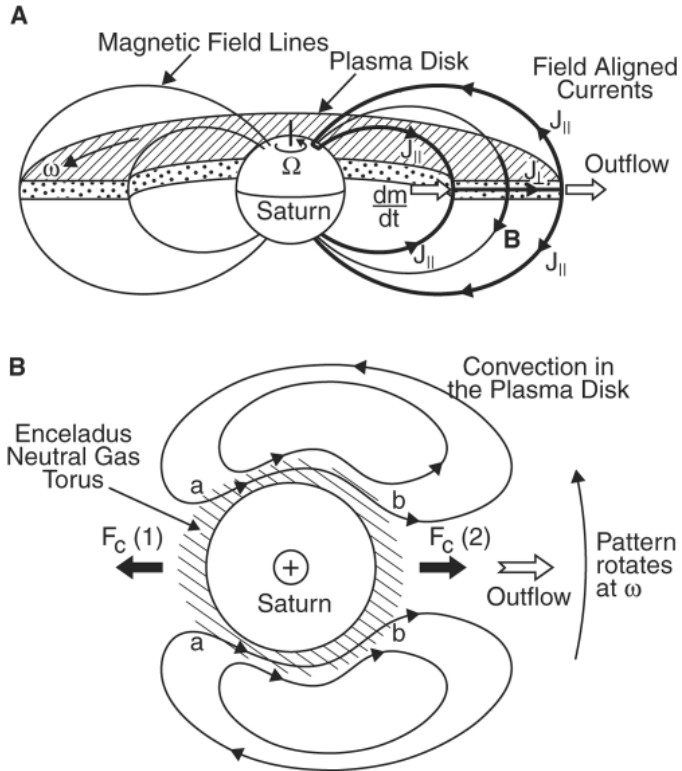


Figure 2.20: Theoretical model of the coupling between the rotating plasma disc and Saturn's ionosphere. Panel (a) shows field aligned currents $j_{||}$ flowing into and out of the plasma disc, closing via a perpendicular current j_{\perp} , the resulting $j_{\perp} \times \mathbf{B}$ force acts to accelerate the plasma disc towards corotation with the ionosphere. Panel (b) shows an equatorial projection of the plasma flow lines. From *Gurnett et al. [2007]*.

southern ionospheres would not produce a colatitudinal field on the equatorial plane as observed by *Andrews et al. [2008]*.

Meanwhile, *Provan et al. [2009a]* have put forward a model in which the north-south anti-symmetry of the interhemispheric field aligned currents in the *Southwood and Kivelson [2007]* model is broken, such that more current flows through the southern ionosphere during southern summer conditions. The excess current flowing into and out of the equatorial plane then closes in the equatorial plane in the vicinity of the quasi-static ring current. This is effectively equivalent to the addition of a rotating partial ring current to the system presented by *Southwood and Kivelson [2007]*, and serves to explain the observed oscillations in the colatitudinal field component observed by *Andrews et al. [2008]*, along with the quasi-dipolar fields observed by *Provan et al. [2009a]* at high northern and southern latitudes. The overall field aligned and equatorial currents are sketched, along with the implied field perturbations in

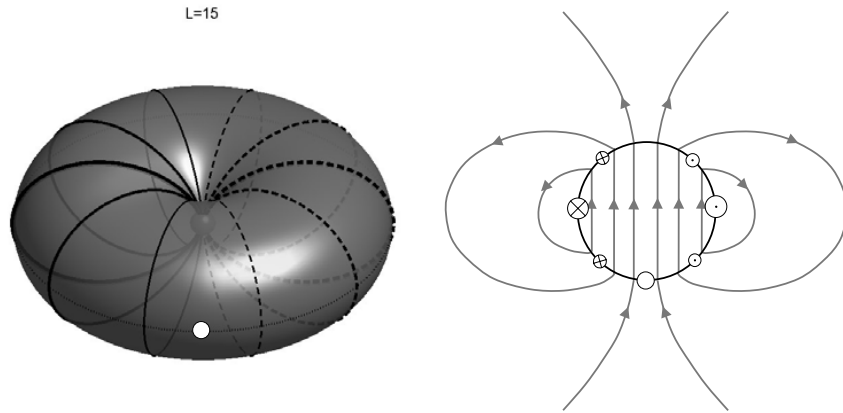


Figure 2.21: Sketches showing the ‘camshaft’ model proposed by *Southwood and Kivelson* [2007]. The shell of dipolar field lines at $L \sim 15$ in which currents flow between the northern and southern hemispheres is shown on the left. Current density is indicated by the thickness of the black lines, with north-south currents shown solid and south-north shown dashed. The induced equatorial field perturbations are shown on the right by the grey lines, with the $L \sim 15$ circle and the currents flowing through the equatorial plane in black. From *Southwood and Kivelson* [2007].

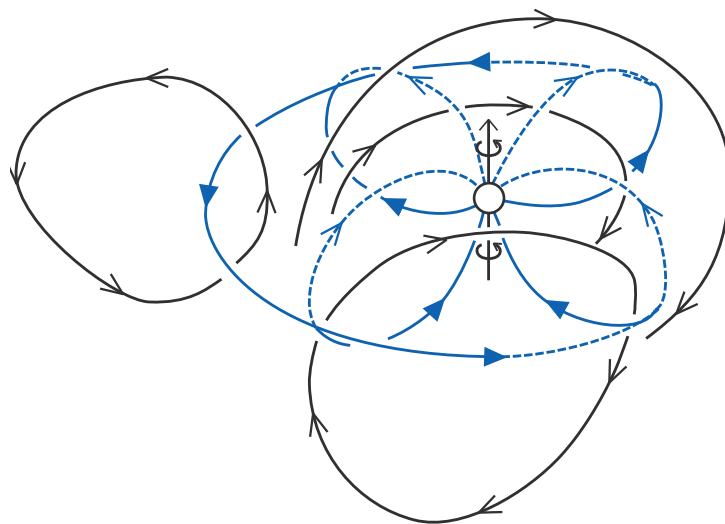


Figure 2.22: 3-D sketch showing the rotating partial ring current model proposed by *Provan et al.* [2009a]. Currents are shown in blue, with dashed lines indicating weaker currents flowing into the northern ionosphere. Corresponding magnetic field perturbations are shown in black. From *Provan et al.* [2009a].

Figure 2.22.

2.8.8 Summary

It is clear that the source of these rotational modulations is far from simple. Recent discoveries of secular changes in the period of these phenomena, and the difference

of the emission period of the SKR in the northern and southern hemispheres have further hampered efforts to develop a consistent theoretical framework of their origin. The studies presented in Chapters 4, 5, and 6 of this thesis will serve to further understanding of the rotating magnetic field perturbations and their relationship to the SKR and related phenomena. Specifically, in Chapter 4, the form of the rotating field perturbations in the equatorial plane is determined from analysis of field data, using the *Provan et al.* [2009a] phase model as a ‘guide’. In Chapter 5, evidence for different magnetic rotation periods in the northern and southern open field regions is presented. Finally, in Chapter 6, magnetic field phase data are used to show that the modulation in the SKR emission is not in fact ‘strobe like’, as hitherto assumed, but rather rotates around the planet in the same manner as the field perturbations. Consequently, this thesis relies heavily on data obtained with various instruments on board the Cassini spacecraft, and it is therefore pertinent to review both the mission itself as well as some details of the instruments used, as is done in the following chapter.

Chapter 3

Instrumentation

3.1 Overview

In this chapter, the Cassini-Huygens mission is introduced in section 3.2. The three instruments from which data are used in subsequent chapters are described in sections 3.3, 3.4 and 3.5. The Cassini orbital tour is then briefly described in section 3.6.

3.2 The Cassini-Huygens mission to Saturn

Cassini is the fourth robotic spacecraft to visit the Saturnian system, following the successful flybys of the planet made by Pioneer-11 in September 1979, and Voyager-1 and -2 in November 1980 and August 1981, respectively, on their ‘grand tour’ of the outer solar system. The development, construction, and pre-flight testing of Cassini, along with the Huygens Titan lander that accompanied it to Saturn, began in the years following these three flybys. Much of the design of the spacecraft and its scientific instruments can be traced back to those earlier missions, along with the Ulysses and Galileo spacecraft (a solar orbiter, which used a Jupiter flyby to launch itself into a polar orbit, and the first Jupiter orbiter, respectively). Collaboration between the National Aeronautical and Space Administration (NASA) and the European Space Agency (ESA) ensured that the project secured sufficient funds and progressed through the design and construction phases during the 1990s.

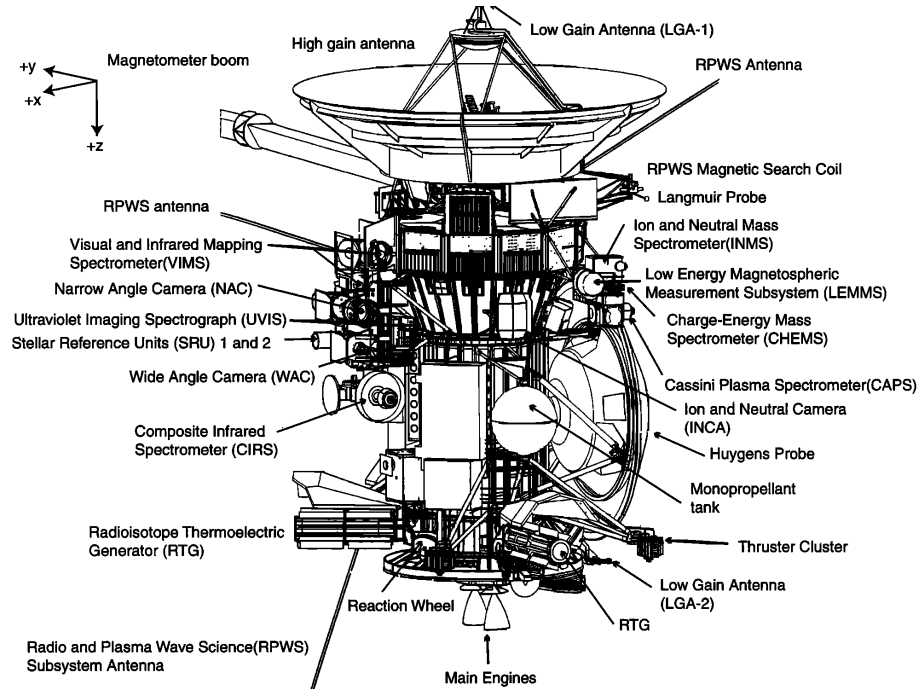


Figure 3.1: Schematic of the Cassini spacecraft and its instruments, from *Burton et al.* [2001].

A schematic illustration of Cassini, with the Huygens probe attached, is shown in Figure 3.1. Cassini is a 3-axis stabilised spacecraft, meaning its attitude is controlled by multiple sets of thrusters and reaction wheels, rather than constantly spinning about its axis. It has a dry mass of 2125 kg (its mass at launch with fuel and the Huygens descent probe attached was 5712 kg) and is 6.7 m tall with a diameter of 4 m. Consequently, Cassini is the third-largest interplanetary spacecraft ever launched (after the two Soviet Phobos spacecraft, which visited Mars). The spacecraft is powered by three radioisotope thermoelectric generators (RTGs), which together will provide \sim 660 W at the end of mission. During its orbital tour of Saturn, the one-way light travel time between to Earth is greater than an hour, meaning that real-time control is impossible and the spacecraft must operate autonomously.

The spacecraft carries 11 separate instrument packages, as listed in Table 3.1. Instruments from which data are used in this thesis are outlined in the following sections.

<i>Instrument Package</i>	<i>Science outline</i>
Cassini Plasma Spectrometer	Described in section 3.4
Composite Infrared Spectrometer	Thermal mapping of Saturn's atmosphere, moons, rings
Cosmic Dust Analyser	Dust particle origin and distributions
Imaging Science Subsystem	Studies of Saturnian system at visible light wavelengths
Ion & Neutral Mass Spectrometer	High resolution mass spectrometry of organic compounds
Dual Technique Magnetometer	Described in section 3.3
Magnetospheric Imaging Instrument	Imaging of high energy charged and neutral particles
Radar & Radio Science Subsystem	Radar mapping, atmospheric occultation
Radio & Plasma Wave Science	Described in section 3.5
Ultraviolet Imaging Spectrograph	Ultra-violet imaging and spectrophotometry
Visible & Infrared Mapping Spectrometer	Infrared imaging and spectrophotometry

Table 3.1: Cassini instrument packages.

3.3 The Cassini Magnetometer Instrument

The Cassini magnetic field investigation consists of two separate magnetic field sensors: a Flux-Gate Magnetometer (FGM) and a Vector Helium Magnetometer (VHM), which are both mounted on a rigid 11 m long boom deployed from the spacecraft during the Earth flyby. A full and detailed description of this experiment is provided by *Dougherty et al.* [2004], from which the salient points are summarised here.

The stated objectives of the Cassini magnetic field investigation are manyfold, with each posing some requirement on the capabilities of the instrument. For example, characterisation of the magnetic field of Saturn requires the ability to accurately measure field strengths up to \sim 10,000 nT during closest approach (CA). Detection of high-order multipolar terms (e.g. $n > 3$ in equation (2.2)) requires an accuracy of the order of a few tens of nT, or \sim 0.1% of the background during CA. Similarly precise measurements within a large background field are necessary to detect magnetic signatures of the interaction between the Saturnian magnetic field and the icy satellites. Meanwhile, characterisation of the magnetic environment of Titan, orbiting at the edge of the Saturnian magnetosphere, necessitates measurements made to \sim 0.1 nT accuracy in much weaker background fields of \sim 10 nT. The dynamic range that must be covered by the magnetometer instrument is therefore substantial.

The configuration of the two instruments on the boom is shown in Figure 3.2.

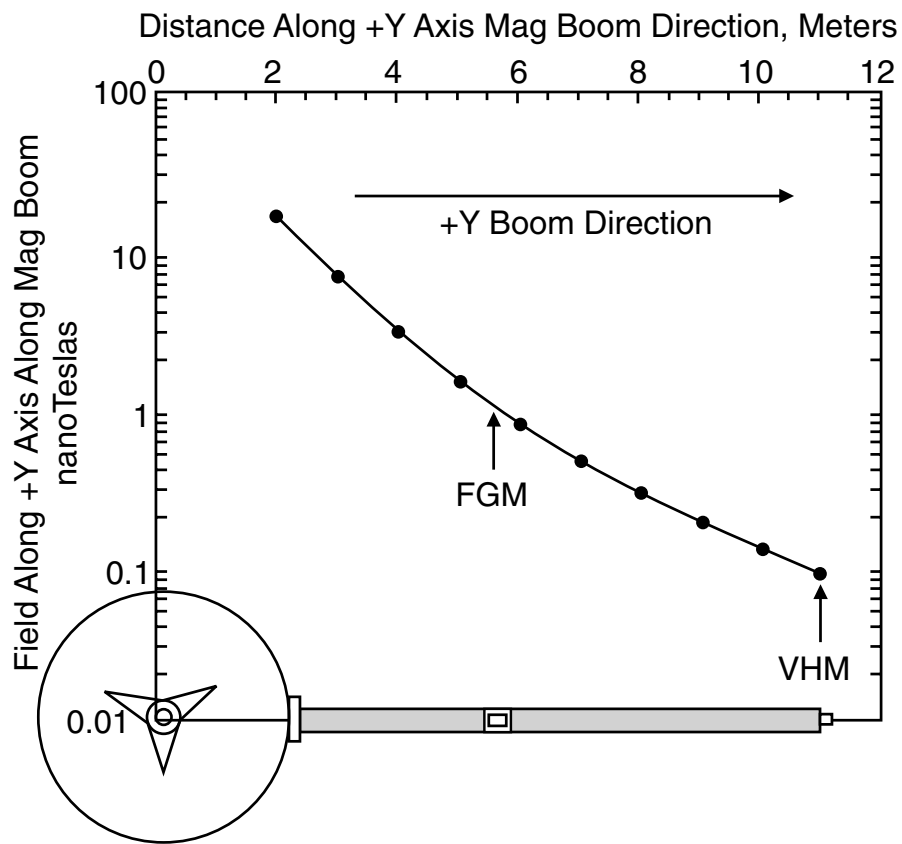


Figure 3.2: Plot of the modelled (solid line) and measured (filled circles) magnetic field produced by the spacecraft along the deployed magnetometer boom. The spacecraft HGA is shown for scale, as is the boom with the positions of the FGM and VHM sensors indicated. From *Narvaez* [2004].

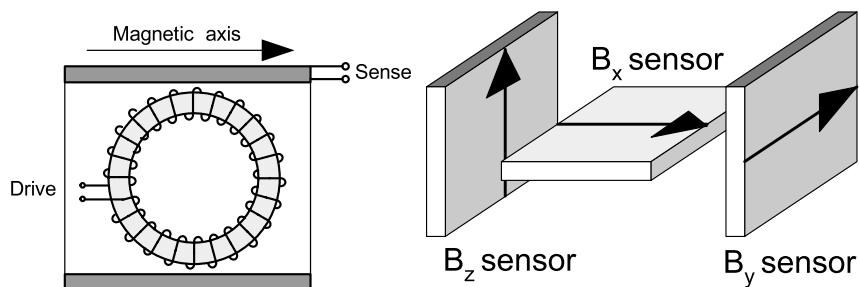


Figure 3.3: Schematics showing the configuration of the sense and drive coils of a single FGM on the left, and three such sensors arranged orthogonally to measure three orthogonal field components on the right. From *Balogh* [2010].

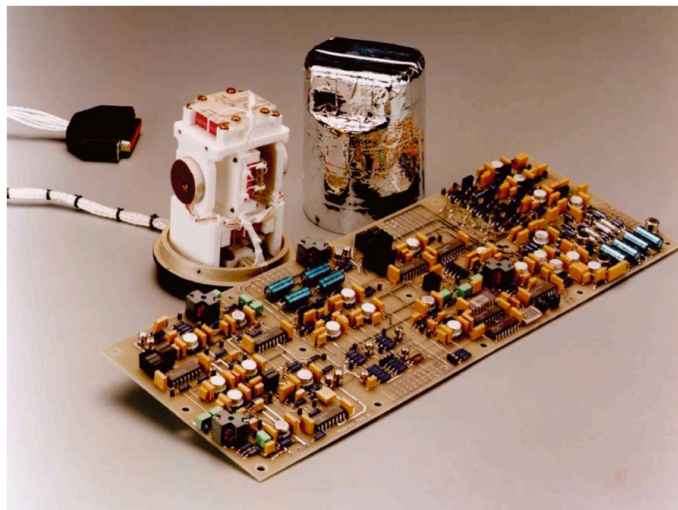


Figure 3.4: Photograph of the FGM instrument (with cover off) and its electronics. From *Dougherty et al.* [2004].

To ensure that the residual magnetic field produced by the spacecraft does not substantially influence the performance and accuracy of the magnetometers, in addition to the use of a boom platform, a strict program of ‘magnetic cleanliness’ and pre-flight testing and calibration was used during the design and construction of the other spacecraft systems and instrument packages [Narvaez, 2004]. This involved substitution of magnetic for non-magnetic materials, use of magnetic shielding, and placement of compensating magnets to reduce the spacecraft fields to ~ 1 nT at the FGM and ~ 0.1 nT at the VHM, though these values are expected to fluctuate somewhat during operation. Two switchable coils mounted inboard on the spacecraft hull provide a square-wave magnetic field oscillation of known amplitude, with a period of 4 s that was used to calibrate the two magnetometers during the deployment of the boom. Simultaneous operation of both the FGM and VHM sensors, along with routine rolls of the spacecraft about its Z-axis, can be used to accurately measure and remove the spacecraft residual field from the magnetometer data and maintain precise calibration of both instruments.

The two magnetometers operate on separate, complementary physical principals. The FGM consists of three orthogonal high-permeability ring cores, each with a toroidal ‘drive’ winding around it, along with a surrounding orthogonal ‘sense’ coil, as shown (singly) in Figure 3.3. Bipolar, symmetric current pulses with a frequency

of ~ 10 Hz are driven through the drive winding, forcing the ring core around its hysteresis cycle. With no net external field along the sensor axis ($H_{\text{ext}} \equiv 0$), the net magnetic flux through two halves of the core is zero. However, in the presence of an external field ($H_{\text{ext}} \neq 0$), the field in the two halves of the core will saturate at different points in the cycle, such that their fluxes will not continuously cancel and a net flux will therefore thread the surface, varying at twice the frequency of the drive current. Consequently, a voltage signal is induced in the sense coils, the magnitude of which is directly proportional to H_{ext} . A feedback current is sent through the sense coils to oppose the effect of the external field, such that the sensor operates near its null-point, at which it is most sensitive. The magnitude of the feedback current is varied in four steps, two provide four different ranges within which the sensor can operate, from ± 40 nT at a resolution of 4.9 pT, up to ± 44000 nT at a resolution of 5.4 nT. The FGM is capable of recording 32 vectors per second. A 1 W heater maintains the instrument within its operating threshold of -30 to $+40$ °C. A photograph of the sensor and its associated electronics, which are mounted inboard rather than on the magnetometer boom, is shown in Figure 3.4.

The VHM instrument failed in-flight shortly after Saturn orbit insertion (SOI) in July 2004, and consequently no data from this instrument is used in this thesis. Nevertheless, a brief description of the instrument, which is effectively the ‘flight spare’ from the Ulysses mission, is provided here. This instrument consists of a cell of helium, which is optically pumped into a meta-stable state using circularly polarised light of wavelength $1.08\ \mu\text{m}$. The efficiency of this pumping processes, and therefore the transmission of this infra-red light through the helium cell, is proportional to the external magnetic field. A ‘sweep’ magnetic field generated by coils surrounding the cell can be used to determine the orientation of the field, while an alternating field can be applied to determine the absolute magnitude of the magnetic field. It is this ability to accurately measure the absolute field magnitude that led to its selection for the mission.

3.4 The Cassini Plasma Spectrometer

The Cassini Plasma Spectrometer (CAPS) investigation consists of three separate instruments, designed to study the lower-energy plasma populations throughout the Saturnian environment [Young *et al.*, 2004]. All are electrostatic analysers, separating incident particles according to their charge state and energy, counting the charge deposited on micro-channel plate detectors. The three instruments are mounted on an rotating platform, which is able to scan 2π sr of ‘sky’ every 3 minutes. The configuration of the three instruments is shown in Figure 3.5, while the placement of the instrument platform on the spacecraft was shown previously in Figure 3.1.

The Electron Spectrometer (ELS) instrument samples the distribution of electrons with energies in the range 0.6 to 28250 eV in 64 logarithmically spaced energy channels. The instantaneous instrument field of view is 5° in azimuth and 160° in elevation, with an angular resolution of 5° in azimuth (i.e., a single azimuth bin), and 20° in elevation. The energy range covered is thus sufficient to sample both ‘cold’ plasma at low latitudes in the inner magnetosphere, through to the ‘warm’ and ‘hot’ populations of ring-current electrons in the outer magnetosphere. Furthermore, the instrument has been used to study heavy negatively charged ions in the vicinity of Titan [see e.g., Coates *et al.*, 2007].

The remaining two constituent instruments of CAPS, the Ion Beam Spectrometer (IBS) and Ion Mass Spectrometer (IMS) measure the distribution of ions, with energies from 1 eV to \sim 50 keV in each case. The IBS has particularly high angular resolution, $\sim 1.5^\circ$ in both azimuth and elevation, such that it is able to accurately resolve beam-like distributions of energetic ions. Meanwhile, the IMS incorporates a time-of-flight mass spectrometer, capable of resolving species with mass to charge ratios from 1 to \sim 400 amu/e.

3.5 Radio & Plasma Wave Science Instrument

The Radio and Plasma Wave Science (RPWS) instrument package [Gurnett *et al.*, 2004] consists of three (almost) orthogonal monopole electric antennas, each 10 m long, capable of measuring electric fields over the frequency range from 1 Hz to 16 MHz. Processing of the signals received from each antenna allows the polarisation characteristics of the incident radiation to be discerned, and furthermore makes it possible to determine the Poynting vector of the field and thus their direction of arrival at the spacecraft.

The RPWS instrument package also contains a) an orthogonal set of three search coil magnetometers, capable of measuring waves in the magnetic field with frequencies from 1 Hz to 12 kHz, b) a Langmuir probe consisting of a 5 cm diameter titanium sphere mounted on an 0.8 m boom that can be used, under certain circumstances, to measure the electron plasma density and temperature, c) a sounder transmitter able to produce fields from 3.6 kHz to 115 kHz, used to excite local plasma oscillations and d) a complex receiver system to process inputs from the various antennas and the Langmuir probe.

In addition to being able to measure and characterise incident radio waves over a wide range of frequencies, the RPWS instrument can also be used to detect the impact of large ($> \mu\text{m}$) dust particles. On collision with the spacecraft, these dust particles, and part of the spacecraft surface, are vaporised and heated. The charge from the resulting plasma cloud occasionally collects on the antenna surfaces causing a brief ($\sim\text{ms}$) voltage pulse in the electric field antennas.

3.6 The Cassini orbital tour

Cassini was successfully launched from Cape Canaveral on 15 October 1997. Its high mass necessitated the selection of a somewhat circuitous trajectory for the mission to Saturn, involving gravitational assists from Venus (twice), Earth and Jupiter during its \sim 6.5 year interplanetary cruise, depicted in Figure 3.7.

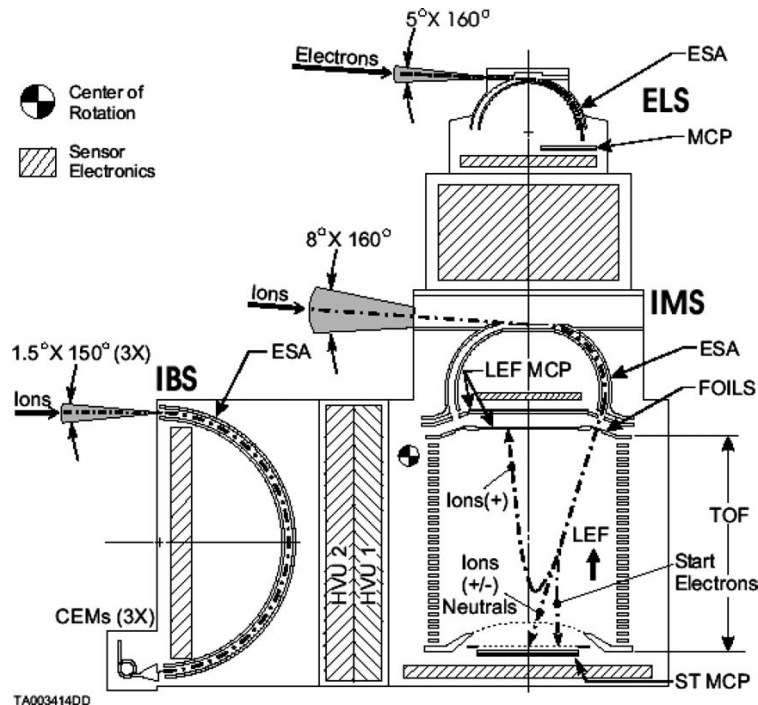


Figure 3.5: Schematic of the CAPS instrument. Cross-sections of the instruments in the spacecraft $X - Y$ plane are shown, the rotation axis of the instrument platform being parallel to the spacecraft Z axis. Grey wedges indicate the azimuthal field of view of each instrument, and typical particle trajectories are shown by the dot-dashed lines. From *Young et al.* [2004].

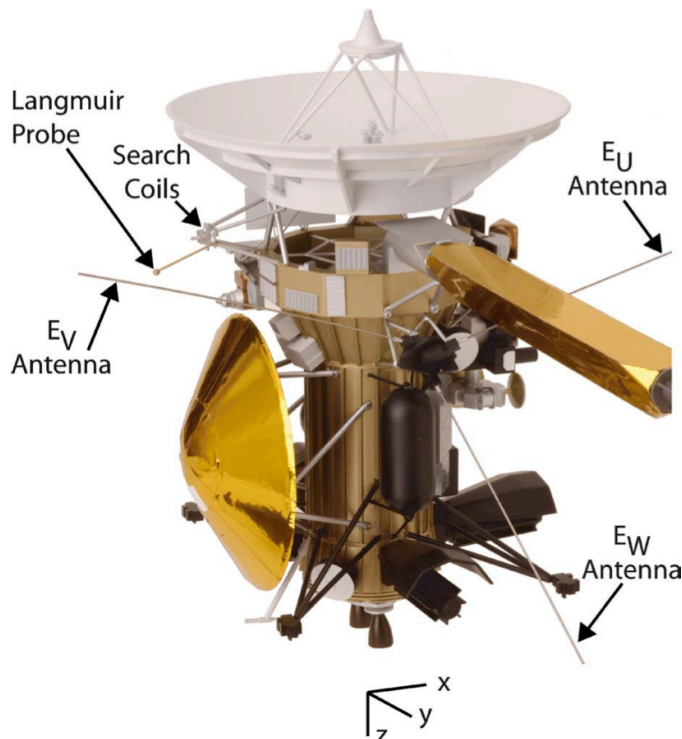


Figure 3.6: Model of the Cassini spacecraft showing the locations of the RPWS sensors, after deployment. From *Gurnett et al.* [2004].

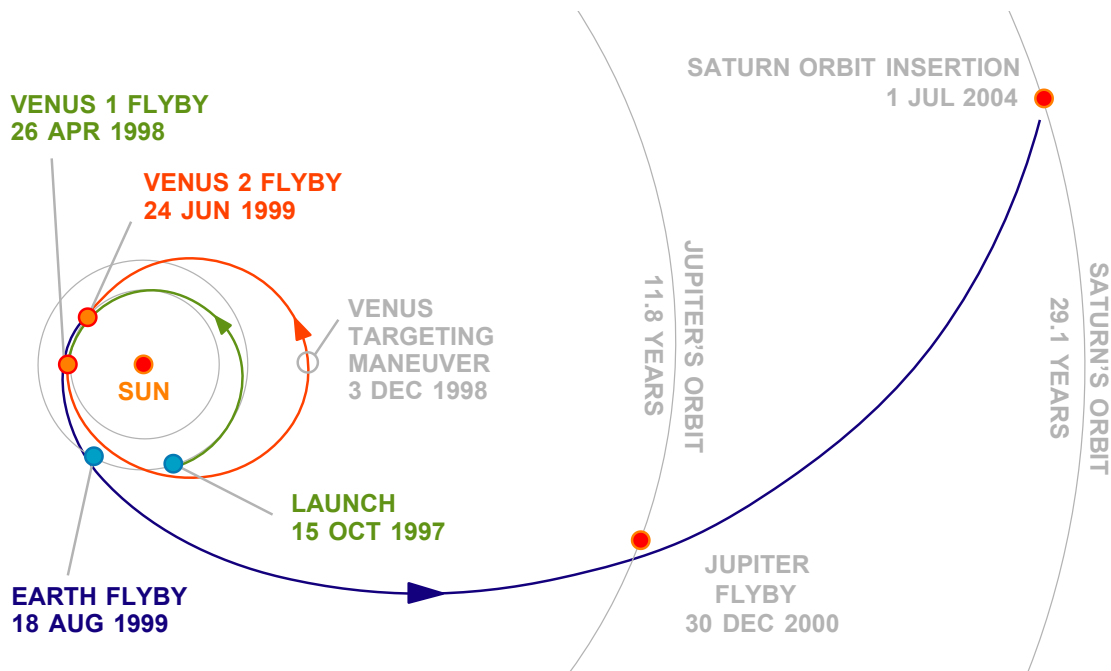


Figure 3.7: Cassini's interplanetary trajectory [Image credit: NASA/JPL].

Cassini became the first spacecraft to orbit Saturn after SOI on 1 July 2004. This marked the beginning of the ‘prime’ mission phase, which was to last ~4 years until 1 July 2008, and consisted of 75 orbits of the planet (termed ‘Revolutions’, or simply ‘Revs’), along with 45 targeted flybys of Titan and 3 of Enceladus. Shortly after its arrival at Saturn, the Huygens probe was detached from the spacecraft, descending through the thick atmosphere of Titan some weeks later, and became the first probe to land on a moon other than that of the Earth on 14 January 2005.

The second phase of the mission, termed the ‘equinox’ phase, consisted of a further 64 orbits along with many more flybys of Saturn’s moons, including the only targeted flyby of Mimas, and followed the progression of the Saturnian year through its vernal equinox on 11 August 2009. The ‘equinox’ mission phase concluded in October 2010, when Cassini began the ‘solstice’ mission phase in a good state of health. The end of mission is currently scheduled for 15 September 2017, when Cassini will enter Saturn’s atmosphere and be destroyed. During the last few orbits, the altitude of periapsis will be lowered to within the planet’s ring system, and the spacecraft will pass within 2000 km of the planet (10 times closer than during SOI). In total, it will have completed 294 orbits of the planet, and have travelled almost 13×10^9 km around it.

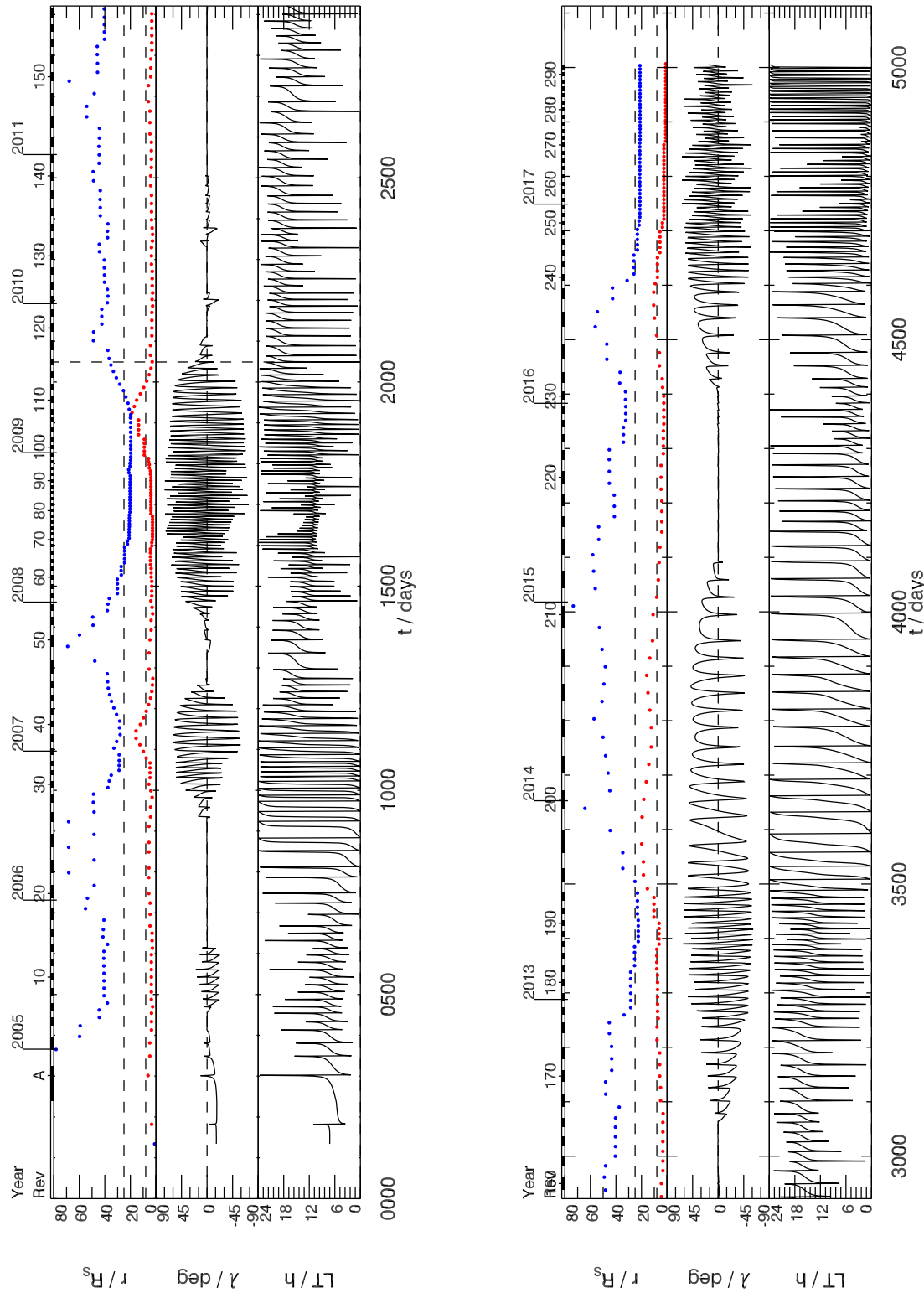


Figure 3.8: Plots showing the planned Cassini orbital tour. The three panels in each row show, from top to bottom, (a) the radial distance of periapsis (red circles) and apoapsis (blue circles) of each Rev, along with two horizontal dashed lines indicating their respective averages, (b) spacecraft latitude and (c) local time (in hours) throughout the orbital tour. Alternate black and white blocks at the top of each plot indicate the duration of each Rev.

The extremely varied orbital geometry of the Cassini tour is shown in detail in Figure 3.8, showing the altitude of apoapsis and periapsis (in R_S), latitude, and azimuth in the three panels. The tour is designed to visit as much of the Saturnian magnetosphere as is possible, as well as providing good opportunities to remotely image the planet along with its moons and rings, and conduct flybys of Saturn's moons. Sets of high-latitude orbits are evident, separated by extended intervals of equatorial orbits. Over the mission the spacecraft achieves excellent coverage of azimuth (equivalent to LT) around the planet over a large range of radial distances.

Chapter 4

Variation of equatorial field oscillation amplitude and phase with radial distance and local time

4.1 Introduction

In this chapter, the dependence of the amplitude and phase of the equatorial magnetic field oscillations on radial distance and local time is studied. As was mentioned in Chapter 2, previous studies have shown that within the quasi-dipolar ‘core’ region of the magnetosphere, out to equatorial radial distances of $\sim 12 R_S$ (where the planetary radius $1 R_S$ is equal to 60,268 km), the perturbations in the spherical polar radial (r) and azimuthal (φ) field components take the form of a rotating quasi-uniform field of $\sim 1\text{-}2$ nT amplitude, which does not vary strongly with co-latitude about the equator [Espinosa *et al.*, 2003b,a; Southwood and Kivelson, 2007; Andrews *et al.*, 2008]. Expressed in terms of the relative phase of these field components, the azimuthal component oscillations are consistently in lagging quadrature with the radial component oscillations. Neither this polarisation, nor the weak amplitude dependence on radial distance is consistent with a rotating asymmetric source in the planet’s internally generated field, the amplitude of which would fall off with radius as r^{-3} or faster. Instead, the field perturbations must thus be associated with some external current

system. With regard to the connection with the SKR modulation, it has been found that the emission power peaks when the rotating field points towards $\sim 2\pm 2$ h LT, i.e. tailwards and downwards. In addition to the oscillations in the radial and azimuthal field components, it has been found that oscillations of comparable amplitude are also present in the colatitudinal (θ) field component in the ‘core’ region [Andrews *et al.*, 2008; Khurana *et al.*, 2009]. These field oscillations in the north-south component have been found to be in phase with the radial component oscillations in this region. Evidence has also been presented for outward radial propagation of these modulations, such that the overall phase fronts of these disturbances form spiral structures in and near the equatorial plane [Cowley, 2006; Gurnett *et al.*, 2007; Carberry *et al.*, 2007c].

An empirical model of the phase of the magnetic field oscillations within the ‘core’ region has been determined by Andrews *et al.* [2008] using data from 23 near-equatorial periapsis passes during the early part of the Cassini orbital mission, spanning October 2004 to July 2006. A cross-correlation technique was used that accounted for Doppler-shifting of the oscillation due to the azimuthal motion of the spacecraft, and employed the SKR phase model of Kurth *et al.* [2007] as an exact ‘guide-phase’ with which to track the variation of the magnetic phase from pass to pass. Subsequently, Provan *et al.* [2009a] used the same technique together with the Kurth *et al.* [2008] SKR phase model to analyse a longer interval of magnetic field data, thereby deriving a magnetic phase model valid between July 2004 and December 2007. These studies showed that the ‘core’ region field oscillations and the SKR modulation exhibit a period which is common to within ~ 5 s ($\sim 0.01\%$) over the ~ 3 year interval of joint data examined. This small difference in period was detected through the presence of a slow relative phase drift of ~ 0.12 deg day $^{-1}$ between the two phenomena, which while small leads to substantial deviations in phase over seasonal timescales. Thus, while the magnetic field oscillations and the modulations in SKR are suggested to be of common origin, a complete theory of their source must explain the slow drift in their relative phases, and consequently the nature of this phase drift is studied in detail in Chapter 6.

Provan *et al.* [2009a] used their magnetic phase model to study related field oscillations observed by Cassini at high latitudes on open field lines, while Provan

et al. [2009b] also employed the same model to study the phase of the magnetospheric period oscillations of Saturn's auroral oval discovered by *Nichols et al.* [2008]. The *Provan et al.* [2009a] magnetic phase model also provides the basis for the analysis presented here.

While the magnetic phase model determined by *Provan et al.* [2009a] accounts for the secular changes in the period of the field oscillations and the SKR modulation, it was however constructed prior to the recent discovery by *Gurnett et al.* [2009a] of a somewhat shorter period emission originating from the northern hemisphere. During the interval studied here, corresponding to southern-summer conditions leading up to Saturn's vernal equinox in August 2009, the southern hemisphere SKR sources were dominant over the northern, and furthermore were more reliably detected at the spacecraft [*Lamy et al.*, 2008b]. Thus, the phase models determined by *Kurth et al.* [2007], *Kurth et al.* [2008], *Andrews et al.* [2008] and *Provan et al.* [2009a] represent the modulations in the southern hemisphere SKR emission, and the field oscillations that have a corresponding rotation period. Subsequent analysis has shown that the modulation period of the southern hemisphere SKR emission increased from ~ 10.77 h to ~ 10.83 h over the interval studied here, while the corresponding northern hemisphere emission remained more constant at ~ 10.58 h [*Lamy*, 2011]. The spacing between the northern and southern SKR periods was therefore ~ 0.22 h (~ 800 s), much larger than their variation about their central values. Previously, deviations of only a few tens of seconds were found between the magnetic field rotation period and what is now therefore known to be the southern hemisphere SKR modulation period [*Andrews et al.*, 2008; *Provan et al.*, 2009a]. The dominant magnetic field oscillations thus have a period much closer to the southern rather than the northern SKR modulation over the interval studied here.

More recently, separate northern and southern hemisphere SKR phase models have now been derived by *Lamy* [2011], and these are used in subsequent chapters. We also note that *Provan et al.* [2011] have shown that oscillations are present in the equatorial magnetic field at a period corresponding to the northern hemisphere SKR emission, though they are of significantly weaker amplitude, $\sim 30\text{-}40\%$ of the

dominant oscillations occurring at the southern hemisphere SKR period. These weaker oscillations were detected through the deterministic phase ‘jitter’ they impose on the phase of the dominant oscillations, which has an amplitude of $\sim 25^\circ$ and varies at the ‘beat period’ between the northern and southern oscillation periods, being ~ 23 days.

In this chapter we build on the analyses of *Andrews et al.* [2008] and *Provan et al.* [2009a] to examine how the oscillations in Saturn’s equatorial magnetic field depend both on radial distance and LT from the inner region out to ~ 30 R_S , thus extending the investigation well beyond the equatorial ‘core’ region examined previously. In addition, for the first time we determine not only the phase of the oscillations, but also their amplitude throughout this region. From these data we can also derive the pattern of oscillatory currents flowing north-south through the equatorial plane, and compare these with the theoretical pictures proposed e.g. by *Southwood and Kivelson* [2007] and *Provan et al.* [2009a]. Furthermore, we note that for the purposes of this study in which we are principally concerned with the spatial structure of the dominant (southern period) field oscillations during the pre-equinox interval, the jitter imposed by the weaker (northern period) field oscillation is rapidly averaged over, as will be discussed in the next section. Consequently, however, the results presented in this chapter are only reflective of the nature of the field oscillations present in near-equatorial data with periods close to that prescribed by the *Provan et al.* [2009a] phase model. In the next section we begin by describing the Cassini data set employed, together with the method of analysis.

4.2 Data selection and analysis

4.2.1 Cassini equatorial data coverage

Our initial data set consists of 1-min averaged magnetic field data in spherical polar coordinates referenced to the planet’s spin axis, that were obtained by the Cassini fluxgate magnetometer [*Dougherty et al.*, 2004]. These data were obtained during the

interval from July 2004 to December 2007, corresponding to the 56 orbits designated ‘Saturn orbit insertion’ (SOI) through to the end of Rev 54. During this interval the spacecraft was predominantly orbiting near Saturn’s equatorial plane, as can be readily seen from the trajectory summary shown in the previous chapter in Figure 3.8. The data obtained on these orbits are therefore well suited to a comprehensive analysis of the magnetospheric period field oscillations in the near-equatorial region, defined here to be the region within $\pm 5^\circ$ latitude of the planet’s equator. However, on Revs SOI and 30-43 the spacecraft trajectory was significantly tilted with respect to the equatorial plane, thus providing insufficient contiguous data within this region for the study of ~ 11 h oscillations. The data for these orbits have thus been removed from our data set. Revs 14 and 15 are further excluded due to the presence of substantial gaps in the magnetometer data during the spacecraft’s passage through the region considered. The volume of data from the remaining 39 orbits is largely insensitive to the latitude cut-off employed, since the trajectories of these orbits generally lie close to the equatorial plane within a few degrees. Extending the latitude cut-off to $\pm 10^\circ$, for example, does not greatly expand the data set available or its coverage in radial distance and local time.

We note that this set of Cassini orbits is effectively the same as that employed by *Provan et al.* [2009a] to study the phase of the field oscillations within the quasi-dipolar ‘core’ region, defined in that study as dipole $L \leq 12$. However, here we set the outer edge at a radial distance of $30 R_S$ so that we cover a significantly larger region, extending from the vicinity of the magnetopause on the dayside into the inner tail on the nightside. The region studied here, therefore, extends beyond the quasi-dipolar ‘core’ into the region where the near-equatorial field forms a ‘magnetodisk’ structure [*Arridge et al.*, 2008b], merging into the tail plasma sheet on the nightside. Since radial distances of $30 R_S$ can also sometimes extend beyond the magnetopause on the dayside, we have examined these data by hand to remove all magnetosheath and solar wind data, as informed by the magnetopause model of *Arridge et al.* [2006]. The innermost radial range sampled on these orbits is typically $\sim 3 R_S$.

The data employed here were thus obtained on Revs A-13 (August 2004 – Au-

gust 2005), 16-29 (October 2005 – October 2006), and 44-54 (May – December 2007), which provide coverage of the equatorial plane as shown in Figure 4.1. In this figure black points represent 1 h of magnetic field data obtained within modular latitudes $|\lambda| \leq 5^\circ$ plotted along the spacecraft trajectory, which is projected onto the planet's equatorial plane as viewed from the north, with the Sun to the right. The dashed circles are shown at $5 R_S$ intervals in radial distance and 2 h intervals in LT. The gray-scale coding according to the scale on the right indicates the total number of 1 min data points that fall into non-overlapping spatial bins of $3 R_S$ in radial distance and 2 h in LT, as typically used in subsequent sections of this study. It can be seen that there is good data coverage in both radial distance and LT beyond $\sim 3 R_S$, with the notable exception of gaps in the afternoon sector (14-16 h LT) at radial distances beyond $\sim 7 R_S$, and in the pre-dawn sector (04-06 h LT) at radial distances of 6-12 R_S .

The latitudinal coverage of the data employed in this study is shown in the upper panel of Figure 4.2, where again the black points represent 1 h of magnetic field data plotted along the spacecraft trajectory, now shown in cylindrical (ρ, z) coordinates. Approximately $\sim 70\%$ of the data are confined to within 1° of the planet's spin equator, while the remainder at large modular latitudes are distributed approximately equally $\sim 15\%$ to the north and $\sim 15\%$ to the south. We note, however that under the southern summer conditions prevailing during the interval of the study, the magnetic equatorial plane (where the radial field component reverses sign) is displaced consistently north of the planet's spin equator due to the component of the solar wind flow along the spin axis [e.g. Cowley, 2006]. The location of the magnetic equatorial plane as modelled by *Arridge et al.* [2008b] is indicated in the figure by the red and green solid lines, corresponding to the start and end of this interval, respectively. It can be seen that the northward displacements are a fraction of an R_S within the quasi-dipolar region, increasing to $\sim 2 R_S$ at the outer limit of the region studied here. It can also be seen that the magnetic equator is almost entirely contained within the $\pm 5^\circ$ range of latitudes employed, as indicated by the grey dashed lines in the figure. Thus the majority of the data were obtained within just a few R_S of the magnetic equatorial plane. The lower panel of Figure 4.2 shows the displacement of the spacecraft above

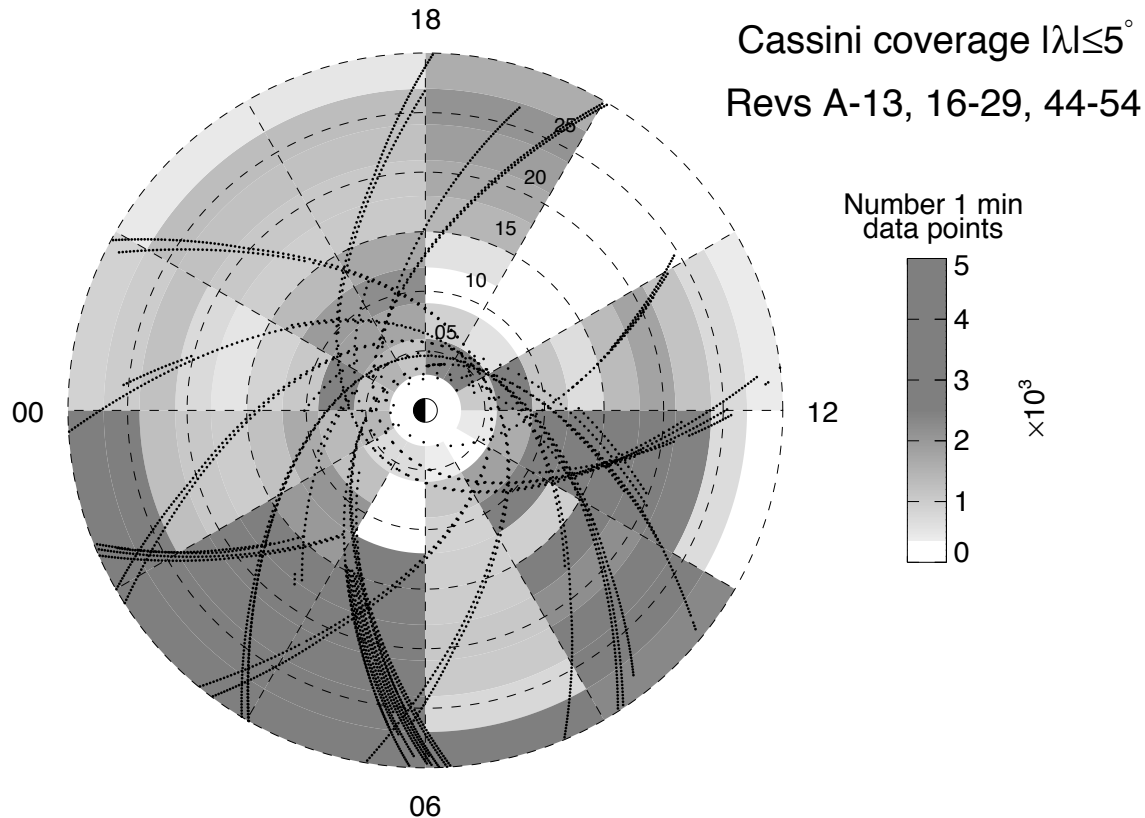


Figure 4.1: Plot of the Cassini coverage of Saturn's equatorial region during the interval of this study. The view is from the north looking down on to the equatorial plane, with the Sun to the right. LT is indicated around the perimeter of the plot, with dashed lines at 2 h intervals. The outer radius of the plot corresponds to $30 R_S$, with dashed circles being shown every $5 R_S$. Each black point indicates the spacecraft position projected onto the equatorial plane at 1 h intervals when the spacecraft is located at latitudes within $\pm 5^\circ$ of the equator, and magnetic data are available. The grey-scale coding indicates the number of 1 min-averaged magnetic field measurements that are available within non-overlapping spatial bins of $3 R_S$ in radial distance and 2 h in LT, as indicated by the scale on the right. Each bin typically contains $\sim 1000\text{-}5000$ points, giving good coverage outside of $\sim 3 R_S$ at all LTs, except at 12–14 h LT beyond $\sim 7 R_S$, and 04–06 h LT in the $\sim 6\text{-}12 R_S$ radial range.

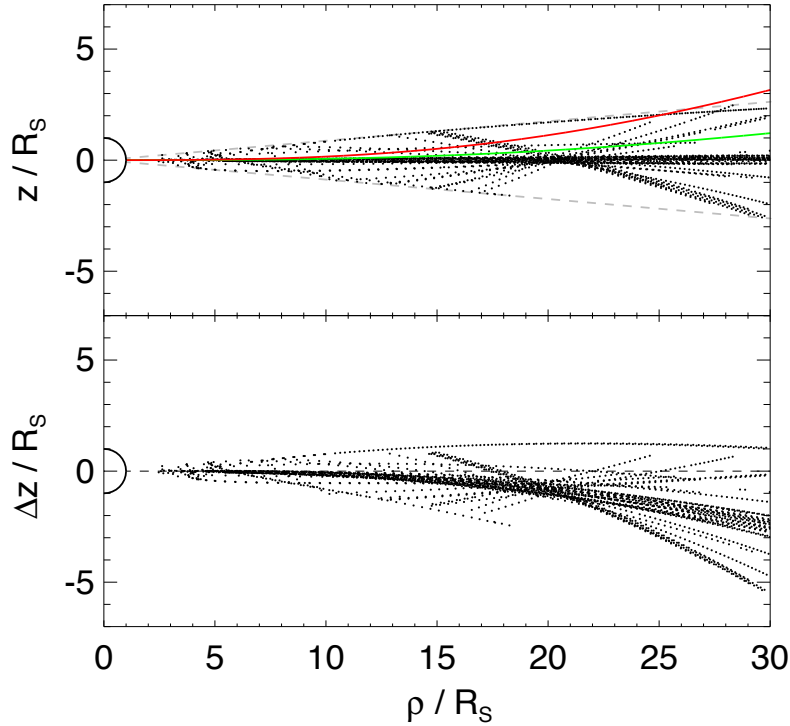


Figure 4.2: Plots showing the latitudinal coverage of the data during the interval of this study. The black points again show 1 h intervals containing magnetic data, as in Figure 4.1, but now plotted in cylindrical coordinates, where z is directed along the planet's spin and magnetic axis and ρ is the perpendicular distance from the axis. The solid lines show the position of the magnetic equator at the beginning (red) and end (green) of the interval according to the model of Arridge *et al.* [2008b] (using a ‘hinging distance’ of $29 R_S$). The $\pm 5^\circ$ latitude band employed in this study is indicated by the grey dashed lines. The lower panel then shows the axial displacement of the spacecraft, Δz , relative to the instantaneous modelled magnetic equator.

or below the instantaneous modelled magnetic equator, the averaged modular value being $\sim 0.8 R_S$. Although these displacements are therefore typically very small, the northward offset of the magnetic equator is still sufficient to result in $\sim 88\%$ of our data set being located south of the equator, according to this model. Nevertheless this should not be a significant factor if the oscillatory perturbation fields are in phase either side of the magnetic equator, as suggested by the previous studies cited above.

4.2.2 Analysis procedure

As indicated in section 4.1, the analysis procedure employed here is based on the results of Provan *et al.* [2009a], whose study spans the whole of the interval we examine. Provan *et al.* [2009a] determined the oscillation phase of each magnetic

field component within the ‘core’ region during each periapsis pass of the spacecraft, by cross-correlating suitably processed field data with a model rotating oscillation determined from the phase of the SKR modulation derived by *Kurth et al.* [2008], employed as an exact guide phase. While subsequently shown to reflect only the variation in the period of the dominant southern hemisphere SKR emission, its use as an exact guide phase is justified in studying these field data, both in the interval studied by *Provan et al.* [2009a] and here, for the reasons outlined in section 4.1. As mentioned in section 4.1, the analysis showed that the oscillations in the r and θ field components are generally in phase with each other, while those in the φ field component are generally in lagging quadrature. They consequently modelled the field oscillations in the ‘core’ region for field component ‘ i ’ as

$$B_i = B_{i0} \cos(\Psi_{Mc}(\varphi, t) - \psi_i), \quad (4.1)$$

where $\Psi_{Mc}(\varphi, t)$ is the ‘core’ magnetic phase function and the polarisation of the oscillation is expressed as $\psi_r = \psi_\theta = 0^\circ$ and $\psi_\varphi = 90^\circ$. The ‘core’ phase function is expressed as

$$\Psi_{Mc}(\varphi, t) = \Phi_M(t) - \varphi, \quad (4.2)$$

where φ is the azimuthal angle (equivalent to LT) measured from noon positive towards dusk, thus corresponding to an ‘ $m = 1$ ’ oscillation as indicated in section 2.8. The near-linear magnetic phase function $\Phi_M(t)$ which defines the period of the field rotation is related to the corresponding function for the (dominant, southern hemisphere) SKR modulation by

$$\Phi_M(t) = \Phi_{SKR}(t) - \psi_M(t), \quad (4.3)$$

where relative phase $\psi_M(t)$ is a function determined empirically from the cross-correlation fits to the periapsis pass data described above. Since both phase functions Φ_M and Φ_{SKR} depart only slightly from linear dependence on time t during one oscillation, the period of the oscillations at any time is well approximated by

$$\tau_{SKR}(t) = \frac{360^\circ}{\left(\frac{d\Phi_{SKR}(t)}{dt} \right)} \quad \text{and} \quad \tau_M(t) = \frac{360^\circ}{\left(\frac{d\Phi_M(t)}{dt} \right)}, \quad (4.4)$$

where the phase functions are expressed in degrees. The absolute value of Φ_{SKR} is defined such that maxima in radiated SKR power occur when

$$\Phi_{SKR}(t) = 360^\circ N, \quad (4.5)$$

for any integer value of N . Similarly, we note that if $B_{r0} = B_{\varphi 0}$ in equation (4.1), the resulting rotating uniform field in the ‘core’ points in the direction $\varphi_M(t)$ relative to the Sun given by

$$\varphi_M(t) = \Phi_M(t), \quad (4.6)$$

again measured from noon positive towards dusk. The equatorial ‘core’ field thus points in the sunward direction when $\Phi_M(t) = 360^\circ N$ for integer N , and towards dusk for $\Phi_M(t) = 360^\circ N + 90^\circ$ and so on, rotating in the same sense as the planet. The results of *Andrews et al.* [2008] and *Provan et al.* [2009a] then show that over the interval of simultaneous magnetic field and SKR phase data analysed, the relative phase $\psi_M(t)$ is approximately constant (within the rather broad scatter of the SKR phase data), with an averaged value of $\sim 150^\circ$. Equations (4.6), (4.5) and (4.3) then imply that at the time of SKR maxima, the direction of the equatorial ‘core’ field is given by

$$\varphi_M \approx 360^\circ N - 150^\circ \approx 360^\circ N' + 210^\circ, \quad (4.7)$$

thus pointing radially outwards at ~ 02 h LT as previously indicated in section 4.1.

We also note at this point that the SKR-based ‘SLS longitude’ system discussed by *Kurth et al.* [2007, 2008] is defined in terms of the above parameters by

$$\lambda_{SKR}(\varphi, t) = \Phi_{SKR}(t) - \varphi + 100^\circ, \quad (4.8)$$

such that at a given instant λ_{SKR} increases in the sense opposite to φ , and hence opposite to the sense of planetary rotation. It is thus directly related to our ‘core’ region magnetic phase (from equation (4.2)) by

$$\lambda_{SKR}(\varphi, t) = \Psi_{Mc}(\varphi, t) + \psi_M(t) + 100^\circ. \quad (4.9)$$

Since the results of *Andrews et al.* [2008] and *Provan et al.* [2009a] have then shown that ψ_M is approximately constant over the interval of simultaneous data, with an averaged

value of $\sim 150^\circ$ as indicated above, we thus have

$$\lambda_{SKR}(\varphi, t) \approx \Psi_{Mc}(\varphi, t) + 250^\circ. \quad (4.10)$$

We may therefore approximately convert Ψ_{Mc} values to ‘SLS longitude’ values by adding 250° to Ψ_{Mc} , or equivalently by subtracting 110° .

The slowly-varying period of the SKR and magnetic field oscillations is then described by expressing the phase functions as polynomials of time t , specifically of fifth order for $\Phi_{SKR}(t)$ and third order for the relative phase $\psi_M(t)$. Expressing t in days since the beginning of 1 January 2004, the fifth order polynomial for Φ_{SKR} determined by *Kurth et al.* [2008] from fits to SKR phase data over the interval 1 January 2004 to 10 August 2007 (corresponding to $0 \leq t \leq 1317$ days) is given by

$$\Phi_{SKR}(t) = 360^\circ \frac{t}{\tau_0} - \Delta\Phi_{SKR}(t), \quad (4.11)$$

where τ_0 is precisely 0.4497 days (10.793 h), and

$$\Delta\Phi_{SKR}(t) = k_0 + k_1 t + k_2 t^2 + k_3 t^3 + k_4 t^4 + k_5 t^5, \quad (4.12)$$

where the empirically-determined constants $k_0 \dots k_5$ are given by

$$\begin{aligned} k_0 &= 86.6681 & \text{deg} & & k_1 &= -2.7537 & \text{deg day}^{-1} \\ k_2 &= 4.7730 \times 10^{-3} & \text{deg day}^{-2} & & k_3 &= -4.8755 \times 10^{-6} & \text{deg day}^{-3} \\ k_4 &= 3.5653 \times 10^{-9} & \text{deg day}^{-4} & & k_5 &= -9.1485 \times 10^{-13} & \text{deg day}^{-5}. \end{aligned} \quad (4.13)$$

Similarly, the magnetic phase function $\psi_M(t)$ determined by *Provan et al.* [2009a] is given by

$$\psi_M(t) = k_{M0} + k_{M1} t + k_{M2} t^2 + k_{M3} t^3, \quad (4.14)$$

where

$$\begin{aligned} k_{M0} &= 209.2 & \text{deg} & & k_{M1} &= -0.5718 & \text{deg day}^{-1} \\ k_{M2} &= 1.1446 \times 10^{-3} & \text{deg day}^{-2} & & k_{M3} &= -0.5995 \times 10^{-3} & \text{deg day}^{-3}. \end{aligned} \quad (4.15)$$

We note that as a consequence of the high-order terms present in the above expressions, necessary to accurately describe the subtle changes in the magnetic and SKR

phase data, these phase models cannot be reliably extrapolated more than a few tens to hundreds of days beyond the interval for which they are collectively defined. To do so rapidly introduces modulo- 360° ambiguities in phases determined relative to these functions. Substitution into equation (4.4) then shows that the sidereal period of the magnetic field oscillations increased from ~ 10.77 h at SOI in mid-2004 to ~ 10.83 h by the end of 2007, closely mirroring the corresponding variation in the SKR period over the interval from 2004 to August 2007 determined by *Kurth et al.* [2008]. The underlying source of the variation of the magnetic phase function $\psi_M(t)$ on secular timescales is later investigated in Chapter 6.

In this chapter we use the *Provan et al.* [2009a] phase model, taken as an exact ‘guide phase’, to define the slowly varying period of the magnetic field oscillations in Saturn’s magnetosphere during 2004-2007, thus allowing us to combine together the near-equatorial field data over this interval to study how the properties of the oscillations vary with radial distance and LT. Specifically we divide the field data (processed as described below) into various bins of radial distance and LT, and plot these binned values versus the ‘core’ phase $\Psi_{Mc}(\varphi, t)$ (modulo 360°). We note that this grouping of data into spatial bins prior to further analysis rapidly reduces the influence of the deterministic phase ‘jitter’ imposed by the weaker field oscillation that is also present in these data at a period corresponding to the weaker SKR emission from the northern hemisphere. A sinusoid is then fitted to the binned data for each component ‘ i ’ using a simple least-squares algorithm, thus yielding both the amplitude $B_{i0}(r, \varphi)$ of the oscillation in that bin, and the phase $\psi_i^*(r, \varphi)$ with respect to the ‘core’ phase $\Psi_{Mc}(\varphi, t)$. The data in each bin is thus represented as

$$B_i(r, \varphi, t) = B_{i0}(r, \varphi) \cos(\Psi_{Mi}(r, \varphi, t)), \quad (4.16)$$

where

$$\Psi_{Mi}(r, \varphi, t) = \Psi_{Mc}(\varphi, t) - \psi_i^*(r, \varphi) = \Phi_M(t) - \varphi - \psi_i^*(r, \varphi). \quad (4.17)$$

Clearly, given this procedure we expect to find $\psi_r^* \approx \psi_\theta^* \approx 0^\circ$ and $\psi_\varphi^* \approx 90^\circ$ within the ‘core’ region inside $\sim 12 R_S$, in conformity with the previous analyses of *Andrews et al.* [2008] and *Provan et al.* [2009a], and equation (4.1). We note that this analysis

method is similar to that previously employed by *Gurnett et al.* [2007] to determine the amplitude and phase of the oscillations in the φ field component with radial distance using the SLS2 longitude system of *Kurth et al.* [2008]. Here, however, we extend the analysis to cover all three field components, and determine how the oscillation properties vary with LT as well as with radial distance.

Prior to fitting equation (4.16) to the data in each spatial bin, we first process the magnetic field data by subtracting the planet's internal magnetic field using the 'Cassini SOI' field model of *Dougherty et al.* [2005], leaving the residual field due to external sources. These data are then band-pass filtered using a Lanczos-squared filter with graduated cut-offs at periods of 5 and 20 h to extract the periodic effects potentially associated with the ~ 11 h magnetospheric periodicity. The width of the filter band allows for the variable Doppler-shifting that the oscillating signal undergoes due to the motion of the spacecraft [see e.g., *Cowley*, 2006]. In keeping with *Provan et al.* [2009a] we also exclude data from certain field components on certain orbits that contain significant field variations due to the planet's ring current that occur on comparable timescales to the magnetospheric period oscillations. On this basis we exclude r and θ component data from Revs 29-33 and 41, and r component data only from Revs 6-14, 34-36, 42, 46 and 54. We also exclude data in all cases that are obtained within ± 5 h of data gaps of more than 5 h duration, such that our filtered data are not significantly influenced by our practice of linearly interpolating over small (< 5 h) data gaps. For this purpose, we note that data external to the magnetopause is treated as if it were a data gap.

Finally, with regard to the size of the spatial bins employed in our analysis, we note that this necessarily involves a compromise between the amount of data in each bin and hence the accuracy of the resultant fit, and the spatial resolution of the amplitude and phase determinations. In practice the smallest bins we employ here (with hence the highest spatial resolution) are of $3 R_S$ in radial distance and 2 h in LT, as employed in Figure 4.1.

4.2.3 Sample results

Figure 4.3 shows sample results from a radial chain of 9 bins centred on local midnight which in this case are of 4 h width in LT, such that each bin contains data from 22-02 h LT. The radial width of each bin is $3 R_S$ as indicated above, covering intervals of 3-6, 6-9, ..., 27-30 R_S . Data for the r , θ , and φ field components are plotted separately in the three panels from left to right, with data in each panel stacked with increasing radial distance. In each bin, band-pass filtered residual magnetic field data are plotted as a function of the *Provan et al.* [2009a] ‘core phase’ Ψ_{Mc} , modulo 360° , shown by the black lines. The dashed lines indicate the zero values for each radial bin, with each successive bin being displaced upward by 10 nT. The red traces show the least-squares fits of equation (4.16) to the data points in each bin. The amplitude of the fit in nT is indicated to the right of each plot along with the radial position of the bin, while the phase ψ_i^* in degrees is indicated at the peak of the sinusoid. Data coverage of ‘core’ phase Ψ_{Mc} is good throughout this region, such that the fitted parameters are well constrained by the data, though there are some bins (e.g. 15-18 R_S) where phase gaps of $\sim 90^\circ$ are present. In general we place a limit of 330 on the minimum number of data points that must be present in a bin before amplitudes and phases are calculated, corresponding (with 1 min data) to $\sim 50\%$ of an oscillation cycle, in an attempt to ensure a minimum reasonable phase coverage. However, each bin in Figure 4.3, typically contains ~ 1000 -5000 points, so this criterion is well-satisfied in all bins in this case.

It can readily be seen from Figure 4.3 that the oscillatory field in the inner 3-4 bins, corresponding to radial distances of ~ 3 -15 R_S , is in good agreement with the results of previous studies, with oscillation phase values near zero for the r and θ field components, and near 90° for the φ component, as expected. The phases are then seen to increase from these values with increasing radial distance, suggesting outward radial phase propagation as found previously by *Gurnett et al.* [2007] (in the φ field component only), but by varying amounts in the three components of the field. The phase increase observed across the $\sim 27 R_S$ radial range covered here is $\sim 90^\circ$ in the r

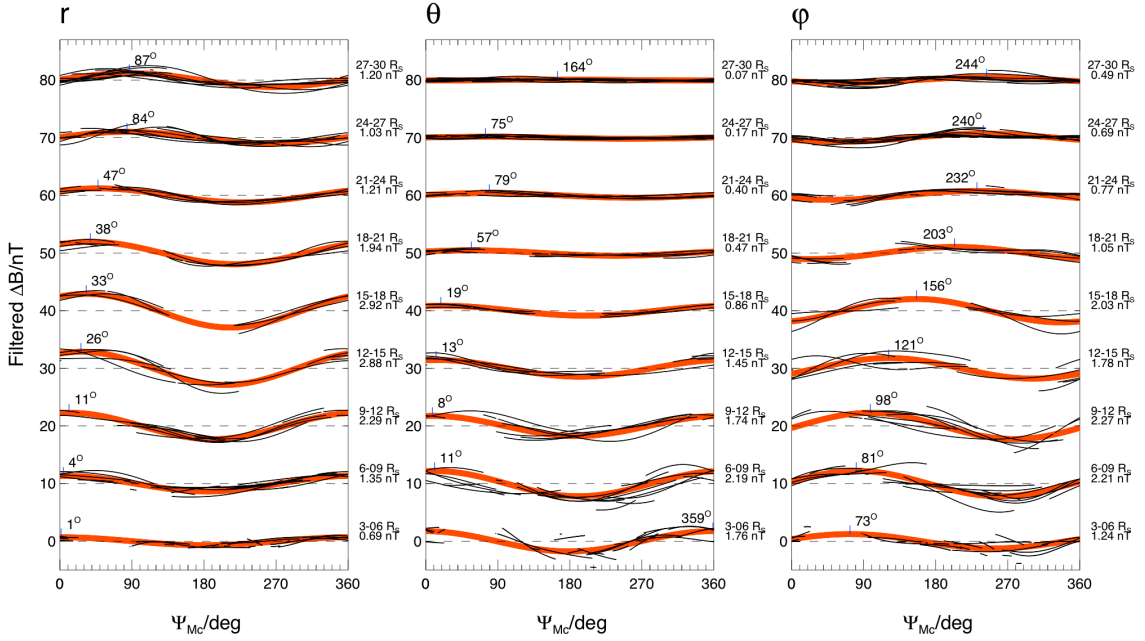


Figure 4.3: Plot showing processed magnetic field data (black lines) plotted versus the ‘core’ phase, Ψ_{Mc} , for each spherical polar component of the field (r , θ , and φ from left to right), in a radial chain of 9 bins covering 22–02 h LT centred on local midnight. The bins are $3 R_S$ in radial width spanning the radial range ~ 3 – $30 R_S$, and are stacked in the plot in order of increasing radial distance. The processed data consists of 1 min resolution band-pass filtered residual magnetometer data as described in section 4.2.2. The red traces show a sinusoidal fit to the data in each bin (equation (4.16)), obtained by a linear least-squares method. The phase of the sinusoid, ψ_i^* , is indicated at its peak value in the plot for each bin, while the oscillation amplitude is indicated to the right of the data set to which it applies.

and θ field components, but increases to $\sim 160^\circ$ in the φ component, the implications of which will be discussed in later sections. Similarly, the amplitude is observed to increase with radial distance in each field component, before reaching a peak and then declining at larger radial ranges. Peak values of ~ 2.2 nT at 6–9 R_S are seen in the θ field component, ~ 2.3 nT at 9–12 R_S in the φ field component, and ~ 2.9 nT at 15–18 R_S in the r field component. In the following section we survey corresponding results for all LT ranges, thus presenting an overall picture of the oscillating field in the equatorial region.

First, however, we briefly discuss the uncertainties in our phase and amplitude determinations. The uncertainty in the phase is taken to be given by the change in the value required to yield a significant increase of 10% in the RMS deviation between the data and the best-fit sinusoid away from the minimum value. The uncertainty in

the amplitude is then taken to be given by the corresponding change between best-fit values, and the mean of the values at the extrema of the above range of phases. While uncertainties calculated in this manner do not give statistical confidence intervals in the strict sense, they nevertheless accurately express the relative confidence of the fitted parameters within different bins. The mean phase uncertainty of the data in Figure 4.3 estimated using this method is $\sim \pm 20^\circ$, comparable to the phase ‘jitter’ in the data from individual passes [Andrews *et al.*, 2008; Provan *et al.*, 2009a], varying from a minimum of $\sim \pm 7^\circ$ for the r component in the range 15-18 R_S , to a maximum of $\sim \pm 92^\circ$ in the θ component at 27-30 R_S . Analysis shows that, in general, the phase uncertainty grows approximately linearly with the ratio of the RMS deviation over the best-fit amplitude, with the uncertainty increasing to $\sim \pm 90^\circ$ when the latter ratio increases to ~ 1.5 . In the sections below, therefore, values are not shown when the RMS deviation exceeds this limit. The uncertainty in the amplitude values in Figure 4.3 is found to be typically $\sim \pm 10\%$, varying between $\sim \pm 2\%$ for the r component in the range 12-15 R_S and $\sim \pm 90\%$ in the θ component in the range 27-30 R_S . Application of the above criterion also leads to the removal of data with such large amplitude uncertainties, approaching $\pm 100\%$. In practice, the criterion leads to the exclusion of results from a small number bins where the number of field measurements is low (though exceeding the initial limit of 330 data points), the phase coverage poor, or the amplitude of the oscillation is very small. In Figure 4.3, for example, only the results from the outermost bin of the θ field component are excluded, in which the fitted amplitude is ~ 0.07 nT, a factor of ~ 3 smaller than the RMS deviation of the data about that fit. The phase determined from the fit in this bin is indeed notably discrepant relative to the phases in adjacent bins.

4.3 Amplitude and phase of the field oscillations in the equatorial region

4.3.1 Variation with radial distance and LT

Overall results are shown in Figure 4.4. In Figure 4.4a we plot the amplitude and phase of the oscillations versus radial distance in fixed LT sectors, while in Figure 4.4b we plot these quantities versus LT at fixed radial distances in a complementary format. Specifically, in Figure 4.4a we use bins of $3 R_S$ in radial distance (i.e. 3-6, 6-9, ..., 27-30 R_S) and 4 h bins in LT (as in Figure 4.3), where the colour-coding indicates the different LT sectors as indicated in the diagram in the top-left corner of the figure (which has a format similar to Figure 4.1). Thus, for example, the black traces in Figure 4.4a correspond to the 4 h LT sector centred on midnight (22-02 h LT), as shown previously in Figure 4.3. Similarly, in Figure 4.4b we employ bins of 2 h in LT and $6 R_S$ in radial distance (3-6, 6-12, ..., 24-30 R_S), where the plots are now colour-coded according to radial range as again indicated in the diagram in the top-left corner. The plots in the top-right corner of each figure indicate the number of 1 min data points, N , in each bin, for each field component. The lower panels in these figures then show from left to right, the amplitudes and phases of the oscillations in the r , θ , and φ field components, respectively.

We begin our discussion with the oscillation in the θ field component (directed north-south through the equatorial plane), the amplitudes and phases of which are plotted in the middle and lower central panels of Figure 4.4a and b. The radial profiles of amplitude in Figure 4.4a show a peak at $6-9 R_S$, falling modestly by ~ 0.5 nT in the inner $3-6 R_S$ range, and near-monotonically to small values at larger radial distances, particularly beyond $\sim 15 R_S$. The peak values themselves are somewhat larger on the nightside, $\sim 1.5-2$ nT, than on the dayside, $\sim 1-1.5$ nT, though the overall variation with LT is not large as can be seen explicitly in Figure 4.4b. Turning to the phase values shown in the lower central panels it can be seen that values are close to zero throughout the ‘core’, as expected, but rise slowly with increasing radial distance,

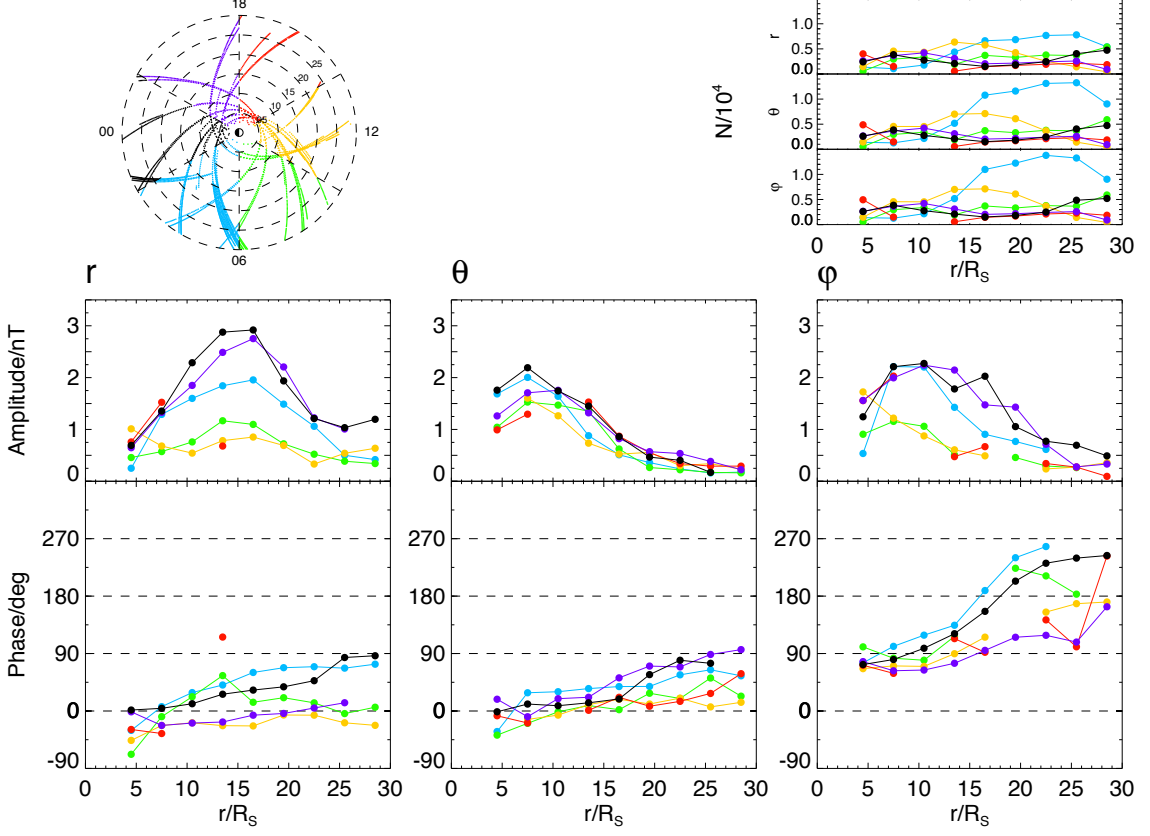


Figure 4.4: (a) Plots of the oscillation amplitude and phase versus radial distance, using bins of $3 R_S$ in radial distance and 4 h in LT, with the colour coding indicating the LT sector of each bin, as depicted in the top-left corner of the figure (which has a format similar to Figure 4.1). The number of 1 min data points in each bin is indicated in the panels shown in the top-right corner of the figure, for each field component. The middle and lower panels indicate the amplitude and phase of the oscillation, respectively, determined as outlined in section 4.2, for each field component r , θ , and φ from left to right.

suggestive of an outward-propagating disturbance. Phase delays with increasing radial distance are larger on the nightside than on the dayside, reaching $\sim 90^\circ$ in the post-dusk and midnight sectors at the outer edge of the region examined, such that the oscillations in this sector at these distances are in approximate lagging quadrature with respect to those in the ‘core’, as previously noted in the discussion of Figure 4.3. Phase variations with radius are generally significantly smaller on the dayside, with almost no phase change with radial distance occurring in the noon sector. These results thus suggest that the effective radial phase speed is significantly larger on the dayside than on the nightside, as will be quantified in section 4.4.

We now examine the oscillations in the r and φ field components (lying in the

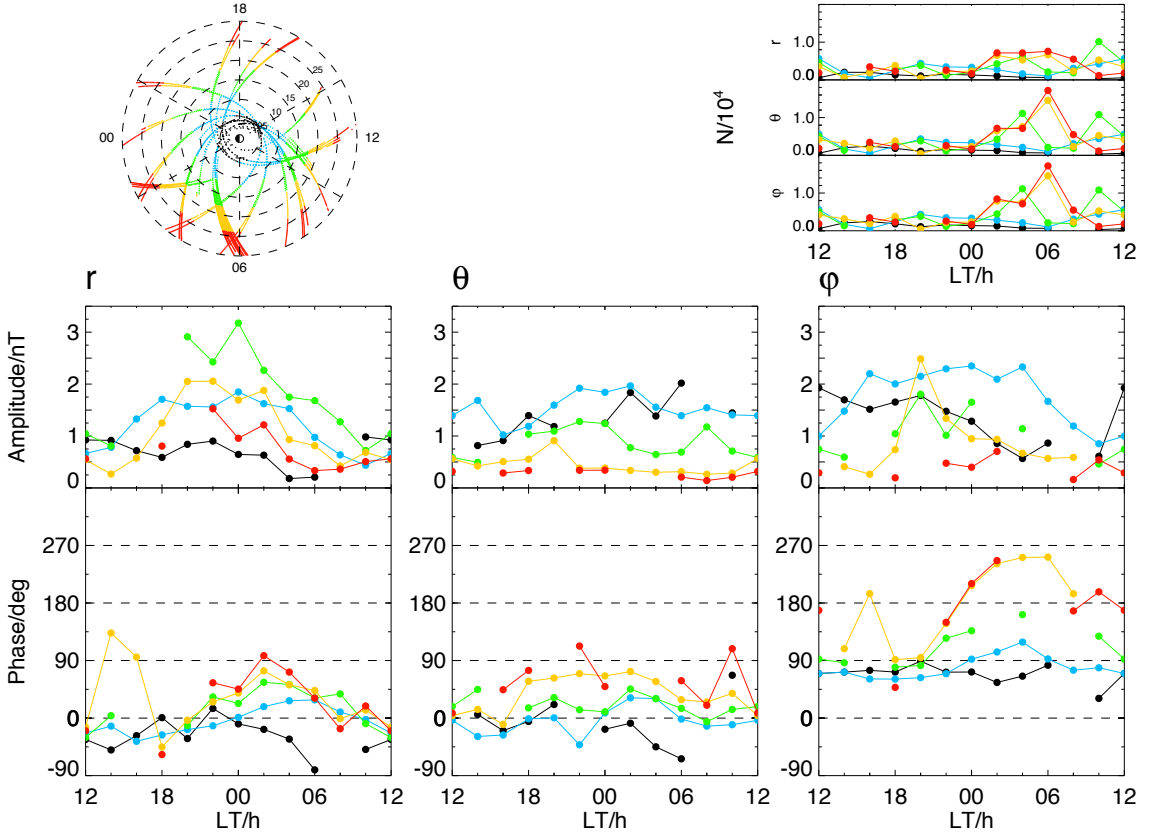


Figure 4.4: (b) Similar to Figure 4.4a, but now with the amplitude and phase of the oscillation plotted versus LT using 6 R_S bins of radial distance and 2 h in LT, with the colour coding indicating radial distance as depicted in the diagram in the top-left corner.

equatorial plane), results for which are shown in the middle and lower left- and right-hand panels of Figures 4.4a and 4.4b. The amplitude variations in these two field components show generally similar behaviour, rising from small values in the inner region to peak at larger distances, before falling to small values at the outer edge of the region considered. However, there is a much stronger dependence on LT evident in these components than in the θ component, with peak amplitudes typically maximising in the pre-midnight sector ($\sim 20\text{-}24$ h LT) as can be seen in both Figures 4.4a and 4.4b. Indeed, it can be seen that in the noon sector (orange traces in Figure 4.4a) no significant peak in amplitude is present at all, the amplitudes being small and approximately constant with radius in the r field component, and monotonically falling with increasing radius in the φ component.

In more detail, the amplitude of the φ field component is $\sim 1\text{-}1.5$ nT in the inner

region at $3\text{-}6 R_S$ (comparable to that in the θ component), peaks on the nightside at ~ 2 nT in the radial range $6\text{-}15 R_S$ corresponding to the outer ‘core’ region, and then generally falls with radial distance with values on the nightside typically larger than that of the θ component beyond $\sim 9 R_S$. The amplitude of the r field component, however, is significantly smaller than that of the φ and θ components in the inner region, with values of $\sim 0.5\text{-}1$ nT, while growing to larger peak values of $\sim 2\text{-}3$ nT on the nightside at larger radial distances of $\sim 15\text{-}18 R_S$. The nightside amplitudes of the r field component then remain larger than those of both the φ and θ components as they again fall with increasing radial distance. Overall, therefore, the oscillations in the equatorial field components are dominated by the φ component in the inner region between 3 and $9 R_S$, and by the r component beyond $\sim 12 R_S$. The significance of this result for the form of the oscillating field will be discussed further in section 4.5.

Examining now the phase values of the r and φ field components, it can be seen that the phase behaviour of the r component is generally similar to that of the θ component, with near-zero values in the inner region, increasing slowly with radial distance, more rapidly on the nightside than on the dayside. However, a significant departure is observed in the post-dusk sector (purple trace in Figure 4.4a), where the phase of the r field component increases by only a small amount between the inner and outer regions, similar to the behaviour on the dayside, while the phase of the θ component increases by $\sim 90^\circ$ in the same sector. Thus while our results indicate that these field components generally oscillate in phase throughout the equatorial region, the r component moves into approximate leading quadrature with the θ component in the post-dusk sector. The behaviour of the φ field component is somewhat more complex. In the inner region, out to $\sim 15 R_S$, the phase values are near $\sim 90^\circ$ as expected, increasing gradually with radial distance in a manner similar to that of the r and θ components, such that φ remains in approximate lagging quadrature with r and θ throughout this region. However, the φ component phase increases much more rapidly across $15\text{-}21 R_S$, by $\sim 90^\circ$ in the midnight and dawn sector (black, blue, and green traces in Figure 4.4a) and by lesser amounts at noon and dusk (orange, red, and purple traces), before levelling out once more in the outer region. The net result is that

while the φ field component remains in lagging quadrature with the r component to large distances in the dusk sector, it moves towards anti-phase at other LTs, and even towards leading quadrature with r in a region near dawn.

4.3.2 Phase fronts and phase differences

A more graphic representation of the above phase data is presented in Figure 4.5, where we show colour-coded plots of the full oscillation phase function (given by equation (4.16)), i.e. $\Psi_{Mi} = \Phi_M - \varphi - \psi_i^*$ (modulo 360°) for field component ‘ i ’, versus radial distance and LT in the equatorial plane, at two points in the oscillation cycle. Plots are shown for the r , θ , and φ field components from left to right, as in Figure 4.4, where the top row of plots corresponds to $\Phi_M = 0^\circ$, and the second row to $\Phi_M = 45^\circ$. The colour scale is shown on the right, and is such that field components are positive in the red and orange regions, with $\cos \Psi_{Mi} = 1$ at their interface, and negative in the green and blue regions, with $\cos \Psi_{Mi} = -1$ at their interface. Correspondingly, zeros in the field are present at the interfaces between the red and green, and the blue and orange regions. The inset icons in the top-left of each panel indicate the expected results within the ‘core’ region if the phase exactly obeys the model derived by *Provan et al.* [2009a], given by equation (4.1). For example, at $\Phi_M = 0^\circ$ when the equatorial ‘core’ field points towards the Sun (equation (4.6)), the ‘core phase’ is zero on the noon meridian, and increases clockwise around the plot such that the r and θ field components are positive on the dayside and negative on the nightside. For the φ field component at $\Phi_M = 0^\circ$ this pattern is rotated clockwise through 90° , such that the field is positive at dawn and negative at dusk. Similarly when $\Phi_M = 45^\circ$ in the bottom row, the equatorial ‘core’ field points 45° duskward, and each ‘core’ phase pattern is rotated anticlockwise by 45° .

We now compare these model ‘core’ phases with the phase plots shown, which have been determined using radial bins of $3 R_\oplus$ as before, but now with 2 h bins in LT computed every hour (such that adjacent bins overlap by 0.5 h LT). Beginning as before with results for the θ field component shown in the central column, it can be seen

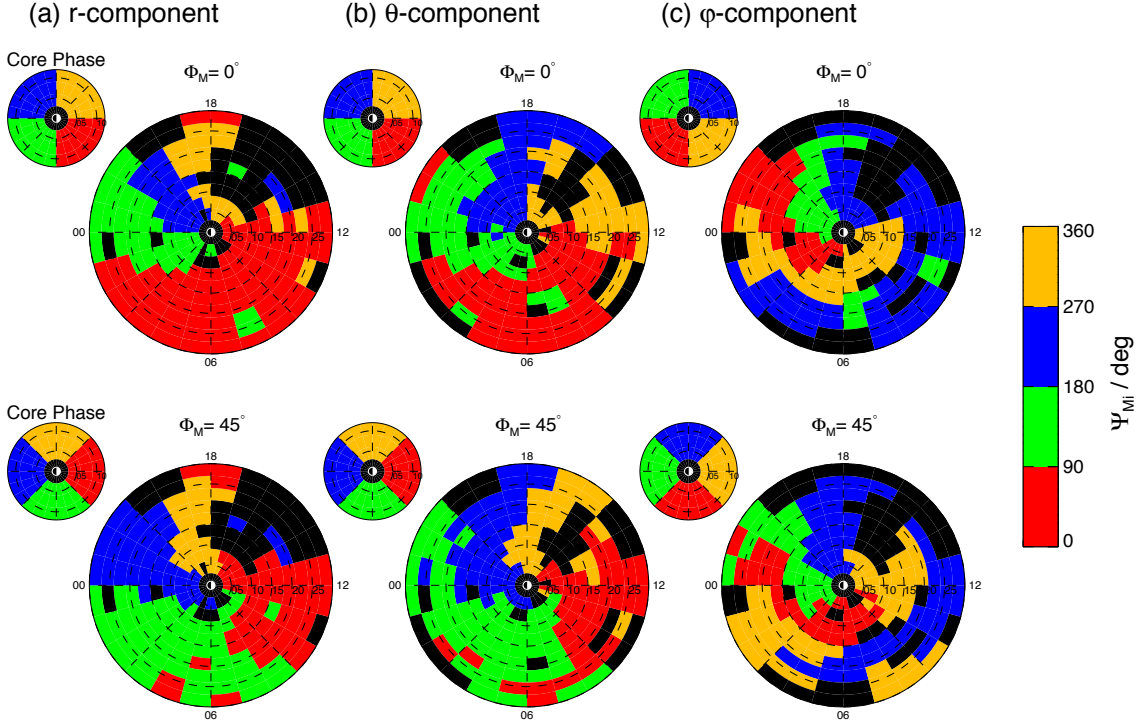


Figure 4.5: Plots showing the oscillation phase Ψ_{Mi} for each magnetic field component, given by equation (4.16), at two instances of Φ_M , plotted versus radial distance and LT on the equatorial plane, determined using bins of $3 R_S$ in radial distance and 2 h in LT, computed every hour. The phase is colour-coded in 90° increments as indicated by the colour bar on the right of the figure, such that the field in any component is positive in the red and orange sectors, and negative in the blue and green. The format is otherwise similar to Figure 4.1. The inset icon in the top-left corner of each plot shows the expected ‘core’ phase out to $\sim 12 R_S$ as determined by Provan *et al.* [2009a], given by equation (4.2). Results for the r , θ , and φ field components are shown from left to right, where the upper row of plots corresponds to $\Phi_M = 0^\circ$, and the lower row to $\Phi_M = 45^\circ$.

that the phase is largely in agreement with the ‘core’ model out to $\sim 15 R_S$ as expected, but that beyond this the nightside phase fronts become increasingly ‘swept back’ to earlier LT with increasing radius such that the phase in the outer nightside region is approximately in lagging quadrature with the ‘core’, as indicated in section 4.3.1. However, the effect on the dayside is much less marked. As a consequence of this dependency on LT, the phase fronts become compressed together in the dusk sector, and expanded away from each other in the dawn sector. Thus, for example, at larger radii the ‘blue’ region at $\Phi_M = 0^\circ$ is generally confined to a narrow region in the post-dusk sector, while the ‘red’ region extends from noon all the way through the post-midnight sector. The effect of this on the azimuthal propagation of the oscillation

becomes evident on comparing the plots for $\Phi_M = 0^\circ$ and $\Phi_M = 45^\circ$. Here the ‘orange’ phase region becomes compressed in the outer region within the dusk sector, while the ‘green’ phase region expands rapidly through the dawn sector, confining the ‘red’ sector largely within the noon quadrant. Thus, in the outer region the azimuthal phase propagation is retarded at dusk and enhanced at dawn, as will be quantified in section 4.4. Further evolution of this phase pattern with increasing Φ_M can readily be envisaged from the plots shown in Figure 4.5 through transformation of the colours. For example, at $\Phi_M = 90^\circ$ the blue areas in the $\Phi_M = 0^\circ$ plots transform into green, the green into red and so on. Alternatively, animations of the propagating phase fronts may be viewed in the auxiliary online material¹ in Movies S1-3 for each of the three field components.

Turning now to the phase of the r field component shown on the left-hand side of Figure 4.5, it can be seen that the behaviour is similar to the θ component as expected from the largely in-phase behaviour of these components. However, the phase fronts post-dusk are now advanced compared with the ‘core’ region, rather than being ‘swept back’, such that r is in leading quadrature with θ in this sector as noted in section 4.3.1. As a consequence, the phase fronts in the outer region are even more compressed in this sector than for the θ field component, with the result that at $\Phi_M = 0^\circ$ negative radial field values are confined to a narrow ~ 6 h range of LT between ~ 20 and 02 h (blue and green regions) while positive values are found over the remaining ~ 18 h of LT (red and orange regions). Of course, these polarities reverse sense at $\Phi_M = 180^\circ$. Again, this implies azimuthal phase propagation that is retarded in the dusk sector and enhanced in the dawn sector for this field component.

Results for the φ field component on the right-hand side of Figure 4.5 again show good agreement with the ‘core phase’ within ~ 15 R_S , as anticipated from the discussion in section 4.3.1. However, at LTs from midnight to dawn and noon, much stronger ‘sweep-back’ of the phase fronts occurs in the radial range just beyond this region, such that the phase in the outer region is in approximate lagging quadrature with those of the ‘core’ at the same LT. An exception to this occurs in the dusk sector where the

¹Available online at <http://www.agu.org/journals/ja/ja1004/2009JA014729/>.

phase does not vary greatly with radial distance, except towards the edge of the region considered.

The implications of these results for the phase difference between the three field components, and thus the overall structure of the oscillatory field, are quantified in Figure 4.6. Here, the left-hand column of plots examines the phase difference between the r and θ field components, the centre column the phase difference between the φ and θ components, and the right-hand column the phase difference between the φ and r components. The labels at the top of the plots ' $i - j$ ', for field components ' i ' and ' j ' thus indicate that the phase differences plotted beneath correspond to $\Delta\psi^* = \psi_i^* - \psi_j^*$. The upper row of plots then show the phase difference versus radial distance colour-coded according to LT in the same format as Figure 4.4a, the middle row shows these values versus LT colour-coded according to radial distance in the same format as Figure 4.4b, while the bottom row shows the colour-coded phase difference in a format similar to Figure 4.5. However, the colour scale of the latter, shown on the right, has been revised relative to the Figure 4.5, such that red corresponds to the $\pm 45^\circ$ band of phase centred on 0° , green to the $\pm 45^\circ$ band centred on 90° , and so on. Red regions thus indicate that field component ' i ' is approximately in-phase with component ' j ', while blue indicates anti-phase. Green indicates ' i ' is in lagging quadrature with ' j ' and orange vice-versa.

Examining first the $r - \theta$ results in the left-hand column, it can be seen that these field components are approximately in phase not only in the 'core' region but also throughout the dawn-side magnetosphere (red region in the bottom plot). However, the r field component moves into leading quadrature with θ (orange region) at larger distances in the post-dusk sector as indicated above, while there is also some indication of θ being in leading quadrature with r (blue regions) at similar distances in the pre-dusk sector, within the limited spatial coverage of that data. Similarly, the $\varphi - r$ results in the right-hand column show that φ is in lagging quadrature with r throughout the 'core' region, extending into the outer dusk sector (green region in the lower plot). However, φ is approximately in anti-phase with r in the outer region at the other LTs (blue), extending from midnight through dawn to noon, with the phase

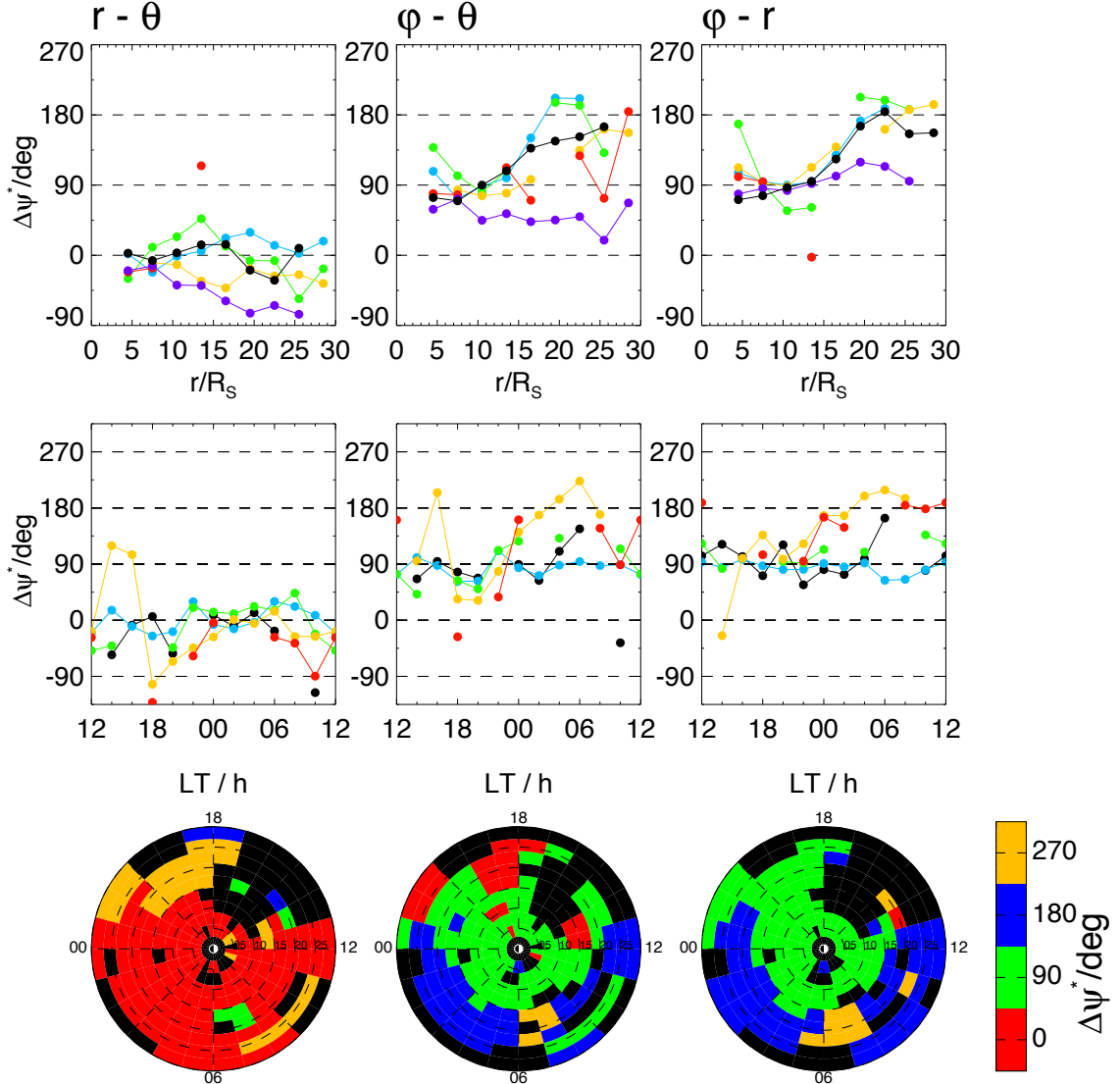


Figure 4.6: Plots showing the phase differences between each pair of field components, $\psi_r^* - \psi_\theta^*$, $\psi_\phi^* - \psi_\theta^*$, and $\psi_\phi^* - \psi_r^*$ from left to right, plotted versus radial distance in the top row, LT in the middle row, and projected onto the equatorial plane in the bottom row. From top to bottom the differences plotted in each row thus correspond to the differences in the individual component phase data presented in Figures 4.4a, 4.4b, and 4.5, respectively. The colour coding in the top row thus indicates LT using the same format as Figure 4.4a, while that in the middle row indicates radial distance in the same format as Figure 4.4b. The colour-code employed in the bottom plots, shown in the colour bar on the right, is such that the two components are approximately in phase ($\pm 45^\circ$) in the red regions and anti-phase in the blue regions, while the first component (e.g. r in the left-hand column) is in lagging quadrature with the second (θ in the left-hand column) in the green regions, and vice-versa in the orange regions.

difference increasing such that φ becomes approximately in leading quadrature with r in the outer region near the dawn meridian (orange region). The $\varphi - \theta$ plots in the centre column of Figure 4.6 are then essentially similar to the $\varphi - r$ plots on the right, as expected from the mainly ‘in-phase’ $r - \theta$ relationship. However, the changing phase between r and θ in the outer post-dusk sector leads to φ and θ becoming approximately in-phase in that region. The consequences of these relationships for the overall structure of the oscillatory field in the equatorial plane will be discussed in section 4.5.

4.4 Radial and azimuthal phase speeds

In section 4.3 it was noted that the generally increasing values of the oscillation phase with radial distance implies outward radial propagation of the phase fronts with a speed that is generally larger on the dayside than on the nightside. The related LT dependence of the ‘sweep-back’ of the phase fronts similarly suggests slower azimuthal propagation at dusk than at dawn. In this section we quantify these effects by calculating the radial and azimuthal phase velocities explicitly from the phase data.

The rate of change of the phase $\Psi_{Mi} = \Phi_M(t) - \varphi - \psi_i^*(r, \varphi)$ (equation (4.16)) for a point (r, φ) on the equatorial plane moving with velocity (v_r, v_φ) in the stationary (non-rotating) frame is given by

$$\frac{d\Psi_{Mi}}{dt} = \frac{\partial\Psi_{Mi}}{\partial t} + \boldsymbol{\nu} \cdot \nabla \Psi_{Mi} = \Omega_M - v_r \frac{\partial\psi_i^*}{\partial r} - \frac{v_\varphi}{r} \left(1 + \frac{\partial\psi_i^*}{\partial\varphi} \right), \quad (4.18)$$

where

$$\Omega_M = \frac{d\Phi_M}{dt} \quad (4.19)$$

is the instantaneous angular frequency of the ‘core’ phase model of *Provan et al.* [2009a], obtained by differentiation of equation (4.16) (using equations (4.13) and (4.15)). We then obtain an expression for the radial phase speed by setting $v_\varphi = 0$, and determining the speed v_r so that $d\Psi_{Mi}/dt = 0$, such that we move exactly radially

with a point of given phase Ψ_{Mi} . The radial phase speed is thus given by

$$\nu_{ri} = \frac{\Omega_M}{\left(\frac{\partial \psi_i^*}{\partial r} \right)}. \quad (4.20)$$

We note that Ω_M in the above expression is not quite constant, but varies over the interval of this study by $\sim 1\%$ as discussed in section 4.2. However, since this variation is very small, for simplicity we here employ a fixed representative value taken to be $\Omega_M = 0.16160 \times 10^{-3} \text{ rad s}^{-1}$, equivalent to a rotation period of 10.800 h, thus corresponding specifically to $t \approx 650$ d, near the centre of the interval considered (12 October 2005). Similarly, setting $\nu_r = 0$ in equation (4.18), we obtain an expression for the azimuthal phase velocity, normalized to Ω_M , as

$$\frac{\Omega_i}{\Omega_M} = \frac{1}{\left(1 + \frac{\partial \psi_i^*}{\partial \varphi} \right)}. \quad (4.21)$$

Considering first the radial phase speed given by equation (4.20), we reproduce the phase values ψ_i^* versus radial distance in the top panels of Figure 4.7a, as shown previously in Figure 4.4a, determined in bins of $3 R_S$ in radial distance and in six colour-coded 4 h bins in LT. To evaluate the radial phase speed from equation (4.20) we first need to determine the radial gradient of ψ_i^* , and given the nature of these data only an overall linear fit seems appropriate (piecewise for the φ field component as discussed below). These fits are shown by the similarly colour-coded solid lines in Figure 4.7a, the gradients of which yield the overall phase speed in each LT sector, for each field component oscillation, as plotted in the lower panels of Figure 4.7a. The error bars shown are determined from the $1-\sigma$ uncertainties in the gradients of the linear fits.

Beginning with results for the θ field component shown in the centre panels of Figure 4.7a, it can be seen that the phase speeds in the midnight and pre-midnight sectors are typically $\sim 150 \text{ km s}^{-1}$, increasing to $\sim 200 \text{ km s}^{-1}$ in the pre-dusk and dawn sectors, though with larger error bars. The estimated phase speed peaks in the noon sector at $\sim 500 \text{ km s}^{-1}$, with substantially larger error bars. Similar, but more scattered results are obtained for the r field component, as shown on the left of Figure 4.7a, with values of $\sim 150 \text{ km s}^{-1}$ in the midnight and pre-dawn sectors, increasing to ~ 400 - 600 km s^{-1} post-dusk and post-dawn and to $\sim 700 \text{ km s}^{-1}$ in the noon sector, the latter

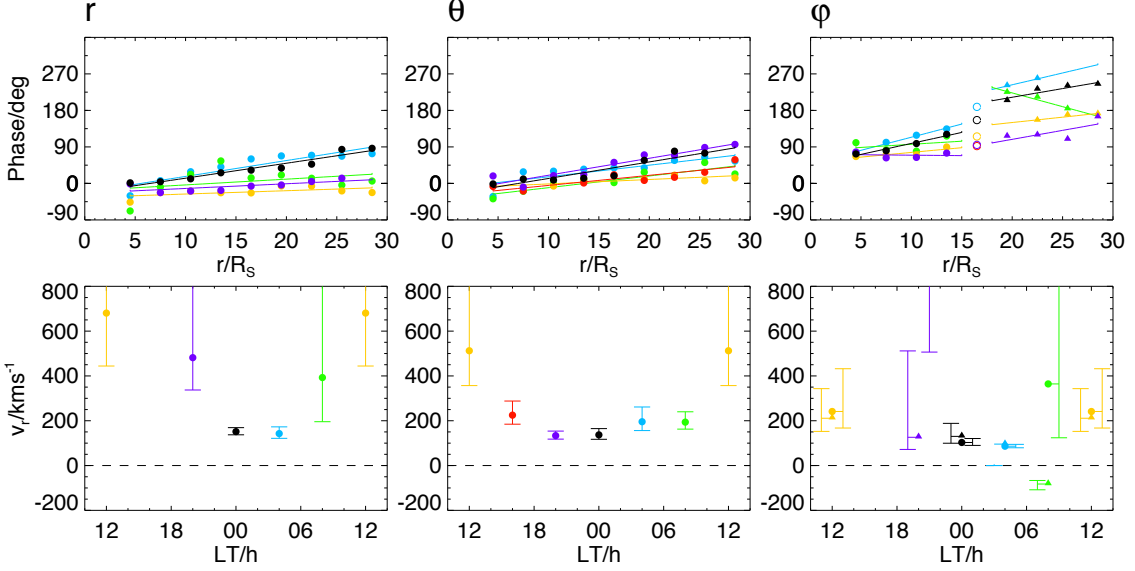


Figure 4.7: (a) Plots related to the radial phase velocity discussed in section 4.4. The top row shows the phase ψ_i^* plotted versus radial distance for each field component (r , θ , ϕ from left to right), in a format similar to the bottom panels of Figure 4.4a, where the colour-coding indicates the LT range as in the latter figure. Here, the similarly colour-coded solid lines show linear fits to these data (piecewise for the ϕ field component data as described in section 4.4, omitting data in the 15–18 R_S radial range shown by the open circles). Radial phase velocities determined from the gradients of these fits using equation (4.20) are then plotted versus LT in the lower panels, where the error bars are determined from the $1-\sigma$ uncertainties in the gradient of the fit. The velocities determined in the inner and outer region in the ϕ field component are indicated by solid circles and triangles, respectively, with the error bars offset to the right and left.

again with large error bars. The significance of these results is commented on in section 4.7.

Results for the ϕ component have been treated somewhat differently due to the presence of the rapid phase increase near $\sim 15 R_S$ associated with the spatial structure of the oscillatory field, as will be discussed in section 4.5. Consequently, we have made separate linear fits to the data in the inner region ($3-15 R_S$) shown by solid circles, and to the data in the outer region ($18-30 R_S$) shown by solid triangles, omitting data from $15-18 R_S$ shown by the open circles. Corresponding radial phase speeds are shown by the solid circles and triangles in the lower plot, with offset error bars for clarity. Phase speeds are again $\sim 100-150 \text{ km s}^{-1}$ on the nightside, increasing to $\sim 250-350 \text{ km s}^{-1}$ on the dayside, though with larger error bars. The phase speed determined within the $18-30 R_S$ radial range in the post-dawn LT sector is apparently negative, indicating inward

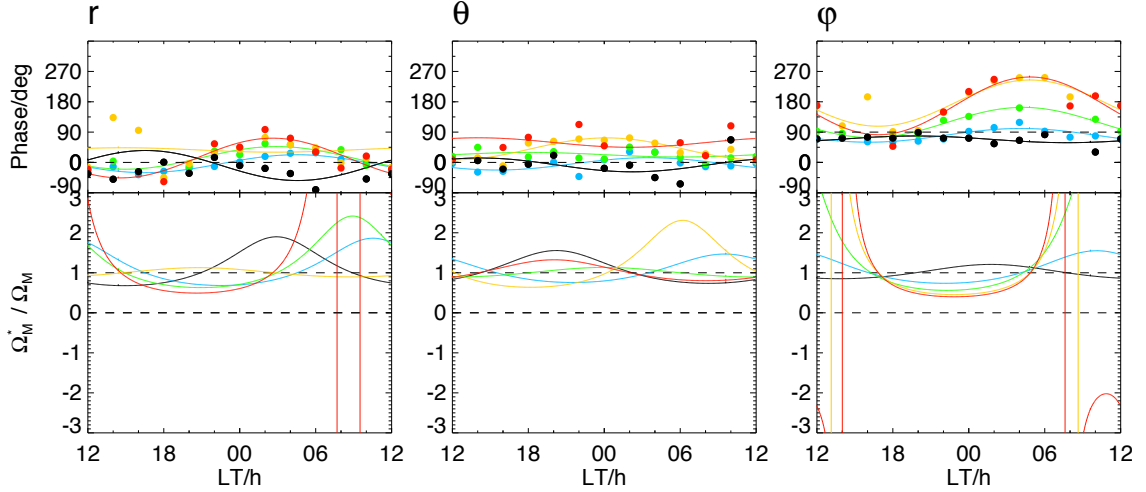


Figure 4.7: (b) Plots related to the azimuthal phase velocity discussed in section 4.4. The top row shows the phase ψ_i^* plotted versus LT for each field component in a format similar to the bottom panels of Figure 4.4b, where the colour-coding indicates the radial distance as in the latter figure. The similarly colour-coded solid lines show a two-term Fourier series fit to these data. The lower panels show the corresponding azimuthal phase velocities versus LT in each radial range, expressed as a fraction of the angular frequency of the ‘core phase’ model as given by equation (4.21), colour-coded in the same format as the top panels. Regions in which the azimuthal gradient in the two-term Fourier series fit becomes sufficiently large and negative that the normalized angular velocity becomes negative, indicating retrograde motion, are bounded by the vertical lines in the lower panels where the function passes through $\pm\infty$.

motion of the phase fronts. However, this is the only region for which this reversal of the sense of phase gradient is observed, and furthermore it is relatively poorly constrained by the further subdivision of the φ component data into two distinct radial ranges.

Results for the normalized angular velocity associated with azimuthal phase propagation are similarly shown in Figure 4.7b. The upper panels again reproduce the phase values ψ_i^* as plotted previously in Figure 4.4b (using bins of 6 RS in radial distance and 2 h in LT), with the values colour-coded according to radius such that black corresponds to 3-6, blue to 6-12, green to 12-18, orange to 18-24, and red to 24-30 RS. A two-term Fourier series fit of the form $\psi_i^*(\varphi) = \psi_{i0}^* + \psi_{i1}^* \cos(\varphi - \varphi_i)$ is then computed for these data, where the three constants ψ_{i0}^* , ψ_{i1}^* and φ_i have been determined using a simple linear-least squares algorithm. These fits are shown in the upper panels of Figure 4.7b by the similarly colour-coded solid lines, yielding the

normalized angular velocity profiles shown in the bottom panels of Figure 4.7b when substituted into equation (4.21).

Examining first the results for the θ field component shown in the centre panels of the figure, it can be seen that the results in the radial ranges 6-12 (blue) and 18-24 R_S (orange) are in conformity with expectations based on Figure 4.5, namely smaller angular velocities falling to minima of $\sim 0.7 \Omega_M$ in the dusk and post-dusk sectors, and larger angular velocities peaking at $\sim 1.5\text{-}2 \Omega_M$ in the dawn sector. Differing variable results occur in the radial ranges 3-6, 12-18, and 24-30 R_S (black, green and red traces) where the rather scattered phase values are not well-modelled by the two-term Fourier fit.

Similar results to the blue and orange curves in the θ component are observed in the left-hand panels of Figure 4.7b for the r field component, except that the minima and maxima are typically shifted to later LT by ~ 3 h compared with the θ component. In the innermost region (black trace) the minimum angular velocity occurs at ~ 15 h LT and the maximum at ~ 03 h LT, while in the outer regions the minima occur at ~ 21 h LT and maxima at ~ 09 h LT (except for the 18-24 R_S range shown by the orange trace where again the phase data are not well represented by the Fourier fit). We also note that the azimuthal gradient of ψ_i^* becomes sufficiently large and negative at large radial distances 24-30 R_S (red traces) in the post-dawn sector that the angular velocity given by equation (4.21) reverses sense to negative, indicating retrograde motion of the phase fronts in this sector. The negative values are too large to display in Figure 4.7b, but the interval where they occur is bounded by the red vertical lines in the angular velocity plot where Ω_i/Ω_M^* passes through $\pm\infty$.

Results for the φ field component in the right-hand panels of Figure 4.7b show somewhat differing behaviour, with low angular velocities throughout the nightside sector with consistently reducing minima with increasing radial distance. While the angular velocity in the innermost radial range 3-6 R_S (black trace) remains close to Ω_M , the slightly pre-midnight minima decrease from $\sim 0.7 \Omega_M$ for 6-12 R_S to $\sim 0.4 \Omega_M$ for 24-30 R_S (red trace). Phase speeds exceeding Ω_M are then found throughout the dayside, again increasing with radial distance, once more becoming retrograde in a

band of LT centred near noon in the $18\text{-}30 R_S$ radial range (orange and red traces).

4.5 Form of the oscillating field in the equatorial region

In order to visualise the overall structure of the oscillatory field implied by the amplitude and phase results presented in section 4.3, in Figure 4.8 we show plots of the oscillating field vectors in the equatorial plane at fixed values of Φ_M in 45° increments, displaying the evolution of the field over a complete cycle. As in previous related figures, the Sun is to the right in each plot, with dusk at the top. The spatial bins used to construct the figure are identical to those in Figure 4.5 and the lower panels of Figure 4.6, corresponding to $3 R_S$ bins in radial distance and 2 h in LT, computed every hour. The vectors shown in Figure 4.8 are derived from the r and φ field component data, plotted at the centre of each bin using a non-linear length scale as indicated on the right-hand side of the figure, such that the orientation of the field vectors is still discernible when the field amplitude is small. The vectors themselves are colour-coded, indicating the sign and magnitude of the θ field component oscillations, with reds corresponding to positive values (pointing southward into the plane of the figure), and blues to negative values (northward out of the plane of the figure), according to the colour scale shown on the right of the figure. The oscillation phase, Φ_M , is indicated in the top-left corner of each panel, together with an arrow showing the expected orientation of the ‘core’ field according to the *Provan et al.* [2009a] model (equation (4.1)). The second icon below the ‘core’ field arrow in each panel indicates the approximate SKR power modulation phase, given by $\Phi_{SKR} \approx \Phi_M + 150^\circ$ according to equation (4.3) with $\psi_M = 150^\circ$ as discussed in section 4.2, with SKR maxima occurring when $\Phi_{SKR} = 360N$ deg. The trace plotted in this icon is a simple cosine, with the position of the overplotted solid circle indicating the instantaneous phase of each plot relative to SKR maxima and minima, with SKR maximum occurring when the solid circle reaches the peak of the cosine. The SKR maximum at $\Phi_M \approx 210^\circ$ occurs close to the conditions shown in panel (*f*) for $\Phi_M = 225^\circ$, while SKR minimum correspondingly occurs at $\Phi_M \approx 30^\circ$, close to the conditions shown in panel (*b*) for

$\Phi_M = 45^\circ$. We note, of course, that by virtue of the cosine fit to the data given by equation (4.16), the top four panels in Figure 4.8 are related to the bottom four panels simply by a reversal in the direction of each individual field vector (and an inversion of their colour), but it is useful to include these panels such that the oscillation can be viewed over a complete cycle. Additionally, we animate the data presented in Figure 4.8 at 2° increments of Φ_M in Movie S4 as part of the auxiliary online material².

We first examine panel (*a*) in Figure 4.8, for which $\Phi_M = 0^\circ$ such that the ‘core’ field is expected to point towards the Sun. It can be seen that this is generally the case out to $\sim 15 R_S$, but with a pronounced ‘deflection’ of the field vectors around the planet now evident in this format, together with an exclusion of the equatorial field from the inner region. In terms of the previous discussion, these effects are a consequence of the increasing dominance of the φ field component relative to r inside of $\sim 9 R_S$ noted in section 4.3, combined with an overall weakening of both components in the inner region. In the outer region, the dominant nightside r field component points inward in a narrow range of LT in the pre-midnight sector (the green and blue regions in the top-left panel of Figure 4.5), and outward at other LTs, while the approximately anti-phase φ component is positive (directed clockwise) in a narrow LT sector near midnight (the red and orange regions in the top-right panel of Figure 4.5) and is negative elsewhere. Overall the field in the equatorial plane points inward in the pre-midnight sector, around the planet via dusk and dawn to the dayside and then ‘returns’ via major circulations of the field vectors in the outer regions at dusk and dawn. The circulation cell at dusk is associated with an anticlockwise ‘semi-circular’ rotation of the field vectors beyond $\sim 15 R_S$ that is centred near ~ 20 h LT (within the limitations imposed by the data coverage available in this sector), while the clockwise field circulation at dawn takes the form of a more ‘sheet-like’ shear in the field vectors across $\sim 15 R_S$ that extends from ~ 3 to 9 h LT, associated with the rapid phase increase in the φ field component in this sector, as noted in section 4.3.1. Consideration of Ampère’s law indicates that the anticlockwise field circulation in the dusk sector is associated with a northward current flow through the equatorial plane, while the clockwise circulation near dawn

²Available online at <http://www.agu.org/journals/ja/ja1004/2009JA014729/>.

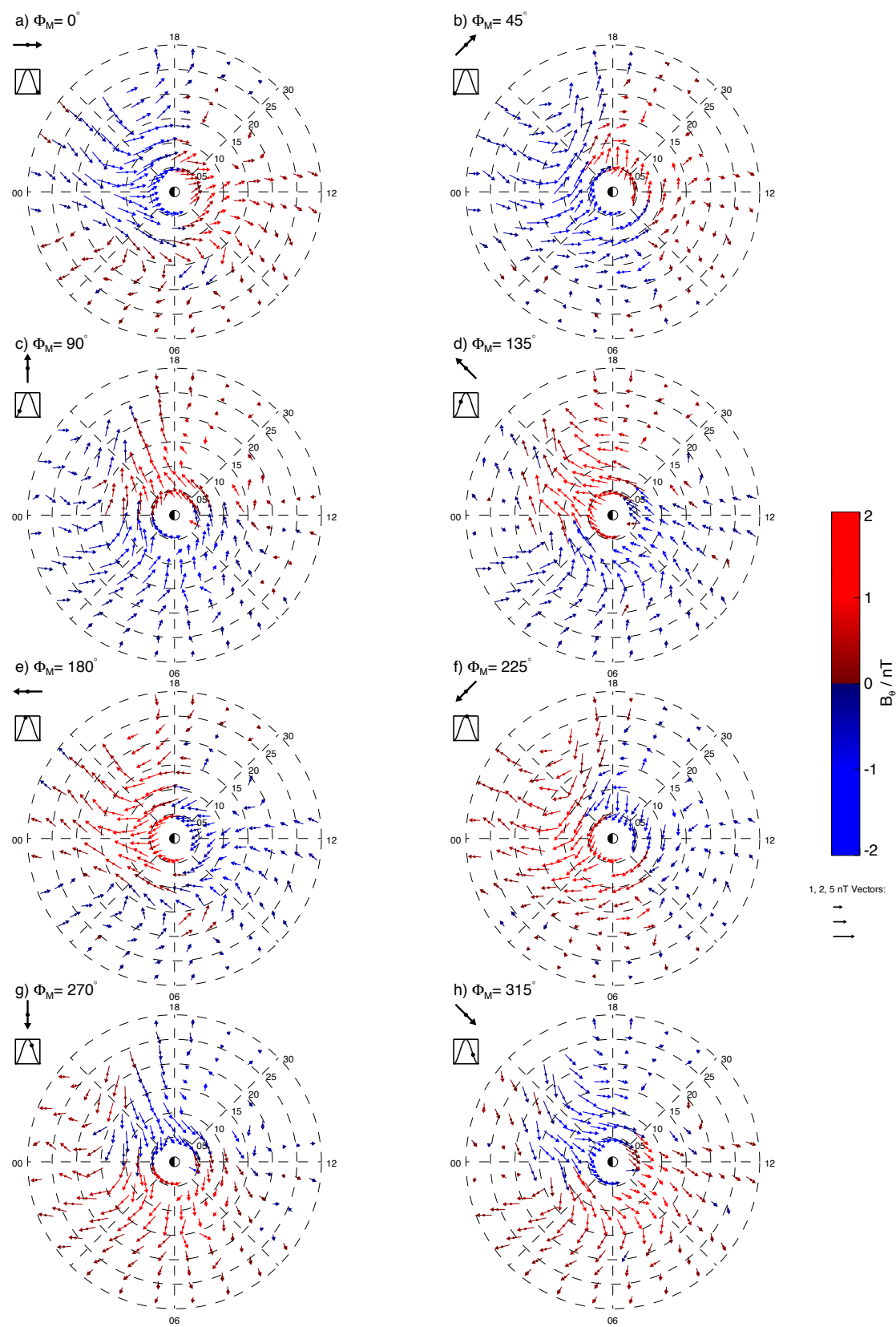


Figure 4.8: Caption overleaf.

is associated with a southward current flow. We also note that the field exclusion effect in the inner region also implies north-south current flows at dusk and dawn, directed opposite to that in the adjacent outer region. Both inner and outer north-south currents will be quantified in section 4.6 below. With regard to the oscillation in the θ field component, we note that this is largely negative (northward) in the dusk and midnight sector (blue and green regions in top-centre panel of Figure 4.5), and positive elsewhere.

We now consider how this pattern evolves over a complete oscillation cycle. In panel (b) for $\Phi_M = 45^\circ$ the field in the interior region has rotated to point duskward of the Sun as expected, the anticlockwise cell near dusk has rotated somewhat towards midnight, and the clockwise shear region near dawn has extended into the pre-noon sector. Further evolution to $\Phi_M = 90^\circ$ as depicted in panel (c) results in largely duskward-directed fields becoming present throughout the equatorial region investigated, with the outer anticlockwise circulation cell becoming broadened and centred in the midnight sector, while the clockwise circulation on the dayside has weakened substantially and all but disappeared. In panel (d) for $\Phi_M = 135^\circ$ the anticlockwise circulation cell now intrudes into the dawn sector, beginning to form a shear layer of the opposite rotation sense than was present at the start of the cycle,

Figure 4.8: Plots showing the evolution of the oscillatory magnetic field in the equatorial plane over a complete cycle, as discussed in section 4.5. The magnetic phase Φ_M is 0° in panel (a), and increases by 45° in each subsequent panel, up to 315° in plot (h). The main plot in each panel shows the equatorial field vectors derived from the r and φ component amplitude and phase data, where the vectors are shown using a non-linear scale indicated on the right of the figure. The colour of each vector indicates the sense and magnitude of the θ component according to the colour scale on the right of the figure, with reds indicating positive (southward directed), and blues negative (northward directed) field values. The icons in the top-left corner of each plot indicate the expected orientation of the ‘core’ equatorial field components according to the phase model of *Provan et al.* [2009a] (equation (4.6)), together with the approximate SKR phase according to equation (4.11). The latter is indicated by a solid circle moving on a sinusoid such that the SKR power maximises when the solid circle reaches the peak of the sinusoid. This condition occurs nearest to the field configuration shown in panel (f), with SKR minimum correspondingly occurring nearest to panel (b). Note that the field vectors in the lower four panels are exactly reversed in sense compared with the upper four panels, and with a reversed colour-code.

while indications of clockwise circulation appear near dusk. These features develop further in panel (*e*) for $\Phi_M = 180^\circ$, where the vectors are directed exactly opposite to those in panel (*a*) as previously indicated. Subsequent evolution through panels (*f*) to (*h*) is then identical to (*b*) to (*d*) but with field directions reversed.

An important feature that can be discerned on careful inspection of Figure 4.8, but is more readily evident when viewed in Movie S4, concerns the polarisation of the field oscillation in the equatorial plane. Over most of this region, the φ field component is in approximate lagging quadrature with the r , resulting in rotation of the field vectors in the equatorial plane in the same sense as the planet, as noted by *Espinosa et al.* [2003b], *Andrews et al.* [2008], and *Provan et al.* [2009a] as discussed in section 4.1. More specifically, this sense of rotation applies when $0^\circ < \Delta\psi^* < 180^\circ$ in the bottom right-hand panel of Figure 4.6, where $\Delta\psi^* = \psi_\varphi^* - \psi_r^*$. However, in the outer dawn region beyond $\sim 15 R_S$ the phase difference instead satisfies $180^\circ < \Delta\psi^* < 360^\circ$, under which condition the field vectors rotate in the opposite sense to planetary rotation. The region in which this condition is met in Figure 4.8 corresponds approximately to the orange region in the lower right-hand panel of Figure 4.6. We note that this sense of polarisation corresponds to that of a rotating transverse dipole. Indeed, it can be seen from Figure 4.8 that the overall form of the equatorial field vectors in the outer region resembles that of a transverse dipole, the dipole moment concerned being that of the outer current system flowing north-south through the equatorial plane, as will be discussed further in section 4.6.

4.6 North-South currents in the equatorial plane

As just discussed in relation to Figure 4.8, the circulation of the r - φ oscillation field vectors in the equatorial plane implies the presence of currents flowing north-south through the plane, as does the deflection and weakening of the ‘core’ field in the inner region. Applying Ampère’s law (equation (1.19)) in spherical polar coordinates to the equatorial plane ($\theta = 90^\circ$) yields the following expression for the colatitudinal

component of the equatorial current density

$$j_\theta(r, \varphi, t) = \frac{1}{\mu_0 r} \left(\frac{\partial B_r}{\partial \varphi} - \frac{\partial}{\partial r}(r B_\varphi) \right), \quad (4.22)$$

which we apply here to the oscillatory field only, thus yielding values of the oscillatory current density. We note that at least within the equatorial quasi-dipolar ‘core’ region within $\sim 15 R_S$, the non-oscillatory background field is also principally directed north-south, so that the current density given by equation (4.22) is essentially the field-aligned component. The outer portion of these currents are thus expected to relate to the field-aligned current systems discussed by *Southwood and Kivelson* [2007] and *Provan et al.* [2009a] and are thus of direct significance to the origin of these oscillatory phenomena. Outside these distances, however, in the magnetodisk region where radial fields are also important, the north-south currents may also generally contain some field-perpendicular component. While it would also be of interest to examine the other current components flowing in the equatorial plane, these currents depend not only on the variations of the θ field component with radial distance and LT, but also on the undetermined variations of the r and φ field components with colatitude. Therefore these currents cannot be calculated from the field oscillation data determined in this chapter.

The north-south current density has been calculated from equation (4.22) using a centred finite-difference scheme in which the amplitude and phase of the oscillatory r and φ field components have first been calculated in a set of overlapping bins that are each of width $3 R_S$ in radial distance and $2 h$ in LT, as above, computed every hour in LT. For the φ field component the radial bins are $3-6, 6-9, \dots, 27-30 R_S$, identical to those employed in creating Figure 4.8, such that field difference values for a given Φ_M corresponding to the $\partial(rB_\varphi)/\partial r$ term in equation (4.22) are evaluated at $6, 9, \dots, 27 R_S$, at each LT. The radial bins used to determine the oscillatory r field component have then been displaced by $1.5 R_S$ to $4.5-7.5, 7.5-10.5, \dots, 28.5-31.5 R_S$, thus also being centred on $6, 9, \dots, 30 R_S$, with the values employed to determine $\partial B_r / \partial \varphi$ at that Φ_M being obtained from the bins displaced by $1 h$ of LT on either side of the bins used to determine the corresponding $\partial(rB_\varphi)/\partial r$ value. The difference values that

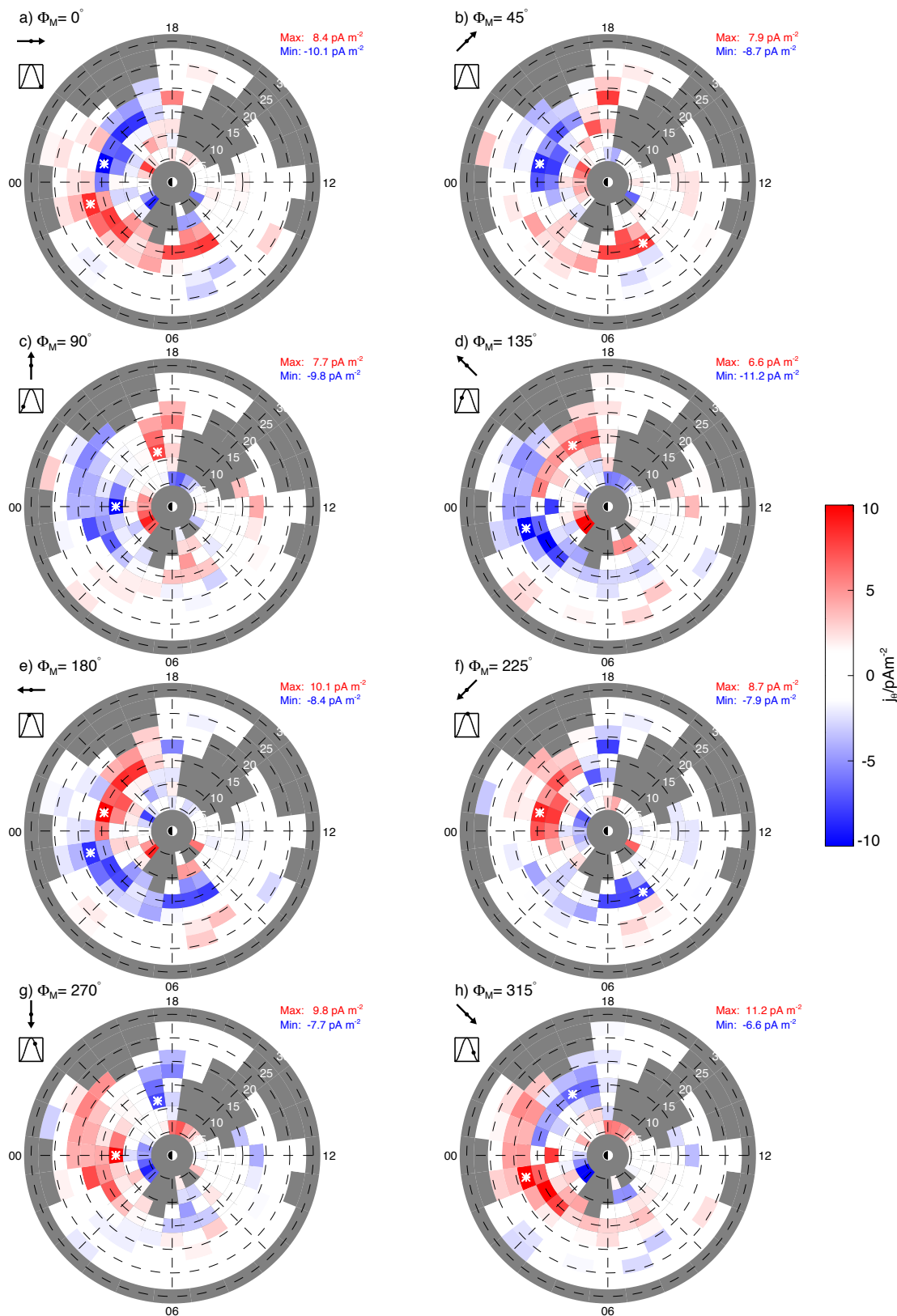


Figure 4.9: Caption overleaf.

are combined together in equation (4.22) to determine the current density are thus centred on the same point as each other in the equatorial plane, and employ adjacent, but non-overlapping data sets to estimate the field gradients. We note that while the spatial resolution of this scheme is relatively modest, such that the structure of the current will not be fully resolved, nevertheless the implications of Ampère's law in integral form is that the total integrated current should be well determined, provided that the sense of the current does not vary strongly on spatial scales similar to the bins employed.

Results are plotted in Figure 4.9 in a format similar to Figure 4.8, showing the evolution of the currents over a complete oscillation cycle. The current density determined in each bin is colour-coded according to the scale on the right, such that reds correspond to positive currents, directed southward into the plane of the figure, while blues correspond to negative currents directed northward out of the plane of the figure. Examination of the uncertainties in the current density values, dependent on the uncertainties in the amplitude and phase of the oscillating field discussed in section 4.2.3, indicates that typical uncertainties are $\sim \pm 2.5 \text{ pAm}^{-2}$ (corresponding to $\sim 25\%$ of $\sim 10.0 \text{ pAm}^{-2}$). Accordingly, the colour scale for the currents has been chosen such that uncertain values within $\sim \pm 2.5 \text{ pAm}^{-2}$ of zero are shown as near-white. Bins in which the current density could not be calculated due to lack of data in one or more field components are coloured gray. The value of the oscillation phase Φ_M , the orientation of the 'core' field according to the *Provan et al.* [2009a] model, and

Figure 4.9: Plots showing the north-south current density in the equatorial plane computed from equation (4.22) using a finite-difference scheme as outlined in section 4.6, where the panels (a)-(h) correspond to the same phases as those in Figure 4.8, namely $\Phi_M = 0^\circ$ to 315° in 45° steps. The colour scale, as given on the right of the figure, indicates the current density determined in each bin, with reds corresponding to positive currents (southward directed) and blues to negative (northward) currents. Grey regions indicate bins for which the current density cannot be computed due to the lack of field component data. The bins in which the current densities in the outer region (beyond radial distances of $10.5 R_S$) are maximally positive and negative are indicated by white stars, with the corresponding peak positive and negative current densities being given in the top-right corner of each panel. The icons in the top-left corner of each panel are the same as in Figure 4.8.

the approximate SKR modulation phase are indicated in the top-left corner of each panel in a format identical to Figure 4.9. Examination shows that the currents derived here are predominantly associated with radial gradients in the azimuthal field (the second term in equation (4.22)). An exception to this occurs in the dusk and post-dusk sectors, where the azimuthal gradients in the radial field are of similar magnitude.

We first examine the currents shown in panel (*a*) of Figure 4.9, corresponding to $\Phi_M = 0^\circ$, together with the corresponding field vectors shown in Figure 4.8. Examination shows that, in broad terms, the currents can be divided into two radial regions, an inner-region corresponding to the two inner rings in the current density plots spanning 4.5-10.5 R_S , and an outer region spanning 10.5-28.5 R_S . The currents in the inner region relate to the deflection and weakening of the equatorial ‘core’ field, being positive (southward) and negative (northward) at dusk and dawn, respectively, as anticipated. The currents in the outer region, however, are somewhat more complicated. The primary regions of positive and negative current take the form of broad spirals that extend clockwise from the inner region to the outer boundary. The region of negative current extends from the midnight sector to pre-dusk, associated with the anti-clockwise circulation in the field vectors that is evident in Figure 4.8 in this region, while the region of positive current similarly extends from mid-morning to pre-midnight, associated with the strong clockwise ‘shear’ in the field that is evident in the dawn sector. Bins containing the peak positive and negative current densities in the outer region are marked in Figure 4.9 with stars, with the values concerned being given in the top-right hand corner of the plot. The peak current densities at $\Phi_M = 0^\circ$ are $\sim 10 \text{ pAm}^{-2}$ in each case, located at $\sim 15 R_S$ in the pre-midnight sector for the negative current, and in the post-midnight sector for the positive current. In addition to these primary current regions we also note the presence of secondary regions of weaker current that prove to be of significance in the overall evolution of the current system during the oscillation cycle. Specifically, a region of positive current is present near the dusk meridian (within the limitations of the data coverage in the afternoon sector), while a region of weak negative current is located post-dawn at radial distances beyond $\sim 20 R_S$. Overall, therefore, we identify four current regions

in the outer equatorial magnetosphere, two of each sign.

We now consider panels (b)-(e) in Figure 4.9, showing how these current regions evolve over half an oscillation cycle. Alternatively, Movie S5 in the auxiliary online material provides an animation at 2° intervals of Φ_M ³. In the inner region it can be seen that the current pattern rotates approximately uniformly with the ‘core’ field as expected, with the sense of the currents reversing on either side of the planet between $\Phi_M = 0^\circ$ and 180° . In the outer region, however, it can be seen that the secondary region of positive current near dusk at $\Phi_M = 0^\circ$ strengthens, rotates and expands to form the primary region of positive current at $\Phi_M = 180^\circ$ extending from dusk to midnight, while the pre-midnight primary region of negative current at $\Phi_M = 0^\circ$ similarly rotates and expands to form the primary region of negative current spanning mid-morning to pre-midnight at $\Phi_M = 180^\circ$. At the same time, the primary dawn-side region of positive current at $\Phi_M = 0^\circ$ weakens and moves radially outward to form the secondary region of positive current at $\Phi_M = 180^\circ$, while the dawn-side secondary region of negative current at $\Phi_M = 0^\circ$ dissipates at large radial distances in the dawn sector and can no longer be discerned. The evolution of the current system in the second half-cycle shown in panels (e)-(h) then follows the same pattern, but with the sense of current reversed. Although the detailed behaviour of the current in the outer region is somewhat obscured by lack of data coverage in the post-noon sector, it thus appears that we may regard each current region as first intensifying in the dusk sector over a broad radial range, then propagating in LT around the planet to form an extended clockwise spiral stretching from mid-morning to pre-midnight via dawn after one cycle, and decaying at large radial distance in the dawn and dayside sectors during the following cycle. Each individual current region thus remains identifiable for two complete cycles, with an angular frequency of rotation which is roughly half that of the ‘core’ field. The properties of the current system associated with the field oscillations thus appears to be somewhat more complex than envisaged by *Southwood and Kivelson [2007]* and *Provan et al. [2009a]*.

In simple terms, the above behaviour of the north-south currents results from

³Available online at <http://www.agu.org/journals/ja/ja1004/2009JA014729/>.

the fact that in the outer region the azimuthal variation of the field has a significant component with azimuthal wavenumber $m = 2$, giving rise to two current regions of each sign, one major and one minor, in addition to the $m = 1$ variation that is dominant in the ‘core’. We note that our model only specifies the period of the oscillation, $2\pi/\Omega_M$, and not the spatial scale of its structure (except that the data are averaged in bins of finite size), the latter being wholly determined from independent fits to the spatially binned data. Thus while the primary variations with $m = 1$ are described by the function $\exp[i(\Omega_M t - \varphi)]$, with consequent azimuthal phase speed Ω_M , the secondary variations with $m = 2$ are described by the function $\exp[i(\Omega_M t - 2\varphi)]$ (which still varies at the model period $2\pi/\Omega_M$), with an azimuthal phase speed of $\Omega_M/2$.

In Figure 4.10 we further quantify the evolution of the current regions discussed qualitatively above. At given values of the oscillation phase Φ_M we have divided the equatorial plane into six contiguous current regions, two in the inner region and four in the outer, in accordance with the above discussion. These are shown on the left side of Figure 4.10 at 10° intervals of Φ_M between 0° and 170° in a format similar to Figure 4.9. In the inner region the positive and negative current regions are shown as red and blue respectively, while in the outer region the two positive current regions are shown as red and orange, and the two negative current regions as blue and green. The interface between the inner and outer regions is taken to lie at $10.5 R_S$ at the interface of the second and third radial bins, as indicated by the white dashed circle in the figure. To follow the evolution beyond $\Phi_M = 170^\circ$ we return to $\Phi_M = 0^\circ$ and switch colours, e.g. from red to blue and vice versa in the inner region. In the outer region the red current region at 170° transforms to blue at 0° , blue transforms to orange, orange to green, and green to red. Thus each outer current region can be followed using Figure 4.10 over the two full cycles of its evolution. We note that while the identification of the current regions is reasonably clear when the current is strong, it becomes more subjective where the currents are weaker and more spatially structured (e.g. the outer dawn sector). However, the latter weaker current regions are of lesser significance in the overall discussion.

For each individual current region at each Φ_M we have computed the position of its

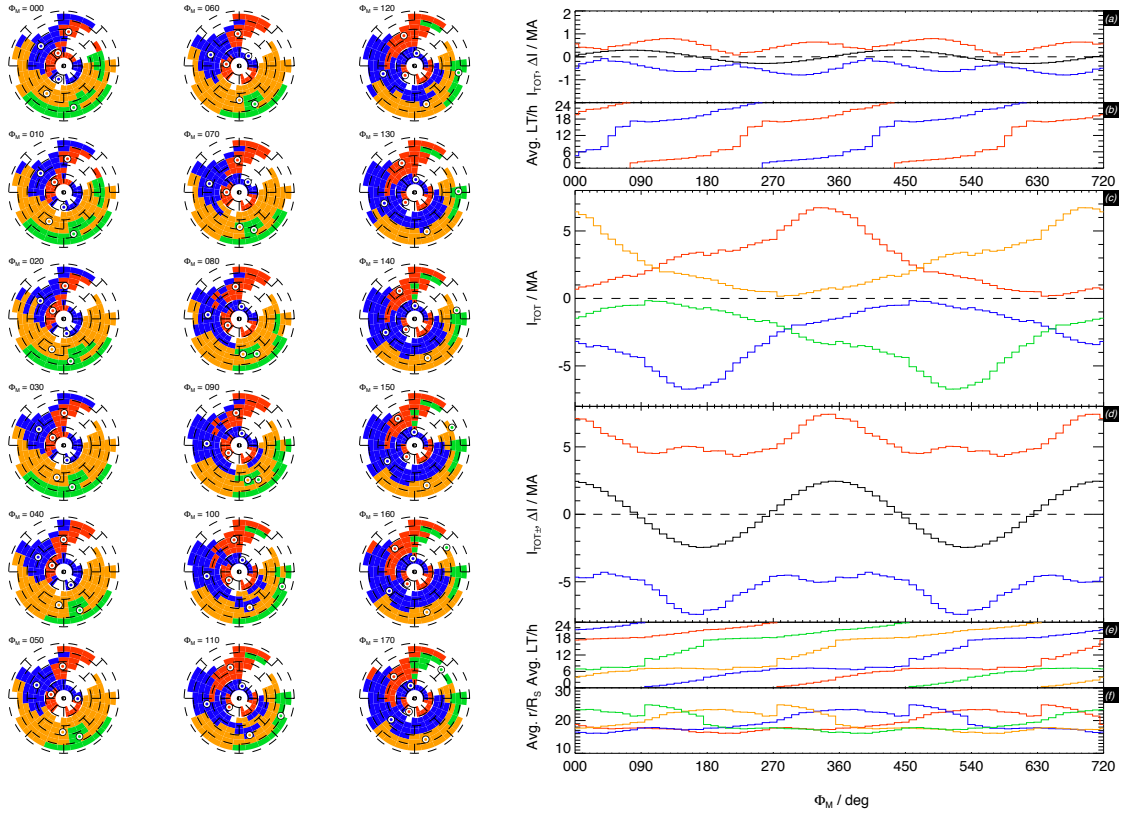


Figure 4.10: The diagrams on the left of the figure colour-code the six regions of north-south current flowing through the equatorial plane at 10° increments of Φ_M between 0° and 170° as discussed in section 4.6, two in the inner region, four in the outer region, the dividing line between them at $10.5 R_S$ being shown by the white dashed circle. The format of these plots is similar to Figures 4.8 and 4.9, such that noon is to the right and dusk at the top. In the inner region, the red area indicates positive (southward) current, while the blue indicates negative (northward) current. In the outer region, the red and orange areas indicate positive current, while the blue and green indicate negative current. The evolution of each area between $\Phi_M = 180^\circ$ and 350° can then be obtained by suitable anti-clockwise transformations of the colours shown. The current-weighted average radial distance and LT of each region are shown as colour-coded dots in the left-hand plots and are plotted versus Φ_M over two cycles in the right-hand panels together with the summed currents flowing through these regions. From top to bottom the latter panels show (a) the summed positive (red) and negative (blue) currents flowing in the inner region, together with their difference (black), (b) the averaged LT of the inner current regions, (c) the summed currents in the four outer regions using the same colour-code as in the left-hand panels (for $\Phi_M = 0^\circ$ to 170°), (d) the total positive (red) and negative (blue) current flowing in the outer region, together with their difference (black), (e) the averaged LT of the four outer current regions, and (f) the averaged radial distance of the outer current regions.

'centre' (as a current-weighted mean radial distance and LT), and have also summed the total current through its area. These quantities are shown on the right side of Figure 4.10, plotted versus Φ_M over two full oscillation cycles (since each individual outer current region evolves over two full cycles), while the centre position data are also shown as coloured dots in the equatorial plane plots on the right side of the figure. Results for the two inner current regions (whose full evolution occurs over one cycle) are shown in panels (a) and (b), specifically for the total current and averaged LT. The mean radial distance of the current regions are not shown in this case, since these are essentially invariant at $\sim 7.5 R_S$. The red lines in these panels refer to the region of positive (southward) current, while the blue lines refer to the region of negative (northward) current. First examining panel (a), it can be seen that the total positive and negative currents typically lie between ~ 0.5 MA and ~ 1 MA, with two maxima per cycle near $\Phi_M \sim 125^\circ$ and 315° , and two minima near $\sim 45^\circ$ and 225° . Examination shows that the oscillatory nature of the currents is due to a combination of physical and accidental features of our data, relating to the spatial variation in the oscillatory fields, particularly the LT dependence in the φ component shown in the right-hand column in Figure 4.4b, and the position of data gaps. The difference between the two currents is shown by the black line in panel (a), which oscillates as a strict sinusoid (as must be the case for the net current through a fixed area in the presence of sinusoidally varying fields) with an amplitude of ~ 0.5 MA. This net current must be due to overall current closure taking place either inside or outside the radial range considered, or within the regions containing data gaps. The averaged LT of the currents shown in panel (b) generally increase approximately uniformly with phase Φ_M , completing one rotation in each oscillation cycle, but show a pronounced 'jump' at $\sim 240^\circ$ for the positive current region and at $\sim 60^\circ$ for the negative current region, which occur as these regions cross the data gap in the afternoon sector.

Results for the outer current regions are shown in panels (c)-(f) on the right side of Figure 4.10. Panel (c) shows the integrated currents in the four outer regions colour-coded as in the left-hand diagrams, panel (d) shows the total summed positive (red) and negative (blue) currents and their difference (black), while panels (e) and (f)

show the averaged radial distance and LT of each region respectively. We first focus on the evolution of one specific current region, that shown by the red line in panels (c), (e), and (f), corresponding to the red region in the left-hand plots during the Φ_M interval from 0° to 170° (followed by the blue region for Φ_M from 180° to 350° and so on). At $\Phi_M = 0^\circ$ this region is centred near dusk at $\sim 18 R_S$, and carries a total current of ~ 0.5 MA. The current in this region then rises near-monotonically to ~ 6.5 MA over the following cycle, whilst rotating to ~ 3 h LT via midnight at an approximately constant averaged radial distance. Over the next cycle the current then near-monotonically declines to its initial value, while the ‘centre’ of the region increases its radial distance to $\sim 24 R_S$ in the dawn sector. We note that the orange, blue, and green lines in these panels all follow exactly the same behaviour, with appropriate changes in the phase and in the sign of the current. Considered together, it can be seen that the outer current system can be approximately described in terms of two main current regions of opposite sign in some ranges of Φ_M , such as the ‘orange’ and ‘blue’ current regions at $\Phi_M = 0^\circ$, and the ‘red’ and ‘blue’ current regions at $\Phi_M = 180^\circ$. At other phases, such as near $\sim 90^\circ$ and $\sim 270^\circ$ the current region can more appropriately be described in terms of three main current regions, a region of one sign centred near local midnight, sandwiched between two regions of opposite sign centred near dawn and dusk. We note that the former condition applies when the ‘core’ equatorial field is directed approximately toward or away from the Sun, while the latter condition applies when the ‘core’ field points approximately to dawn or dusk. Turning finally to the summed positive and negative currents in the outer region shown in panel (d) on the right side of Figure 4.10, it can be seen that these vary more modestly in magnitude between minimum values of ~ 4.5 MA and maximum values of ~ 7.5 MA, with a sinusoidally-varying difference of ~ 2 MA amplitude. We note that these currents (and their difference) are thus considerably larger than the currents in the inner region.

4.7 Summary of results

In this section we summarise and comment further on the main results reported above. In common with the earlier discussions e.g. of *Cowley* [2006] and *Southwood and Kivelson* [2007] it has been found that the properties of the equatorial oscillatory fields can be divided into inner and outer radial regions at a radial distance of $\sim 15 R_S$. This division also approximately separates the inner region dominated by the near-dipolar planetary field, referred to here as the ‘core’ region of the magnetosphere, from the outer region dominated by the fields of the magnetodisk and nightside plasma sheet [*Bunce et al.*, 2008; *Arridge et al.*, 2008b]. A major distinctive feature of the inner region is the presence of few-nT oscillations in the radial and azimuthal components of the field, that have commonly been described as forming an approximately uniform magnetic field in the equatorial plane that rotates in the sense of planetary rotation near the planetary period [e.g. *Espinosa et al.*, 2003b]. The implication of such a description is that the oscillation amplitudes of the two field components are spatially uniform in this region, equal to each other, and with the phase of the azimuthal component in lagging quadrature with the radial component. Our results show that while the quadrature phase relationship is maintained to a good approximation throughout the inner region, the amplitudes of the components generally differ significantly from each other, and vary strongly with both radial distance and LT. Specifically, the amplitudes generally grow with radial distance from small values in the innermost region ($3\text{--}6 R_S$), are larger on the nightside than on the dayside, and with the azimuthal component exceeding the radial out to $\sim 12 R_S$ and vice-versa beyond. Rather than forming a quasi-uniform field in the inner region, therefore, the equatorial field vectors inside $\sim 12 R_S$ are instead deflected ‘around’ the innermost region, and are strongly suppressed in magnitude inside $\sim 6 R_S$, and on the dayside, compared with the nightside. These results thus suggest the presence of a rotating equatorial field that is principally generated outside $\sim 6 R_S$, with largest amplitudes on the nightside, and suppressed inside that distance. The field suppression and deflection effects imply the presence of a rotating system of field-aligned currents flowing north-south

through the equatorial plane which reduces the rotating field within their interior, the currents being directed northward on one side of the planet where the azimuthal field is positive, and southward on the other where the azimuthal field is negative. We have estimated the total field-aligned current in these regions to be ~ 1 MA, flowing principally in the radial range inside ~ 7.5 R_S , thus corresponding to the Enceladus plasma torus lying inside the main hot plasma ring current region [e.g. *Young et al.*, 2005; *Bunce et al.*, 2007; *Schippers et al.*, 2008]. We note that these field lines map to Saturn's ionosphere at latitudes of $\sim 68^\circ$, thus typically lying well equatorward of Saturn's auroral oval centred near $\sim 75^\circ$ [e.g. *Badman et al.*, 2006].

Outside this innermost current system, the oscillatory radial and azimuthal fields, directed essentially transverse to the north-south quasi-dipolar planetary field, result in oscillatory tilting of the magnetospheric field lines. As a consequence, the magnetic equator becomes displaced south of the planetary dipole equator where the oscillatory radial field is positive, and north of the dipole equator where the radial field is negative. This is illustrated in Figure 4.11, where we show a sketch of the field lines in a meridian plane at an instant when the oscillatory equatorial field points from left to right as indicated by the horizontal solid arrows. The magnetic equator, where the sign of the total radial field reverses, is shown by the dashed line. In effect, beyond ~ 6 R_S the northward normal to the magnetic equator is tilted towards the direction of the equatorial field (to the right in Figure 4.11), approximately towards azimuth $\Phi_M(t)$ according to equation (4.6), and rotates with the oscillatory field at the period given by equation (4.4). Further discussion of Figure 4.11 with regard to the outer region will be given below.

Oscillations of comparable amplitude are also present in the north-south co-latitude field component, as reported by *Andrews et al.* [2008] and *Provan et al.* [2009a]. Our findings firstly confirm that these oscillations are generally in phase with the radial field oscillations throughout the inner region, though moving towards lagging quadrature in the outer 'core' near dusk. The implication of the general in-phase behaviour is that the field lines are extended outward from the planet where the oscillatory radial field is directed inward, thus weakening the southward-directed

planetary field, and are contracted inward (relative to the mean) where the radial field is directed outward, thus strengthening the southward field. These relationships are also indicated schematically in Figure 4.11. Our results also show that the spatial dependency of the amplitude of the co-latitudinal field oscillation is rather different to that of the radial and azimuthal components. The field suppression effect in the innermost region is less evident, and there is significantly less variation with LT. Physically, it is evident that the nature of these oscillations is different to that of the equatorial components, the latter being associated with oscillatory tilting of the equatorial quasi-dipolar field lines in the inner region as just discussed, while co-latitudinal field oscillations are instead related to changes in the equatorial field strength which must be connected to related changes in the energy density (kinetic or thermal) of the plasma. Indeed, both *Provan et al.* [2009a] and *Khurana et al.* [2009] have linked these co-latitudinal field oscillations with a rotating LT asymmetry in the ring current plasma. The radial amplitude profile of the co-latitudinal field oscillations found here is indeed similar to the radial profile of the quasi-steady equatorial co-latitudinal field perturbations produced by the ring current. The co-latitudinal ring current field typically peaks at $\sim 10\text{-}15$ nT near its inner edge at $\sim 7 R_S$, where the co-latitudinal component oscillation amplitude also peaks, and falls near-monotonically to small values at and beyond $\sim 15 R_S$, as does the co-latitudinal oscillation amplitude *Bunce et al.* [2007, 2008]. Typically, the oscillations found here correspond to $\sim 20\%$ of the quasi-steady co-latitudinal field perturbations produced by the ring current. Possible physical relations between these oscillations and those of the radial and azimuthal fields will be discussed in section 4.8.

In the outer region beyond $\sim 15 R_S$ the oscillation amplitudes of all field components fall near-monotonically with radial distance, with the largest amplitudes being observed on the nightside in the radial and azimuthal components, the former being larger than the latter, with both being larger than that of the co-latitudinal component. The phases of the oscillations also show increasing values with radial distance in all components. This trend is already evident within the inner region where the phase gradient is $\sim 1\text{-}3^\circ R_S^{-1}$, giving a phase change of $\sim 10^\circ\text{-}30^\circ$ over the radial range

between ~ 5 and ~ 15 R_S . The trend continues at similar rates in the outer region, where it becomes evident that the gradients are significantly larger on the nightside than the dayside, the associated overall radial phase speeds being ~ 150 km s^{-1} on the nightside, and ~ 500 km s^{-1} on the dayside (the latter with large uncertainty estimates). Detailed radial profiles of characteristic wave propagation speeds in the plasma based on field and particle measurements with which these values may be compared have yet to be published. However, estimates based on Cassini density and temperature measurements presented by *Wilson et al.* [2008] and *McAndrews et al.* [2009] suggest typical sound and Alfvén speeds within the equatorial ring current region of ~ 100 - 400 km s^{-1} . Such values are thus at least of the same order as the radial phase speeds deduced here.

The phase lag between the innermost region and ~ 30 R_S associated with these radial phase speeds is typically $\sim 30^\circ$ on the dayside, increasing to $\sim 90^\circ$ on the nightside. This LT asymmetry thus implies that the oscillation phase fronts are ‘swept back’ to earlier LTs with increasing radial distance much more on the nightside than on the dayside, with the consequence that in the outer region they become compressed together in the pre-midnight sector, and expanded away from each other in the post-midnight sector. This also implies a LT asymmetry in the azimuthal phase speed, with smaller values than the overall angular velocity of the oscillations Ω_M in the pre-midnight sector, where the azimuthal phase speed is reduced to $\sim 0.7 \Omega_M$, and larger angular velocities in the post-midnight sector where the phase speed is increased to $\sim 1.5 \Omega_M$.

In addition to the gradual increase in phase with radial distance, the azimuthal field component also shows a much more rapid increase in phase across a narrow layer just outside the ‘core’ (~ 15 - $18 R_S$) in the LT sector from midnight via dawn to noon, but not in the dusk sector. The azimuthal field oscillations thus remain in approximate lagging quadrature with the radial field oscillations at dusk, while moving towards anti-phase in the midnight and noon sectors, and to leading quadrature near dawn. As indicated above, the implication of lagging quadrature with the radial component is that the oscillation field vectors in the equatorial plane rotate with time in the same sense

as planetary rotation. Our results show that this sense of polarisation is maintained throughout the equatorial region to $30 R_S$, though moving towards anti-phase in the outer region near noon and midnight, except for a restricted LT sector near dawn beyond the ‘core’ where the equatorial vectors rotate opposite to planetary rotation. We note that anti-phase oscillations of the azimuthal and radial field components is characteristic of a north-south oscillating magnetodisk containing a ‘lagging’ field configuration, while azimuthal oscillations in leading quadrature with the radial, such that the field rotates opposite to planetary rotation, is characteristic of a rotating transverse dipole. The relation between these results will be discussed further below.

Now considering the spatial structure of the oscillatory field in more detail, we note that due to the LT dependencies of the oscillation amplitudes and phases discussed above, particularly the day-night asymmetries, the overall structure of the oscillating fields in the equatorial region depends somewhat on oscillation phase, rather than simply being an almost fixed pattern that rotates around the planet. We first consider $\Phi_M = 0^\circ$, such that the oscillatory field in the equatorial plane points approximately towards the Sun in the inner region. Figure 4.8 then shows that the equatorial field vectors overall form a partial twin-vortex centred on the nightside, with anti-clockwise circulation in the dusk sector, and clockwise (sheared) circulation at dawn. The anti-clockwise circulation at dusk relates to the lagging quadrature of the azimuthal component with respect to the radial, but with the radial field being dominant such that the perturbation field lines become convex relative to the planet. The sheared-field region at dawn then relates to the rapid increase in phase of the azimuthal component across $\sim 15\text{-}18 R_S$, from lagging to leading quadrature with respect to the radial component. The corresponding perturbations in the co-latitudinal field component, being approximately in phase with the radial component, are positive (southward) on the dayside and negative (northward) on the nightside within the inner region, while in the outer region negative values are confined to the dusk and midnight sector due to the nightside sweepback of the phase fronts, with positive values being found at all other LTs from dusk

As the oscillation phase increases to $\Phi_M = 90^\circ$, the pattern rotates such that the

vectors in the equatorial plane form an anti-clockwise circulation centred near midnight, with dawn-to-dusk magnetic fields in the inner region as expected. However, there is now no corresponding rotated clockwise shear region in the outer dayside sector. The equatorial field vectors in this case may thus be described as forming a single partial anti-clockwise vortex centred on the nightside of the planet. With regard to the oscillatory co-latitudinal field, this is now generally positive on the dusk side and negative on the dawn side as expected, but negative values extend into the pre-midnight sector in the outer region (together with positive radial fields) due to the phase front sweep-back in this region. With further increase in oscillation phase the pattern then repeats, but with oppositely-directed fields at $\Phi_M = 180^\circ$ compared with $\Phi_M = 0^\circ$, and at $\Phi_M = 270^\circ$ compared with $\Phi_M = 90^\circ$. Individual field circulation regions thus appear to form in the dusk sector, anti-clockwise when $\Phi_M \approx 0^\circ$ and clockwise when $\Phi_M \approx 180^\circ$, which rotate to become the dominant circulation at midnight, anti-clockwise at $\Phi_M \approx 90^\circ$ and clockwise at $\Phi_M \approx 270^\circ$, and then expand into the dawn sector to form the anti-clockwise and clockwise shear-field regions in that sector for $\Phi_M \approx 180^\circ$ and $\Phi_M \approx 270^\circ$. The circulation regions finally dissipate in the mid-morning sector.

The nature of the oscillatory currents flowing through the equatorial plane in the outer region follows from the description of the equatorial field patterns, with individual current regions emerging near dusk, propagating via midnight, and dissipating post-dawn. At $\Phi_M = 0^\circ$ the currents consist of two main regions, northward pre-midnight and southward post-midnight, each carrying ~ 5 MA, the currents being reversed in sense for $\Phi_M = 180^\circ$. These currents are most intense near $\sim 15 R_S$ where the dominant oscillatory field changes from radial to azimuthal, and are flanked by weaker oppositely-directed currents of ~ 1 MA at dusk and dawn which interface the regions of stronger equatorial field with the weaker fields at large radii and on the dayside. At $\Phi_M = 90^\circ$ three significant current regions are then present, a main northward region of ~ 5 MA centred near midnight, and two southward regions of ~ 2.5 MA at dusk and dawn, which are again reversed in sense for $\Phi_M = 270^\circ$. Overall, the main current regions have the senses expected from the simple hemisphere-to-hemisphere field-

aligned current system of *Southwood and Kivelson* [2007], though the evolution with oscillation phase is somewhat more complicated than the simple rotation envisaged by these authors, with no strong north-south currents flowing from mid-morning to post-noon.

If we assume that much of these equatorial north-south currents are indeed associated with field-aligned currents closing in the ionosphere, as seems reasonable, we note that our results imply that the overall current system flowing in the outer region has an associated magnetic dipole moment lying in the equatorial plane that has the same direction as the field within the inner region, associated with the twin-vortex equatorial field system that is generally observed. This is evident for oscillation phases in which the ‘core’ field points toward or away from the Sun ($\Phi_M \approx 0^\circ$ and 180°), such that two main current regions are present in the outer region, pre- and post-midnight, with (net) current flowing from north to south in one region and from south to north in the other. However, brief consideration shows that this is also true for phases in which the ‘core’ field is directed dawn-dusk ($\Phi_M \approx 90^\circ$ and 270°), when three main current regions are present, a region of one sense at midnight, and two near-equal opposite currents at dawn and dusk. A simple estimate of the magnetic moment concerned gives a value of $\sim 10^{25} \text{ A m}^2$, about $\sim 20\%$ of the spin-aligned planetary dipole moment. Added vectorially, the combined dipole has a tilt of $\sim 10^\circ$ relative to the spin axis, comparable with but smaller than the estimate made by *Southwood and Kivelson* [2007]. The oppositely-directed dipole moment of the currents in the ‘core’ region associated with the field deflection and suppression effect is about a factor of ~ 50 smaller than that of the outer currents, due to the smaller current involved and the smaller radial distance of the associated field lines.

An implication of the oscillatory field perturbations in the outer region having the approximate form of a transverse dipole is that the plane of the magnetodisk and plasma sheet in the outer region is tilted in like manner to the magnetic equatorial plane in the inner region described above. That is to say, the magnetodisk current sheet centre is displaced southward where the oscillatory radial field is positive, and northward where it is negative, such that overall the northward-directed normal of the

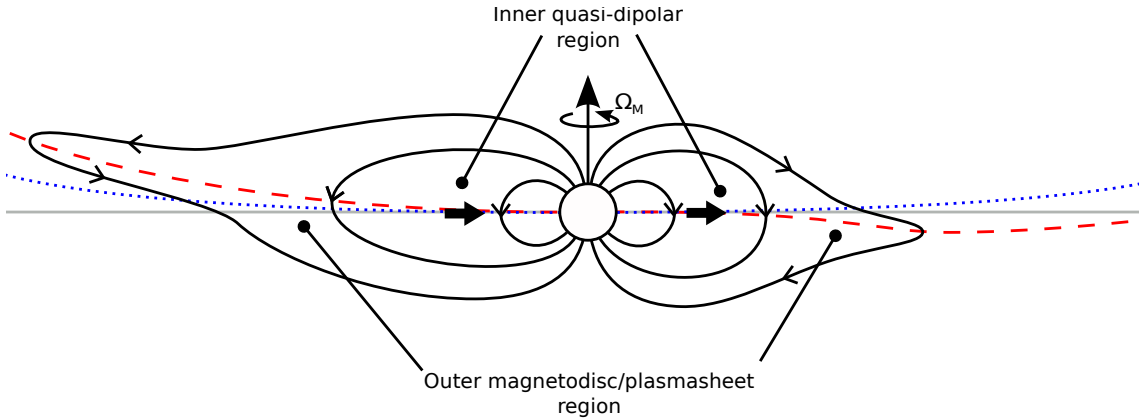


Figure 4.11: Meridional sketch of field lines in Saturn's magnetosphere, showing the displacement of the magnetic equator out of the planet's equatorial plane, for the situation in which the oscillatory radial field points from left to right (solid black arrows). The planet's spin equatorial plane is shown by the grey solid line, while the averaged position of the magnetic equator is shown by the blue dotted line, being everywhere above the equatorial plane for the southern summer conditions prevailing during the interval of this study [Arridge *et al.*, 2008b]. The instantaneous magnetic equator is shown by the red dashed line. At the instant depicted, the magnetic equator is displaced northward of its mean position where the radial field points inward, and southward of its mean position where the radial field points outward. The pattern then rotates in the same sense as the planet at the magnetospheric period $2\pi/\Omega_M$, such that a stationary observer will observe a periodic north-south 'flapping' motion of the magnetic equator.

current sheet is tilted towards the direction of the oscillatory radial field, essentially in the direction of the transverse dipole moment associated with the related current system. Since the radial fields in the outer and inner regions are essentially in phase with each other, allowing for the modest increase in phase in all field components with radial distance discussed above, the implication is that the rotating tilting of the magnetic equatorial plane in the inner region noted above continues into a rotating tilting of the magnetodisk and plasma sheet in the region beyond, as also sketched in Figure 4.11. The blue dotted line in the figure indicates the undisturbed magnetic equatorial plane which is blown northward of the planetary spin equator beyond $\sim 20 R_S$ due to the flow of the solar wind relative to the spin axis during the southern summer conditions prevailing at Saturn during the interval studied here [Arridge *et al.*, 2008b], while the red dashed line shows the relative position of the magnetic equatorial plane at an instant when the oscillatory equatorial field points from left to right. The magnetodisk is displaced to the north on the left of the diagram,

and to the south on the right, as is the magnetic equator in the inner region. In general we also expect the field in the magnetodisk to be ‘swept back’ out of magnetic meridian planes due to sub-corotation of the plasma. That is, the quasi-static fields in this region possess an anti-phase relationship between the radial and azimuthal component, with negative azimuthal fields above the centre of the disc where the radial field is positive, and positive azimuthal fields below the centre of the disc where the radial field is negative. An anti-phase oscillation of these fields will thus be introduced in the outer region as the magnetodisk is swept north-south across the spacecraft during the oscillation cycle, which will combine with other oscillations of the same period to move the overall phase towards anti-phase, as found in section 4.3. As noted above, we also illustrate in Figure 4.11 that at the oscillation phase shown, the oscillatory co-latitudinal field is negative (northward) on the left of the diagram and positive (southward) on the right, in phase with the radial component. This then implies a stronger ring current and more stretched-out field lines on the left than on the right as illustrated. Our results thus suggest that the current sheet has its most northward deflection about the mean position in the sector with the strongest ring current field, and its most southward deflection in the sector with the weakest ring current field. This is then the opposite of the effect suggested by *Khurana et al.* [2009], such that this aspect merits further more detailed study.

4.8 Discussion of results

We first briefly discuss the relation between our results and the modulation of SKR emitted power. As indicated in section 2.8, SKR is believed to be due to cyclotron maser emission from auroral electrons accelerated into the ionosphere in regions of upward-directed field-aligned current [e.g. *Zarka*, 1998]. The modulation of these currents by the magnetospheric period oscillations investigated here should thus be directly relevant. If the north-south currents we deduce simply flow from hemisphere-to-hemisphere as envisaged by *Southwood and Kivelson* [2007], then they will be directed upward in one hemisphere, potentially leading to auroral acceleration and

SKR emission, and downward in the other, leading to no emission, contrary to the findings of *Lamy et al.* [2008b] that SKR enhancements occur in phase in the two hemispheres. However, this result itself is apparently now in conflict with recent observations of different periods in the northern and southern hemisphere SKR emissions, such that the northern hemisphere emission is expected to slip backwards in phase relative to the southern. Instead, as discussed by *Andrews et al.* [2008] and *Provan et al.* [2009a], our north-south currents may reflect a north-south seasonal asymmetry in a field-aligned current system that has the same sense relative to the ionosphere in the two hemispheres, that would produce no radial and azimuthal fields on the equator if the currents were equal in magnitude. Thus counting upward currents relative to the ionosphere as positive for simplicity, if the current is I_N in the northern hemisphere and I_S in the southern, where $|I_S| > |I_N|$ for the southern summer conditions prevailing during the interval of this study, and noting that both these currents are taken to rotate at the dominant ‘southern hemisphere’ period. We may then consider these currents as being due to the sum of a pair of equal currents flowing in the two hemispheres, of magnitude $(I_N + I_S)/2$, and a northward-directed hemisphere-to-hemisphere current of magnitude $(I_N - I_S)/2$. The former of these current systems, being anti-symmetric about the equator, produces no equatorial field components on the equator, such that the north-south currents deduced here correspond only to the north-south difference current, due to the seasonal inter-hemispheric asymmetry. In this case, southward-directed currents in the equatorial plane imply downward currents in the two hemispheres, with the northern current weaker than the southern, while northward-directed currents imply upward currents in the two hemispheres, with the northern current again the weaker for southern summer conditions.

Although this discussion thus makes it clear that we cannot deduce the full field-aligned currents from the north-south equatorial currents estimated here, it suggests a focus on regions of northward-directed equatorial current as indicative of upward-directed current flows in both hemispheres, certainly in the dominant southern summer hemisphere. Our results then show no obvious simple connection with the SKR

modulation, since northward equatorial currents of approximately constant ~ 6 MA magnitude are present in the outer region throughout the oscillation cycle, though rotating in local time e.g. from the post-dusk sector when $\Phi_M = 0^\circ$ to the dawn sector when $\Phi_M = 180^\circ$, and so on. As indicated in section 4.2.2, the maximum SKR power occurs for $\Phi_M = 210^\circ$, when (within the limits of our data coverage) northward currents extend in the outer region from midnight via dawn to dusk (though being weak in the noon sector as usual). However, we note that a specific feature of this and adjacent oscillation phases is a region of strong northward-directed current lying at ~ 15 R_\oplus in the 06-08 h LT sector, corresponding to the blue starred region in panels (e) and (f) of Figure 4.9, that will map to the ionosphere at a latitude of $\sim 73^\circ$ [Bunce *et al.*, 2008]. It seems possible that this current region could be the source of the strong high-latitude pre-noon SKR emissions reported e.g. by Galopeau *et al.* [1995]. With regard to the current densities, as opposed to the area-integrated currents quoted above, we note from Figure 4.9 that the peak equatorial values are typically ~ 10 $pA m^{-2}$ for both northward- and southward-directed currents, again almost independent of oscillation phase. Southwood and Kivelson [2009] have suggested that the intense modulation in the SKR observed in the dawn to noon sector is the result of the superposition of the rotating current systems studied here, and adjacent regions in which quasi-static currents flow associated with plasma sub-corotation [e.g., Talboys *et al.*, 2009a,b]. While our method for determining current densities gives only overall values on scales of ~ 3 R_\oplus in radius and ~ 2 h in LT, and may thus underestimate peak values, we note nevertheless that the above values imply substantial current densities flowing at ionospheric levels, of order ~ 100 $nA m^{-2}$. Currents of such magnitude, or higher if they represent only the difference current between the two hemispheres as discussed above, are clearly significant in considerations of auroral particle acceleration and wave emission [e.g. Cowley *et al.*, 2004, 2008; Bunce *et al.*, 2008].

Turning now to the nature of the rotating current system implied by our results, we note that it is consistent with the asymmetric ring current picture suggested by Provan *et al.* [2009a], as indicated schematically in Figure 4.12. This shows a view looking onto the equatorial plane from the north, with the azimuthally-varying ring current j_φ

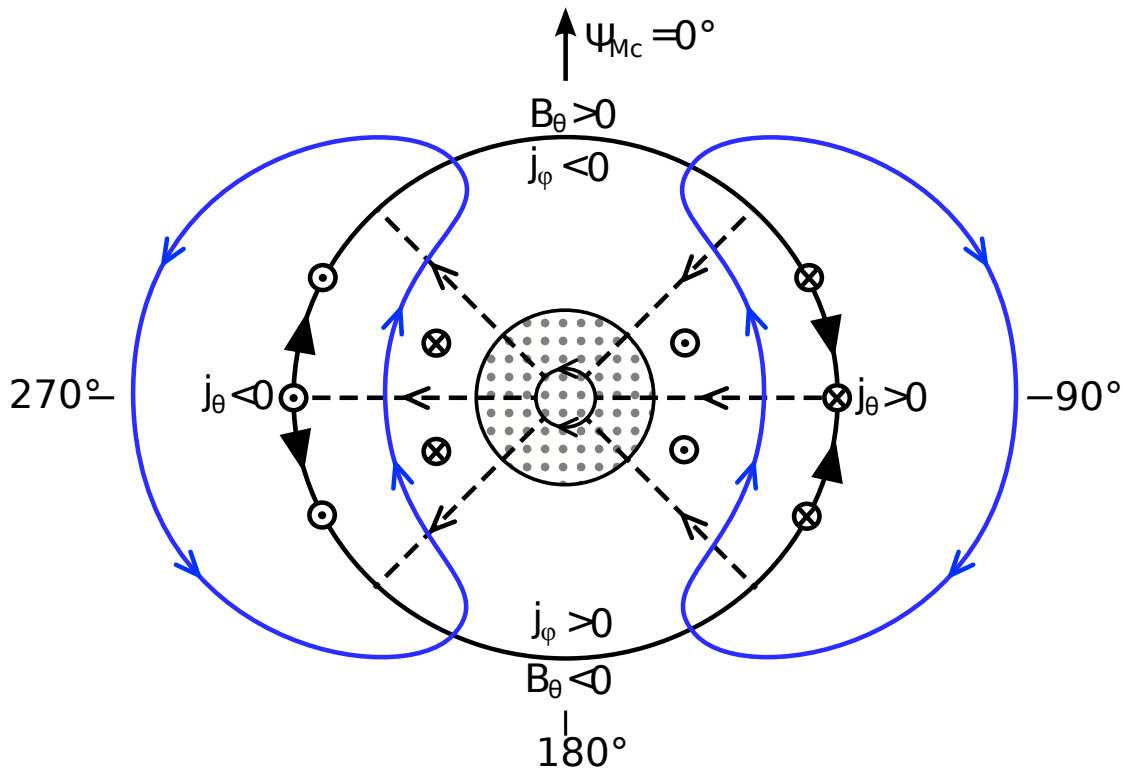


Figure 4.12: Sketch of rotating currents and fields associated with the oscillatory phenomena observed in Saturn's magnetosphere, viewed looking down on the equatorial plane from the north. The outer solid arrowed black lines indicate the modulation of Saturn's equatorial ring current (j_ϕ), while the radial dashed arrowed black lines indicate the associated field-aligned current flow to and from the ionosphere required by current continuity. The net north-south field-aligned current flow (j_θ) associated with the hemispheric asymmetry for southern summer conditions is shown by the circled dots for northward current flow (out of the plane of the diagram) on the left of the figure, and by circled crosses (into the plane of the diagram) on the right of the figure. The magnetic perturbations produced in the equatorial field components in the equatorial plane are shown by the solid arrowed blue lines, forming a twin-vortex field system. We also indicate by circled dots and crosses the directions of the inner field-aligned currents associated with the deflection and suppression of the latter fields near the planet. With increasing time this pattern of field and current then rotates anti-clockwise around the planet with the magnetospheric period.

shown by the solid arrowed black lines. At the oscillation phase depicted, j_φ is positive at the bottom of the diagram and negative at the top, it being understood that these represent perturbations superposed upon a larger near-constant positive current so that the total current flows consistently eastward as expected. The enhanced positive current at the bottom of the diagram then causes increased outward inflation of the planetary field lines in that LT sector, leading to a decrease in the co-latitudinal field, as indicated in the sketch, while the reduced positive current at the top of the diagram similarly leads to an increase in the co-latitudinal field relative to the mean. At the instant shown in the sketch, the ‘core’ phase Ψ_{Mc} is thus zero at the top of the diagram (corresponding to the maximum in the θ field component), and increases clockwise around the planet as indicated, as given by equations (4.1) and (4.2). Current continuity then requires field-aligned currents to flow between the ring current and the ionosphere (central dotted region), that are directed toward the planet on the right of the diagram (about $\Psi_{Mc} = 90^\circ$), and away from the planet on the left (about $\Psi_{Mc} = 270^\circ$), as indicated by the dashed arrowed black radial lines. If conditions were the same in the northern and southern ionospheres, we would expect equal field-aligned currents to flow in both hemispheres, thus producing no equatorial fields (r and φ field components) lying in the equatorial plane. However, in the northern winter/southern summer conditions that prevailed in the present study, we expect the currents to be greater in the southern hemisphere than in the northern, due to the greater Pedersen conductivity of the former ionosphere compared with the latter. The ‘difference’ current discussed above is then directed southward (i.e. $j_\theta > 0$) on the right of the diagram and northward (i.e. $j_\theta < 0$) on the left, as also indicated in the diagram. As in the discussion of *Southwood and Kivelson* [2007], these effective hemisphere-to-hemisphere field-aligned currents then produce the equatorial field shown by the blue arrowed solid lines in the diagram. In the region inside the main north-south currents, corresponding to the ‘core’, the field is directed from the bottom to the top of the diagram, such that the radial component is in phase with the co-latitudinal as required, with the azimuthal component being in lagging quadrature with both.

We have also included in the sketch a schematic indication of the smaller

oppositely-directed north-south field-aligned currents flowing in the inner region that lead to the deflection of the ‘core’ field around the planet as indicated. In the region outside the main north-south currents the equatorial field then forms a twin vortex system as found in our study, akin to the field of a transverse dipole, the dipole concerned being formed by the net hemisphere-to-hemisphere field-aligned current system. A partial ring current system with equal field-aligned currents in the two hemispheres has no associated transverse dipole moment. In view of the recent discovery of the separate northern-hemisphere modulation, it might be reasonably assumed that two such rotating transverse dipoles and associated current systems are present, with the southern being dominant during the interval studied here. This possibility is explored in the following chapter.

With regard to the magnitudes of the currents, we note that our results imply effective hemisphere-to-hemisphere currents of ~ 5 MA, which in terms of the above discussion implies that the positive and negative modulations in the ring current at the top and bottom of the diagram are at least ± 5 MA. This compares with estimates by *Bunce et al.* [2007] of the total dayside ring current, effectively the mean value, of $\sim 10\text{-}15$ MA, with perhaps a further ~ 5 MA flowing in the plasma sheet to our outer nightside boundary of $30 R_S$, based on the field strength within the tail lobes. The total averaged field-perpendicular current flowing in the equatorial plane in the region studied is thus $\sim 15\text{-}20$ MA, so that modulations of ± 5 MA correspond to remarkably large variations of the equatorial current of $\sim \pm 25\text{-}35\%$.

While this picture thus provides a basic description of the fields observed, we note that it is not obviously consistent with all the details found in our study. In particular, our results show that while the oscillations in the co-latitudinal field do not vary greatly in LT, thus indicating the presence of rotating perturbations in the ring current of approximately constant amplitude independent of LT, the oscillations in the radial and azimuthal components do depend strongly on LT, being significantly larger on the nightside than on the dayside. One possible explanation in terms of the above picture, is that while the total field-aligned current flows to and from the ionosphere required by the varying ring current remain approximately constant independent of oscillation

phase, the north-south difference current that leads to the equatorial field components may depend on LT, being smaller on dayside field lines than on nightside field lines. This could happen, for example, if the difference between the Pedersen conductivities of the northern and southern ionosphere is less on the dayside than on nightside.

As stated in the introduction to this chapter, the recent discovery of the distinctly shorter period of the weaker modulation in SKR emission from the northern hemisphere further complicates this discussion. It might be expected that a secondary system of rotating field perturbations and currents with a form similar to that depicted in Figure 4.12, associated with the modulation of the SKR at a shorter period in the northern hemisphere, is superimposed upon the dominant system of field perturbations and currents associated with the modulation in the southern hemisphere SKR. The analysis performed in this chapter is not expected to be significantly influenced by the presence of such a secondary system, as the magnetic phase model determined by *Provan et al.* [2009a] (and the SKR phase models of *Kurth et al.* [2007, 2008] upon which it relies) clearly depend only upon the dominant modulation present. While the periods of both the northern and southern SKR modulations are shown to be seasonally dependent, and appear to converge some time after Saturn's vernal equinox in August 2009 [*Gurnett et al.*, 2009a; *Lamy*, 2011], during the interval studied here the weaker northern-period signal merely serves to produce the deterministic phase ‘jitter’ with amplitudes of a few tens of degrees, as shown by *Andrews et al.* [2008] and *Provan et al.* [2011]. The phase jitter varies at the ‘beat period’ between the northern and southern signals, being \sim 23 days, though as was noted in section 4.1, the spatial binning of data performed in this study rapidly removes the effect of this jitter from the determined phase values.

Finally we briefly comment on the physical origins of these oscillatory phenomena. As discussed in section 2.8, most theoretical discussion to date has centred on the existence of a ‘corotating convection’ system that is centrifugally-driven by plasma mass-loading in the inner magnetosphere that originates from the emission of water from the moon Enceladus. In terms of the picture presented in Figure 4.12, we would expect the region with enhanced azimuthal currents to be the outward-moving ‘heavy’

sector, thus corresponding to the region at the bottom of the figure. Dynamically, we would then interpret the equatorial field perturbations shown by the blue lines in the figure as being due to field tilting effects in the presence of differential ionospheric drag between the northern and southern hemispheres, with the drag in the southern summer hemisphere being larger than that in the northern winter hemisphere, as expected. In this case the blue field lines in the sketch then also represent streamlines of the corotating convection system, with the flow being directed opposite to the field. As previously pointed out by *Andrews et al.* [2008] and *Provan et al.* [2009a], however, an apparent inconsistency with this picture then concerns the phase of the cold plasma density modulation in the Enceladus plasma torus observed in the inner region ($\sim 3\text{-}5 R_S$) by *Gurnett et al.* [2007], whose ‘heavy’ sector is in phase with the azimuthal field component, thus peaking at $\Psi_{Mc} = 90^\circ$ on the right of Figure 4.12, rather than being in anti-phase with the radial and co-latitudinal field components as just outlined. It thus appears that we must suppose the larger-scale flow to be responding primarily to asymmetries that occur at a larger phase angle at larger distances, a suggestion that requires further study to elucidate. However, it is unclear how such rotating azimuthal asymmetry in the equatorial plasma is capable of producing the recently observed north-south asymmetry in the SKR.

Chapter 5

Comparison of equatorial and high-latitude magnetic field periods with north and south SKR periods

5.1 Introduction

As was noted in Chapter 2, it has recently been shown that the SKR emissions originating from the northern and southern hemispheres are modulated at distinctly different periods. In this chapter, evidence for a similar asymmetry in the magnetic field oscillations observed on high-latitude Cassini orbits is presented.

Previous studies have shown that in the near-equatorial core region of the magnetosphere within radial distances of $\sim 10\text{--}15 R_S$ where the overall field is dominated by the quasi-dipolar field of the planet, the oscillatory perturbation field takes the form of a quasi-uniform field in the equatorial plane that rotates in the sense of planetary rotation with a period close to the SKR period [Espinosa *et al.* 2003a,b; Southwood and Kivelson 2007; Andrews *et al.* 2008; Provan *et al.* 2009a; Chapter 2 of this thesis]. The polarisation characteristics of such a rotating perturbation field are illustrated for future reference in Figure 5.1a, which shows a view of the equatorial ($x - y$) plane looking from the north. The quasi-uniform perturbation field is indicated schematically by the blue lines, which is such that a maximum in the spherical polar

radial (r) field component occurs at point P at the instant depicted. As the perturbation field pattern rotates around the axis as indicated by the arrowed red dashed circle, it can be seen that the maximum in the r component at P will be followed a quarter cycle later by a maximum in the azimuthal (φ) component. For such a field, therefore, the φ component oscillates in lagging quadrature with the r component, as indicated by the above-cited authors. Oscillations in the co-latitudinal (θ) field component are also present in the equatorial region, which are in phase with the r component [Andrews *et al.* 2008; Provan *et al.* 2009a; Chapter 2 of this thesis]. The near-equatorial perturbation field lines thus form arches with apices in the north, as illustrated schematically in Figure 5.1b, which shows perturbation field lines projected onto the principal magnetic meridian ($z - \rho$) of the disturbance (where ρ lies in the direction in which the perturbation field points radially outward in the equatorial view). The phase of the field oscillations relative to the SKR modulations is found to be such that the SKR power peaks when the quasi-uniform field points radially outward in the post-midnight sector, at \sim 02 h local time (LT). However, considerable ‘jitter’ in the phase of the equatorial magnetic oscillations is also found to be present, with amplitude \sim 20° [Andrews *et al.*, 2008; Provan *et al.*, 2011]. We note in this context that variations in the SKR phase on 20-30 day time scales have also been found to be present, which appear to be connected to variations in the solar wind speed [Zarka *et al.*, 2007].

Magnetic oscillations in the high-latitude magnetosphere on open field lines were first studied by Provan *et al.* [2009a], who found that unlike the equatorial region, the polarisation characteristics are those of a planet-centred rotating transverse dipole in both hemispheres. The characteristics of such a rotating field are illustrated schematically in Figures 5.1c and 5.1d, which have similar formats to Figures 5.1a and 5.1b. Consideration of the equatorial projection in Figure 5.1c shows that in this case the φ component oscillates in leading quadrature with the r component (both on and away from the equator), while Figure 5.1d shows that the θ and r components are in phase south of the equatorial plane (as in the core region), but are in anti-phase north of the equatorial plane. These are the relative phases between the field components

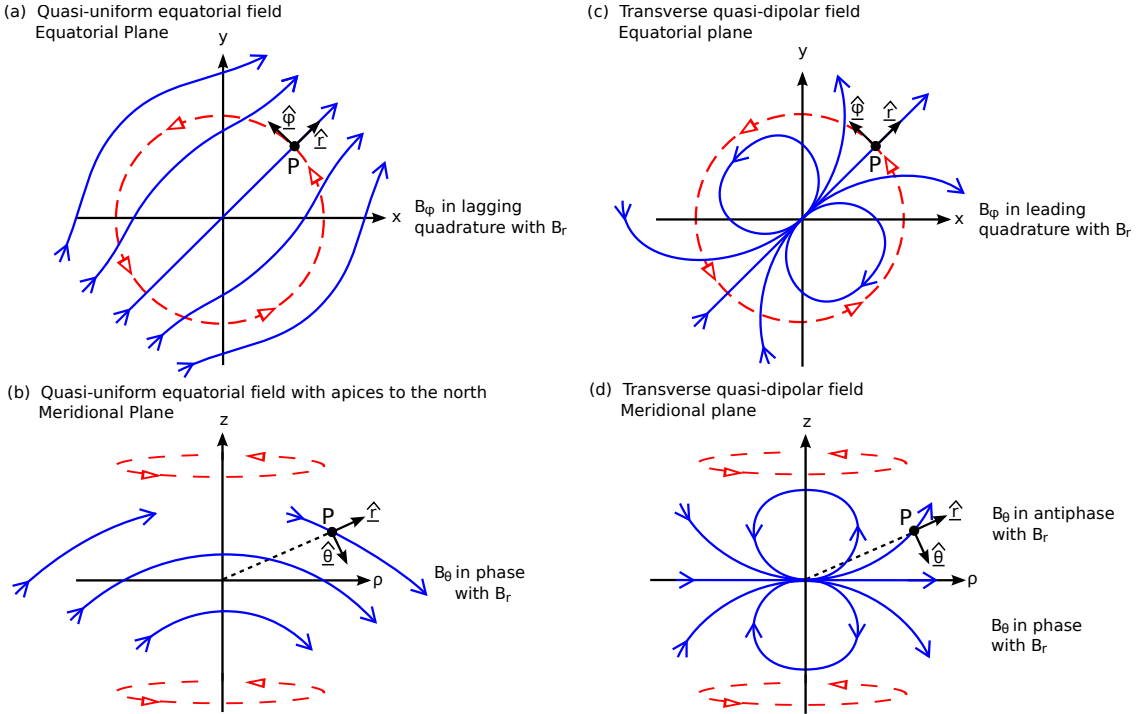


Figure 5.1: Sketches illustrating the polarisation characteristics of the rotating perturbation field patterns discussed in this study, where Panels (a) and (b) correspond to the rotating quasi-uniform field observed in the near-equatorial core region of the magnetosphere, while Panels (c) and (d) correspond to the planet-centred rotating transverse dipole fields observed on high-latitude open field lines. Panels (a) and (c) show the equatorial ($x - y$) plane in each case viewed from the north, while Panels (b) and (c) show a meridional ($z - \rho$) view, where ρ lies in the direction in which the perturbation field points radially outward in the equatorial view. The arrowed blue lines in each panel indicate the perturbation field lines, while the arrowed red dashed lines indicate the sense of rotation of the field pattern with time. The phase relationships of the consequent oscillations in the field components at any spatial point in each Panel (such as at the arbitrary points P shown) are indicated on the right.

found on open field lines in both hemispheres by *Provan et al.* [2009a]. These authors also showed that the r and θ oscillations at southern high-latitudes are approximately in phase with those within the core region, such that the φ components in the two regions oscillate approximately in anti-phase. Thus the effective transverse magnetic dipole moment vector corresponding to the southern hemisphere oscillations, which rotates in phase with the r component of the perturbation field (see Figure 5.1c), is directed approximately parallel to the quasi-uniform field in the core region. This effective transverse dipole thus again points down-tail and towards dawn at SKR maxima. However, *Provan et al.* [2009a] also found that the relative phase between

the core region oscillations and the northern high-latitude quasi-dipolar oscillations is somewhat scattered, such that the relative orientation of the effective transverse dipoles in the two hemispheres remains uncertain.

Considering now the SKR emissions, these are believed to be generated predominantly in the extraordinary (X) mode by accelerated auroral electrons on high-latitude field lines via the cyclotron maser instability, with emissions generated in the northern and southern hemispheres having opposite circular polarisation [*Wu and Lee*, 1979; *Warwick et al.*, 1981; *Lecacheux and Genova*, 1983; *Galopeau et al.*, 1995; *Zarka*, 1998; *Lamy et al.*, 2008b, 2009, 2010; *Cecconi et al.*, 2009]. Emission sources may occur at any local time, co-located with the UV auroral oval [*Lamy et al.*, 2009], but as indicated above are generally dominated by those in the dawn-to-noon sector. Most recently, however, it has been discovered that in the initial Cassini era (2004-2008), emissions from the two hemispheres are modulated at distinctly different periods, ~ 10.6 h in the north and ~ 10.8 h in the south [*Gurnett et al.*, 2009a], while the overall emitted power during the interval is generally dominated by the longer-period emissions from the southern summer hemisphere. The presence of two distinct SKR modulation periods was previously reported in Cassini data by *Kurth et al.* [2008], and in Voyager-era data by *Desch and Kaiser* [1981] (with closer periods in that case of 10.66 and 10.69 h). Corresponding distinct modulation periods have also subsequently been reported in both auroral hiss and magnetospheric energetic electron data [*Gurnett et al.*, 2009b; *Carbary et al.*, 2009b].

From the magnetic field results presented by *Andrews et al.* [2008] and *Provan et al.* [2009a], it is evident that the magnetic field oscillations observed in the near-equatorial and southern high-latitude regions in the initial Cassini era relate to the dominant longer-period southern SKR modulations. Thus the phase relationships outlined above between the field oscillations in these regions and the SKR power modulations refer specifically to radio emissions originating in the southern hemisphere. The relationships between the field oscillations and the shorter-period SKR modulations originating from the northern hemisphere remain to be investigated in detail. However, at the Magnetospheres of Outer Planets (MOP) meeting held in Köln,

Germany, in July 2009, A. Lecacheux and D.J. Southwood provided initial evidence that the quasi dipolar northern high latitude field oscillations occur at the shorter northern SKR period¹, thus potentially providing a basis for understanding the more scattered northern phase results of *Provan et al.* [2009a].

In the previous study by *Provan et al.* [2009a], the phases of the near-equatorial and northern and southern high-latitude magnetic field oscillations were thus (in effect) compared with those of the dominant southern SKR modulations over the interval from Cassini Saturn orbit insertion (SOI) in mid-2004 to the end of 2007. In this chapter we now considerably extend this analysis to cover all such magnetic field data obtained in the pre-equinox interval to mid-2009 (Saturn's vernal equinox occurred on 11 August 2009), and compare the phases of the field oscillations with both the northern and southern SKR modulations. We show that the periods of the equatorial and southern high-latitude oscillations are close to the southern SKR period throughout this interval, while the period of the northern high-latitude oscillations is close to the northern SKR period.

5.2 Data selection, processing, and analysis

5.2.1 Magnetic oscillation model

The basis of the analysis presented here follows that previously employed by *Andrews et al.* [2008] and *Provan et al.* [2009a], where the phase of the magnetic field oscillations is obtained (to modulo 360°) relative to those of the SKR modulations, employed as exact ‘guide phases’. Assuming that the magnetic oscillations rotate in the sense of planetary rotation as a ‘ $m = 1$ ’ disturbance (i.e., varying with azimuth φ as $e^{jm\varphi}$ with $m = 1$), as opposed to the modulations of the SKR emissions whose phase is independent of position, we express the variation of each field component B_i as

$$B_i(\varphi, t) = B_{i0} \cos(\Phi_{SKRn,s}(t) - \varphi - \psi_{iMn,s}). \quad (5.1)$$

¹Their study was subsequently published by *Southwood* [2011], shortly after the publication of the study presented in this chapter [*Andrews et al.*, 2010].

In this expression φ is the azimuthal angle measured positive from noon towards dusk, $\Phi_{SKRn,s}(t)$ is the phase of the northern ('n') or southern ('s') SKR modulations defined such that emission maxima occur when $\Phi_{SKRn,s}(t) = 360N$ degrees for integer N , and $\psi_{iMn,s}$ is the corresponding relative phase of the oscillation in magnetic field component i . The latter phase is determined separately for equatorial and high-latitude field data from individual spacecraft orbit revolutions ('Revs') by fitting equation (5.1) to magnetic field data suitably processed as described below, with φ given by the azimuthal angle of the spacecraft (equivalent to LT), and B_{i0} and $\psi_{iMn,s}$ as free parameters. If the period of the rotating magnetic oscillations is the same as that of the corresponding SKR modulations, the $\psi_{iMn,s}$ values obtained will be constant from pass to pass for each field component, with the phase differences between the components depending on the oscillation polarisation characteristics as described in section 5.1 (Figure 5.1). Deviations between the magnetic and SKR periods are then revealed by changes in the $\psi_{iMn,s}$ values for each component from Rev to Rev.

5.2.2 Northern and southern SKR phases

In this study, we employ the phases of the SKR modulations in each hemisphere, $\Phi_{SKRn,s}(t)$, derived from Cassini RPWS instrument data [Gurnett *et al.*, 2004] by Lamy [2011]. The numerical phase data set, along with a summary of its derivation, is available online at the LESIA Observatoire de Paris website². Briefly, the radio data are first separated into northern and southern emissions on the basis of their polarisation and the latitude of the spacecraft, with right- and left-handed emissions corresponding to the northern and southern hemispheres, respectively. The separated flux densities are then integrated in the SKR frequency band 40-500 kHz and normalized with respect to radial distance from the planet, and the dominant period in each hemisphere, $\tau_{SKRn,s}(t)$, is then computed using a Lomb-Scargle analysis with a 200 day sliding window [Lomb, 1976; Scargle, 1982; Horne and Baliunas, 1986]. This time series

²<http://www.lesia.obspm.fr/kronos/guest.php>

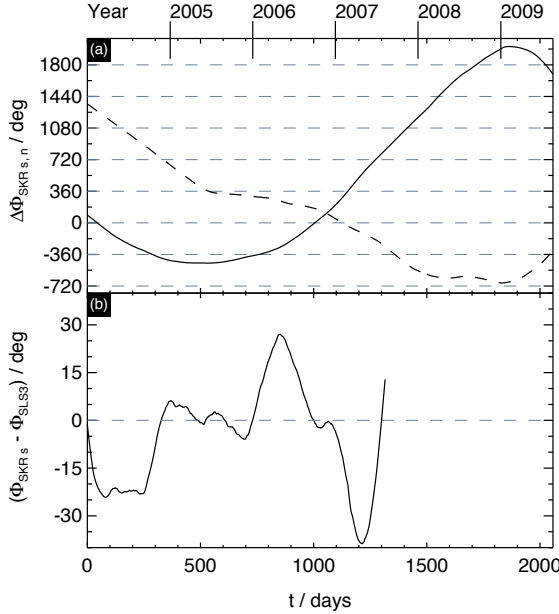


Figure 5.2: Plots relating to the numerical northern and southern hemisphere SKR phases employed in this chapter given by equation (5.2), shown over the interval $t = 0 - 2057$ days, where $t = 0$ corresponds to the 00 h UT, 1 January 2004. Panel (a) shows the empirically-determined phase of the northern (dashed line) and southern (solid line) SKR modulations relative to oscillations with fixed periods of exactly 10.6 and 10.8 h, respectively, as given by equation (5.3). The phases of each have been adjusted by arbitrary whole 360° cycles for presentation purposes. Panel (b) shows the difference between the numerical southern hemisphere SKR phase employed in this chapter, Φ_{SKRs} , and the polynomial-based SLS3 SKR phase model of Kurth *et al.* [2008], Φ_{SLS3} , shown versus time t over the interval of validity of the SLS3 phase, $t = 0 - 1317$ days. Calendar year boundaries are shown at the top of the plot.

is then numerically integrated to determine the SKR phase for each hemisphere using

$$\Phi_{SKRn,s}(t) = \int_0^t \frac{dt}{\tau_{SKRn,s}} + \Phi_{0n,s}, \quad (5.2)$$

where $t = 0$ corresponds 00 h UT, 1 January 2004, and $\Phi_{0n,s}$ is a constant determined (to modulo 360°) by requiring SKR power maxima to correspond to phases of $360 N$ degrees as indicated above.

The northern and southern SKR phases so determined are shown in Panel (a) of Figure 5.2 over the interval $t = 0 - 2057$ days (from 1 January 2004 to 19 August 2009), encompassing the interval for which magnetic field phases are determined in this chapter as will be outlined in section 5.3 below. The northern phase (dashed line) is shown relative to the phase of a fixed period of exactly 10.6 h, while the southern phase (solid line) is shown relative to that of a fixed period of exactly 10.8 h. Specifically, the

quantities shown are

$$\Delta\Phi_{SKRn,s}(t) = 360^\circ \frac{t}{\tau_{n,s}^*} - \Phi_{SKRn,s}(t), \quad (5.3)$$

where the phases are expressed in degrees, $\tau_n^* \equiv 10.6$ h, and $\tau_s^* \equiv 10.8$ h. An arbitrary integer number of 360° cycles have also been added to optimise the presentation. Intervals for which these quantities are approximately constant thus indicate an SKR modulation period that is close to that of the respective reference period, while positive or negative gradients indicate a period that is longer or shorter, respectively. The overall deviation about near-linear behaviour of these phases can be seen to be by around a cycle or two in either direction over this ~ 5.6 year interval.

We also note that the previous studies of the phases of the rotating magnetic oscillations by *Andrews et al.* [2008] and *Provan et al.* [2009a] employed the SKR phase models provided by *Kurth et al.* [2007, 2008], in which the phase is expressed as a polynomial in time t obtained from fits to the SKR phase data. The most recent model of *Kurth et al.* [2008] employed by *Provan et al.* [2009a] is expressed as a fifth order polynomial, obtained over the interval $t = 0 - 1317$ days (to 10 August 2007). To gauge the changes in the results expected over this interval due to differences between the SKR phase models, in Panel (b) of Figure 5.2 we plot the difference between the southern hemisphere numerical SKR phase employed here and the corresponding value of the *Kurth et al.* [2008] (SLS3) model, $\Phi_{SKRs} - \Phi_{SLS3}$, over the interval of validity of the latter. With the exception of the region near the end of the end of the interval, it can be seen that deviations are generally limited to within about $\pm 20^\circ$, the overall RMS value of the difference being 16° . Such differences are thus much less significant than the overall phase deviations due to the longer-term variability of the SKR modulation period indicated in Panel (a) of the figure. As will be seen in section 5.3 below, these differences are only of minor significance to the magnetic field phase results presented here, such that our results may be compared directly with those of *Andrews et al.* [2008] and *Provan et al.* [2009a] despite the differing SKR phases employed.

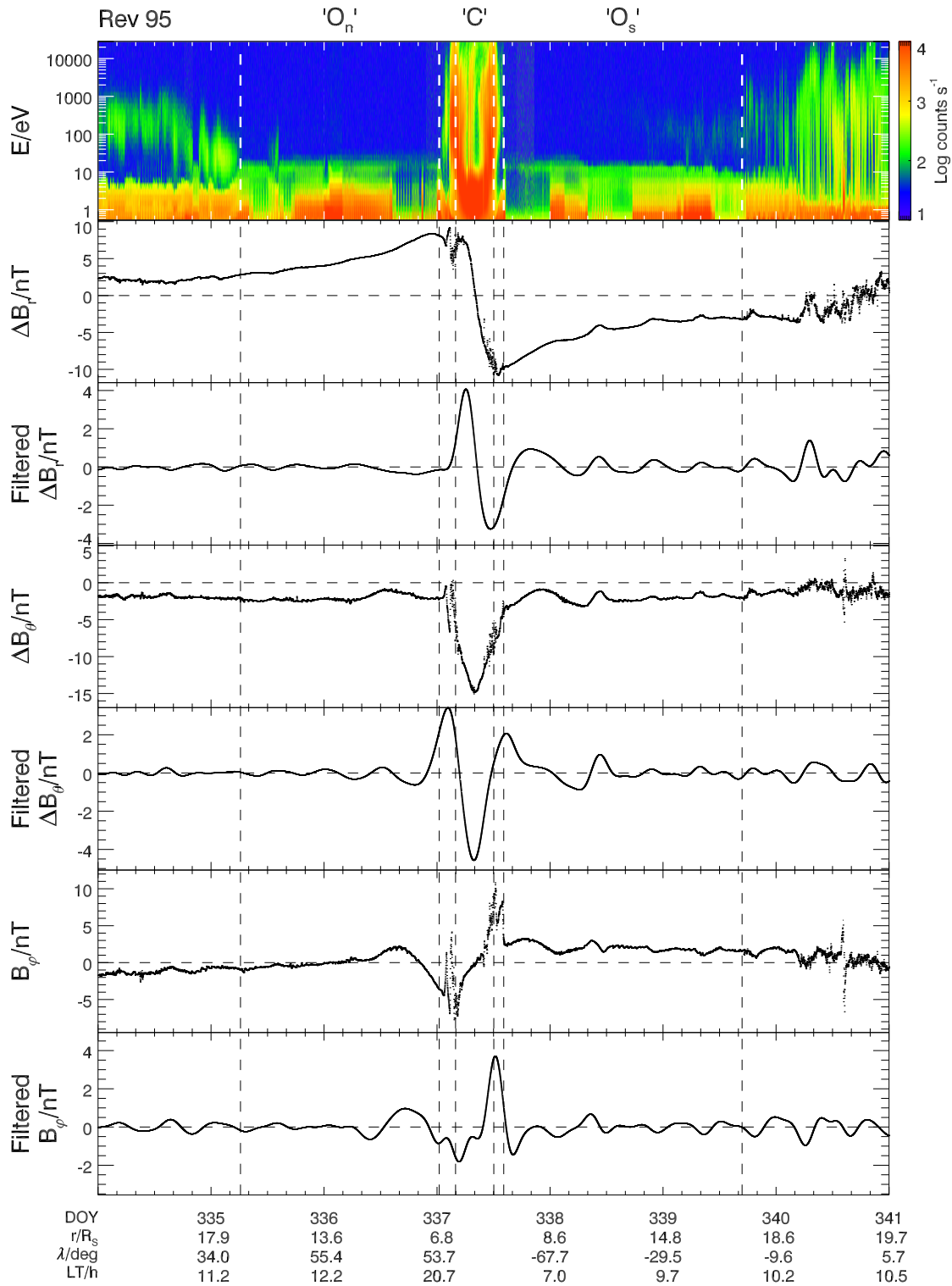


Figure 5.3: Caption overleaf.

5.2.3 Selection and processing of magnetic field data

We now discuss the selection methods and processing procedures employed for the magnetic field data. Intervals of core and high-latitude field data to be employed in the analysis have first been identified using an automated procedure that has been checked and moderated (if required) by visual inspection of the data. As discussed further below, core intervals in this study correspond to regions with dipole $L < 8$, while the high-latitude data correspond to northern and southern open field regions within radial distances of $25 R_S$ where warm and hot electron fluxes are close to instrumental background (see below). We note in passing that these radial distance limitations have resulted in our taking no account in equation (5.1) of changes in magnetic oscillation phase with radius r , as was done in the previous chapter. Detailed examination has shown that radial phase gradients within the core of $\sim 2 \text{ deg } R_S^{-1}$ (see section 4.4) produce insignificant effects on our results, while variability in the phase determinations has not allowed us to verify the presence or otherwise of gradients of similar order in the high-latitude data employed here.

Region identification using the above criteria is illustrated in Figure 5.3 for Cassini Rev 95 in December 2008, on which, somewhat unusually, the spacecraft trajectory allowed sampling of all three regions considered. On this Rev the spacecraft passed from a near-equatorial apoapsis at a radial distance of $\sim 20.3 R_S$ in the pre-

Figure 5.3: Plot showing 7 days of electron flux and magnetic field data from Cassini Rev 95 during December 2008 (days 334 to 340 inclusive), typical of the orbit geometry during this phase of the mission. The top panel shows an electron energy-time spectrogram covering the energy range 0.6 eV to 28 keV, while the lower three pairs of panels show residual and band-pass filtered magnetic field data for each of the three spherical polar field components referenced to the planet's spin and magnetic axis. The residual components have the Cassini SOI internal field model subtracted, while since the azimuthal field of this model is zero, this field component is shown as measured. Spacecraft position information is indicated at the bottom of the figure, specifically the radial distance (R_S), the latitude (degrees), and the local time (hours). The three intervals whose data have been selected for oscillation phase determinations on this Rev are delimited by the vertical dashed lines, and are labeled ‘ O_n ’, ‘ O_s ’, and ‘C’ for the northern and southern hemisphere open field regions, and the closed field core region, respectively.

noon sector (10.6 h LT) near the beginning of the plot, over the north polar region to a near-equatorial periapsis at a radial distance of ~ 5.2 R_S in the pre-midnight sector (22.6 h LT) near the centre of the plot, and then over the southern polar region to apoapsis again towards the end of the plot. From top to bottom of the figure we show an electron spectrogram between 0.6 eV and 28 keV from the CAPS-ELS instrument [Young *et al.*, 2004], followed by residual and filtered spherical polar (r , θ , φ) magnetic field components obtained by the fluxgate magnetometer [Dougherty *et al.*, 2004]. The residual field data have the ‘Cassini SOI’ internal model subtracted [Dougherty *et al.*, 2005], but since this field is exactly symmetric about the planet’s spin axis, with zero azimuthal component, the azimuthal field shown is that measured. As in previous related analyses, the residual field data have then been band-pass filtered between periods of 5 and 20 h using a standard Lanczos filter, in order to isolate oscillations centred in the magnetospheric period band (see Andrews *et al.* [2008] and Provan *et al.* [2009a] for further discussion).

Northern and southern open field regions, designated ‘O_n’ and ‘O_s’ in Figure 5.3, are identified specifically by requiring the integrated electron counts between 50 and 500 V to be close to instrument background (noting that the variable intense fluxes below a few tens of eV in Figure 5.3 are spacecraft photoelectrons), with such intervals persisting for at least ~ 6 h being selected for study. Short data segments with moderately higher electron count rates are allowed within such intervals, provided they are not recurrent near the magnetospheric period, potentially indicative of an oscillating boundary region. In Figure 5.3 both northern and southern open field regions so identified, bounded by the vertical dashed lines, have durations of ~ 2 days. Since this corresponds to ~ 4 oscillations at either northern or southern SKR periods, the oscillation phases $\psi_{iMn,s}$ in each field component can be well-determined by least-squares fitting equation (5.1) to the filtered residual data. Uncertainties in the fitted phase are estimated by determining the phase shifts required to give a significant 10% increase in the root-mean-square (RMS) deviation between the field data and the fitted model.

We note, however, that on other Revs during the interval of study, regions of

open field data can be observed closer to the planet during which large and rapid field variations also occur due to spacecraft motion through the high-latitude field perturbations produced by the near-equatorial ring current and magnetotail. Such variations then introduce significant power into the filter band that is unrelated to the magnetospheric period oscillations, so that the phases determined from such data must be excluded from the analysis. However, since the ring current fields are observed to be near-axisymmetric to a first approximation with little azimuthal component (e.g., *Bunce et al.* [2007]), related to the major current contribution of the near-axisymmetric cool water ion plasma transported outward from the Enceladus torus [*Kellett et al.*, 2010; *Sergis et al.*, 2010], this problem affects only the r and θ components of the field, while phases can still be determined from the φ component.

Turning now to the data from the closed-field core region, designated ‘C’ in Figure 5.3, we note that the limitation of the region to dipole $L < 8$ employed here is more restrictive than in the studies by *Andrews et al.* [2008] and *Provan et al.* [2009a], where dipole $L < 12$ was employed. This limitation is required to exclude the highly-structured magnetic signatures of field-aligned currents that flow predominantly in the outer magnetosphere between the core and the open field region [*Talboys et al.*, 2009a,b], at lower latitudes on the nightside than on the dayside. In the figure it can be seen that these current signatures are localised mainly in the short intervals between the regions ‘C’ and ‘O_{n,s}’ on either side of periapsis. On more extended lower-latitude traversals through the core region during some intervals of the Cassini mission, the core oscillation phases can be determined for all three field components by fitting equation (5.1) to the filtered data, as for the high-latitude data. However, ring current fields can again introduce spurious phases into the r and θ component data on some Revs which also must be rejected, as before leaving data only for the φ component. This restriction on the r and θ component data also applies to shorter highly-inclined passes through the core region, such as that shown in Figure 5.3, where, as can be seen, the filtered φ component data are also contaminated by the field-aligned current signatures on either side. In these cases, therefore, we fit equation (5.1) to the unfiltered core region φ component data (only). This should in principle still

give reasonable phase values even for relatively short data segments (e.g., ~ 8 h in Figure 5.3) since there are no other major sources of azimuthal field within the core. Even so, the phases so determined are clearly expected to have greater uncertainty (again determined using the above algorithm) and scatter than those determined from filtered data acquired over several oscillations.

We finally note that phase data are also excluded from our analysis when the RMS deviation between the data and equation (5.1) becomes sufficiently large, or when the fitted amplitude becomes sufficiently small. Reasonable empirically-determined limits are RMS deviations more than twice the fitted amplitude, and field oscillation amplitudes less than 0.2 nT. In practice, these limits result in the removal of only $\sim 14\%$ of the otherwise acceptable phase values determined here.

5.2.4 *Overview of magnetic oscillation phase data availability*

In Figure 5.4 we provide an overview of those Cassini Revs, governed principally by the orbit characteristics, which yield magnetic phase data for each of the three regions examined here (i.e. the core region, and the northern and southern open field regions), within the limitations outlined above. The plot covers the interval from $t = 100$ (beginning of 10 April 2004) to $t = 2057$ days (end of 19 August 2009, just past the vernal equinox), thus spanning the whole of the Cassini orbital tour from SOI in mid-2004 to Rev 116. The intervals of individual Revs defined from apoapsis to apoapsis are indicated by the successive black and white stripes at the top of the figure, which are marked and numbered at the periapsis of every tenth Rev. Year boundaries are also marked. Data Panels (a) and (b) beneath this then show some relevant characteristics of the spacecraft orbit. Panel (a) shows the radial distance of apoapsis and periapsis (blue and red dots, respectively), while the horizontal dashed lines at 8 and 25 R_S indicate the equatorial extent of the core region and the outer radius of the open field regions employed here, respectively. Beneath this in Panel (b) we plot the latitude λ of the spacecraft, showing the presence of two intervals of high-latitude orbits that allow observations of the northern and southern open field regions.

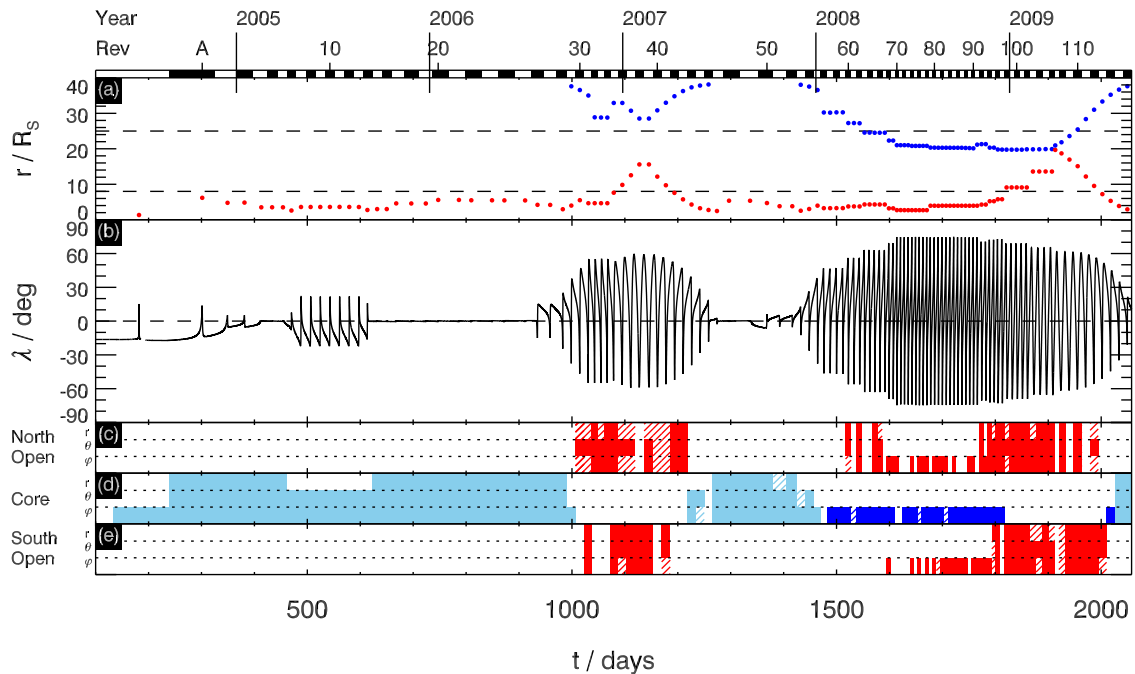


Figure 5.4: Plot showing characteristics of the Cassini orbital tour that govern measurements of the magnetic field phase in each of the three regions studied in this chapter. The interval covered by the plot is from $t = 100$ to 2057 days, spanning mid-April 2004 to mid-August 2009. Alternate black and white boxes at the top of the plot indicate the duration of each spacecraft Rev from apoapsis to apoapsis spanning SOI to Rev 116, marked and labeled at the periapsis of every tenth Rev. Year boundaries are also marked. Data Panel (a) then shows the radial distance (R_S) of periapsis (red points) and apoapsis (blue points) on each Rev, while the horizontal dashed lines shown at 8 and $25 R_S$ indicate the equatorial extent of the core region and the outer radius of the open field regions employed in this study, respectively. Panel (b) then gives the latitude λ of the spacecraft (degrees), showing the two extended high-latitude intervals of the orbital tour. Panels (c) to (e) then indicate the Revs that yield magnetic phase data for the northern open region, the core region, and the southern open region, respectively. Each of these panels is sub-divided into three, corresponding to the three spherical polar field components as marked. A particular Rev is shown coloured, red for the two open regions, and blue for the core region, if a phase measurement for that region and field component was obtained from that Rev. In the core region panel light blue indicates phase data determined from filtered magnetic field data, while dark blue indicates phase data determined from unfiltered azimuthal component data during short traversals of the core region, as outlined in section 5.2. Blank areas indicate that valid phase data were not obtained for a particular region and component for a particular Rev. Hatching of an appropriate colour indicates phase data that have further been excluded due to limitations on the RMS deviation between model and data and on the oscillation amplitude, as discussed in section 5.2.

We also note the increases in periapsis radius during parts of these intervals that result in a lack of simultaneous core observations during portions of both of them.

The consequent availability of magnetic phase data for each of the three regions is then shown on a Rev-by-Rev basis in Panels (c) to (e) at the bottom of Figure 5.4, where Panel (c) corresponds to the northern open field region, Panel (d) to the core region, and Panel (e) to the southern open field region. Each of these panels is subdivided into three corresponding to the three spherical polar field components as marked, and coloured red in the open field regions and blue in the core region when a phase value for a specific field component has been determined for a particular Rev. Light blue colouring in the core region panel corresponds to Revs for which phase values have been determined using filtered data, while dark blue colouring corresponds to Revs for which core phase determinations have been made using shorter intervals of unfiltered φ component data only. Blank intervals then indicate a lack of corresponding data because either the spacecraft did not enter a particular region on a particular Rev, or the phase value for a particular component is invalid for reasons given above, or there is an extended data gap such that phase values cannot be determined. Phase values discounted due to limitations on the RMS deviation and oscillation amplitude are shown hatched in the appropriate colour.

Figure 5.4 thus provides a summary of the extent and limitations of the magnetic field data set employed here, together with its relationship to previous studies. We note that the first interval of core region data, obtained from the near-equatorial orbits of Rev A to Rev 28 (into the second half of 2006), was that studied by *Andrews et al.* [2008], while *Provan et al.* [2009a] extended this study to include data from both SOI and the second near-equatorial mission interval, to Rev 54 at the end of 2008. Subsequent core data, new to this study, span 2008 to mid-2009, and predominantly consist of measurements obtained from unfiltered φ component data as illustrated in Figure 5.3 (the last two Revs excepted). Similarly, the first interval of open field data, obtained between August 2006 and April 2007 on Revs 30 to 43, was that studied by *Provan et al.* [2009a]. The second longer interval of open field data between February 2008 and June 2009, corresponding to Revs 60 to 113, is newly studied here. We note that the

latter interval contains the only extended period of essentially simultaneous core and open field phase data presently available.

5.3 Magnetic oscillation phase results

5.3.1 Overview

We now present the magnetic oscillation phase data determined for each of the three regions as outlined in section 5.2. The results of *Provan et al.* [2009a] indicate that the oscillations on southern hemisphere open field lines during the interval they investigated have a period close to the southern SKR period, as may be expected, while the results of both *Andrews et al.* [2008] and *Provan et al.* [2009a] show that the oscillations in the core region have the same southern SKR period. The results obtained by *Provan et al.* [2009a] for the northern hemisphere open field line region with respect to the southern SKR period were more scattered. In this section we thus begin by re-examining the issue of the phase and period of the oscillations in the southern open region and core region over the more extended interval examined here, and then consider the oscillations in the northern open region.

5.3.2 Southern hemisphere open field lines

Results for the southern open field region are shown in Figure 5.5, where the plot now spans the two high-latitude intervals of the Cassini mission between August 2006 and August 2009, rather than the whole mission interval as shown in Figure 5.4. Specifically we show the interval from $t = 950$ to 2057 days, corresponding to Revs 27 to 116, as indicated by the bar at the top of the figure, which has the same format as in Figure 5.4. Panel (a) of Figure 5.5 shows the magnetic oscillation phases ψ_{MIs} relative to the southern hemisphere SKR phase determined using equation (5.1) for each field component as available. Noting that these phases are determined only to modulo 360° , we have plotted these data over two cycles between -180° and $+540^\circ$, with each data point thus being shown twice, in order to demonstrate the banded nature of the values,

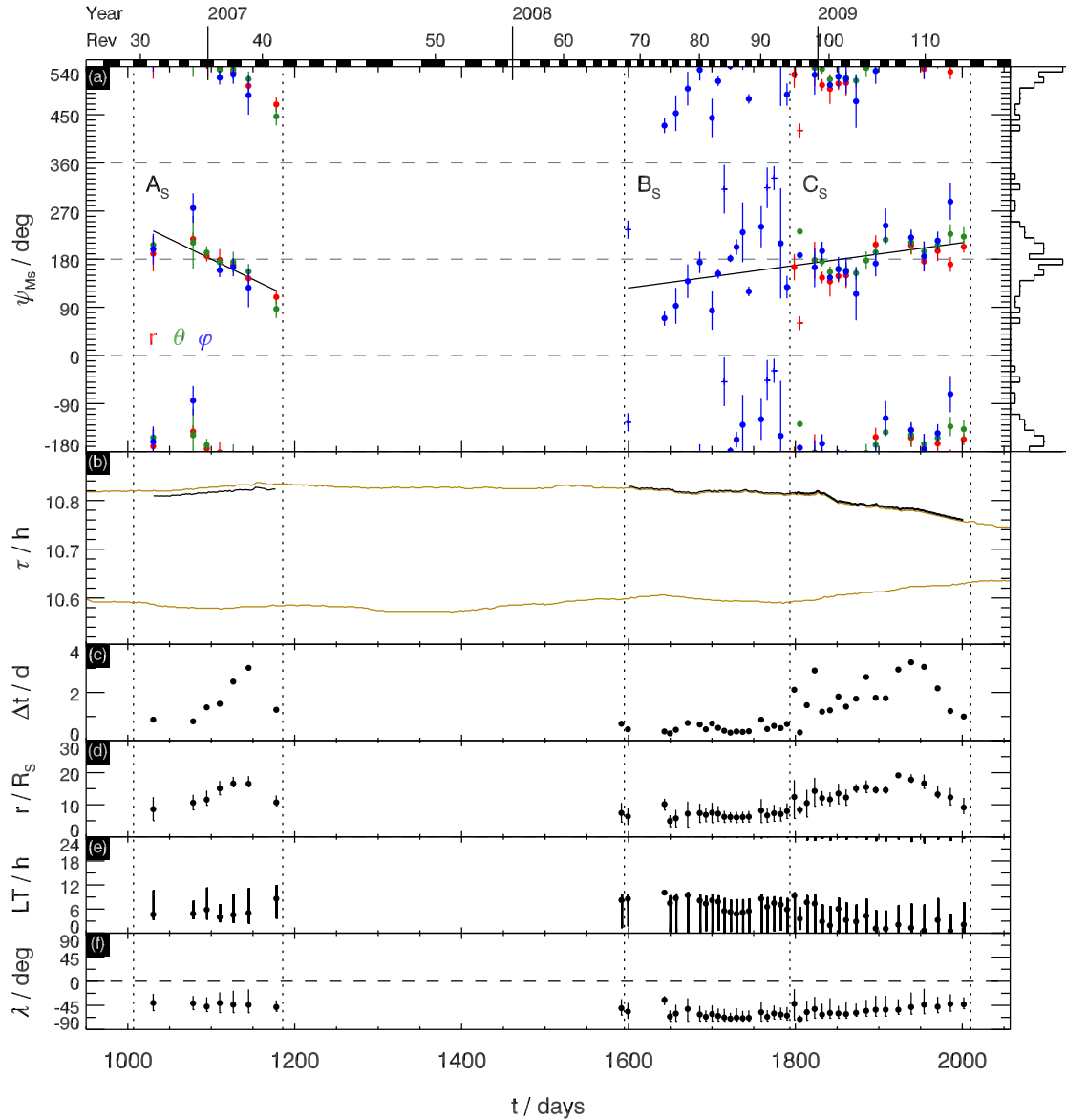


Figure 5.5: Caption overleaf.

if such is present. The data obtained from the r , θ , and φ components of the field are indicated by the red, green, and blue symbols, respectively, with vertical bars showing their uncertainties determined as described in section 5.2. As indicated in section 5.1, the previous results of *Provan et al.* [2009a] have shown that the polarisation of the oscillations on southern open field lines corresponds to a planet-centred rotating transverse dipole, with r and θ oscillations in phase, and φ in leading quadrature with both (Figures 5.1c and 5.1d). In anticipation of this result, while the r and θ component phases in Figure 5.5 are shown as measured, we have added 90° to the φ component phases, to bring them to a common value with the r and θ component

phases, if they are indeed in leading quadrature. It can be seen that the phases so plotted have common values for all field components throughout the interval when simultaneous data are available, thus confirming the polarisation found by *Provan et al.* [2009a]. The yellow lines in Panel (b) then show the southern (upper) and northern (lower) hemisphere SKR modulation periods (hours) determined as outlined in section 5.2, while the black lines show inferred magnetic oscillation periods as will be discussed below. Panels (c) to (f) then provide information about the southern open field intervals used to derive the phase data. Panel (c) indicates the duration Δt in days of each interval for which magnetic field phases are determined, while Panels (d) to (f) indicate the spacecraft location during each interval, with regard to radial distance (R_S), LT (hours), and latitude (deg), respectively. In the latter panels, the black dots correspond to the centre of each open field interval, while the vertical bars indicate the range of the parameter over the open field interval.

The centrally important result in Figure 5.5 is the clear banding of the magnetic

Figure 5.5: Plot showing results for the southern hemisphere region of open field lines, spanning the interval from $t = 950$ to 2057 days, corresponding to Revs 27 to 116 as shown by the bar at the top of the plot having the same format as in Figure 5.4. Panel (a) shows the magnetic oscillation phase values relative to the southern SKR modulation phase, plotted over two cycles between -180° and $+540^\circ$ so that each data point is plotted just twice. Phase data for the r , θ , and φ components are shown by the red, green, and blue symbols respectively, with vertical bars indicating the uncertainty in each measurement. The r and θ component phases are shown as measured, while since the φ component oscillations are in leading quadrature, 90° has been added to these values to bring them to a common phase with the r and θ component data. Piecewise linear fits to these phase data are shown by the black solid lines. Phase data included in these fits are shown by the coloured dots, while values excluded are shown by the crosses (no dots), as outlined in the text. Banding of the overall phase values is indicated in the histogram plotted vertically to the right of Panel (a), computed in 10° phase bins. The solid yellow lines in Panel (b) then show the southern (upper, longer) and northern (lower, shorter) hemisphere SKR periods, in hours, while the black lines show the magnetic field oscillation periods corresponding to the linear fits shown by the black solid lines to the phase data in Panel (a). Panel (c) indicates the duration (days) of the southern open field intervals employed to determine the magnetic field phases. Panels (d) to (f) then show corresponding spacecraft position data, specifically the radial distance (R_S), LT (hours), and latitude (deg), respectively. Black circles in the latter panels indicate the spacecraft position at the centre of each interval, while the vertical bars indicate the range of the relevant quantity over the whole interval employed in the determination of the magnetic field phases.

phase values about $\sim 180^\circ$ (modulo 360°) over the whole interval of the plot, spanning ~ 2.5 years. This implies that the magnetic field oscillations on southern open field lines are well organised by, and thus have a period very close to, that of the southern hemisphere SKR modulations. The banding is quantified by the histogram of phase values (including all field components) plotted vertically on the right of Panel (a) in 10° bins of phase. This shows that the phase values over the interval are strongly grouped about a peak in the 170° - 180° bin, with 88% of the data lying within the 80° phase range between 140° and 220° . The weighted mean of the phase data within the 0° - 360° range is 179° , with a standard deviation of 44° . In these and subsequent related values, the data are weighted according to the inverse of the estimated uncertainties.

With regard to the relationship between the field oscillations and the SKR modulation implied by these results, we note from equation (5.1) that at SKR modulation maxima (i.e. at times t when $\Phi_{SKRn,s}(t) = 360N$, where N is any integer), the maximum in field component i occurs at azimuth $\varphi_{\max i}$ given (to modulo 360°) by

$$\varphi_{\max i} = -\psi_{Min,s}. \quad (5.4)$$

The mean ψ_{Ms} value of 179° and standard deviation of 44° found here with respect to the southern SKR phase thus implies that at southern SKR maxima the effective southern hemisphere transverse dipole (in phase with the r component, see Figure 5.1c) points towards azimuth $-179^\circ \pm 44^\circ$ (or equivalently $+181^\circ \pm 44^\circ$), i.e. on average tailward and slightly towards dawn at a local time of 0.1 ± 2.9 h. We note that a similar result has been obtained previously for the core region oscillations by *Andrews et al.* [2008] and *Provan et al.* [2009a], who found that the quasi-uniform field in this region points radially outward at a local time of 2 ± 2 h at southern SKR maxima. As mentioned in section 5.1, these results thus imply approximate in-phase behaviour of the r and θ component oscillations between the core and the southern open field region (and with each other), and anti-phase behaviour of the φ component in these regions (being in leading quadrature with r and θ on southern open field lines, and in lagging quadrature in the core). These relationships, in agreement with *Provan et al.* [2009a], will be examined in greater detail using our full data set in section 5.3.3 below.

We now consider the results in Figure 5.5 in more detail, noting that the phase data fall into three main sets, as indicated previously in Figure 5.4. The first set, marked ‘A_S’ in the figure and delimited by vertical dotted lines, corresponds to the first high-latitude mission interval between October 2006 and March 2007 (Revs 30-41), previously studied by *Provan et al.* [2009a]. In this case the open field intervals have durations of ∼1-3 days, located at radial distances of ∼10-20 R_S in the dawn and dayside sector of the magnetosphere, from which reliable phases can generally be obtained from the filtered data for all three field components. These magnetic phase data exhibit a slow decrease in value across the ∼150 day interval of the data, very similar to the results derived previously by *Provan et al.* [2009a] with respect to the *Kurth et al.* [2008] southern SKR modulation phase model, as expected from the discussion of Figure 5.2b in section 5.2.2. The decreasing phase values are indicative of a small difference in the magnetic and SKR oscillation periods with the magnetic period being shorter than the SKR period. We quantify this difference using a weighted linear least-squares fit to these data given by

$$\psi_{Ms}(t) = \psi_{Ms0} + \psi_{Ms1} t, \quad (5.5)$$

shown by the black solid line in interval A_S in Figure 5.5a. The corresponding period of the magnetic oscillations is then given by

$$\tau_M(t) = \frac{360}{\frac{d}{dt}(\Phi_{SKRs}(t) - \psi_{Ms}(t))} \approx \tau_{SKRs} \left(1 + \frac{\psi_{Ms1} \tau_{SKRs}}{360}\right). \quad (5.6)$$

where all phases are expressed in degrees. The phase gradient of the fit is $\psi_{Ms1} = -0.760 \pm 0.014 \text{ deg day}^{-1}$, and since $\tau_{SKRs} \approx 10.83 \text{ h}$ during this interval (Figure 5.5b), we find from equation (5.6) that the magnetic oscillation period is shorter than the southern SKR modulation period by ∼37 s. The value of $\tau_M(t)$ given by equation (5.6) is plotted as the black line during interval A_S in Figure 5.5b, essentially representing the southern SKR period reduced by this amount. It is evident that the magnetic period is still close to the southern SKR period, and far removed from the period of the northern SKR modulations. An oscillation at the northern period would result in a negative phase gradient relative to the southern SKR phase of ∼15-20 deg day⁻¹, a factor of ∼25 larger than that found here during interval A_S.

The second set of southern hemisphere open field phase data, marked ‘B_S’ in Figure 5.5, was obtained between June and November 2008 (Revs 74-94) during the first part of the second high-latitude mission interval. These measurements were obtained from shorter ~ 0.5 day intervals, at smaller $\sim 5\text{-}10 R_S$ radial ranges, while again spanning dawn between midnight and mid-morning local time. Phase values are determined from the φ component only (due to ring current effects in the r and θ components), and exhibit significantly larger scatter and correspondingly larger uncertainties than in interval A_S. Nevertheless these data are still distinctly banded in phase over a similar range of phases as in interval A_S. They also form a near-continuous series of measurement with those from the third set of southern hemisphere phase data, marked ‘C_S’ in Figure 5.5. These were obtained between November 2008 and June 2009 (Revs 95-112), during the second part of the second high-latitude mission interval. Similar to interval A_S, these measurements were obtained from longer $\sim 1\text{-}3$ day intervals at $\sim 10\text{-}20 R_S$ radial distances, centred in the post-midnight sector (see, e.g., Figure 5.3 for Rev 95). These data again produce relatively un-scattered phase measurements from all three field components, with near-constant values around $\sim 180^\circ$ over the whole interval. A linear fit to the data in intervals B_S and C_S, shown by the black solid line in Figure 5.5a, has a phase gradient of $\psi_{Ms} = +0.211 \pm 0.004 \text{ deg day}^{-1}$. From equation (5.6) this implies an oscillation period that is ~ 26 s longer than the southern SKR modulation period, as shown by the corresponding black line in Figure 5.5b.

We note that in this and other related least-squares linear fits to the phase values, significant outliers in the modulo- 360° data are present, which necessitates the use of a robust fitting algorithm. Here we have employed the iterative RANSAC algorithm with an outlier ‘threshold’ of 90° [Fischler and Bolles, 1981], such that noticeably discrepant points do not influence the least-squares parameters. Further details are provided in Appendix A. Outliers removed in this way are indicated by appropriately coloured crosses in Figure 5.5a (i.e. points with no central dot), though all the data are shown in the adjacent histogram. Typically this results in the removal of $\sim 3\text{-}7$ points from the fits in each interval ($\sim 7\%$ of the total), depending on the scatter in the data, though none were removed from the less scattered data in interval A_S.

The data in Figure 5.5 thus principally demonstrate that the magnetic field oscillations on southern open field lines are closely tied to the southern hemisphere SKR modulations, with $\sim 88\%$ of the phase data lying within a $\sim 80^\circ$ band of phase centred near $\sim 180^\circ$. We note that an overall phase difference of at most $\sim 80^\circ$ over a ~ 2.5 year interval indicates that the two periods differ on average by at most ~ 4 s (i.e. by at most $\sim 0.01\%$). Nevertheless, it is also seen that extended intervals of near-monotonic phase drift can also occur, both positive and negative, indicative of differences in period over such shorter intervals of a few tens of seconds as indicated above. Given the intermittent nature of the southern hemisphere magnetic phase determinations available, the question then arises of how long each of these intervals can last, and thus how large the overall ‘slip’ in phase can become. The data in Figure 5.5 suggests durations of at least ~ 200 days, with overall ‘slips’ of at least $\sim 90^\circ$. We will return to this issue in the following section where measurements of the magnetic oscillation phase in the core region are presented. As mentioned above and in section 5.1, the previous results of *Provan et al.* [2009a] indicate that the r and θ component oscillations are in phase between the core and southern open field lines, while the φ component oscillations are in anti-phase, such that we should expect agreement and continuity between the core oscillation phase data and the southern hemisphere open field phase data presented here.

5.3.3 Closed field core region

Results for the core region of the magnetosphere (dipole $L \leq 8$) are shown in Figure 5.6 in the same format as Figure 5.5, except that the plot now extends over the full interval considered here from $t = 100$ to 2057 days as shown previously in Figure 5.4, spanning SOI to Rev 116. In conformity with the discussion in section 5.1 concerning a rotating quasi-uniform field in this region following the results of *Andrews et al.* [2008] and *Provan et al.* [2009a] (Figures 5.1a and 5.1b), the r and θ component phase data in Figure 5.6a are again shown as measured, while 90° has now been subtracted from the φ component data to bring them to a common phase (as opposed to 90° being added

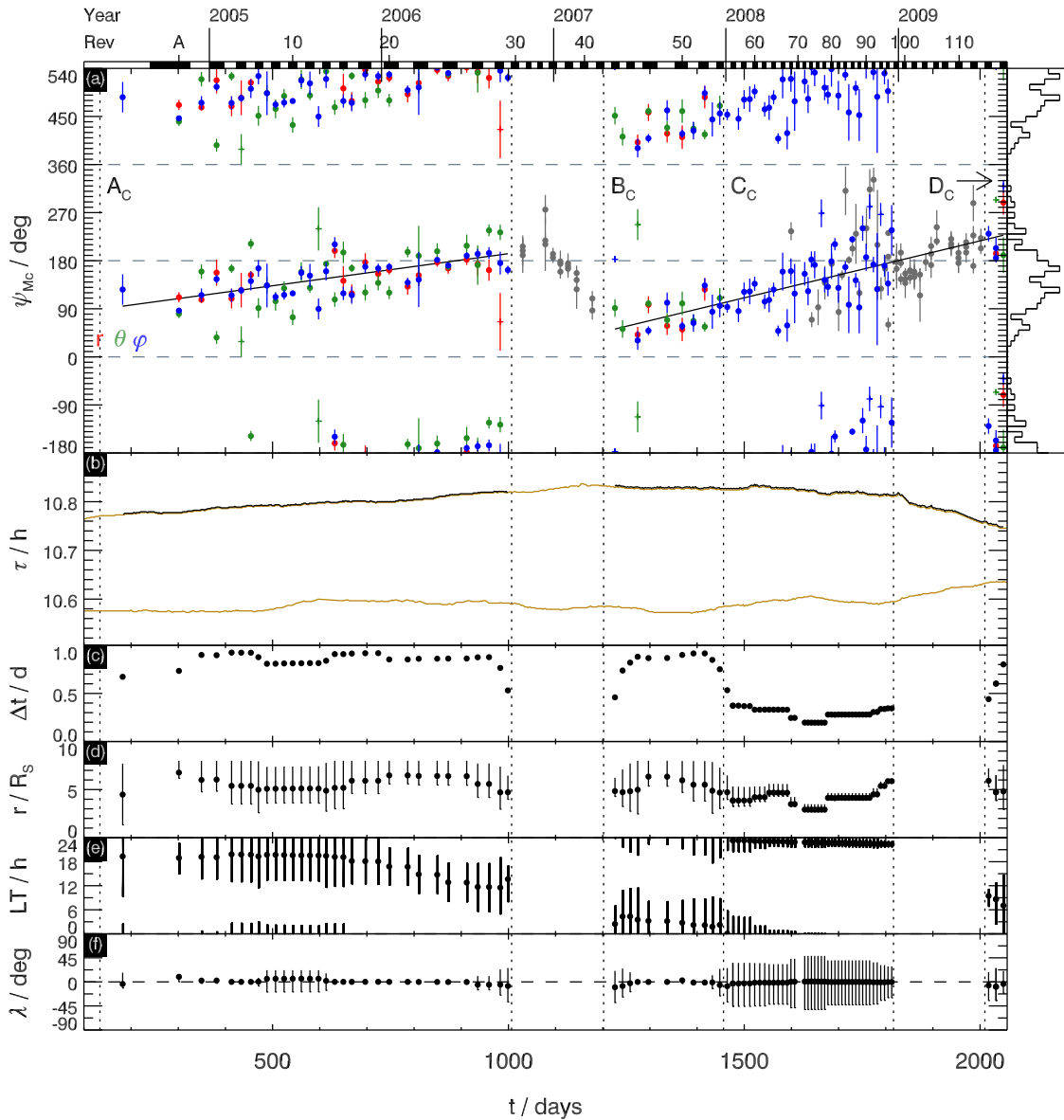


Figure 5.6: Plot showing oscillation phase results for the core region of closed field lines in a format similar to Figure 5.5, but now spanning the full interval of the study from $t = 100$ to 2057 days as in Figure 5.4. The r (red) and θ (green) component phases are shown as measured as in Figure 5.5, while since the φ (blue) component oscillations are in lagging quadrature, 90° has been subtracted from these values to bring them to a common phase with the r and θ component data. In addition, phase values for the southern hemisphere open field region shown in Panel (a) of Figure 5.5 are re-plotted in Panel (a) here as gray symbols for comparison with the core region data shown by the coloured symbols.

in Figure 5.5), in anticipation of the lagging quadrature of these oscillations. It can be seen that the phases so plotted again have common values for all the field components throughout, thus confirming the expected polarisation. In addition, in order to readily examine the relationships between these phase data and those obtained on southern hemisphere open field lines, we have re-plotted the phase data from Figure 5.5 as gray symbols in Figure 5.6a, though of course these data are not included in the core phase statistics discussed below.

Once more, the principal result for the core region is that the phase data in Figure 5.6a are clearly banded in phase throughout the ~ 5 years of the study, showing that the averaged period of the dominant oscillations in this region is very close to that of the southern SKR modulations. This is again demonstrated by the histogram plotted to the right of Figure 5.6a, in which $\sim 73\%$ of the data fall within the 110° band between 90° and 200° , centred on 145° . The weighted average of the 0 - 360° data is 147° , with a standard deviation of 55° . An overall phase difference of at most $\sim 110^\circ$ over the ~ 5 -year interval now implies an averaged difference in period between the core field oscillations and the southern SKR modulations of at most ~ 3 s, again corresponding to $\sim 0.01\%$. From equation (5.4), the mean value of the phase and the standard deviation imply that at southern SKR maxima the quasi-uniform equatorial field points radially outward at azimuth $-147^\circ \pm 55^\circ$ or equivalently $+213^\circ \pm 55^\circ$, corresponding to a LT of 2.2 ± 3.7 h, consistent with the previous results of *Andrews et al.* [2008] and *Provan et al.* [2009a] mentioned in sections 5.1 and 5.3.2 above. The phase data in Figure 5.6a also demonstrate a close correspondence between the phases of the oscillations in the core region and those on southern open field lines. Together, they provide evidence of slow secular changes in the relative phase over the interval, both positive and negative within the above overall limits, indicative of extended intervals in which small differences in the magnetic and southern SKR oscillation periods occur, as will be quantified below.

Thus examining the core region data in somewhat more detail, we note that in this case the data can be divided into four sets according to the overview shown in Figure 5.4. The first two, labeled ‘ A_C ’ and ‘ B_C ’ in Figure 5.6 (Revs SOI to 29 and 43

to 54, respectively), correspond to the first two near-equatorial orbit phases of the Cassini mission studied by *Andrews et al.* [2008] and *Provan et al.* [2009a], in which the spacecraft made \sim 1 day passes through the core region (as defined here), centred in the dusk and dayside sector for interval A_C , and in the post-midnight sector for interval B_C . Relatively un-scattered phase values can generally be obtained from the filtered data for all three field components. The third set, labeled ' C_C ' in Figure 5.6 (Revs 55 to 97), corresponds to the first part of the second high-latitude phase of the mission, in which the spacecraft made rapid north-south transits through the near-midnight core region at radial distances of \sim 4-5 R_S , as illustrated in Figure 5.3 for Rev 95, from which more scattered phase values have been obtained from unfiltered φ component data only. Nevertheless, these data are still clearly banded in phase, and are consistent with, and continue the trend of the phase data in near-equatorial interval B_C . The fourth set, labeled ' D_C ' in Figure 5.6 (Revs 114 to 116), then corresponds to three Revs at the end of the second high-latitude mission phase as the spacecraft returned to lower latitudes.

Overall, the core phase data for intervals A_C and B_C - D_C both show slow upward drifts with time over a similar band of phase values. This drift occurs over an interval of \sim 700 days during interval A_C , in conformity with the prior results of *Andrews et al.* [2008] and *Provan et al.* [2009a], and over \sim 800 days during intervals B_C - D_C . Individual linear fits to these data, shown by the black lines in Panel (a) of Figure 5.6, yield gradients of $\psi_{Ms1} = +0.120 \pm 0.002 \text{ deg day}^{-1}$ and $\psi_{Ms1} = +0.213 \pm 0.002 \text{ deg day}^{-1}$, respectively, implying that the magnetic oscillations have a slightly longer period than that of the southern SKR modulations, by \sim 6 and \sim 10 s, respectively. These differences are barely perceptible in the separation between the black and southern period yellow lines in Figure 5.6b.

We now compare these core region data with the southern hemisphere open field phase data re-plotted as the gray symbols in Figure 5.6a. Despite the fact that the averaged values of these two data sets differ by 32° (147° for the core region data and 179° for the southern hemisphere data), it can nevertheless be seen that these data sets agree closely with each other over the interval, and together form a continuous set of combined data. Specifically, the rapidly-falling phase data from southern open field

interval A_S clearly span across the gap between core intervals A_C and B_C , joining the higher phase values at the end of interval A_C to the lower phase values at the start of interval B_C . Similarly, the simultaneous core and southern open field data corresponding to intervals B_S and C_S , though with considerable scatter, both show similar rising trends over the same range of phase values, while the subsequent southern data from interval C_S are seen to continue this rising trend towards the few core field data points in interval D_C . We note that the two separate linear fits to the southern data from the combined intervals B_S and C_S and the core data from combined intervals B_C – D_C are highly comparable, having identical gradients ($\psi_{Ms1} = +0.211 \pm 0.004 \text{ deg day}^{-1}$ and $\psi_{Ms1} = +0.213 \pm 0.002 \text{ deg day}^{-1}$) and intercepts ($\psi_{Ms0} = 149 \pm 8^\circ$ and $\psi_{Ms0} = 151 \pm 4^\circ$, respectively), within determined errors.

This close correspondence between the two data sets thus confirms the phase relationship between the dominant oscillations in the core region and the field oscillations on southern hemisphere open field lines over this interval, with r and θ component oscillations in phase and φ component oscillations in anti-phase, with both data sets showing slow drifts in phase relative to the southern SKR modulations that are clearly linked. The modest 32° difference in the mean phases of these data sets noted above thus appears to be related to the specific intervals over which these data were obtained relative to the long-term drifts. Combining the data sets yields an overall mean phase value of 157° and a standard deviation of 54° , which we suggest form the best overall estimates of the mean phase and its range for the core region and southern open field region taken together, relative to the southern SKR phase. These values imply that at southern SKR maxima the core region quasi-uniform field and effective southern open region transverse dipole point radially outward at 1.5 ± 3.6 h LT. We also note that a phase shift between these magnetic oscillations and the southern SKR modulations of at most $\sim 110^\circ$ during the ~ 5 years of the study implies an overall difference in period of at most ~ 3 s (i.e. 0.01% of the period).

It should be noted, however, that the above $\pm 54^\circ$ ‘uncertainty’ estimate in the relative phase is not simply due to scatter in the magnetic phase measurements, but that the systematic phase drifts evident in Figure 5.6 also provide a significant

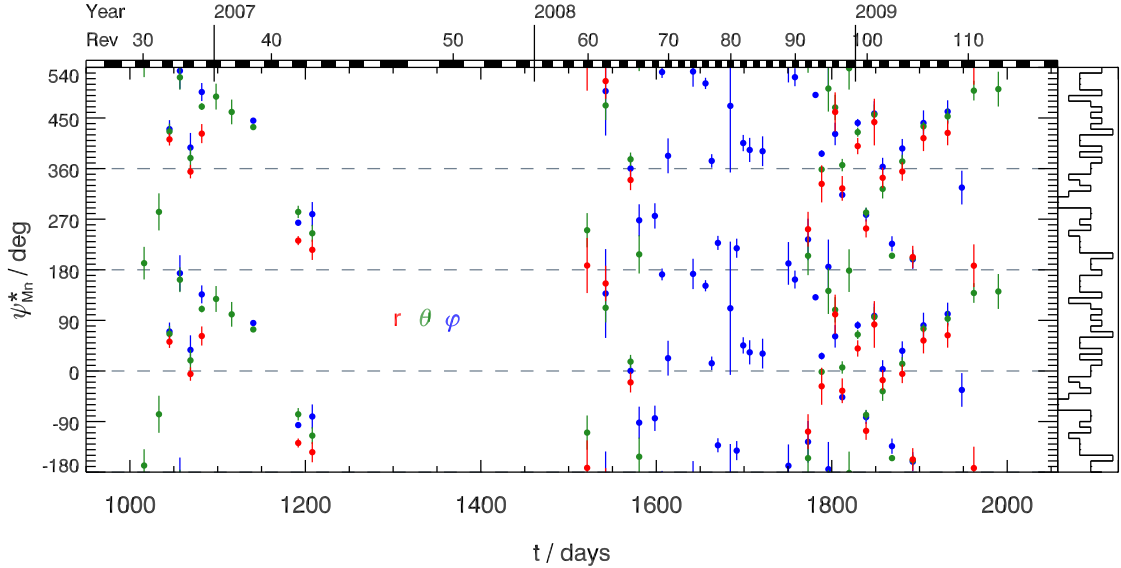


Figure 5.7: Plot showing the magnetic oscillation phases on northern hemisphere open field lines relative to the southern hemisphere SKR modulation phase, in a similar format and over the same interval as Panel (a) of Figure 5.5. The r (red) component phases are shown as measured, while 90° has been added to the leading quadrature φ (blue) component data, and 180° to the anti-phase θ (green) component data, to bring them to a common phase with the r component data, as seen in the plot. Corresponding ancillary data are shown in Figure 5.8.

contribution. These drifts take the form of two slow rises in phase with gradients of ~ 0.120 and $\sim 0.213 \text{ deg day}^{-1}$ each over ~ 800 days, thus spanning $\sim 100^\circ$ and $\sim 180^\circ$, joined by a more rapid decrease of $\sim 150^\circ$ over ~ 200 days occurring principally during the first high-latitude mission interval. Fitting some suitable curve through these data in future work would yield an overall core and southern hemisphere magnetic phase model with significantly reduced relative scatter in the data points. The origin of these phase drifts is studied in Chapter 6.

5.3.4 Northern hemisphere open field lines

We now turn to the oscillations on open field lines in the northern hemisphere, and, given the above results, we first examine whether the phases of these oscillations are also ordered by the southern hemisphere SKR modulation phase, as was (in effect) investigated previously by *Provan et al.* [2009a]. In Figure 5.7 we show these results in the same format and over the same restricted interval covering the two high latitude mission phases as employed for the corresponding southern hemisphere results in

Figure 5.5a (ancillary position data is shown later in Figure 5.8). In anticipation of the planet-centred rotating dipole polarisation found by *Provan et al.* [2009a], while the phase of the r component data is again shown as measured, as in Figures 5.5 and 5.6, in this case 90° has been added to the phase of the φ component (in leading quadrature with r for a rotating transverse dipole), and 180° to the phase of the θ component (in anti-phase with r in the northern hemisphere for a rotating transverse dipole), to bring all the phase data to a common value (see Figures 5.1c and 5.1d). It can be seen that these shifts generally do bring the phase data successfully together for each Rev, thus confirming the polarisation results of *Provan et al.* [2009a] for this larger northern data set.

It can also be seen in Figure 5.7 that the data corresponding to the first high-latitude mission interval (Revs 30 to 43) are somewhat grouped in phase, as reported by *Provan et al.* [2009a], though comparison with Figures 5.5 and 5.6 shows that they are not continuous with the southern hemisphere and core data, as would be expected, for example, if the northern field oscillations were due to the same effective rotating transverse dipole as observed in the south (which would give r component oscillations in the two hemispheres in phase throughout). Furthermore, the later data newly examined here (Revs 60–112) show no consistent banding in phase, as is clearly evident in the histogram shown on the right of the plot, which indicates instead that the data overall are distributed almost uniformly across a complete cycle. We thus conclude that the grouping previously reported by *Provan et al.* [2009a] is essentially accidental, and that there is no overall organisation of the northern open region oscillation phases by the southern SKR modulation phase.

We thus consider instead whether the northern open field phase data are organised by the northern SKR modulation phase, noting that such organisation is not inconsistent with the scattered results with respect to the southern SKR phase seen in Figure 5.7. As indicated in section 3.1, the phase of an oscillation at the northern SKR period shifts by $\sim 15\text{--}20 \text{ deg day}^{-1}$ relative to the phase of the southern SKR period (and vice versa), leading to Rev-to-Rev shifts in phase of a large fraction of a full cycle over the 10–20 day intervals between Revs. Consistent shifts of such magnitude are

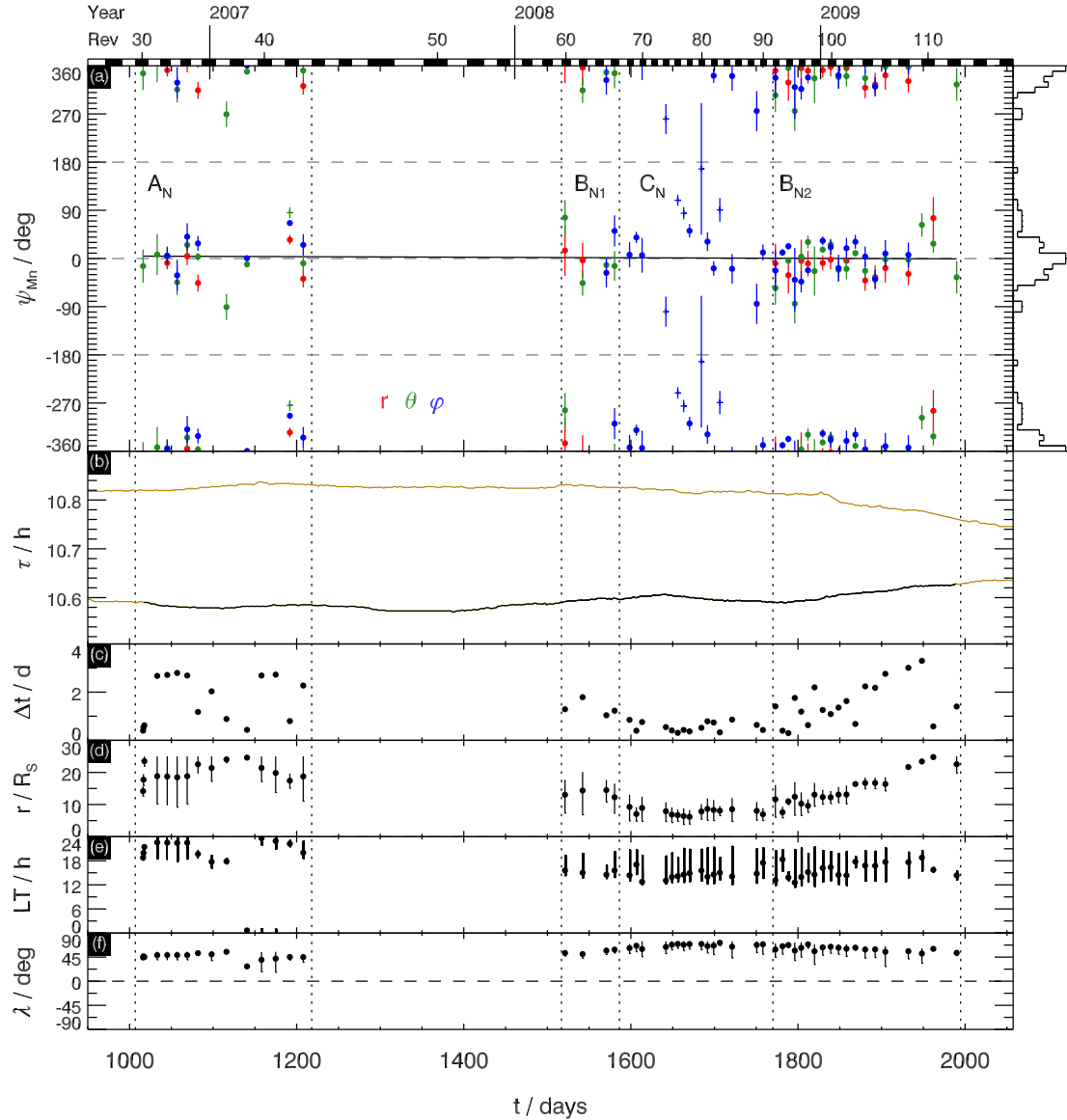


Figure 5.8: Plot showing the magnetic oscillation phases on northern hemisphere open field lines relative to the northern hemisphere SKR modulation phase, in a similar format and over the same interval as Figure 5.5. As in Figure 5.7, the r (red) component phases are shown as measured, while 90° has been added to the leading quadrature φ (blue) component data, and 180° to the anti-phase θ (green) component data, to bring them to a common phase with the r component data. We also note that in Panel (a) we have shifted the two-cycle phase range to between -360° and $+360^\circ$ in order to centrally accommodate the banded phase data.

not discernible in Figure 5.7. We note that if the southern hemisphere open field data or core region data shown in Figures 5.5 and 5.6 are similarly analysed relative to the northern SKR phase, the results (not illustrated here) also show scattered behaviour similar to that in Figure 5.7.

In Figure 5.8 we thus show the phases of the magnetic field oscillations on northern

hemisphere open field lines relative to the northern SKR modulation phase, in a similar format, and over the same interval, as in Figures 5.5 and 5.7. The phase shifts applied to the individual component data to bring them to a common value are the same as indicated above for Figure 5.7, corresponding to a planet-centred rotating transverse dipole, with the r component phase (having the same phase as the effective transverse dipole) being as measured. It can be seen that the phase data are now strongly banded, with 76% of the data lying in the 90° phase band between -50° and $+40^\circ$ centred near 0° . We note that, compared with previous related figures, we have shifted the two-cycle phase range in Figure 5.8a to between -360° and $+360^\circ$ in order to centrally accommodate these banded data. This result then demonstrates that the period of the northern magnetic field oscillations is closely similar to that of the northern SKR modulation, with a phase difference of at most $\sim 90^\circ$ over the ~ 3 year interval implying an overall difference in period of at most ~ 4 s (i.e. $\sim 0.01\%$).

With regard to the value of the phase in Figure 5.8, we note that the weighted average phase of the -180° to $+180^\circ$ data is 6° , with a standard deviation of 36° . Recalling from equation (5.4) that the effective dipole, in phase with the r component, points towards azimuth $-\psi_{Mn}$ at northern SKR maxima, the latter result implies that the northern dipole points sunward on average and slightly towards dawn, at 11.7 ± 2.4 h LT, at northern SKR maxima. Thus while the southern-period quasi-uniform field and high-latitude effective dipole point down-tail (and towards dawn) at southern SKR maxima, the northern-period high-latitude effective dipole points sunward (and also slightly towards dawn) at northern SKR maxima.

As with the southern hemisphere open field and core regions examined above, the phase data for the northern hemisphere open field region can again be divided into three groups with differing characteristics depending on the nature of the Cassini orbit, as overviewed in Figure 5.4. The first group marked ‘ A_N ’ in Figure 5.8 (Revs 30–43) corresponds to the first high-latitude mission phase previously studied by *Provan et al.* [2009a]. This contains extended ~ 1 – 3 day passes through the northern open region at radial distances in the range ~ 10 – 25 R_S centred in the pre-midnight sector, from which phase data can generally be obtained for all three field components.

The second and third groups correspond to the second high-latitude mission phase shown in Figure 5.4. These data can broadly be divided into earlier and later intervals marked ‘ B_{N1} ’ and ‘ B_{N2} ’ (Revs 60-66 and 92-112) consisting of \sim 1-2 day passes at radial distances \sim 10-20 R_S , from which phase data can again generally be obtained for all three field components (see Figure 5.3 for Rev 95), and a central interval marked ‘ C_N ’ (Revs 68-90) consisting of short \sim 6-24 h passes at radial distances of \sim 5-10 R_S , from which more scattered data can be obtained only from the φ component. The data for intervals B_N and C_N all span the post-noon and dusk sector in local time. It is thus seen that the nature of the northern open field data are similarly variable as for the southern open field and core region data. Nevertheless, the results in Figure 5.8 indicate that these form an apparently featureless data set (assuming the variability in interval CN is mainly due to scatter), with little indication of significant long-term drifts in phase over the \sim 2.5 year interval covered like those seen in Figures 5.5 and 5.6. In particular, the weighted average of the phase data for well-separated intervals A_N and B_{N2} are 8° (with a standard deviation of 36°) and -1° (with a standard deviation of 25°), respectively, thus being essentially consistent with each other within the uncertainties. If we then make a weighted linear fit to all these data, shown by the black solid line in Panel (a) of Figure 5.8, we find an overall gradient of only $-0.005 \pm 0.001 \text{ deg day}^{-1}$. This corresponds to a difference in period between the northern open field oscillations and the northern SKR modulations of only \sim 0.2 s (i.e. 0.0005%), a difference which is not discernible in Figure 5.8b.

5.4 Summary and discussion

In this chapter we have made a first detailed investigation of the phase of the magnetic field oscillations near the planetary rotation period in Saturn’s magnetosphere relative to the phases of the separate northern and southern SKR emission modulations, as recently discovered by *Gurnett et al.* [2009a]. We have employed \sim 5 years of magnetic field observations spanning the interval from SOI in July 2004 during Saturn southern summer conditions, to Rev 116 in August 2009 close to vernal equinox, and have

compared the magnetic oscillation phases with the SKR modulation phases derived from X mode radio powers from the two hemispheres by *Lamy* [2011], as described in section 5.2.2. The results thus build on the previous related studies of *Andrews et al.* [2008] and *Provan et al.* [2009a] that examined earlier sub-sets of the magnetic data in relation to the dominant southern SKR modulations during this interval analysed by *Kurth et al.* [2007, 2008]. Here, following *Provan et al.* [2009a], we have examined the oscillations in three distinct magnetospheric regions, corresponding to the high-latitude northern and southern open field regions to radial distances of $25 R_s$, characterised by the lack of warm or hot plasma, and the quasi-dipolar core region of the magnetosphere within dipole $L \leq 8$, defined so as to exclude the magnetic signatures of field-aligned currents flowing near the boundary between open and closed field lines at all local times.

Our analysis demonstrates that there exists two systems of field oscillations in Saturn's magnetosphere associated with the two SKR periods. The oscillations on southern open field lines and in the quasi-dipolar core region take place near the southern SKR period of ~ 10.8 h, while the oscillations on northern open field lines take place near the northern SKR period of ~ 10.6 h. Maximum overall phase shifts between the magnetic field oscillations and the corresponding SKR modulations of $\sim 110^\circ$ over ~ 5 years in the first case, and $\sim 90^\circ$ over ~ 2.5 years in the second imply maximum overall differences in period of only $\sim 3\text{-}4$ s, corresponding to $\sim 0.01\%$ of the respective SKR periods. Concerning the nature of the oscillatory field, our results show that in the core region the southern-period perturbations take the form of a rotating quasi-uniform field in the equatorial plane, with the addition of a co-latitudinal field which is such that the perturbation field lines form arches with apices to the north. In other words, the φ component oscillates in lagging quadrature with the r component, while the θ component oscillates in phase with the r component, as shown previously by *Andrews et al.* [2008]. The corresponding oscillations on southern open field lines instead have the form of a planet-centred rotating transverse dipole, in other words, the φ component now oscillates in leading quadrature with the r component, while the θ component oscillates in phase with the r component, as shown previously

by *Provan et al.* [2009a]. The results derived here then show that the rotating quasi-uniform field in the equatorial region and the effective rotating transverse dipole on southern open field lines maintain approximately the same direction as each other over the ~ 5 years of our study. In other words, the r and θ components in the two regions oscillate in phase at the southern period, while the φ components in the two regions oscillate in anti-phase.

Overall, these results indicate that the southern-period perturbation field lines form loops passing through the equatorial region and closing at southern high latitudes, as sketched in Figure 5.9a. This shows fields in the principal meridian of the perturbation field at a given instant, as in Figure 5.1b and 5.1d, where the black dashed lines show the quasi-static ‘background’ magnetospheric field, with closed field lines at lower latitudes (gray region) and open field lines at high latitudes (clear region) mapping into the northern and southern polar regions. The perturbation field lines of the southern system at this instant are then indicated by the red solid lines, forming arches with apices to the north in the equatorial region, and closing over the southern pole in the southern region of open field lines. The effective centred transverse dipole corresponding to the latter field points to the left at the instant depicted in Figure 5.9a, approximately parallel to the near-equatorial field, as indicated by the central red arrow. To a first approximation the perturbation field lines out of the plane shown can then be obtained simply by displacing these field loops directly into or out of the plane of the figure. This perturbation field pattern then rotates in time approximately rigidly about the central axis at close to the southern SKR modulation period as indicated, giving rise to field oscillations with the relative polarisation found in this study. It should be emphasised, however, that although it is difficult to represent the true perturbation field geometry in a simple 2-D sketch, the intention here is to indicate that the equatorial quasi-uniform field region corresponds to the inner region of closed field lines, while the quasi-dipolar field which closes these field loops over the pole corresponds to the region of open field lines. The implied associated currents that flow between these regions will be discussed further below.

Our results for the northern-period oscillations on northern open field lines also

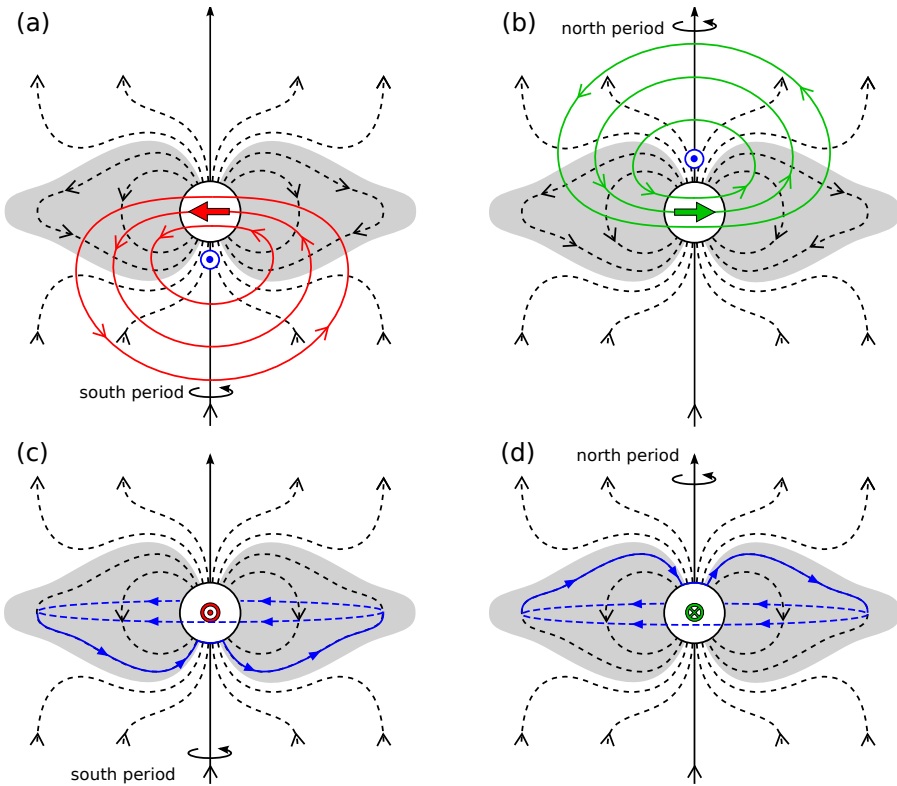


Figure 5.9: Sketches showing the form of the oscillatory perturbation fields deduced from the results of presented in this chapter, together with the implied current systems. Sketches (a) and (b) show the principal meridian of the perturbation at a given instant (as in Figures 5.1b and 5.1d), where the black dashed lines show the quasi-static ‘background’ magnetospheric field, with closed field lines at lower latitudes (gray region) and open field lines at higher latitudes (clear region) mapping into the northern and southern polar regions. The perturbation field lines are then indicated by the coloured solid lines, red for the southern system in Panel (a) and green for the northern system in Panel (b). To a first approximation the perturbation field lines out of the planes shown can be obtained simply by displacing the perturbation field loops directly into or out of the plane of the figure. The direction of the centred transverse dipole corresponding to the quasi-dipolar perturbation field in the open field region is shown by the solid arrow, while the sense of the current associated with the overall field perturbations given by Ampère’s law indicated by the blue symbols, directed out of the plane in both diagrams. The patterns shown correspond to SKR maxima when the Sun is on the right in both panels, such that at these times the associated current flows approximately from dusk to dawn. A more detailed view of the current systems associated with Panels (a) and (b) is given in Panels (c) and (d), respectively, where both Panels (a) and (b) are viewed from the left. Field-aligned and ionospheric currents flowing from left to right in each panel are indicated by the solid blue lines, while the return currents flowing from right to left through the equatorial region outside the quasi-dipolar equatorial magnetosphere are indicated by the dashed blue lines. These perturbation field patterns and current systems then rotate independently in time approximately rigidly about the central axis at close to the southern SKR period in Panel (a) and close to the northern SKR period in Panel (b), as indicated.

show that they have the form of a planet-centred rotating transverse dipole, such that the φ component oscillates in leading quadrature with the r component, while the θ component oscillates in anti-phase with the r component, as shown previously by *Provan et al.* [2009a]. The form of this field is shown by the green lines in the north polar region of Figure 5.9b, corresponding to an effective centred transverse dipole pointing to the right at the instant depicted as shown by the green arrow. If these perturbation field lines also close in the equatorial region equivalent to that shown for the southern-period oscillation in Figure 5.9a, the implication is that an additional northern-period field oscillation should also be present in the equatorial region as sketched in Figure 5.9b. These field oscillations would again have the φ component in lagging quadrature with r , as for the southern-period oscillations, but now the θ component would be in anti-phase with r , such that the equatorial field lines form arches with apices to the south. The presence of such oscillations, at amplitudes less than those of the southern-period oscillations, is by no means ruled out by the data analyses conducted to date, and indeed, may contribute to the considerable phase ‘jitter’ observed in this region in Figure 5.6 and noted in section 5.1 [*Andrews et al.*, 2008]³, in addition to that possibly produced by solar wind-related effects [*Zarka et al.*, 2007].

In addition to determining the form of the oscillatory fields, our results also determine the phase between the magnetic oscillations and the corresponding SKR modulations. In agreement with the previous results of *Andrews et al.* [2008] and *Provan et al.* [2009a], we find from our combined core and open-field region results that at times of southern SKR maxima, the southern-period quasi-uniform equatorial field and the high-latitude southern effective transverse dipole point tailward and on average towards dawn, i.e. radially outward at 1.5 ± 3.6 h LT. However, we find that the corresponding high-latitude northern effective transverse dipole and suggested secondary equatorial field point sunward and also on average slightly towards dawn at northern SKR maxima, i.e. radially outward at 11.7 ± 2.4 h LT. Thus our results indicate

³*Provan et al.* [2011] subsequently investigated this in detail, and concluded that the phase jitter observed in the equatorial region is indeed the result of the superposition of two systems of field oscillations with different periods, corresponding to those of the northern and southern SKR emissions.

that the perturbation fields of the northern system at northern SKR maxima point essentially opposite to the perturbation fields of the southern system at southern SKR maxima. The implications of this for the associated current systems will be discussed further below.

While the above description forms a basic picture of the magnetic field oscillations determined in our study, more subtle effects are also evident. In particular, in common with the results of *Andrews et al.* [2008] and *Provan et al.* [2009a], we find that slow variations in the phase of the southern-period oscillations are evident relative to the phase of the southern SKR modulations, which appear to be present as a consistent phenomenon in both the core region and on southern open field lines. Over the 5-year interval of this study, these take the form of two slow increases in the magnetic phase relative to the southern SKR phase over intervals of ~ 800 days, separated by a shorter ~ 200 day interval of more rapid decrease, which is such that the increases on either side cover much the same range of relative phase values in each case. Slow increases in the magnetic phase indicate that the period of the magnetic oscillations is slightly longer than those of the corresponding SKR modulation, and vice versa for slow decreases in the magnetic phase. It should be emphasised, however, that the implied differences in period are small, certainly when compared with the ~ 10 min difference in period between the southern and northern oscillations (and the secular variations in period observed in both). Specifically, the positive phase gradients during the two slow increases in phase seen in Figure 5.6 of ~ 0.120 and ~ 0.213 deg day $^{-1}$ imply differences in period of only ~ 6 and ~ 10 s (i.e. ~ 0.02 and $\sim 0.03\%$ of the southern period), while the negative phase gradient during the interval of more rapid phase decrease that occurs between of ~ -0.760 deg day $^{-1}$ implies a difference in period of 37 s (i.e. $\sim 0.10\%$ of the southern period). We note that the overall peak-to-peak ‘slip’ in the relative phase associated with this phenomenon is $\sim 150^\circ$, this effect being a significant contributor to the error estimate (standard deviation) quoted above for the direction of the equatorial quasi-uniform field and southern transverse dipole at southern SKR maxima. Results for the northern-period oscillations, however, indicate that the relative phase drifts are significantly smaller than for the southern-period

system, with no long-term trends with magnitudes larger than $\sim 0.1 \text{ deg day}^{-1}$ being discernible throughout. In the following chapter we discuss the possibility that these phase drifts are not in fact reflective of small differences between the periods of the magnetic oscillations and the SKR modulations, but rather arise as a consequence of ‘rotational modulation’ of the SKR (rather than the hitherto assumed ‘strobe-like’ modulation).

With regard to the origins of the magnetic field effects investigated here, our results clearly indicate the presence of two physically distinct current systems that rotate with different periods in the two hemispheres. This is already evident in Figures 5.9a and 5.9b, where Ampère’s law applied to the perturbation field loops imply rotating currents which flow out of the plane of the diagram in both cases at the instants depicted, as indicated very schematically by the blue symbols shown in those figures. The current systems envisaged are indicated in more detail in Figures 5.9c and 5.9d, which correspond to Figures 5.9a and 5.9b, respectively, each viewed from the left. Following the prior discussions of *Southwood and Kivelson* [2007] and *Provan et al.* [2009a], we envisage the presence of field-aligned currents flowing from left to right in both cases as shown by the blue solid lines, located in the interface between the regions of quasi-uniform and quasi-dipolar oscillatory perturbation field, and passing centrally through the polar ionosphere. These currents then reach the equatorial plane on outer closed field lines, bounding the region occupied by the rotating quasi-uniform field to the central quasi-dipolar (core) region of the magnetosphere, within equatorial radial distances of $\sim 15 R_S$ according to the results presented in Chapter 4. These currents must then close in the equatorial magnetosphere beyond the core region, as indicated schematically by the dashed blue lines. It may be noted that these overall current systems indeed have a magnetic moment in the sense depicted in Figures 5.9a and 5.9b, as also indicated by the red and green symbols in Figures 5.9c and 5.9d. The current systems in the two hemispheres then rotate independently with different periods, giving rise to oscillations dominated by the corresponding period at high-latitudes on open field lines, while potentially superposing in the equatorial region as sketched in Figures 5.9a and 5.9b. Our results show, however,

that the southern-period current system and related oscillations are dominant in the core region throughout the pre-equinox southern summer interval investigated here, perhaps due to higher conductivities and currents in the southern summer ionosphere. We may then speculate that dominance could shift to northern-period oscillations in the equatorial region some time post-equinox. Continued study of the post-equinox oscillations will undoubtedly yield further insight into the origins of these phenomena.

As was indicated in sections 2.8 and 5.1, SKR emissions are believed to be generated by accelerated auroral electrons via the cyclotron maser instability, and may thus be expected to be associated both with the UV auroral oval [Lamy *et al.*, 2009] and regions of strong upward-directed field-aligned current [Lamy *et al.*, 2010]. The implications of the phasing of the magnetic oscillations in the two hemispheres with respect to the SKR modulations is then such that the SKR emission maxima in both cases occur when the rotating upward-directed field-aligned current region passes through the dawn sector in the two hemispheres, due possibly to an interaction between the rotating current systems discussed here and quasi-static currents set up e.g. by the solar wind interaction with the magnetosphere [Galopeau *et al.*, 1995; Cecconi and Zarka, 2005; Southwood and Kivelson, 2009]. The senses of the perturbation fields and currents in Figure 5.9 thus show the condition for SKR maxima in the two hemispheres if the Sun is located to the right in each in Figures 5.9a and 5.9b, and into the plane of the plots in Figures 5.9c and 5.9d. The region of downward-directed field-aligned current on the opposite side of the planet then plausibly forms the rotating source of upward-directed auroral hiss, in agreement with the phasing of the latter in the two hemispheres reported by Gurnett *et al.* [2009b]. We also note that the periodic oscillations of the plasma sheet in the outer magnetosphere and tail, discussed previously in terms of the effect of a rotating transverse dipole formed by a rotating external current system [e.g., Southwood and Kivelson 2007, Provan *et al.* 2009a; Chapter 4 of this thesis], must now be augmented to include two effective transverse dipoles that rotate with differing periods, whose absolute and relative strengths may plausibly depend on Saturn's seasons. Such considerations may then provide an explanation for the

dual periodicity in the fluxes of energetic electrons in Saturn's outer magnetosphere reported by *Carbary et al.* [2009b].

We finally note that while the rotating quasi-uniform field in the core region, directed approximately transverse to the equatorial planetary field, produces both tilting of the field lines and rocking of the magnetic equator as just indicated, the oscillations in the co-latitude field component, near-parallel to the equatorial planetary field, are instead associated with rotating changes in the field strength. Related rotating changes in the plasma pressure are also known to occur, as indicated by the studies of *Burch et al.* [2009] and *Carbary et al.* [2009a, 2010a], that must combine with the field pressure changes to cause rotating changes in the total pressure that modulate the positions of both the magnetopause and bow shock [*Clarke et al.*, 2010a,b]. These latter studies relate specifically to southern-period oscillations that are dominant in the near-equatorial region during the pre-equinox interval analysed here, but in view of the results found here it seems reasonable to suppose that weaker pressure oscillations at the northern period are also simultaneously present. In addition to the transverse perturbations associated with rotating field-aligned currents, therefore, it thus appears that rotating compressional oscillations are also simultaneously present at the two periods. It remains to be determined how these oscillation systems are maintained at periods that not only differ from each other, but also from that of the sub-corotating and drifting plasma.

Chapter 6

Evidence in magnetic field phase data for rotational modulation of Saturn kilometric radiation emissions

6.1 Introduction

This chapter addresses the significant unresolved issue of the apparently variable secular drifts in the phase of the magnetic field oscillations relative to the SKR modulations. These drifts have been present in all previous studies, having magnitudes of $\sim \pm 0.1 - 1 \text{ deg day}^{-1}$ [Andrews *et al.* 2008; Provan *et al.* 2009a; Chapter 5 of this thesis], excepting in the newly analysed northern hemisphere open field data studied in Chapter 5, where the phase drift was consistent with zero. As has been previously stated, these drifts have hitherto been interpreted as representing a refined measurement of a common magnetic and SKR period [e.g., Andrews *et al.*, 2008], rather than representing a physical difference in the periods of the two systems. Here, we explore the hypothesis that these phase drifts can arise as a consequence of an underlying rotational modulation in the SKR, as yet undetected directly, combined with the restricted visibility of the SKR sources known to result from the mechanism through which the emission is generated.

As was discussed in section 2.8, the SKR was first observed by the Planetary Radio

Astronomy (PRA) experiments on the two Voyager spacecraft [Kaiser *et al.*, 1980]. Circularly polarised waves were found to be emitted from the two hemispheres of the planet, predominately right handed from the north and left-handed from the south, indicating emission in the extraordinary (X) mode [Warwick *et al.*, 1981, 1982]. The power of the emissions was found to be strongly modulated near the planetary rotation period, at a period of ~ 10.7 h, despite the lack of a measurable tilt in the internally-generated planetary magnetic field relative to the spin axis [Smith *et al.*, 1980; Connerney *et al.*, 1982]. Furthermore, the phase of these modulations was also observed to be unchanged between the inbound and outbound passes of the Voyager flyby trajectories, at LTs near noon and dawn respectively, thus indicating a ‘strobe-like’ (or ‘clock-like’) modulation independent of the position of the observer, rather than a rotating source like a lighthouse beam [Warwick *et al.*, 1981; Gurnett *et al.*, 1981]. Similar ‘strobe-like’ characteristics have also recently been found for lower frequency narrowband emissions in Saturn’s magnetosphere, occurring in lagging quadrature with the SKR modulations [Wang *et al.*, 2010; Ye *et al.*, 2010].

While the Voyager PRA instruments were not capable of directly locating the sources of the SKR emissions, these were inferred from various considerations of the beaming and visibility of the emissions along the spacecraft trajectories [Kaiser *et al.*, 1981; Kaiser and Desch, 1982; Lecacheux and Genova, 1983]. Assuming fixed sources emitting near the X-mode cut-off frequency (i.e. close to the local electron gyrofrequency) due to the cyclotron maser instability [Wu and Lee, 1979; Zarka, 1998], high-latitude auroral source locations were inferred in both hemispheres, extending typically from the mid-morning sector towards noon [Galopeau *et al.*, 1995].

As was discussed previously in section 2.8, subsequent studies have extended these initial results in two important respects. First, it has been shown, initially using Ulysses data and in more detail with Cassini, that the SKR modulation period varies slowly over time, typically by fractions of a percent over yearly intervals, much too large a rate to be associated directly with the rotation of the planet itself [Galopeau and Lecacheux, 2000; Gurnett *et al.*, 2005; Kurth *et al.*, 2007, 2008]. Moreover, it has also been demonstrated that the modulation periods corresponding to emissions from the northern and

southern hemispheres are distinctly different, ~ 10.6 h in the north and ~ 10.8 h in the south during the southern summer conditions that prevailed in the initial pre-equinox Cassini era, 2004–2009 [Gurnett *et al.*, 2009a, 2010b; Lamy, 2011]. Second, it has been shown from visibility considerations and use of the direction-finding capability of the Cassini Radio and Plasma Wave Science (RPWS) experiment [Gurnett *et al.*, 2004], that SKR emission sources are not confined to the dawn-to-noon sector [Farrell *et al.*, 2005; Cecconi *et al.*, 2009]. Rather, they are broadly distributed around a circumpolar oval in each hemisphere that is coincident with the UV auroral oval [Lamy *et al.*, 2009]. However, the emitted power strongly maximises in the mid-morning sector as found from Voyager results, where UV auroral emissions are also usually brightest [Trauger *et al.*, 1998; Clarke *et al.*, 2005; Grodent *et al.*, 2005; Gérard *et al.*, 2006]. Most recently it has been shown that the UV emission power in the dawn sector is also modulated near the planetary period, in phase with the SKR emissions from the corresponding hemisphere [Nichols *et al.*, 2010a]. Furthermore, and somewhat surprisingly, Lamy [2011] have recently shown that there is some evidence for a secondary component present within the SKR emission from the northern hemisphere which is modulated at the longer of the two periods, i.e. that more generally associated with the dominant southern hemisphere SKR modulation.

The finding of circumpolar auroral SKR sources raises the issue of whether these emissions are modulated near the planetary period at all points around the oval, and if so, how the modulation phase may depend on LT. We note in this regard that while the brighter UV emissions in the dawn sector are modulated in phase with the overall SKR power in each hemisphere as just indicated, the weaker UV emissions in the dusk sector are instead modulated in anti-phase with the overall SKR power [Nichols *et al.*, 2010a]. This result suggests that the UV emissions, and possibly the SKR emissions as well, do not vary in concert around the oval, but rather in anti-phase on opposite sides of the oval, at least between the stronger sources at dawn and the weaker sources at dusk. Initial evidence for rotating modulations of southern hemisphere SKR emissions has recently been obtained from direction-resolved Cassini radio data [Lamy, 2011].

Oscillations believed to be related to the SKR observed in the magnetic field,

plasma populations, magnetopause and bow shock locations, and the brightness and position of the auroral oval were discussed in section 2.8. In each of these phenomena, however, the perturbations rotate around the planet as an ‘ $m = 1$ ’ oscillation (thus varying with azimuthal angle φ as $e^{-jm\varphi}$), with a synodic period that is close to the SKR period. Magnetic field and auroral hiss modulations observed at high latitudes are found to have the same period as the SKR modulations in the corresponding hemisphere [Gurnett *et al.* 2009b, Chapter 5 of this thesis], while the oscillations in the equatorial region contain both periods [Provan *et al.*, 2011], but are dominated by the southern period during the pre-equinox intervals investigated in most of the above studies.

In this chapter we focus on the magnetic field oscillations near the planetary period observed in Saturn’s magnetosphere, the form of which was previously sketched in panels (a) and (b) of Figure 5.9 in the preceding chapter (section 5.4). Briefly recounting the discussion presented in section 5.4, the form of these perturbation fields, being quasi-uniform in the equatorial region and quasi-dipolar at high latitudes, suggests the presence of two independent auroral current systems that rotate in the two hemispheres with differing periods. At any instant, currents flow into the auroral ionosphere in one LT sector, around and/or across the oval, and out of the opposite LT sector, closing in the equatorial magnetosphere. The relative phasing of the magnetic oscillations is such that the southern period quasi-uniform equatorial field and effective high-latitude transverse dipole both point down-tail (and somewhat towards dawn) at southern SKR maxima, while the northern period quasi-uniform equatorial field and effective high-latitude transverse dipole both point sunward at northern SKR maxima. These configurations correspond to those shown in panels (a) and (b) of Figure 5.9 if the Sun is on the right in both cases, thus implying that SKR maxima in both hemispheres correspond to times at which the rotating currents flow out of the ionosphere in the dawn sector and into the ionosphere in the dusk sector. (See Chapter 5 for further details.) Enhanced upward currents in the dawn sector then provide favourable conditions for enhanced downward-directed auroral electron acceleration and UV emission in that sector consistent with the results of Nichols *et al.*

[2010a], together with enhanced SKR wave growth [Mutel *et al.*, 2010]. The dominance of the modulated UV and SKR emissions from the dawn sector may then result from the combination of this rotating current system with quasi-steady upward currents in this sector resulting from the solar wind interaction [Southwood and Kivelson, 2009]. Simultaneously enhanced downward currents in the dusk sector may then reduce auroral acceleration and UV emission in that sector, also consistent with Nichols *et al.* [2010a], together potentially with corresponding SKR emission. On the other hand, enhanced downward currents will tend to enhance auroral hiss emissions in the dusk sector during such intervals, produced by upward-moving electron beams, consistent with the results of Gurnett *et al.* [2009b]. The latter authors show that the rotating auroral hiss modulations maximise in the dusk sector in each hemisphere at the times of corresponding SKR maxima.

Overall, therefore, the existence of rotating magnetic perturbations implying the existence of rotating current systems in the two hemispheres also suggests the occurrence of rotating modulations in the SKR emissions, corresponding to (but in approximate anti-phase with) the rotating modulations in auroral hiss. If an observer could then in effect see all of the SKR emission sources at any instant, the combined modulations would correspond to those of the most intense sources in the mid-morning sector, giving a ‘strobe-like’ modulation overall whose phase is independent of the position of the observer, as reported by Warwick *et al.* [1981] and Gurnett *et al.* [1981]. However, in practice the visibility of the sources around the oval is strongly constrained by the beaming of the radiation, which is emitted from the ‘source surface’ near the corresponding electron gyrofrequency into an outward-facing hollow cone of angles around the field direction [Cecconi *et al.*, 2009; Lamy *et al.*, 2008a, 2009, 2010]. With a cone angle relative to the field of typically $\sim 70^\circ$ and an angular width of only $\sim 5^\circ$ about that direction, modelling and observations show that at typical near-equatorial spacecraft locations emissions near the peak in the SKR spectrum can only be observed from two narrow bands ~ 1 h LT wide around the oval, displaced $\sim 3\text{-}4$ h LT on either side of the spacecraft location [Cecconi *et al.*, 2009; Lamy *et al.*, 2008a, 2009]. This implies that the spacecraft can view the most intense SKR sources in the mid-

morning sector, in one or other of these two azimuthal ‘windows’, only over a relatively restricted range of LTs extending roughly 4 h to either side of these sources, thus typically spanning the pre-dawn to post-noon sector. Within this range of LTs the observed modulations will thus be dominated by the mid-morning sources, giving rise to ‘strobe-like’ modulations approximately independent of LT. This conclusion is then consistent with the Voyager findings, whose inbound and outbound passes were located near noon and dawn, respectively. Away from the pre-dawn to post-noon sector, however, the observed emissions will arise from other LT sectors around the oval, potentially giving rise to position-dependent SKR modulation phases if these modulations indeed rotate around the oval like the field and plasma perturbations. We note that *Zarka et al.* [2007] previously provided evidence that the SKR period varies somewhat with the orbital motion of the spacecraft.

This discussion may then be relevant to a significant unresolved issue concerning the existence of slow long-term phase drifts between the southern period magnetic field oscillations at both high and low latitudes and the related southern SKR modulations. These phase drifts are typically only a few tenths of a degree per day, both positive and negative in different intervals, corresponding to apparent differences in period of a few tens of seconds. However, they integrate over intervals of hundreds of days to relative phase shifts of several tens of degrees. Such variations have been evident from the initial investigations of the relative phases between the SKR and magnetic field oscillations [*Andrews et al.*, 2008; *Provan et al.*, 2009a], and remain present at comparable values using the most recent phase determinations (see Chapter 5). We note, however, that phase drift effects of comparable magnitude do not appear in the northern high-latitude field oscillations relative to the northern SKR modulations, though the northern oscillations have been significantly less continuously monitored by Cassini than have the southern-period oscillations. A possible explanation for the relative phase drift in the southern system lies in the anticipated slow variations of SKR modulation phase due to the position-dependent effects outlined above, as the orbit of the spacecraft around the planet evolves during the mission. In this chapter we develop a simple theoretical model of the SKR phase shifts that might be expected

on this basis, and examine whether these could give rise to the relative phase drifts observed.

6.2 Methodology

6.2.1 Theoretical Model of Position-Dependent SKR Modulation Phases

In panel (a) of Figure 6.1 we show the variation of the SKR intensity with azimuth φ around Saturn's auroral oval, normalised to the peak intensity, derived from the direction-finding study of *Lamy et al.* [2009]. Northern and southern emissions were found to yield similar results, and are shown combined in this plot. Here azimuth φ , equivalent to LT, is measured from noon positive towards dusk as in previous related studies [*Andrews et al.* 2008; *Provan et al.* 2009a, 2011, and Chapters 4 and 5], such that dusk corresponds to 90° and dawn to 270° , as marked at the top of the panel. The peak in the emission intensity in the mid-morning sector is evident. We then consider the emitted SKR power per unit azimuthal angle, $p(\varphi)$, which we take to be proportional to the quantity shown, and assume for simplicity that the periodic modulations in power around the oval correspond to some fixed fraction k of this power. Following the discussion in section 6.1 related to rotating field and current systems, we also assume that the power modulations rotate as an ' $m = 1$ ' oscillation around each auroral oval, such that we can write for the modulations

$$\delta p(\varphi, t) = kp(\varphi)e^{j(\Phi_{SKR}(t)-\varphi)}, \quad (6.1)$$

where $j = \sqrt{-1}$ and we take the real part of the complex function. The phase function $\Phi_{SKR}(t)$ defines the slowly variable SKR modulation period (separately for each hemisphere, $\Phi_{SKR\,n}(t)$ and $\Phi_{SKR\,s}(t)$ for the north and south, respectively) through

$$\tau_{SKR}(t) = \frac{360}{\left(\frac{d\Phi_{SKR}(t)}{dt}\right)}, \quad (6.2)$$

where the phase function is expressed in degrees, and its absolute value is such that SKR modulation maxima occur at noon ($\varphi = 0^\circ$) when

$$\Phi_{SKR}(t) = 360 N \text{ deg}, \quad (6.3)$$

where N is any integer.

If an observer can then see all of the sources present, independent of azimuth, the power modulations integrated over all the sources will be

$$\delta P(t) = \int_{0^\circ}^{360^\circ} \delta p(\varphi, t) d\varphi = k e^{j\Phi_{SKR}(t)} \int_{0^\circ}^{360^\circ} p(\varphi) e^{-j\varphi} d\varphi = k P_{SKR} e^{j(\Phi_{SKR}(t) - \varphi_{SKR})}, \quad (6.4)$$

where we have written

$$\int_{0^\circ}^{360^\circ} p(\varphi) e^{-j\varphi} d\varphi = P_{SKR} e^{-j\varphi_{SKR}}, \quad (6.5)$$

where P_{SKR} is purely real, the modulus of the integral, and argument phase angle φ_{SKR} is the effective azimuth corresponding to the total integrated SKR modulation. Application of equation (6.5) to the azimuthal power profile shown in panel (a) of Figure 6.1 yields the value $\varphi_{SKR} \approx 296^\circ$ corresponding to a LT of ~ 7.7 h in the post-dawn sector, marked by the vertical dashed line in the figure. As expected, this azimuth corresponds closely to that of the peak in the SKR emission intensity. The ‘true strobe’ (or ‘clock’) phase of the SKR modulation may thus be taken to be

$$\Phi_{SKR}^*(t) = \Phi_{SKR}(t) - \varphi_{SKR}, \quad (6.6)$$

such that the total integrated power exhibits maxima when

$$\Phi_{SKR}^*(t) = 360 N \text{ deg}, \quad (6.7)$$

where N is any integer.

Following the discussion in section 6.1, however, we now consider that due to the conical beaming of the radio emissions, a given observer has only a restricted view of the sources distributed around the auroral oval. Specifically, on the basis of the results presented by *Lamy et al.* [2008a, 2009] and *Cecconi et al.* [2009] we suppose that emission sources near the peak of the SKR spectrum (few hundred kHz) that contribute most to the observed power modulation are confined to two narrow bands of LT ~ 1 h wide, displaced ~ 4 h LT on either side of the spacecraft position. This picture applies to the usual near-equatorial Cassini observing positions extending well outside the $\sim 4 R_S$ SKR shadow zone [*Lamy et al.*, 2008b,a], to typical radial distances of a few

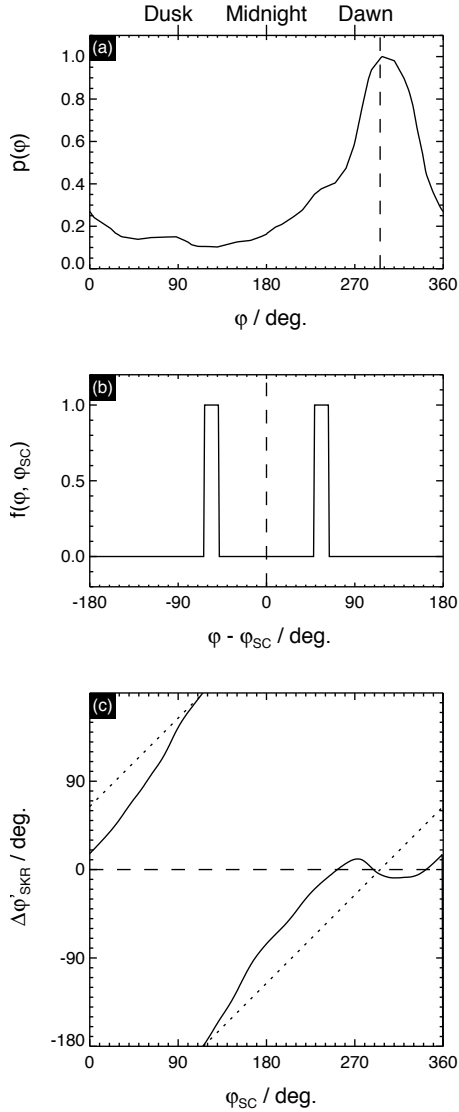


Figure 6.1: Panel (a) shows a profile of the SKR emitted power $p(\varphi)$ around Saturn's auroral oval versus azimuth φ , derived from northern and southern emissions combined by Lamy *et al.* [2009] (see their Figure 5). The values shown here have been normalised to the peak value. The vertical dashed line indicates the effective azimuth of the combined 'true strobe' emissions, $\varphi_{SKR} \approx 296^\circ$, determined from equation (6.5). Panel (b) shows the model SKR 'seeing function' $f(\varphi, \varphi_{sc})$ around the auroral oval employed in this chapter, corresponding to two windows 15° (1 h LT) of azimuth wide, centred $\pm 55^\circ$ (3.7 h LT) on either side of the spacecraft azimuth φ_{sc} . Function f is shown plotted versus $\varphi - \varphi_{sc}$. Panel (c) (solid line) shows the SKR modulation phase deviation $\Delta\varphi'_{SKR}$ due to restricted 'seeing' of the SKR sources around the auroral oval defined by equations (6.9)–(6.13), plotted versus spacecraft azimuth φ_{sc} . The horizontal dashed line shows the 'true strobe' limit $\Delta\varphi'_{SKR} = 0$ corresponding to full visibility of all SKR sources, while the inclined dotted line shows the opposite limit $\Delta\varphi'_{SKR} = \varphi_{sc} - \varphi_{SKR}$ in which emissions are detected only from sub-spacecraft sources such that the modulation phase corresponds to the LT of the spacecraft.

tens of R_S . We thus define a ‘seeing function’ for the SKR emissions around the oval that depends principally on the azimuth φ_{sc} of the spacecraft, $f(\varphi, \varphi_{sc})$, whose value lies between 0 and 1, and which for simplicity we take to consist of two top hats where $f = 1$, each of azimuthal width 15° (1 h LT), centred at $\varphi = \varphi_{sc} \pm 55^\circ$ ($\varphi_{sc} \pm 3.7$ h LT), with $f = 0$ otherwise. This form of f is shown in panel (b) of Figure 6.1, plotted versus $\varphi - \varphi_{sc}$.

The observed SKR power modulations are then given by

$$\delta P'(\varphi_{sc}, t) = \int_{0^\circ}^{360^\circ} f(\varphi, \varphi_{sc}) \delta p(\varphi, t) d\varphi \quad (6.8)$$

$$= k e^{j\Phi_{SKR}(t)} \int_{0^\circ}^{360^\circ} f(\varphi, \varphi_{sc}) p(\varphi) e^{-j\varphi} d\varphi = k P'_{SKR} e^{j(\Phi_{SKR}(t) - \varphi'_{SKR})}, \quad (6.9)$$

where we have now written

$$\int_{0^\circ}^{360^\circ} f(\varphi, \varphi_{sc}) p(\varphi) e^{-j\varphi} d\varphi = k P'_{SKR} e^{-j\varphi'_{SKR}}, \quad (6.10)$$

equivalent to equation (6.5) for the fully visible oval when $f \equiv 1$. We note that primed symbols are employed here, and throughout the paper, to indicate ‘observed’ quantities which depend on the seeing function f , and thus on the azimuth of the spacecraft. The modified position-dependent effective azimuth of the SKR modulations is thus $\varphi'_{SKR}(\varphi_{sc})$, such that the observed SKR modulation phase is now

$$\Phi'_{SKR}(t) = \Phi_{SKR}(t) - \varphi'_{SKR}(\varphi_{sc}), \quad (6.11)$$

where $\Phi'_{SKR}(t) = 360$ N deg at observed SKR power maxima. The ‘observed’ phase $\Phi'_{SKR}(t)$ is thus related to the ‘true strobe’ phase $\Phi^*_{SKR}(t)$ by

$$\Phi'_{SKR}(t) = \Phi^*_{SKR}(t) - (\varphi'_{SKR}(\varphi_{sc}) - \varphi_{SKR}) = \Phi^*_{SKR}(t) - \Delta\varphi'_{SKR}(\varphi_{sc}), \quad (6.12)$$

such that the observed phase is shifted to smaller values relative to the ‘true strobe’ phase through phase angle

$$\Delta\varphi'_{SKR}(\varphi_{sc}) = \varphi'_{SKR}(\varphi_{sc}) - \varphi_{SKR}, \quad (6.13)$$

where $\varphi'_{SKR}(\varphi_{sc})$ and φ_{SKR} are given by equations (6.10) and (6.5), respectively. In general we would expect the phase deviation $\Delta\varphi'_{SKR}(\varphi_{sc})$ to take positive values for

observation points having later LTs than those of the most intense mid-morning sources centred at ~ 7.7 h LT, such that observed maxima would then be shifted to somewhat later times, and to take negative values for observation points with earlier LTs than those of the most intense sources, such that observed maxima would then be shifted towards somewhat earlier times.

Application of equations (6.9)–(6.13) with the two top-hat ‘seeing function’ to the power profile shown in panel (a) of Figure 6.1 yields the results shown in panel (c), where we show $\Delta\varphi'_{SKR}$ plotted versus spacecraft azimuth φ_{sc} . The ‘true strobe’ limit $\Delta\varphi'_{SKR} = 0$ corresponding to a complete view of all the SKR sources is indicated by the horizontal dashed line, while the inclined dotted line shows the opposite limit $\Delta\varphi'_{SKR} = \varphi_{sc} - \varphi_{SKR}$ in which the modulation phase corresponds simply to that of the sub-spacecraft sources. In this case $\Delta\varphi'_{SKR}$ passes through zero when the spacecraft azimuth passes through the effective azimuth of the total SKR emission $\varphi_{SKR} \simeq 296^\circ$, and reaches $\pm 180^\circ$ at the antipodal azimuth of $\sim 116^\circ$ in the post-dusk sector (19.7 h LT). The variation of $\Delta\varphi'_{SKR}(\varphi_{sc})$ computed using the seeing function in panel (b) of Figure 6.1 is then shown by the solid line in panel (c). It can be seen that this is indeed ‘strobe-like’, remaining within $\pm 15^\circ$ of zero, over a $\sim 120^\circ$ range of LTs extending from the pre-dawn sector to noon as anticipated in section 6.1, thus being in agreement with the Voyager findings. Away from this sector, however, the modulation phase varies strongly with spacecraft LT, reaching anti-phase with the most intense mid-morning sources when the spacecraft is located at antipodal azimuths in the post-dusk sector. The phase difference exceeds $\pm 90^\circ$ in a band of azimuths $\sim 100^\circ$ wide centred in this sector.

6.2.2 Orbit-Averaged Phase Deviations

The results in Figure 6.1 imply in the first instance that significant deviations in SKR modulation phase will occur around the Cassini orbit on time scales of a few tens of days, though observations on a given orbit will generally be dominated by those near apoapsis where the spacecraft spends most time. However, as discussed in

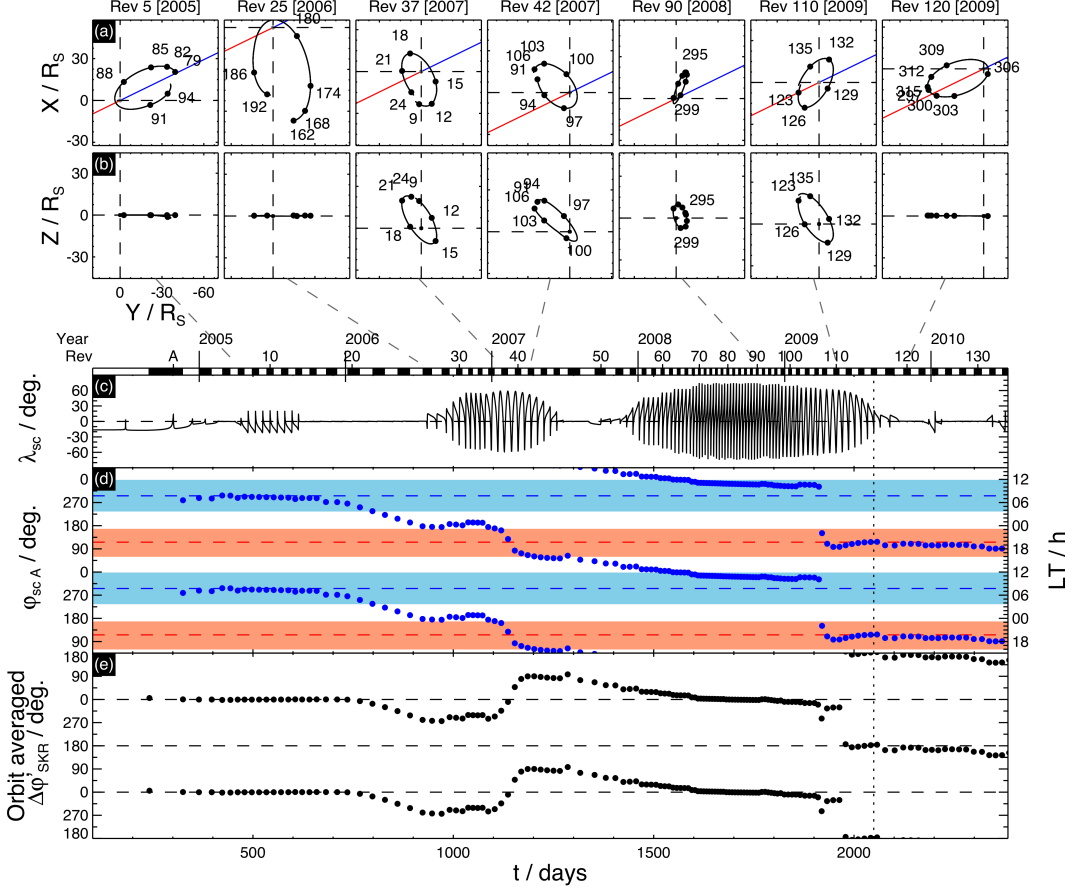


Figure 6.2: Caption overleaf.

section 6.3.1 below, the SKR modulation periods (and hence phases) employed here and in previous studies were determined over significantly longer sliding intervals of 200 days, thus generally encompassing a significant number of individual orbits. As an initial step towards simulating the effect of the position-dependent phase deviations on such long-term values, here we first derive orbit-averaged phase deviations from SOI in July 2004 to Rev 134 in July 2010, the latter corresponding to approximately one year after Saturn equinox.

We begin by outlining the evolution of the Cassini orbit over this interval. In panels (a) and (b) of Figure 6.2 we show a representative selection of seven spacecraft orbits (Revs) plotted from apoapsis to apoapsis, projected into the X-Y and Y-Z planes, respectively. The coordinate system is such that Z is aligned with the planet's spin and magnetic axes, the X-Z plane contains the Sun, and Y points towards dusk, completing the right-handed set. The Sun is therefore at the top of the plots in panel (a) and

into the plane of the plots in panel (b), while dusk and dawn are to the left and right, respectively, in both panels. Each plot box has sides of length $90 R_S$, but the position of the planet (the origin) has been adjusted as required. Day of year is indicated around each orbit at 3 day intervals where space allows, with the year concerned and Rev number (defined from apoapsis to apoapsis) being given at the top of each plot. The blue line in the equatorial plots in panel (a) shows the effective azimuth of the total SKR emission $\varphi_{SKR} \approx 296^\circ$, while the antipodal azimuth $\sim 116^\circ$ is indicated by the red line.

Panels (c) and (d) of Figure 6.2 then show orbit parameters versus time t (days) spanning SOI through Rev 134. As for all the time-series plots in this chapter, the plot covers the interval from $t = 100$ days (10 April 2004) to 2384 days (12 July 2010), where $t = 0$ days corresponds to 00 UT on 1 January 2004. The time of Saturn's vernal

Figure 6.2: Panels (a) and (b) show projections of the spacecraft trajectory onto the $X - Y$ (equatorial) and $Y - Z$ (dawn-dusk meridian) planes, respectively, for a selection of seven Cassini Revs. The orthogonal dashed lines show the corresponding coordinate axes passing through the planet's centre, whose position is varied between plots to best display the orbit, with the plot scale ($90 R_S$ on each side) held fixed. Day of year numbers are indicated by the filled circles along the trajectory at three day intervals where space allows, while calendar year and Rev numbers are given at the top of each pair of plots. The blue and red lines in panel (a) indicated the effective azimuth of the ‘true strobe’ SKR source, and its antipodal azimuth, respectively. The lower three panels then show time-series plots over the interval $t = 100 - 2384$ days (SOI to Rev 134), where $t = 0$ days corresponds to 00 UT on 1 January 2004. Saturn vernal equinox at $t = 2049$ days is indicated by the vertical dotted line. The duration of each Rev from apoapsis to apoapsis is indicated at the top of these panels by the row of alternate black and white blocks, with every tenth Rev numbered. Calendar year boundaries are also marked. Panel (c) shows the latitude of the spacecraft λ_{sc} (degrees). Panel (d) shows the azimuth of spacecraft apoapsis φ_{scA} (degrees), with two cycles being shown to emphasise the continuity of the data (blue dots), such that each point is plotted twice. Equivalent LT (hours) is indicated on the right-hand axis of the panel. The blue and red dashed lines indicate the effective azimuth of the ‘true strobe’ SKR source φ_{SKR} and its antipodal azimuth, respectively. The blue shaded region indicates the azimuthal range about the blue dashed line where the SKR modulation phase differs from the ‘true strobe’ phase by less than $\pm 15^\circ$, i.e. where $|\Delta\varphi'_{SKR}| \leq 15^\circ$, while the red shaded region indicates the azimuthal range about the red dashed line where the SKR phase deviation exceeds $\pm 90^\circ$, i.e. where $|\Delta\varphi'_{SKR}| \geq 90^\circ$. Panel (e) shows the directional mean of the modelled SKR phase deviation values $\Delta\varphi'_{SKR}$, computed over each orbit from periapsis to periapsis, with two complete cycles of phase again being shown.

equinox at $t = 2049$ days (11 August 2009) is indicated by the vertical black dotted line. Calendar year boundaries are indicated along the top of panel (c), along with alternate black and white blocks indicating the duration of each Rev, numbered every ten Revs. Gray dashed lines connect each pair of orbit plots in panels (a) and (b) to their corresponding Rev at the top of panel (c). In the latter panel we plot the latitude of the spacecraft λ_{sc} versus time, showing the presence of two extended intervals of high-latitude orbits, with the orbit otherwise remaining close to equatorial. The first high-latitude interval spans approximately from Rev 30 to Rev 43 ($t \approx 1000\text{--}1200$ days), and the second from Rev 59 to Rev 113 ($t \approx 1500\text{--}2000$ days). Measurements of the polar perturbation magnetic fields are confined to within these intervals.

Panel (d) of Figure 6.2 shows the azimuth of apoapsis (blue circles) of each orbit, φ_{scA} , where for purposes of continuity two complete 360° cycles are shown. Equivalently, the LT of apoapsis is indicated on the right-hand axis of the panel. For comparison, the horizontal dashed lines show the effective azimuth corresponding to the ‘true strobe’ SKR emission $\varphi_{SKR} \approx 296^\circ$ (blue) and its antipodal azimuth $\sim 116^\circ$ (red), corresponding to the red and blue lines in the equatorial plots in panel (a). The blue shaded area then shows the azimuthal extent about the blue dashed line where the SKR modulation is expected to be closely ‘strobe like’, with the modulation phase lying within $\pm 15^\circ$ of the ‘true strobe’ phase (i.e. $|\Delta\varphi'_{SKR}| \leq 15^\circ$), while the red shaded area shows the extent about the red dashed line where the SKR modulation deviates substantially from ‘strobe like’ behaviour, with the modulation phase lying beyond $\pm 90^\circ$ of the ‘true strobe’ phase (i.e. $|\Delta\varphi'_{SKR}| \geq 90^\circ$). It can be seen that for the first ~ 5 years of the mission, up to $t \approx 1900$ days corresponding to the first quarter of 2009, the apoapsis of the orbit, where the spacecraft spends most time, was almost continuously located outside the red shaded region, except for a brief interval around $t \approx 1150$ days (Rev 38) when apoapsis passed rapidly through the antipodal azimuth. The SKR modulation phase should thus remain close to that of the most intense mid-morning sources throughout this period, except possibly during the latter short interval. However, a significant change of orbit geometry took place after $t \approx 1900$ days, when apoapsis was in effect exchanged with periapsis via a near-circular orbit (Rev 108). This manoeuvre

resulted in a rapid $\sim 180^\circ$ switch in the azimuth of apoapsis to values nearly antipodal to φ_{SKR} lying centrally within the red shaded band, a configuration maintained to the end of the interval studied here. The results in Figure 6.1 then suggest the possibility of large deviations of SKR modulation phase from the ‘true strobe’ phase during this later interval, when the spacecraft was principally observing SKR sources on the opposite side of the planet to the most intense mid-morning sources.

The resulting orbit-averaged values of $\Delta\varphi'_{SKR}$ are shown versus time in panel (e) of Figure 6.2, where we again show two complete 360° cycles of phase for purposes of continuity. These values have been obtained by suitably averaging the phase deviations $\Delta\varphi'_{SKR}(\varphi_{sc})$ computed from equations (6.9)–(6.13) at 1 min resolution for each orbit from periapsis to periapsis, with the resulting value being plotted at the mean time of each orbit near the time of corresponding apoapsis. We note that no account has been taken in this procedure of possible spacecraft entry into the ‘shadow zone’ where SKR emissions cannot be observed [Lamy *et al.*, 2008b,a], which corresponds only to very short intervals near periapsis on orbits whose periapsis radius is sufficiently small (less than $\sim 4 R_S$ in the equatorial region). With regard to the ‘averaging’ concerned, as for any cyclic quantity, the standard ‘arithmetic mean’ is not appropriate to these phase angle data. Rather, we employ the ‘directional mean’ [e.g., Mardia and Jupp, 2000], in which we separately average the sine and cosine of the phase values, and then compute the two-argument arctangent of the result. Precisely, if the phase deviation values to be averaged are $\Delta\varphi'_{SKRk}$ for $k = 1$ to K , the directional mean $\overline{\Delta\varphi'_{SKR}}$ is given by the argument of the sum

$$\frac{1}{K} \sum_{k=1}^K e^{j\Delta\varphi'_{SKRk}} = \overline{R_{\Delta\varphi'_{SKRk}}} e^{j\overline{\Delta\varphi'_{SKRk}}}, \quad (6.14)$$

where modulus $\overline{R_{\Delta\varphi'_{SKRk}}}$ (lying between values of 0 and 1), termed the ‘mean resultant length’, gives a measure of the dispersion of the values about the mean. This operation thus simply computes the temporal average of $\Delta\varphi'_{SKR}$ over each orbit. A brief overview of some principal features of ‘directional statistics’ germane to this chapter is provided in Appendix B.

It is readily seen from panel (e) of Figure 6.2 that near-zero values of orbit-

averaged $\Delta\varphi'_{SKR}$ are obtained when the azimuth of apoapsis in panel (d) lies close to the blue shaded region centred on $\varphi_{SKR} \simeq 296^\circ$, implying that the overall modulation phase of the detected SKR emission is close to that of the most intense mid-morning sources. However, larger phase deviations of up to $\sim \pm 90^\circ$ are obtained on either side of Rev 38 at $t = 1150$ days, reversing from negative to positive as the spacecraft passes through the red shaded region. Shortly after Rev 108 at $t = 1900$ days, however, as apoapsis moves into the post-dusk sector, the orbit-averaged model phase then changes by $\sim 180^\circ$, corresponding to observations of SKR sources in the dusk-side oval $\sim \pm 4$ h LT on either side of spacecraft apoapsis, which combine to produce an overall modulation which is in approximate antiphase with the most intense mid-morning sources. Under these circumstances, the orientation of the oscillatory perturbation magnetic field is expected to be essentially reversed in sense at observed SKR maxima compared with that observed during the first ~ 5 years of the mission as reported e.g. by *Andrews et al.* [2008] and *Provan et al.* [2009a], and in Chapters 4 and 5 of this thesis, an effect that should be very evident in the magnetic field phase data.

6.2.3 Effect of SKR Modulation Phase Deviations on Derived Magnetic Oscillation Phases

We thus directly consider the effect of the position-dependent SKR modulation phase deviations on the relative phases of the magnetic field oscillations. The latter are determined empirically by fitting filtered residual (internal planetary field removed) magnetic field data with the ' $m = 1$ ' function

$$B_i(\varphi, t) = B_{i0} \cos(\Phi'_{SKR}(t) - \varphi - \psi'_i), \quad (6.15)$$

such that we obtain the phase value ψ'_i for field component i (to modulo 360°) for a given interval of data relative to the observed SKR phase $\Phi'_{SKR}(t)$, used as an exact guide phase. As in previous analyses, we employ spherical polar field components in the radial (r), co-latitudinal (θ), and azimuthal (φ) directions, referenced to Saturn's spin and magnetic axis. As described in section 6.3.2, the fits are made over spacecraft

passes through particular magnetospheric regions (e.g. the inner quasi-dipolar equatorial region or on high-latitude open field lines in a given hemisphere) that usually last one or two days, thus encompassing two or more field oscillation cycles whose phase can reliably be determined to within a few degrees. It is these phase values ψ'_i that show the slow pass-to-pass phase drifts with time that were discussed in section 6.1.

The values of the phases ψ'_i define the orientation of the perturbation field throughout the SKR modulation cycle observed during a particular epoch. Specifically, from equation (6.15) at observed SKR maxima (when $\Phi'_{SKR} = 360N^\circ$), the oscillation in field component i has a maximum at azimuth $\varphi'_{B_i \max}$ given to modulo 360° by

$$\varphi'_{B_i \max} = -\psi'_i, \quad (6.16)$$

with the pattern then rotating through 360° in the sense of planetary rotation during the SKR modulation cycle (given that the periods are almost equal). Consideration of Figure 5.9 then shows that for the southern system the upward field-aligned current from the ionosphere is expected to be centred approximately 90° ahead in azimuth of the maximum in the radial field component (at both low and high latitudes), with the downward current centred approximately 90° in azimuth behind. For the northern system these directions are reversed. Thus at observed SKR maxima the rotating upward field-aligned current region is expected to be located in a broad azimuthal band centred near azimuth $\varphi'_{uFAC \max}$ given by

$$\varphi'_{uFAC \max} = -\psi'_r \pm 90^\circ, \quad (6.17)$$

where the upper sign corresponds to the southern system and the lower to the northern. The phase relations with the other field components should then be consistent with the polarisations shown in Figure 5.9. If modulation of the SKR emission is positively correlated with modulation of the upward field-aligned current as expected, then equation (6.17) indicates the central azimuth (or LT) of the SKR sources related to the observed modulation, potentially depending on position according to the earlier discussion in this section.

If the SKR modulations are indeed linked to the same rotating current system that is responsible for the rotating magnetic field perturbations, however, we may expect

that the magnetic field phase relative to the ‘true strobe’ phase should be essentially constant in time. Substituting from equation (6.12) into equation (6.15) to express the magnetic oscillations in terms of the ‘true strobe’ phase $\Phi_{SKR}^*(t)$ then yields

$$B_i(\varphi, t) = B_{i0} \cos(\Phi_{SKR}^*(t) - \varphi - (\psi'_i + \langle \Delta\varphi'_{SKR}(\varphi_{sc}) \rangle)) = B_{i0} \cos(\Phi_{SKR}^*(t) - \varphi - \psi_i^*), \quad (6.18)$$

where $\langle \Delta\varphi'_{SKR}(\varphi_{sc}) \rangle$ is some suitably-averaged value of the position-dependent SKR phase deviation. Details of the averaging employed here, related to the derivation of the SKR modulation phase from sliding 200-day intervals of data, is discussed in section 6.3.3. Magnetic phase ψ'_i relative to the observed SKR modulation phase $\Phi'_{SKR}(t)$ and phase ψ_i^* relative to the ‘true strobe’ phase $\Phi_{SKR}^*(t)$ are thus related by

$$\psi'_i = \psi_i^* - \langle \Delta\varphi'_{SKR}(\varphi_{sc}) \rangle, \quad (6.19)$$

where ψ_i^* is expected to be a constant. As the spacecraft orbit then evolves slowly with time, such that the value of $\langle \Delta\varphi'_{SKR}(\varphi_{sc}) \rangle$ also evolves slowly with time, then so too will the phase ψ'_i of the magnetic field oscillations relative to the observed SKR modulations, leading to the appearance of long-term relative phase drifts in the opposite sense to $\langle \Delta\varphi'_{SKR}(\varphi_{sc}) \rangle$. The values of ψ_i^* for field component i , obtained from equation (6.19) through modelling the averaged SKR phase deviation $\langle \Delta\varphi'_{SKR}(\varphi_{sc}) \rangle$, then define the orientation of the perturbation field throughout the ‘true strobe’ SKR modulation cycle, constant over time. Specifically, in correspondence with equation (6.16), at ‘true strobe’ SKR maxima field component i has a maximum at azimuth $\varphi_{B_i \max}^*$ given to modulo 360° by

$$\varphi_{B_i \max}^* = -\psi_i^*, \quad (6.20)$$

while in correspondence with equation (6.17), at ‘true strobe’ SKR maxima the rotating upward field-aligned current region is centred near azimuth $\varphi_{uFAC \max}^*$ given by

$$\varphi_{uFAC \max}^* = -\psi_r^* \pm 90^\circ, \quad (6.21)$$

where again the upper sign corresponds to the southern system and the lower to the northern. For consistency with the above picture we then expect that

$$\varphi_{uFAC \max}^* \approx \varphi_{SKR} \approx 296^\circ, \quad (6.22)$$

such that the ‘true strobe’ SKR maxima occur when the rotating upward current region is co-located with the principal SKR sources in the post-dawn sector. The implied values of $\varphi_{B_i}^* \max$ are $\sim 154^\circ$ for the southern system, and $\sim -26^\circ$ (or equivalently $\sim 334^\circ$) for the northern, corresponding to the equatorial perturbation fields pointing approximately tailward and sunward, respectively, in agreement with previous determinations discussed in section 6.1.

6.3 Determination of Magnetic Phase Values

We now revisit the magnetic oscillation phases determined relative to the observed SKR modulation phases $\Phi'_{SKR\,n}(t)$ and $\Phi'_{SKR\,s}(t)$ for the northern ('n') and southern ('s') hemispheres respectively, as derived previously by *Andrews et al.* [2008], *Provan et al.* [2009a] and in Chapter 5, and compare the long-term phase drifts found in these data with expectations based on equation (6.19) and the position-dependent SKR phase deviations modelled in section 6.2. We begin by briefly reviewing the derivation of the northern and southern SKR modulation phases, and then consider the relative phases ψ'_i of the magnetic field oscillations so determined.

6.3.1 Derivation of SKR Modulation Phases

The northern and southern SKR modulation phases employed here are those derived by *Lamy* [2011], representing a modest revision and temporal extension of the numerical phase values employed previously by *Provan et al.* [2011] and in Chapter 5. Modulation periods $\tau'_{SKR\,n,s}(t)$ for the northern and southern SKR emissions, integrated over the SKR frequency band 40-500 kHz, were determined by Lomb-Scargle analysis using a 200 day sliding window and a time resolution of 1 day (see *Lamy* [2011] for further details). The influence of variations in the SKR period occurring on shorter time scales, such as those found by *Zarka et al.* [2007] to be correlated with changes in solar wind speed on the solar rotation period, are therefore removed. These periods are shown versus time in panel (a) of Figure 6.3, where the red line corresponds to the southern hemisphere, the longer period over most of the interval,

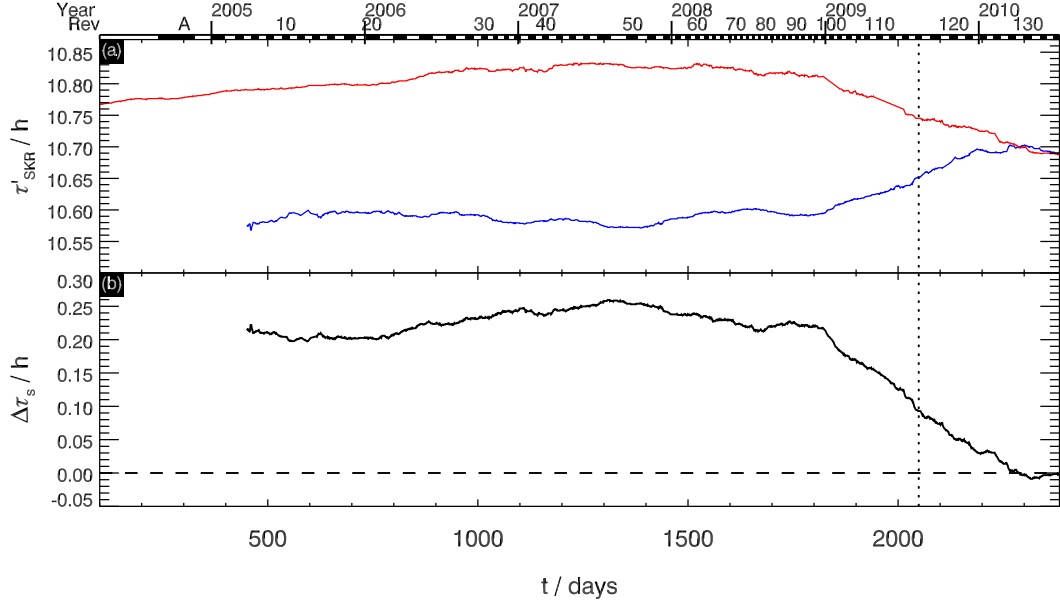


Figure 6.3: Time-series plots of (a) the modulation period of the southern (red) and northern (blue) SKR emissions determined by Lamy [2011], and (b) their difference (south minus north). The vertical black dotted line indicates the time of Saturn vernal equinox. Other figure formatting follows that in Figure 6.2.

and the blue line to the northern hemisphere. The difference between the southern and northern periods is shown in panel (b). It can be seen that the two values are separated by ~ 0.2 h over most of the interval, but following shallow opposite extrema near $t \approx 1300$ days (mid-2007), the periods then converge to an essentially common value after $t \approx 2250$ days (early 2010). This convergence occurs ~ 240 days after vernal equinox, again indicated by the vertical dotted line in the panels. Similar results from a related analysis of SKR modulations have also been reported by Gurnett *et al.* [2010b].

The observed SKR phase in each hemisphere is then determined by interpolating the resulting time series, and numerically integrating the values to give

$$\Phi'_{SKR\,n,s}(t) = 360 \int_0^t \frac{dt^\dagger}{\tau'_{SKR\,n,s}(t^\dagger)} + \Phi_{0\,n,s}, \quad (6.23)$$

Here $\Phi_{0\,n,s}$ is a constant determined (to modulo 360°) by requiring SKR power maxima to correspond to phases of $360 N$ deg as in section 6.2.1 above.

6.3.2 Derivation of Magnetic Oscillation Phases

Magnetic oscillation phases are derived from 1 min-averaged spherical polar field components measured by the Cassini fluxgate magnetometer [Dougherty *et al.*, 2004]. These data are processed by first subtracting Saturn's internal magnetic field using the 'Cassini SOI' model of Dougherty *et al.* [2005], though use of any the existing empirical models would produce closely similar results. We note that in common with these models, the 'Cassini SOI' model is exactly axisymmetric with zero azimuthal component, such that the azimuthal component of the residual field data remain as measured. These residual data are then band-pass filtered between 5 and 20 h using a standard Lanczos filter to isolate oscillations near the ~ 11 h planetary period. The phases of the oscillations in each component ψ'_i relative to the observed SKR phases $\Phi'_{SKR\ n,s}(t)$ are then determined (to modulo 360°) by least-squares fitting the filtered residual data for selected data segments to the function given by equation (6.15) with B_{i0} and ψ'_i as free parameters. Phase values are excluded from further analysis if

- a) the resultant fits are of poor quality such that the fitted amplitude B_{i0} is less than twice the RMS 'noise' in the data,
- b) this amplitude is smaller than 0.2 nT,
- c) the quasi-static field in the r or θ components generated by Saturn's ring current varies along the spacecraft trajectory on time scales similar to the field oscillations thus producing power in the filter band unrelated to the magnetospheric oscillations.

Application of the latter criterion follows that in previous related studies, discussed in detail by Andrews *et al.* [2008] and in Chapter 5. The phase fits rejected via these three criteria are 3%, 8%, and 30%, respectively. The total rejection rate is thus 41%, the largest contributor by far being that associated with the ring current, which effects the r or θ component data only.

The selected data segments, usually intervals of one to two days containing two or more oscillation cycles, correspond to the inner near-equatorial quasi-dipolar

magnetosphere within dipole $L \leq 8$ referred to as the ‘core’ magnetosphere (a limit chosen to avoid the magnetic effects of quasi-static auroral field-aligned currents in the azimuthal field data, see Chapter 5), and to high-latitude open polar field lines in the north and south within radial distances of $25 R_S$ where warm and hot electron fluxes are continuously near instrument background (see Provan *et al.* [2009a] and Chapter 5). These high-latitude intervals are also screened to ensure that no magnetosheath or solar wind data intervals are included. On orbits during the second high-latitude mission phase in 2008 (see Figure 6.2), however, we note that the spacecraft passed through the quasi-dipolar ‘core’ on time scales shorter than the ‘planetary’ period, such that phases can be determined only from unfiltered residual field data in these cases (Revs 55 to 97). However, the r and θ components on these orbits are again compromised by the fields of the ring current, such that phases can be determined only for the azimuthal field component.

The results presented in Chapter 5 show that the magnetic field phases on northern and southern polar field lines are organised by the northern and southern SKR periods, respectively. Those within the ‘core’ are also found to be organised by the southern SKR period over the interval from SOI to $t = 2057$ days (to Rev 116 in mid-2009) which they studied, though with significant $\sim \pm 25^\circ$ Rev-to-Rev phase ‘jitter’ due to the superposition of northern-period oscillations of smaller amplitude [Provan *et al.*, 2011], which contributes significantly to the ‘noise’ in these data. In the following sections we thus consider magnetic field phase drifts in the ‘core’ and southern polar field data combined, and separately in the northern polar field data.

6.3.3 Southern-Period Magnetic Phase Data

Magnetic oscillation phase data for the ‘core’ region (solid dots) and southern polar region (open dots) relative to the observed phase of the southern SKR modulation are shown versus time in panel (a) of Figure 6.4, over the same interval as Figures 6.2 and 6.3. Again, two cycles of phase are shown to clearly display the continuity and banding of the data. The phases of the r (red) and θ (green) components are shown as

measured, while 90° has been subtracted from the phase of the φ (blue) component in the ‘core’ region and 90° added in the polar region due to the opposite quadrature nature of these oscillations (Figure 5.9), to bring them to a common value. Vertical bars give an estimate of the relative uncertainty in these measurements, obtained by determining the range of phase required to produce a significant 10% increase in the RMS deviation of the model fit to the field data. We note that these phase values are essentially identical to those shown in Chapter 5 (sections 5.3.2 and 5.3.3), except for slight differences due to the minor modifications in the numerical SKR phase model mentioned in section 6.3.1, and a temporal extension of the data set from Rev 116 to 134, now newly including Revs with apoapsis in the post-dusk sector.

Information on the location of the spacecraft during each data segment used to determine these phases is shown in panels (b) to (d) of Figure 6.4, where the dots show the centre times of these intervals, solid for the ‘core’ region and open for the southern polar region. The dashed line in panel (b) shows the 200 day directional running-average of the spacecraft azimuth, mainly reflecting the azimuth of apoapsis as shown in panel (c) of Figure 6.2, while the vertical lines show the range of azimuths covered by the phase determinations, generally located at antipodal values near periapsis. Panels (c) and (d) similarly show the radial and latitudinal ranges corresponding to the phase determinations, respectively.

As was previously discussed in Chapter 5, the principal feature of the phase data is their distinct banding in value, though with significant scatter to which the ‘jitter’ effect due to the presence of weaker northern-period oscillations in the ‘core’ data is a significant contributor. This banding shows that the magnetic oscillation phases are strongly organised by the southern SKR modulation phase, such that these phenomena have a nearly common period, within a few seconds overall. We note in particular that the data remain banded with similar relative polarisation in the three field components in the post-equinox data newly shown here, such that there is no evidence in these data for dominance of northern-period oscillations in the ‘core’ data during this interval. Northern dominance would produce highly scattered phase data relative to the southern-period phase over intervals where the two periods

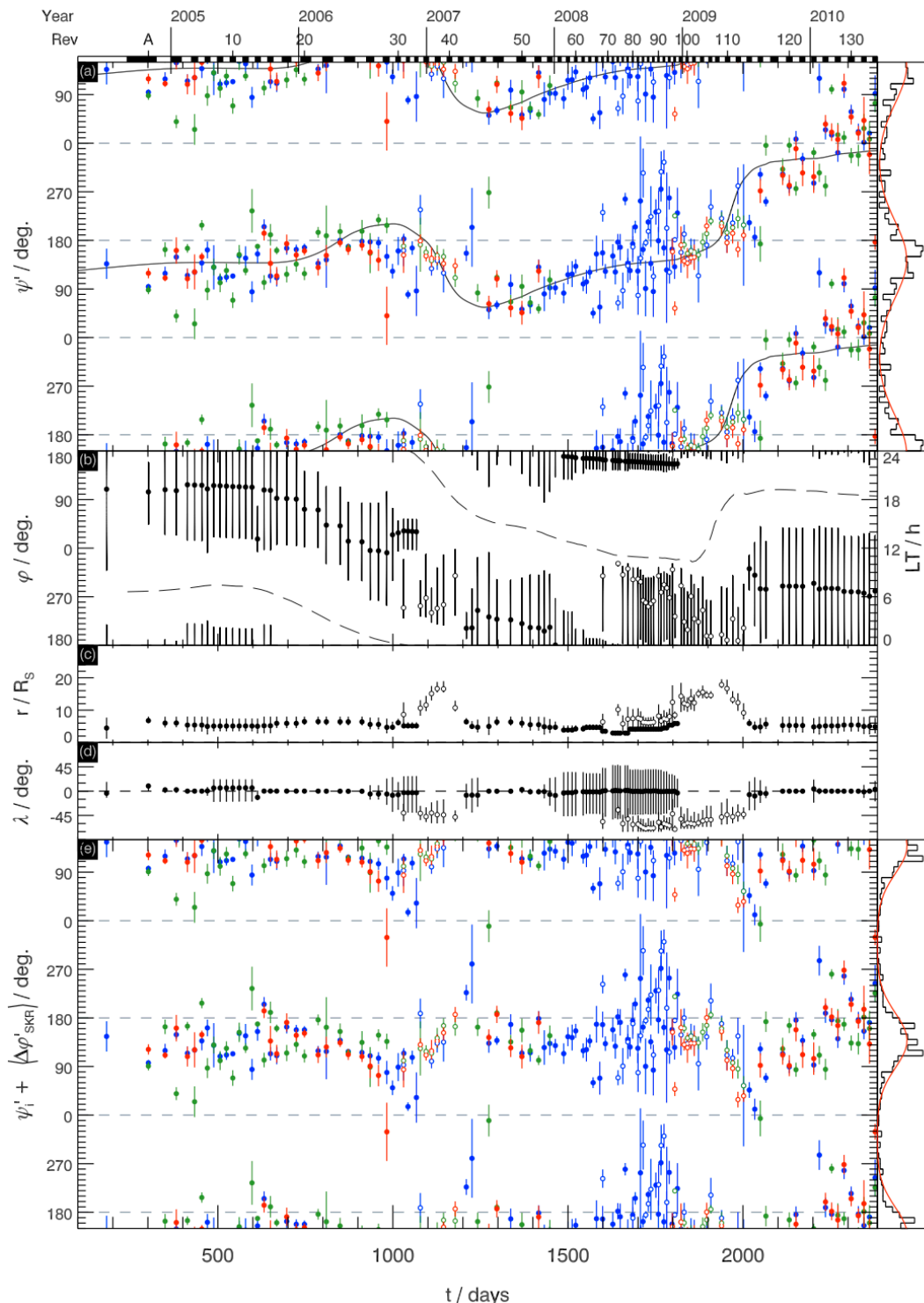


Figure 6.4: Caption overleaf.

are significantly different. We thus take this overall data set to define the relative phase between the southern-period field oscillations and the southern hemisphere SKR power modulations over the whole 6-year interval shown.

As in equation (6.15), the directional mean $\bar{\psi}$ and the mean resultant length $\overline{R_\psi}$ of the phase values are given by

$$\frac{1}{K} \sum_{k=1}^K e^{j\psi_k} = \overline{R_\psi} e^{j\bar{\psi}}, \quad (6.24)$$

where we have now dropped component subscript i since all the phase data are combined together having taken account of the relative polarisation of the oscillations in the three field components (ψ corresponds directly to the phase of the r and θ components). The directional mean phase value $\bar{\psi}$ so determined is 144° , which

Figure 6.4: Plots showing southern-period magnetic field phase data and related parameters. Panel (a) shows magnetic field phases relative to the observed southern hemisphere SKR modulation phase, determined in both the quasi-dipolar ‘core’ region defined by dipole $L \leq 8$ (filled circles) and in the southern polar region (open circles), with red, green, and blue colour-coding for the phases of the r , θ and φ field components, respectively. The phases of the r and θ components are shown as measured, while 90° has been subtracted from the phases of the φ component determined in the ‘core’ region, and 90° added to those determined in the open field region, in order to account for the relative quadrature polarisation of these oscillations. Vertical bars on each symbol give an estimate of the uncertainties determined by the range of phase required to produce a 10% increase in the RMS deviation of the model fit to the field data, and each point is plotted twice over the two cycles of phase shown. The solid black line shows the model phase drift due to the position-dependent SKR modulation phase deviation $\psi' + \langle \Delta\varphi'_{SKR} \rangle$ computed from equation (6.19). The histogram to the right of panel (a) shows the occupancy of 10° intervals of phase normalised to the peak value (black), together with a wrapped normal distribution (red line) having the same directional mean and circular standard deviation (see Appendix B) as the phase data. Calendar year boundaries and Cassini Rev numbers are indicated at the top of the plot in the same manner as Figure 6.2. Vertical bars in panel (b) then show the range of azimuths traversed by the spacecraft during each interval for which phases are determined, with circles showing the position at the mid-point, the latter again being filled or open for ‘core’ and polar data, respectively. The 200 day directional running average of the spacecraft azimuth is also shown by the dashed line, essentially reflecting the LT of spacecraft apoapsis (an equivalent LT scale is shown on the right of the plot). Panels (c) and (d) then show in a similar manner the radial distance and latitude of the spacecraft during each data interval. Panel (e) then shows the same phase data as panel (a), adjusted by the addition of the modelled average phase deviation $\langle \Delta\varphi'_{SKR} \rangle$, with the corresponding histogram and wrapped normal distribution again plotted to the right.

from equation (6.16) indicates that at observed southern SKR maxima the radial field component has a maximum at azimuth -144° , equivalent to $+216^\circ$, at a LT of 2.4 h in the post-midnight sector. This then is the direction of the southern-period quasi-uniform equatorial field and the southern effective polar dipole at these times, both being in phase with the r component, as previously indicated in section 6.1 (Figure 5.9). From equation (6.17) we also note that the centre of the associated upward field-aligned current in the southern ionosphere is then located at an azimuth of $+306^\circ$, i.e. a LT of 8.4 h in the post-dawn centre, essentially co-located with the peak in the SKR intensity shown in Figure 6.1 in accordance with expectation.

The variance V of the data about the directional mean, the latter being the phase value about which the data variance is a minimum, is given by

$$V = 1 - \overline{R_\psi}, \quad (6.25)$$

(see Appendix B). For tightly-grouped data, V is approximately half the mean squared deviation of the phase values (in radians) about the directional mean. Equivalently, the circular standard deviation σ_ψ of the data about the directional mean (in radians), employed here as a useful summary statistic, is given by

$$\sigma_\psi^2 = \ln \left(\frac{1}{\overline{R_\psi}^2} \right), \quad (6.26)$$

(see Appendix B). The circular standard deviation σ_ψ so determined for the data in panel (a) is 71° . To the right of panel (a) in Figure 6.4 we show a histogram of the phase values grouped into 10° bins and normalised to the peak value, together with a ‘wrapped normal’ distribution over-plotted in red having this directional mean and circular standard deviation. The ‘wrapped normal’ distribution is the analogue for circular data of the ‘normal’ (Gaussian) distribution for linear data (see, e.g., *Mardia and Jupp* [2000] and Appendix B).

As was discussed previously in Chapter 5, however, long term drifts are also present in these phase data, specifically slow drifts to larger phase between SOI and Rev 30 and between Revs 45 and 116, joined between by a shorter interval of more rapid drift to lower phase values. Direct interpretation of the positive phase gradients implies

magnetic oscillation periods that are ~ 10 s longer than the southern SKR modulation period during these intervals, while the intervening negative phase gradient implies a period that is ~ 40 s shorter. In addition, as anticipated in the above discussion, we now also see a substantial shift in the phase values from Rev 117 to the end of the interval at Rev 134, these representing the first extended set of orbits with apoapsis in the post-dusk sector. The directional mean phase of the earlier phase data (to end of Rev 116 at $t = 2057$ days) is 150° with a circular standard deviation of 53° , similar to the overall value, such that the equatorial quasi-uniform field and effective polar dipole point toward the post-midnight sector (2.0 h LT) at southern SKR maxima as just discussed. However, the directional mean of the later data (beginning of Rev 17 to the end of the interval) is 357° with a circular standard deviation of 60° , which from equation (6.16) means that the equatorial quasi-uniform field and effective southern dipole now point towards azimuth $+3^\circ$ (12.2 h LT) in the immediate post-noon sector at times of observed southern SKR maxima during this epoch. Thus from equation (6.17) the rotating upward field-aligned current region in the southern hemisphere is now centred at an azimuth of $\sim 93^\circ$ in the immediate post-dusk sector at these times, consistent with the expected response of SKR sources located in the dusk sector which the spacecraft will then be observing, rather than the most intense sources in the mid-morning sector observed earlier in the mission.

We thus consider whether the magnetic field phase variations in Figure 6.4 are due to the position-dependent SKR modulation phase deviations discussed in section 6.2. The apparent magnetic oscillation phase drifts expected to result from the SKR phase deviations are given by equation (6.19), i.e. $\psi' = \psi^* - \langle \Delta\varphi'_{SKR} \rangle$, the position-dependent phase deviation $\Delta\varphi'_{SKR}$ being suitably averaged to mimic the expected effect within the empirical SKR phase data and ψ^* a constant to be determined. Suitable averages of $\Delta\varphi'_{SKR}$ are obtained by interpolating the orbit-averaged values shown in Figure 6.2 at 1 min resolution, with a 200 day directional running average then being calculated to match the 200-day sliding window employed in the analysis of the SKR data. The best-fit value of ψ^* was then determined by minimising the variance about zero of the difference between the data ψ'_k and the

model $\Delta\psi'_k = \psi'_k - (\psi^* - \langle\Delta\varphi'_{SKR,k}\rangle) = (\psi'_k + \langle\Delta\varphi'_{SKR,k}\rangle) - \psi^*$, where k is the index of the phase data values determined during each Rev as in equation (6.24). It is shown in Appendix B that this variance is minimised when $\psi^* = \overline{(\psi' + \langle\Delta\varphi'_{SKR}\rangle)}$, i.e. when ψ^* is equal to the directional mean of the phase sum $(\psi'_k + \langle\Delta\varphi'_{SKR}\rangle)$. The best fit value of ψ^* so determined is 138° , and the resultant fitted curve is shown by the solid black line in panel (a) of Figure 6.4.

These results demonstrate that the phase drifts observed in the core and southern polar field data can be approximately accounted for in both form and magnitude by the position-dependent SKR phase deviations. The curve reproduces the slow drift to larger phase values observed prior to Rev 30 and after Rev 45, and the interval of more rapid fall between. It also reproduces the rapid increase in phase from $\sim 160^\circ$ to $\sim 320^\circ$ that accompanies the transfer of apoapsis into the post-dusk sector after Rev 110. In panel (e) of Figure 6.4 we then show the same magnetic phase data as in panel (a) of Figure 6.4 ‘corrected’ by the addition of the averaged SKR phase deviation $\langle\Delta\varphi'_{SKR}\rangle$ i.e. the phase values $\psi' + \langle\Delta\varphi'_{SKR}\rangle$ (equation (6.19)), thus representing the magnetic phase relative to the southern SKR ‘true strobe’ phase given by equation (6.12). Little remains in these data of the secular phase drifts evident in panel (a), though the behaviour particularly in the regions of rapid predicted phase change is not perfectly reproduced. The directional mean and standard deviation of these ‘corrected’ data are 138° and 51° , respectively, compared with 144° and 71° for the original data set in panel (a). The decrease in standard deviation from 71° to 51° is highly significant, as is clear from the histogram and over-plotted wrapped normal curves to the right of panels (a) and (e). The data are clearly more tightly grouped in panel (e) than in panel (a). We also note from equations (6.20) and (6.21) that the value $\psi^* \approx 138^\circ$ corresponds to $\varphi_{B_r, max}^* \approx -138^\circ = 222^\circ$ (2.8 h LT) and $\varphi_{uFAC, max}^* \approx 312^\circ$ (8.8 h LT), the latter being close to the effective azimuth of the ‘true strobe’ emission $\varphi_{SKR} \approx 296^\circ$ (7.7 h LT) determined in section 6.2.1. Thus at the time of ‘true strobe’ SKR maxima the southern period quasi-uniform equatorial field and effective polar dipole point consistently toward 2.8 h LT in the post-midnight sector (± 3.4 h LT), while the upward field-aligned current region is centred within one hour LT of the effective centre of the most intense SKR

sources in the mid-morning sector (panel (a) of Figure 6.1).

These results imply that the small differences in period mentioned above and discussed previously by *Andrews et al.* [2008], *Provan et al.* [2009a], and in Chapter 5 are in fact due to the restricted view of the SKR emissions influencing the SKR modulation phase rather than to actual differences in period. However, significant $\pm 51^\circ$ scatter about the mean value remains, a significant part of which represents the phase ‘jitter’ effect in the ‘core’ data mentioned above, together with the increased variability of the phases obtained from unfiltered azimuthal field data during the second interval of high-latitude orbits in 2008 as mentioned in section 6.3.2. In addition, inadequacies in the simple SKR ‘seeing function’ employed here may also play a role, particularly with regard to observations at higher latitudes. Overall, however, a maximum possible $\sim 90^\circ$ phase shift between the field oscillations and the southern-period SKR modulations over the whole 6 year interval investigated here, as suggested by the confined band of phase data in panel (e) of Figure 6.4, implies an averaged period which is common to within ~ 2 s (within 0.005%). The implied variation of the common period over the interval will be discussed further in section 6.4.

6.3.4 Northern-Period Magnetic Phase Data

The SKR modulation phase deviation model derived in section 6.2 should in principle apply equally to the northern hemisphere data as to the southern, thus leading to related drifts in the relative phase of the northern-period field oscillations. However, as indicated above, determinations of the phase of the northern-period field oscillations are restricted to observations on northern open field lines, and are thus available only during the two limited intervals of high-latitude orbits indicated in Figure 6.2. Results are shown in Figure 6.5 in a similar format to panels (a) to (d) of Figure 6.4. The phase values relative to the observed northern SKR modulations shown in panel (a) have again been adjusted to account for the polarisation of the oscillations. Specifically, while the r component phase is again shown as measured, 90° has been added to the φ component, and 180° to the θ component to bring them to a common value (see

Figure 5.9). As noted previously in Chapter 5, these phases are well organised by the northern SKR modulation phase, thus indicating a near-common period, but now about a directional mean value of 6° with a circular standard deviation of 40° . From equation (6.16) we note that this mean phase corresponds to the northern hemisphere effective polar dipole pointing towards -6° ($+354^\circ$) azimuth in the immediate pre-noon sector (11.6 h LT) at the times of northern SKR maxima, as indicated in section 6.1. Thus from equation (6.17) the upward field-aligned currents in the northern hemisphere are centred at azimuth 264° (5.6 h LT) at these times during the interval covered by the data, thus being located in the immediate pre-dawn sector ~ 2 h LT earlier than the most intense SKR sources shown in Figure 6.1, but still in reasonable accord with expectation.

Within the limited data intervals in Figure 6.5 there is no consistent evidence for the presence of phase drifts of a similar nature to those observed in the southern-period oscillations. The variation expected on the basis of our model is again shown by the over-plotted fitted solid line, which while not being grossly inconsistent with the data, also shows little clear correspondence. We also note that the circular standard deviation of the ‘corrected’ data $\psi' + \langle \Delta\varphi'_{SKR} \rangle$ (not shown here) is 56° , significantly larger than the initial 40° in the measured phases. Inadequacy of our simple ‘seeing function’ as applied to higher-latitude data is one possible contributor to the lack of correspondence found here, this meriting future study beyond that of the present paper.

6.4 Revised Period of the Southern Hemisphere Oscillations

The results in section 6.3 indicate that due to the dependence of the southern SKR modulation phase determinations on spacecraft position, usually but not always modest in magnitude, the southern periods determined from these data deviate modestly from the true values, as revealed by the slow drifts in relative phase of the magnetic field oscillations. No evidence exists for such deviations in the much more sparsely observed northern period field data, however. In this section we therefore

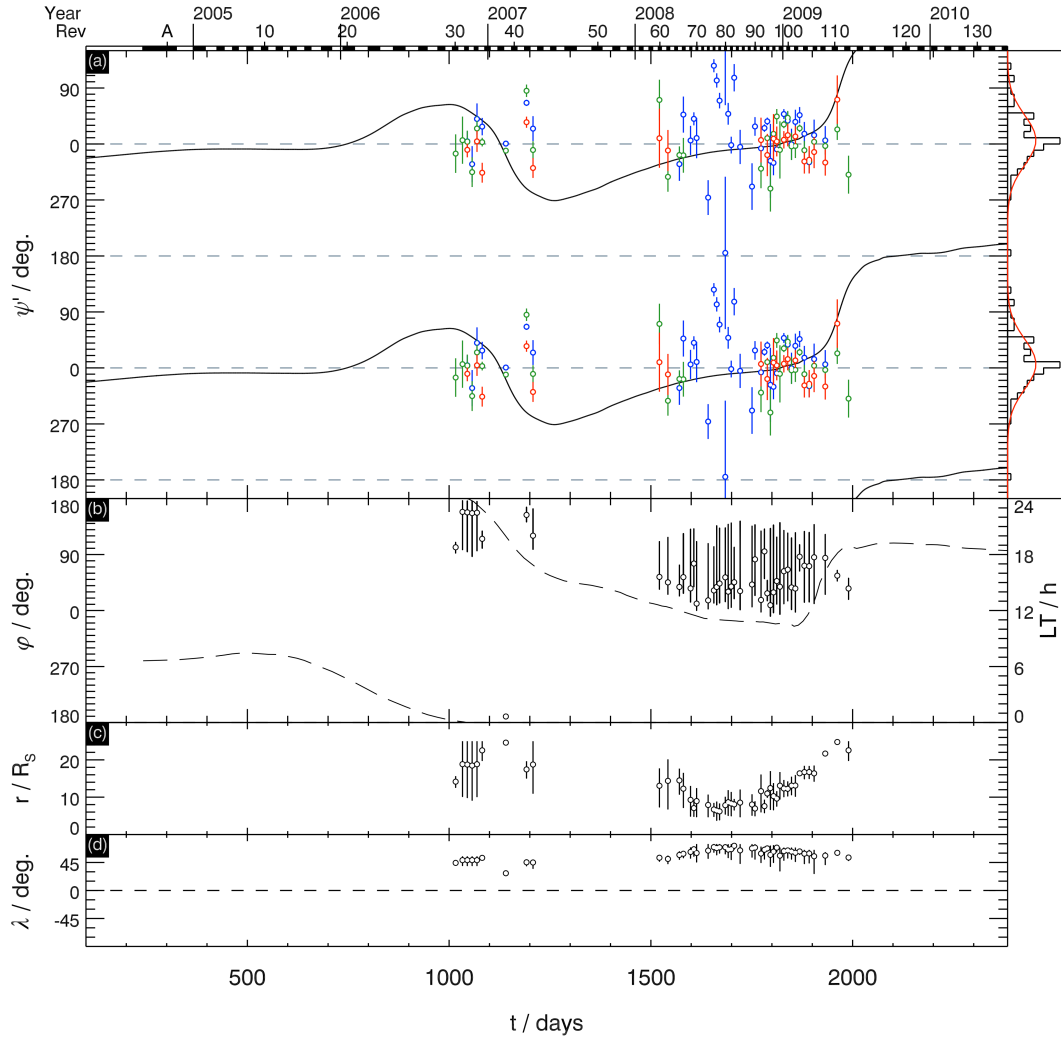


Figure 6.5: Northern-period magnetic field phase data and related orbit parameters, in a format similar to panels (a) to (d) of Figure 6.4. The phases of the r field component are again shown as measured, while those of the θ and φ components have been adjusted by the addition of 180° and 90° , respectively, to bring them to a common value.

first estimate the ‘true strobe’ period of the southern oscillations based on the model fits to the magnetic phase data in section 6.3, and thus quantify the deviations from the period based on the observed SKR modulations alone. We then present an independent determination of the southern hemisphere period based on magnetic phase data alone, and compare the two data sets.

The ‘true strobe’ period of the southern SKR modulations, based on the ‘true strobe’ phase $\Phi_{SKR}^*(t)$ in equation (6.12), is related to the observed SKR period $\tau'_{SKR}(t)$

determined by Lamy [2011] by

$$\tau_{SKR\ s}^*(t) = \frac{360}{\frac{d}{dt}(\Phi_{SKR\ s}^*)} = \frac{360}{\frac{d}{dt}(\Phi'_{SKR\ s} + \langle\Delta\phi'_{SKR}\rangle)} = \frac{\tau'_{SKR\ s}}{1 + \frac{\tau'_{SKR\ s}}{360} \frac{d}{dt}(\langle\Delta\phi'_{SKR}\rangle)}, \quad (6.27)$$

where the angles are again in degrees. Results are displayed in Figure 6.6, where the black line in panel (a) shows the ‘observed’ southern SKR period $\tau'_{SKR\ s}$ determined as described in section 6.3.1, as shown previously by the red line in panel (a) of Figure 6.3. The green line in Figure 6.6 then shows the modified period $\tau_{SKR\ s}^*(t)$ given by equation (6.27), obtained by numerical differentiation of the averaged $\Delta\phi'_{SKR}$ values. It can first be seen that the deviations about $\tau'_{SKR\ s}$ are usually small, except for intervals near $t = 1150$ and 1950 days which correspond to sharp changes in $\langle\Delta\phi'_{SKR}\rangle$ (Figure 6.4) due to rapid evolution of the spacecraft orbit (Figure 6.2). For better clarity in panel (b) we thus show the difference $\Delta\tau'_s = \tau_{SKR\ s}^* - \tau'_{SKR\ s}$ between these periods (green line). The overall values are small, ~ 10 s or less, except near $t = 1150$ and 1950 days as noted above where opposite extrema peaking at ~ -70 and $\sim +110$ s occur. While we do not ascribe significance to the detailed values in these regions, the integrated effect of these differences are just such as to produce the overall negative and positive changes in phase by up to $\sim 180^\circ$ evident in the magnetic phase values in Figure 6.4.

The southern oscillation ‘true strobe’ period shown by the green lines in Figure 6.6 is based initially on southern hemisphere SKR data, corrected for the modelled position-dependent SKR phase drift. However, it is also possible to use the southern-period magnetic field data directly to estimate the variation of the oscillation period. In essence this can be done by computing the magnetic field phases within sliding sub-intervals of the data using guide phases of fixed period, and determining the period for which these phases are most nearly constant. For practical calculation, the phases of the magnetic oscillations are first determined using the same least-squares method as described in section 6.3.2, but relative to a guide phase $\Phi_0(t)$ corresponding to a fixed period of exactly $\tau_0 = 10.82$ h (the period near the centre of the interval) given simply by

$$\Phi_0(t) = 360 \frac{t}{\tau_0} \text{ deg}, \quad (6.28)$$

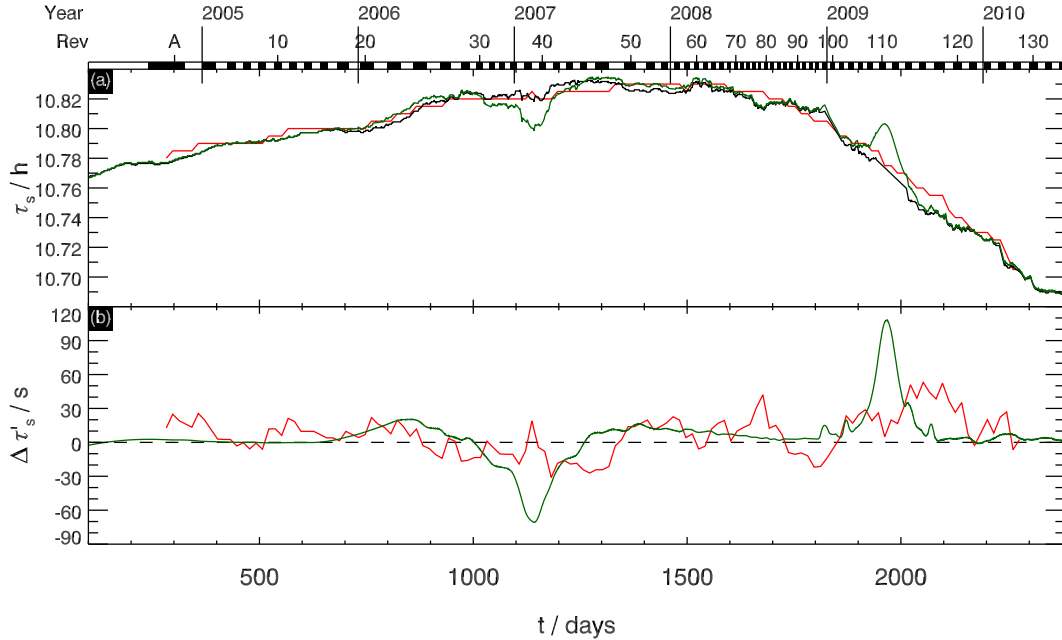


Figure 6.6: Plots comparing differing measures of the period of the southern SKR modulation and magnetic field oscillations. Panel (a) shows the periods of the observed southern SKR modulation $\tau'_{SKR,s}(t)$ determined by Lamy [2011] (black line), the SKR ‘true strobe’ period ‘corrected’ for modelled position-dependent phase deviations $\tau^*_{SKR,s}(t)$ calculated from equation (6.27) (green line), and the independently-determined magnetic field period $\tau_Ms(t)$ (red line) obtained from the continuous peak in the periodogram shown in panel (a) of Figure 6.7. Panel (b) shows the difference between the ‘true strobe’ and observed SKR periods $\tau^*_{SKR,s} - \tau'_{SKR,s}$ (green line), and between the magnetic field period and the observed SKR period $\tau_Ms - \tau'_{SKR,s}$ (red line).

where t is again time since 00 UT on 1 January 2004, and we note that $\Phi_0(0) = 0^\circ$. If the field oscillation phase so determined for a given field component on a given Rev is ψ_0 , then for any other close period τ , the phase is modified to

$$\psi = \psi_0 - 360 t \left(\frac{1}{\tau} - \frac{1}{\tau_0} \right) \text{deg.} \quad (6.29)$$

For a given sub-interval containing N phase measurements from all field components (adjusting the phase of the quadrature φ component to agree with that of the r and θ components as above), the mean resultant length $\overline{R_\psi}$ of these data is calculated from equation (6.24), and the value of τ determined which gives the maximum value of this quantity. We recall from the discussion in section 6.3.3 (see also Appendix B) that $V = 1 - \overline{R_\psi}$ gives the variance of the data about the directional mean (the minimum variance about any phase value), such that maximising $\overline{R_\psi}$ (between limits of 0 and 1) is equivalent to minimising variance V . To best compare with the period determined

from the southern SKR modulations we use sub-interval windows of 200 days, recomputed every 15 days, roughly equal to the average spacing between successive sets of phase measurements. Values of $\overline{R_\psi}$ were then computed for each sub-interval for periods τ between 10.5 and 11.0 h in steps of 0.005 h (18 s).

In panel (a) of Figure 6.7 we show a colour-coded plot of $(\overline{R_\psi})^2$ versus oscillation period τ on the vertical axis and time t on the horizontal axis. Gray vertical bands at the beginning and end of the interval indicate times where results cannot be shown due to the 200 day data window extending beyond the first or last phase data points available. It can be seen that a continuous maximum exists in these values near ~ 10.8 h throughout the interval, which we take to correspond to the period of the southern hemisphere magnetic field oscillations. Secondary short-lived maxima also appear on either side of this main peak with displacements ~ 0.2 h. These are due to aliasing introduced in sub-intervals in which the spacing between successive phase determinations (Revs) is relatively constant. We note that this method unmodified is not expected to simultaneously reveal evidence of the northern oscillation period in Figure 6.7 despite the presence of such oscillations within the ‘core’ region, and indeed none is evident in the periodogram. The magnetic field period given by the peak $(\overline{R_\psi})^2$ value within the continuous band, $\tau_{Ms}(t)$ is shown by the red lines in Figure 6.6, for comparison with the observed southern SKR period determined by Lamy [2011] (black) and the SKR ‘true strobe’ period derived above (green). It can first be seen in panel (a) of Figure 6.6 that the magnetic field period is in close overall agreement with the SKR periods. The deviation in the magnetic field period from the observed SKR values shown in panel (b) (red line) again shows positive and negative values of typically a few tens of seconds, which generally agree in sense and magnitude with those deduced from the magnetic phase drift model in section 6.3 (green line). In particular we note the interval of mainly negative values centred near $t \approx 1150$ days, and the large positive values after $t \approx 1900$ days peaking at ~ 50 s, which represent somewhat smoothed versions of the larger peaks in the green line. A few intervals of modest apparent discrepancy also exist between the two periods, such as the intermittently larger positive values in the red compared with the green curve prior

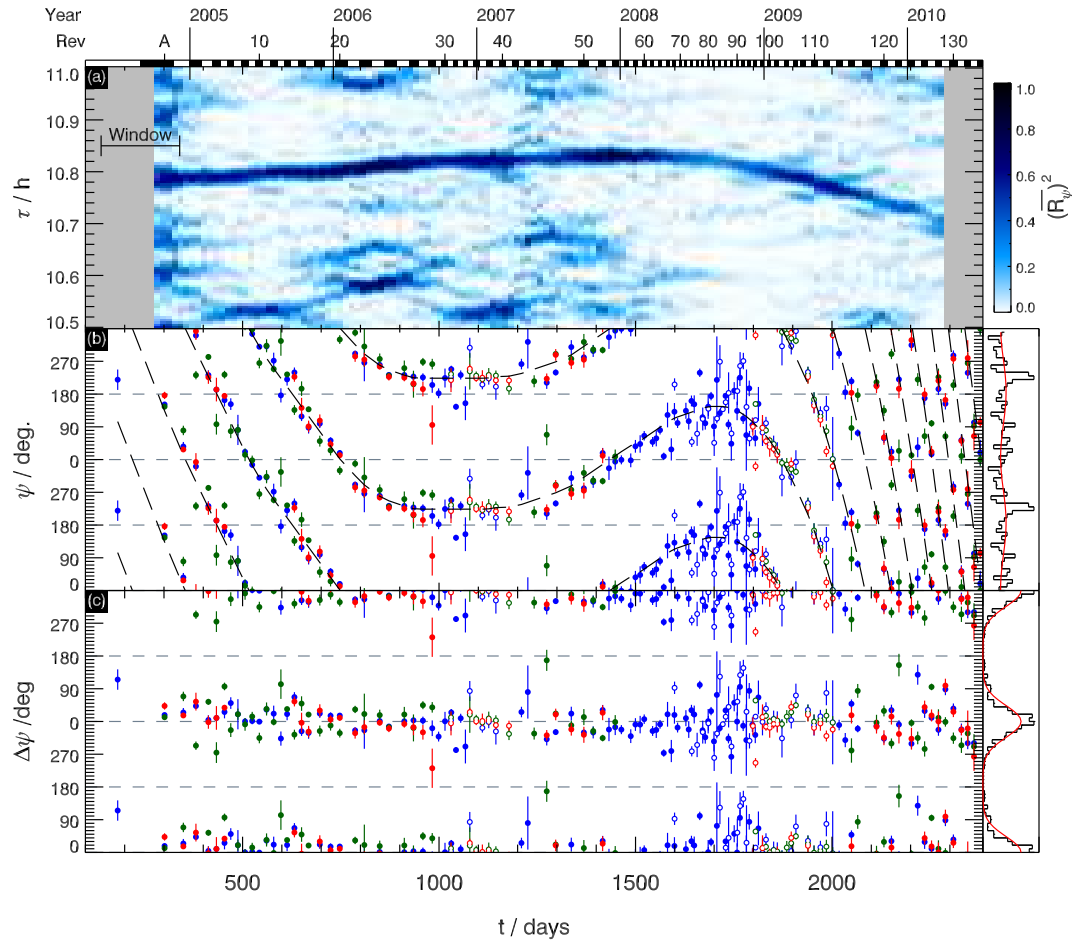


Figure 6.7: Plots relating to the determination of the southern rotation period from magnetic field data alone. Panel (a) shows a colour-coded periodogram of the squared mean resultant length $(\bar{R}_\psi)^2$ of the southern-period magnetic phase data computed with a cadence of 15 days using a sliding window of 200 day length as indicated by the icon on the left of the panel. Oscillation period τ (hours) is shown on the vertical axis versus time t (days) on the horizontal axis. Grey regions at both ends of the plot indicate intervals for which values cannot be computed due to the 200 day window. Rev and calendar year boundaries are indicated at the top of the panel as in Figure 6.2. Panel (b) shows magnetic phases determined relative to the phase of an oscillation of fixed 10.82 h period, using the same intervals of field data as in Figure 6.4, and with the phase of the quadrature φ field component adjusted as in Figure 6.4. The black dashed line shows the difference phase $\Phi_0(t) - \Phi_{Ms}(t)$ between the phase of the fixed-period oscillation $\Phi_0(t)$ and the magnetic phase $\Phi_{Ms}(t)$ computed from the period corresponding to the continuous peak in the periodogram in panel (a). Panel (c) shows the measured phases relative to the difference phase $\Phi_0(t) - \Phi_{Ms}(t)$ shown by the dashed line in panel (b).

to $t \approx 600$ days.

In panels (b) and (c) of Figure 6.7 we demonstrate how this magnetic field period organises the magnetic oscillation phases within the ‘core’ region and on southern open field lines over this interval. In panel (b) we show magnetic phase values determined relative to the guide phase of the oscillation whose period is exactly 10.82 h (equation (6.28)) as described above, in a similar format to Figure 6.4 (the phases of the quadrature φ components being adjusted to that of r and θ as before). The black dashed line then shows the differenced oscillation phase $\Phi_0(t) - \Phi_{Ms}(t)$, where $\Phi_0(t)$ is the guide phase of the 10.82 h oscillation given by equation (6.28), and $\Phi_{Ms}(t)$ is the phase of the southern-period magnetic field oscillations obtained by numerically integrating the magnetic period versus time as for the SKR phase in equation (6.23). The constant in the latter integral, equal to 267° , has then been calculated by determining the best-fit between the resulting curve and the data, obtained by the same method as used to fit the model curves to the phase data in Figures 6.4 and 6.5. In this system the r and θ component field oscillations are thus expressed as

$$B_i(\varphi, t) = B_{i0} \cos(\Phi_{Ms}(t) - \varphi), \quad (6.30)$$

with the φ components being in lagging and leading quadrature in the equatorial and southern polar regions, respectively. At time t the southern-period quasi-uniform equatorial field and southern effective polar dipole thus point towards azimuth

$$\varphi_{B_r \max}(t) = \Phi_{Ms}(t), \quad (6.31)$$

with the southern upward field-aligned current region being centred $\sim 90^\circ$ ahead in azimuth and the downward field-aligned current region $\sim 90^\circ$ behind. Numerical values of the southern magnetic field period $\tau_{Ms}(t)$ and corresponding integrated phase $\Phi_{Ms}(t)$ are available in the supporting online material in the published version of this chapter¹. The difference phase shown in panel (b) decreases with time when the magnetic oscillation period is less than the guide period of 10.82 h, increases with time when the oscillation period is greater than the guide period, and is constant (i.e.

¹<http://www.agu.org/pubs/crossref/2011/2011JA016636.shtml> (in press).

the difference phase has an extremum) when the oscillation period is just equal to the guide period. As expected, the overall fit to the phase data is excellent, though this is less obviously so after $t \approx 1900$ days, when the period of the field oscillations decreases significantly below the 10.82 h period of the guide phase such that the difference phase decreases rapidly with time.

In panel (c) of Figure 6.7 we thus show the deviation $\Delta\psi = \psi - (\Phi_0(t) - \Phi_{Ms}(t))$ of the phase data from the fitted line, equal to the deviation of the data from the phase of the model in equations (6.30) and (6.31). The data cluster about zero over the whole interval, with no indication of sub-intervals with secular change. The circular standard deviation of these data about the directional mean of zero is 43° , significantly lower than the 51° circular standard deviation of the ‘corrected’ magnetic phase data using the SKR phase deviation model shown in panel (e) of Figure 6.4.

We finally compare the three phase functions discussed here whose derivatives define measures of the slowly-varying rotation period of the southern hemisphere oscillations. These are the ‘observed’ phase of the southern SKR modulations $\Phi'_{SKRs}(t)$ derived from RPWS data by *Lamy* [2011], the ‘true strobe’ phase of the southern SKR modulations $\Phi^*_{SKRs}(t)$ ‘corrected’ for position-dependent SKR phase deviations according to the model derived in section 6.2 (equation (6.12)), and the phase determined independently from the magnetic field oscillation data $\Phi_{Ms}(t)$. The black line in panel (a) of Figure 6.8 shows the difference between the ‘true strobe’ and ‘observed’ SKR phases, $\langle\Delta'\varphi_{SKR}\rangle = \Phi^*_{SKRs}(t) - \Phi'_{SKRs}(t)$, which, apart from a constant, is the inverse of the black line in panel (a) of Figure 6.4. Its value varies by several tens of degrees on either side of zero over much of the interval, before declining strongly after $t \approx 1900$ days as the spacecraft apoapsis moves into the post-dusk sector. The red line in this panel then shows the difference between the magnetic oscillation phase and the ‘observed’ SKR phase, $\Delta\Phi'_{Ms} = \Phi_{Ms} - \Phi'_{SKRs}$. Overall, this curve closely mirrors the behaviour of $\langle\Delta'\varphi_{SKR}\rangle$ shown by the black line, apart from a near-constant offset of $\sim 220^\circ$. Substituting $\Phi_{Ms} = \Delta\Phi'_{Ms} + \Phi'_{SKRs}$ into equation (6.30) shows that at observed SKR maxima ($\Phi'_{SKRs} = 360$ N deg) the r component has a maximum at an azimuth $\varphi_{Br,max}$, such that this quantity also shows the azimuth of the quasi-uniform

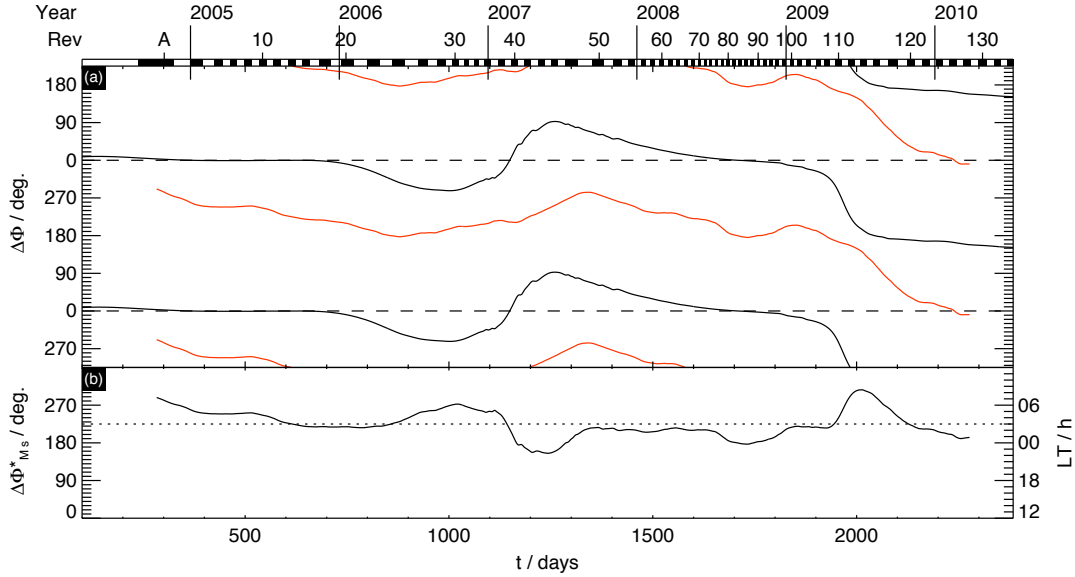


Figure 6.8: Time-series plots of southern-period SKR and magnetic oscillation phase differences. The black line in panel (a) shows the difference between the ‘true strobe’ and ‘observed’ SKR phases, $\langle \Delta'\varphi_{SKR} \rangle = \Phi_{SKR,s}^* - \Phi_{SKR,s}'$, where $\langle \Delta'\varphi_{SKR} \rangle$ corresponds to the averaged position-dependent SKR phase deviation illustrated in panel (a) of Figure 6.4. The red line shows the difference between the independently-determined magnetic oscillation phase and the ‘observed’ SKR phase, $\Delta\Phi_{Ms}^* = \Phi_{Ms} - \Phi_{SKR,s}'$, equal to the azimuth of the quasi-uniform equatorial field and effective southern polar dipole at observed southern SKR maxima. The plot covers two complete cycles of phase, and Rev and calendar year boundaries are indicated to the top of the panel as in Figure 6.2. Panel (b) shows the difference between the magnetic oscillation phase and the ‘true strobe’ SKR phase, $\Phi_{SKR,s}'$, which similarly shows the azimuth of the southern-period field at ‘true strobe’ SKR maxima. The horizontal dotted line shows the directional mean of these data, equal to 225° .

equatorial field and effective southern polar dipole at observed southern SKR maxima. The value lies close to $\sim 220^\circ$ during the initial phase of the mission, before declining rapidly after to near-zero values. The field direction at observed SKR maxima thus rotates from post-midnight to noon via dusk in the latter interval, in accordance with the discussion in section 6.3.3, corresponding to a related rotation of the centre of the southern upward field-aligned current region at these times from post-dawn to dusk via midnight (90° ahead in azimuth of the field direction).

In panel (b) of Figure 6.8 we then show the difference between the magnetic oscillation phase and the ‘true strobe’ SKR phase, $\Delta\Phi_{Ms}^* = \Phi_{Ms} - \Phi_{SKR,s}'$, which similarly shows the azimuth of the southern-period field at ‘true strobe’ SKR maxima. This is now approximately constant with time as expected, with a directional mean value of

225° (corresponding to 3.0 h LT), and a circular standard deviation of 32° (± 2.1 h LT). The corresponding LT of the centre of the southern upward field-aligned current region is then at 9.0 h in the post-dawn sector, one hour later than the effective azimuth of the mid-morning ‘true strobe’ sources.

6.5 Summary

In this study we have examined the phase relationship between the ‘planetary period’ modulations in the intensity of SKR emissions at Saturn and related oscillations in the magnetospheric magnetic field observed by the Cassini spacecraft over the six-year interval from mid-2004 to mid-2010. Specifically, we have examined the origin of the slow long-term phase drifts between these oscillations that have been reported in previous studies [Andrews *et al.* 2008, Provan *et al.* 2009a, and in Chapter 5 of this thesis], which initially suggest the presence of differences in period of a few tens of seconds. Here we have examined the possibility that the SKR modulations are not ‘strobe-like’ as believed hitherto on the basis of Voyager observations, but instead rotate around the northern and southern auroral ovals in the same manner that the magnetic field and plasma oscillations rotate about the planet in the magnetosphere, possibly connected with a rotating system of field-aligned magnetosphere-ionosphere coupling currents. Initial evidence for such rotating modulation has recently been obtained by Lamy [2011] from direction-resolved SKR emission data. Near-‘strobe-like’ behaviour of the SKR modulation phase will still occur in a restricted LT sector from pre-dawn to post-noon in which the most intense mid-morning SKR sources are near-continuously visible, but elsewhere the modulation phase will depend significantly on spacecraft LT due to conical beaming of the emission which severely restricts the view of SKR sources around the auroral oval, especially in the post-dusk sector antipodal to the most intense SKR sources. Here we have modelled these effects and have examined whether they can account for the observed phase drifts between the SKR and magnetic field data. Our principal findings are summarised as follows.

- a) Magnetic field phases have been determined relative to the north-south separated SKR phases derived by *Lamy* [2011] for both the quasi-dipolar ‘core’ region ($dipole L \leq 8$) and the two polar open field regions, extending the study presented in Chapter 5 between SOI (July 2004) and Rev 116 (August 2009) to Rev 134 (July 2010). The newly encompassed near-equatorial post-equinox data represent the first extended observations in which the spacecraft apoapsis lies in the post-dusk sector, nearly antipodal to the most intense mid-morning SKR sources. The relative phase of these oscillations is found to remain well-organised by the southern SKR period over this interval, with a polarisation as expected for southern-period oscillations. The new data are thus taken to extend the near-continuously determined phase of the southern-period field oscillations observed in both the ‘core’ and on southern polar field lines combined over six years of in-orbit observations, relative to the observed phase of the southern SKR emission modulations. Direct observations of northern period field oscillations remain confined to the north polar region observed during two high-latitude phases of the Cassini mission.
- b) Results for the earlier interval of southern-period magnetic field data remain similar to those determined using earlier SKR phase models, with slow drifts in relative phase, both positive and negative, of several tens of degrees over intervals of a few hundred days. On average, however, the relative phase is such that at southern SKR maxima the rotating quasi-uniform equatorial field and effective southern polar dipole point tailward and toward dawn, radially outward at $\sim 2\text{-}3$ h LT. This is consistent with the upward field-aligned currents of the corresponding rotating southern current system being centred at $\sim 8\text{-}9$ h LT at southern SKR maxima, essentially co-located with the most intense SKR sources in the mid-morning sector. However, following the change of spacecraft apoapsis to the post-dusk sector in the first half of 2009 the relative phase of the field oscillations also changed by $\sim 180^\circ$, such that the direction of the quasi-uniform equatorial field and effective southern polar dipole at observed SKR maxima rotated via dusk into the noon sector. The latter orientation implies that at the time of observed SKR maxima in these later

data the southern upward field-aligned currents are instead centred in the dusk sector, approximately corresponding to the LT of apoapsis of the spacecraft. This effect is suggested to be due to the SKR observations then corresponding to sources in the dusk hemisphere whose combined modulation phase is in approximate antiphase with the most intense sources in the mid-morning sector, as observed previously in auroral UV emissions [Nichols *et al.*, 2010a]. The earlier smaller phase drifts are then suggested to correspond to a less extreme expression of this effect during intervals when the spacecraft apoapsis was almost continuously located in the midnight to pre-dusk sector via dawn and noon, where the SKR modulation phase remains closer to the most intense sources in the mid-morning sector.

- c) A simple theoretical model of this effect has been constructed assuming that the rotating SKR emission modulations correspond to a fixed fraction of the LT-dependent SKR intensity determined by Lamy *et al.* [2009], and that due to the conical beaming of the SKR radiation, emission is detected only from two narrow azimuthal ‘windows’ around the auroral oval located on either side of the spacecraft azimuth. Specifically, based on the results of Lamy *et al.* [2008a] and Cecconi *et al.* [2009] we assume ‘seeing windows’ that are 15° of azimuth (1 h LT) wide centred on azimuths 55° (3.7 h LT) on either side of the spacecraft azimuth. Using this model, position-dependent SKR phase deviations have been computed relative to the ‘true strobe’ SKR phase that would be detected by an observer with a complete view of all SKR sources in each hemisphere, which have then been averaged over sliding 200 day intervals to mimic the SKR phases determined by Lamy [2011]. It is found that these phase deviations can indeed account for the relative phase drifts observed in the southern-period magnetic field data, both in sign and magnitude. After ‘correcting’ the SKR phases using the model, it is found that the long-term phase drift effect in the magnetic field data is strongly reduced. At ‘true strobe’ SKR maxima, corresponding to maxima of the most intense sources in the mid-morning sector, the quasi-uniform equatorial field and effective southern polar dipole then point radially outward at $\sim 3 \pm 3$ h LT consistently throughout the 6-year interval.

- d) The ‘correction’ of the observed southern SKR modulation phase for position-dependent phase deviations necessarily also implies a related correction of the southern-hemisphere SKR rotation period. These generally correspond to positive and negative deviations about the ‘observed’ southern SKR period of a few tens of seconds over intervals of a few hundred days, though peaking at several tens of seconds during two intervals of rapid orbit evolution. While not ascribing significance to the details of these variations, overall they integrate over such intervals to give rise to the observed phase deviations in the magnetic field data. We have also for the first time obtained an independent determination of the southern rotation period and integrated phase directly from the ‘core’ and southern polar magnetic field observations. These are found to be in good overall agreement with the ‘true strobe’ values determined from the above model, showing similar deviations from the values obtained directly from the observed SKR modulations. Specifically, at ‘true strobe’ SKR maxima the quasi-uniform equatorial field and effective southern polar dipole are found to point radially outward at $\sim 3 \pm 2$ h LT consistently throughout the interval. Numerical values of the southern magnetic field period and integrated phase data are available in the supporting online material for the published version of this chapter².
- e) Observations of northern-period polar field oscillations remain restricted to two intervals of high-latitude Cassini data investigated previously by *Provan et al.* [2009a] and in Chapter 5, that occur prior to the rotation of the spacecraft apoapsis into the post-dusk sector. These data show no evidence of the more modest phase drifts relative to the northern-period SKR modulation phase expected during these intervals based on the theoretical model. This might be due to an inadequacy in the model SKR ‘seeing function’ as applied to northern high-latitude radio observations, an aspect requiring further investigation. The relative phasing is then such that at northern SKR maxima the effective northern polar transverse dipole points consistently toward $\sim 11.5 \pm 2.5$ h LT in the immediate pre-noon sector. This

²<http://www.agu.org/pubs/crossref/2011/2011JA016636.shtml> (in press).

implies that at these times the northern upward field-aligned current region is centred in the immediate pre-dawn sector, about two hours earlier than the LT of the most intense mid-morning SKR sources determined by *Lamy et al.* [2009].

Chapter 7

Summary and conclusions

In this chapter, the new results presented in this thesis are briefly summarised together, and conclusions drawn. A discussion of the remaining open questions, and possible directions for further study are then proposed.

Firstly, it was shown in Chapter 4 that the equatorial magnetic field perturbations form a consistent pattern that rotates in the same sense as the planet, in which the field is quasi-uniform within a ‘core’ region inside of $\sim 15 R_S$, and beyond that takes the form of a rotating ‘twin-vortex’ structure, through which regions of alternate upward and downward currents flow near dusk and rotate through to dawn. It was suggested that these rotating current systems were responsible for the modulation in the emitted SKR power, though at this stage the discovery of a north-south asymmetry in the SKR modulation periods by *Gurnett et al.* [2009a] had not yet been published. A suppression of this rotating field in the inner magnetosphere was also found, associated with a second, weaker rotating current system. The radial phase speeds with which this pattern moves outward were estimated, and found to be several hundreds of km s^{-1} , and typically faster on the dayside than on the nightside. Azimuthal phase speeds were similarly determined, and were found to be generally higher near dawn than dusk.

Following the recent discovery of a north-south asymmetry in the modulations of the SKR, in Chapter 5 it was shown that the same effect is present in the rotation periods of the magnetic field as evidenced from data obtained during high-latitude orbits on which Cassini passed through the open field regions. It was also shown

that the period of the field oscillations on near-equatorial quasi-dipolar closed field lines remained close to that of the dominant southern-hemisphere SKR modulations. The implications of the observed rotating field perturbations were then discussed in terms of two separately rotating auroral current systems, closing in each case through the equatorial plane. However, while the phase of the field oscillations on northern hemisphere open field lines was found to be fixed relative to that of the corresponding northern SKR modulations over the nearly ~ 3 years of observation, variable drifts were observed in the phase of the oscillations on southern open field lines, and in the ‘core’ region, relative to the southern hemisphere SKR modulations. The presence of phase drifts of up to $\sim 0.76 \text{ deg day}^{-1}$, being of both positive and negative sign, and persisting for several hundreds of days at a time necessarily indicate that the field rotation period is not precisely that of the (observed) modulations in the SKR, although the difference is typically small (less than 40 s).

Finally, in Chapter 6, a simple theoretical model of a rotating SKR source was constructed, which included the effects of the observed local-time dependence in emitted radio power and the restricted visibility of the distributed sources obtained by an orbiting spacecraft. The departure of the ‘observed’ SKR modulation phase from the ‘true’ rotating phase was then shown to be consistent with the phase drifts present in the magnetic phase data when analysed with respect to the published SKR phase models, as was shown e.g. in Chapter 5. This (indirect) detection of a principal rotational modulation in the SKR thus resolves the paradox raised in the previous chapters, namely how can a rotating auroral current system be responsible for strobe-like (non-rotating) modulations in the SKR, particularly given their apparently secular drifts in relative phase. After accounting for the variable phase drifts studied in Chapter 6, it is readily apparent that a near-rigid phase relationship is maintained between these phenomena over the ~ 5 years of data examined, and by extension the modulations in Saturnian plasma populations, the UV auroral oval, and the position and motion of the magnetopause and bow shock.

The new results presented in this thesis thus provide a significantly improved understanding of the nature of the near-planetary period oscillations in Saturn’s mag-

netosphere, and moreover their relationships to rotating auroral current systems and the SKR emission. However, many open questions remain, not least of which concerns the real ‘source’ of these oscillatory phenomena. While this thesis does not directly address the origin of these periodic phenomena, further theoretical developments on the topic must yield predictions which conform with the results presented here, and in related work.

Many additional aspects of the topic remain to be addressed. What physical process breaks the apparently perfect azimuthal symmetry in Saturn’s inner magnetosphere? What is the origin of the weaker modulations in SKR that apparently occur in each hemisphere at the period of the dominant modulation in the opposite hemisphere? Are the rotating field patterns detected in the equatorial magnetosphere imposed by similar rotating vortices in the upper atmosphere? Do the variations in the magnetic and SKR rotation periods arise as a consequence of seasonal changes in the atmosphere?

As of writing, Cassini is in an excellent state of health, and should it remain so, it will continue to explore Saturn’s magnetosphere for the next six years. The extremely varied orbit geometry should afford the opportunity to continue to study these phenomena as the distant Sun rises in Saturn’s northern polar regions and northern summer sets in.

Appendix A

The RANSAC Algorithm

In this appendix we provide a brief overview of the RANSAC (RANdom SAmple Consensus) algorithm *Fischler and Bolles* [1981], employed in Chapter 5 to determine linear fits to the magnetic phase data shown in Figures 5.5, 5.6 and 5.8. Unmodified least-squares algorithms are not suitable for fitting these data since they contain substantial outliers, which significantly influence the fitted parameters. The RANSAC algorithm removes these outliers through an iterative process that searches for a best ‘consensus set’ within the data to be fitted, removing the most significant outliers and yielding an unbiased fit. From the input set of data to be fitted, a random sub-set of given size is selected, which may or may not contain outlying values as well as ‘true’ measurements, and fit parameters are estimated from this sub-set using least-squares. Each remaining data point is then inspected, and included in the sub-set if the difference between the data value and the corresponding fit value is less than some threshold δ . After this operation, provided that the total number of points in the sub-set is now larger than some required fraction f of the original input data set, a ‘consensus data set’ has been found. The least-squares linear fit parameters are then re-evaluated from this consensus set. This procedure is repeated many times for differing randomly-chosen data sets of the same initial size, and the results ranked by use of a ‘cost function’ equal to the modular difference between the data values and the fit to the consensus data set, summed over all of the data, but where the difference is limited to the value δ . The procedure is stopped when no further decrease in the cost function is obtained

after a given number of trials, the latter in practice typically being several thousand. Employed in this manner, the algorithm is not particularly sensitive to the choice of fraction f , 70% of the total data set being employed here, and is typically stable for reasonable values of δ .

The choice of δ , which determines whether a given data point is an outlier with respect to a given fit, must generally be chosen using some a priori knowledge of the data set to be fitted. Here, we have set $\delta = 90^\circ$, such that points more than $\pm 25\%$ of a cycle adrift are flagged as outliers. Our prime concern is then the initial number of points in the randomly selected sub-set. Too many points, and the likelihood of any given sub-set containing one or more outliers increases, meaning that the algorithm must be run for longer to produce reliable results. Too few, and the intrinsic scatter in the data results in a poor model, and subsequent valid measurements are rejected, such that the end result is again unreliable. Here we have chosen this parameter to be 40% of each data set, which is found to produce consistent and reliable results.

Appendix B

Directional statistics

In this appendix we briefly review the numerical techniques employed to analyse the phase data examined in Chapter 5. Suppose we wish to obtain the mean of a set of somewhat scattered phase data, then simply calculating the arithmetic mean in the usual way is inappropriate, since the result depends on the arbitrary choice of the 360° phase interval used to represent the data, e.g. whether -180° to +180° or 0° to 360°. For data that are in effect defined on a circle rather than on a line, ‘directional statistics’ must instead be employed [e.g. *Mardia and Jupp*, 2000].

If we consider a set of K angles θ_k , then the ‘directional mean’ of these angles $\bar{\theta}$ is given by

$$\frac{1}{K} \sum_{k=1}^K e^{j\theta_k} = \bar{R} e^{j\bar{\theta}}, \quad (\text{B.1})$$

where \bar{R} is the modulus and $\bar{\theta}$ the argument of the complex sum. In terms of real functions, if we consider the trigonometric sums

$$\bar{C} = \frac{1}{K} \sum_{k=1}^K \cos(\theta_k) \quad \text{and} \quad \bar{S} = \frac{1}{K} \sum_{k=1}^K \sin(\theta_k), \quad (\text{B.2})$$

then the directional mean is given by

$$\bar{\theta} = \tan^{-1} \left(\frac{\bar{S}}{\bar{C}} \right), \quad (\text{B.3})$$

where account is taken of the signs of both \bar{S} and \bar{C} individually such that the result is defined (to modulo 360°) over the full 360° range. These formulas have been employed in all the averages of phase data in Chapter 6, for example, to calculate the orbit-averaged value of $\Delta\varphi'_{SKR}$ in section 6.2.1, and the mean of the magnetic oscillation

phase values in section 6.3.3 (equations (6.14) and (6.24)), values which span multiple 360° cycles. Parameter \bar{R} , called the ‘mean resultant length’, is given by

$$\bar{R} = \sqrt{\bar{S}^2 + \bar{C}^2}, \quad (\text{B.4})$$

where $0 \leq \bar{R} \leq 1$. We note that the calculation of both \bar{R} and $\bar{\theta}$ involves no selection of phase interval, arbitrary to modulo- 360° , on which to perform the calculation, and that the results are also independent of choice of origin for θ . If the origin is changed such that $\theta \rightarrow \theta - \theta_0$, for example, then multiplying equation (B.1) by $e^{-j\theta_0}$ we have

$$\frac{1}{K} \sum_{k=1}^K e^{j(\theta_k - \theta_0)} = \bar{R} e^{j(\bar{\theta} - \theta_0)}, \quad (\text{B.5})$$

such that \bar{R} is unchanged and $\bar{\theta} \rightarrow \bar{\theta} - \theta_0$. Further, multiplying equation (B.1) by $e^{-j\bar{\theta}}$ we have

$$\frac{1}{K} \sum_{k=1}^K e^{j(\theta_k - \bar{\theta})} = \bar{R}, \quad (\text{B.6})$$

such that

$$\frac{1}{K} \sum_{k=1}^K \cos(\theta_k - \bar{\theta}) = \bar{R} \quad \text{and} \quad \frac{1}{K} \sum_{k=1}^K \sin(\theta_k - \bar{\theta}) = 0. \quad (\text{B.7})$$

Parameter \bar{R} describes the ‘concentration’ of the angles θ_k about the directional mean $\bar{\theta}$, with $\bar{R} \rightarrow 1$, its maximum value, when all $\theta_k \rightarrow \bar{\theta}$, and $\bar{R} \rightarrow 0$, its minimum value, when for every θ_k there is a corresponding value $\theta_k + 180^\circ$ in the data set. An appropriate measure of the ‘variance’ $V_{\bar{\theta}}$ of the angles about the directional mean is

$$V_{\bar{\theta}} = \frac{1}{K} \sum_{k=1}^K (1 - \cos(\theta_k - \bar{\theta})) = 1 - \bar{R}, \quad (\text{B.8})$$

where we note that for small deviations of θ_k from $\bar{\theta}$ we have

$$V_{\bar{\theta}} \approx \frac{1}{2K} \sum_{k=1}^K (\theta_k - \bar{\theta})^2, \quad (\text{B.9})$$

such that in this limit $V_{\bar{\theta}}$ is given by half the mean square deviation of the angles (in radians) from the directional mean. The variance about any other angle α is then given by

$$V_\alpha = \frac{1}{K} \sum_{k=1}^K (1 - \cos(\theta_k - \alpha)) = V_{\bar{\theta}} + 2\bar{R} \sin^2\left(\frac{\bar{\theta} - \alpha}{2}\right), \quad (\text{B.10})$$

where use has been made of equation (B.6). From equation (B.10) we thus see that the directional mean $\bar{\theta}$ is the angle about which the variance of the values θ_k is a minimum, and that the minimum value of the variance is $V_{\bar{\theta}} = 1 - \bar{R}$.

Angular data can conveniently be described by a number of conventional population distributions. Here we choose to use the ‘wrapped normal distribution’ (see e.g., *Mardia and Jupp* [2000]), consisting in essence of a linear normal (Gaussian) distribution ‘wrapped’ around a circle, given by

$$f(\theta) = \frac{1}{\sigma\sqrt{2\pi}} \sum_{n=-\infty}^{n=\infty} \exp\left[-\frac{(\theta - \bar{\theta} + 2\pi n)^2}{2\sigma^2}\right], \quad (\text{B.11})$$

where $\bar{\theta}$ is the directional mean and σ the circular standard deviation of the distribution. For this distribution it can be shown that

$$\bar{R} = e^{-\sigma^2/2} \quad \text{so that} \quad \sigma = \sqrt{\ln\left(\frac{1}{\bar{R}}\right)}, \quad (\text{B.12})$$

where σ is in radians. The circular standard deviation of a set of angular data derived using equations (B.4) and (B.12) then provides a useful summary statistic that is analogous to the usual standard deviation for data on a line, and has been so employed in discussing the scatter of the magnetic phase data in sections 6.2 and 6.4. In Figure B.1 we illustrate the form of this distribution for $\bar{\theta} = 180^\circ$ and various values of σ , in which we include terms in equation (B.11) for $n = -10, \dots, 10$, providing more than adequate accuracy. These forms are those employed to fit the distributions of phase data e.g. in Figures 6.4, 6.5, and 6.7, where they are plotted with the same number of terms.

Related considerations can also be used for curve fitting. In section 6.3.3 we wish to find the value of the constant phase angle ψ^* such that the function $\psi^* - \langle \Delta\varphi'_{SKR k} \rangle$ best fits the phase data ψ_k . In other words we wish to find the value of ψ^* such that the quantity $\Delta\psi_k = \psi_k - (\psi^* - \langle \Delta\varphi'_{SKR k} \rangle)$ has the least variance about zero. Following equation (B.10) this variance is given by

$$V' = \frac{1}{K} \sum_{k=1}^K (1 - \cos(\psi_k + \langle \Delta\varphi'_{SKR k} \rangle - \psi^*)) = 1 - \bar{R}' + 2\bar{R}' \sin^2\left(\frac{\overline{\psi - \Delta\varphi'_{SKR}} - \psi^*}{2}\right), \quad (\text{B.13})$$

where

$$\frac{1}{K} \sum_{k=1}^K e^{j(\psi_k + \langle \Delta\varphi'_{SKR k} \rangle)} = \bar{R}' e^{\psi^* + \Delta\varphi'_{SKR}}. \quad (\text{B.14})$$

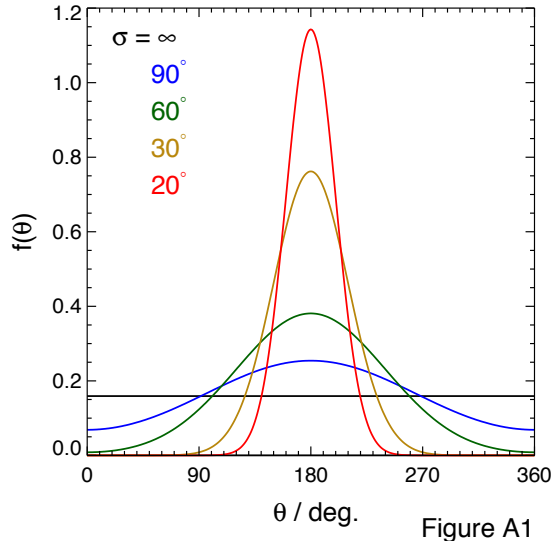


Figure A1

Figure B.1: Plot showing the ‘wrapped normal’ distribution $f(\theta)$ given by equation (A3a) computed with a directional mean of 180° and various colour-coded circular standard deviations as indicated in the figure.

Thus the minimum value of the variance occurs when $\psi^* = \overline{\psi + \Delta\varphi'_{SKR}}$, i.e. when ψ^* is equal to the directional mean of the summed angles $(\psi_k + \langle \Delta\varphi'_{SKR k} \rangle)$. The same methodology is used to fit the difference magnetic phase curve to the data in panel (b) of Figure 6.7.

Appendix C

List of Acronyms

CAPS	Cassini Plasma Spectrometer
CA	closest approach
ELS	Electron Spectrometer
ENA	energetic neutral atom
ESA	European Space Agency
FGM	Flux-Gate Magnetometer
HGA	High-Gain Antenna
HST	Hubble Space Telescope
IAU	International Astronomical Union
IBS	Ion Beam Spectrometer
IMS	Ion Mass Spectrometer
IR	Infra-red
ISS	Imaging Science Subsystem
KG	Kronographic
KGS	Kronographic (stationary)
KRTP	Kronographic (stationary, spherical polar)
KSM	Kronographic solar magnetic
LT	local time
MIMI	Magnetospheric Imaging Instrument
NASA	National Aeronautical and Space Administration
PRA	Planetary Radio Astronomy

RPWS	Radio and Plasma Wave Science
RTG	radioisotope thermoelectric generator
SKR	Saturn kilometric radiation
SLS	Saturn longitude system
SOI	Saturn orbit insertion
UV	ultra-violet
VHM	Vector Helium Magnetometer

References

- Achilleos, N., C. S. Arridge, C. L. Bertucci, C. M. Jackman, M. K. Dougherty, K. K. Khurana, and C. T. Russell (2008). Large-scale dynamics of Saturn's magnetopause: Observations by Cassini. *J. Geophys. Res.*, 113, A11209. doi:10.1029/2008JA013265.
- Achilleos, N., C. Bertucci, C. Russell, G. Hospodarsky, A. Rymer, C. Arridge, M. Burton, M. Dougherty, S. Hendricks, E. Smith, et al. (2006). Orientation, location, and velocity of saturn's bow shock: Initial results from the cassini spacecraft. *J. Geophys. Res.*, 111. doi:10.1029/2005JA011297.
- Acuña, M., MH, J. Connerney, and N. Ness (1983). The Z3 zonal harmonic model of Saturn's magnetic field: Analyses and implications. *J. Geophys. Res.*, 88(A11), 8771–8778.
- Anderson, J. and G. Schubert (2007). Saturn's gravitational field, internal rotation, and interior structure. *Science*, 317(1384). doi:10.1126/science.1144835.
- Andrews, D. J., E. J. Bunce, S. W. H. Cowley, M. K. Dougherty, G. Provan, and D. J. Southwood (2008). Planetary period oscillations in Saturn's magnetosphere: Phase relation of equatorial magnetic field oscillations and SKR modulation. *J. Geophys. Res.*, 113, A09205. doi:10.1029/2007JA012937.
- Andrews, D. J., A. J. Coates, S. W. H. Cowley, M. K. Dougherty, L. Lamy, G. Provan, and P. Zarka (2010). Magnetospheric period oscillations at Saturn: Comparison of equatorial and high-latitude magnetic field periods with north and south SKR periods. *J. Geophys. Res.*, 115, A12252. doi:10.1029/2010JA015666.
- Arridge, C. S., N. Achilleos, M. K. Dougherty, K. K. Khurana, and C. T. Russell (2006). Modeling the size and shape of Saturn's magnetopause with variable dynamic pressure. *J. Geophys. Res.*, 111, A11227. doi:10.1029/2005JA011574.
- Arridge, C. S., N. André, N. Achilleos, K. K. Khurana, C. L. Bertucci, L. K. Gilbert, G. R. Lewis, and M. K. Dougherty (2008a). Thermal electron periodicities at $20R_S$ in Saturn's magnetosphere. *Geophys. Res. Lett.*, 35, L15107. doi:10.1029/2008GL034132.
- Arridge, C. S., K. K. Khurana, C. T. Russell, D. J. Southwood, N. Achilleos, M. K. Dougherty, A. J. Coates, and H. K. Leinweber (2008b). Warping of Saturn's magnetospheric and magnetotail current sheets. *J. Geophys. Res.*, 113, A08217. doi:10.1029/2007JA012963.
- Badman, S. V., S. W. H. Cowley, J.-C. Gérard, and D. Grodent (2006). A statistical analysis of the location and width of Saturn's southern auroras. *Ann. Geophys.*, 24, 3533–3545.

- Balogh, A. (2010). Planetary magnetic field measurements: missions and instrumentation. *Space Sci. Rev.*, 152, 23–97. doi:10.1007/s11214-010-9643-1.
- Bertucci, C., N. Achilleos, M. Dougherty, R. Modolo, A. Coates, K. Szego, A. Masters, Y. Ma, F. Neubauer, P. Garnier, et al. (2008). The magnetic memory of titan's ionized atmosphere. *Science*, 321(5895), 1475.
- Bunce, E. J., C. S. Arridge, J. T. Clarke, A. J. Coates, S. W. H. Cowley, M. K. Dougherty, J.-C. Gérard, D. Grodent, K. C. Hansen, J. D. Nichols, D. J. Southwood, and D. L. Talboys (2008). Origin of Saturn's aurora: Simultaneous observations by Cassini and the Hubble Space Telescope. *J. Geophys. Res.*, 113, A09,209. doi:10.1029/2008JA013257.
- Bunce, E. J., C. S. Arridge, S. W. H. Cowley, and M. K. Dougherty (2008). Magnetic field structure of Saturn's dayside magnetosphere and its mapping to the ionosphere: Results from ring current modeling. *J. Geophys. Res.*, 113, A02207. doi:10.1029/2007JA012538.
- Bunce, E. J., S. W. H. Cowley, I. I. Alexeev, C. S. Arridge, M. K. Dougherty, J. D. Nichols, and C. T. Russell (2007). Cassini observations of the variation of Saturn's ring current parameters with system size. *J. Geophys. Res.*, 112, A10202. doi:10.1029/2007JA012275.
- Burch, J. L., A. D. DeJong, J. Goldstein, and D. T. Young (2009). Periodicity in Saturn's magnetosphere: Plasma cam. *Geophys. Res. Lett.*, 36, L14203. doi:10.1029/2009GL039043.
- Burch, J. L., J. Goldstein, T. W. Hill, D. T. Young, F. J. Crary, A. J. Coates, N. André, W. S. Kurth, and E. C. Sittler (2005). Properties of local plasma injections in Saturn's magnetosphere. *Geophys. Res. Lett.*, 32, L14S02. doi:10.1029/2005GL022611.
- Burch, J. L., J. Goldstein, P. Mokashi, W. S. Lewis, C. Paty, D. T. Young, and N. André (2008). On the cause of Saturn's plasma periodicity. *Geophys. Res. Lett.*, 35, L14105. doi:10.1029/2008GL034951.
- Burton, M. E., B. Buratti, D. L. Matson, and J.-P. Lebreton (2001). The Cassini/Huygens Venus and Earth flybys: An overview of operations and results. *J. Geophys. Res.*, 106(A12), 30,099–30,107.
- Burton, M. E., M. K. Dougherty, and C. T. Russell (2010). Saturn's internal planetary magnetic field. *Geophys. Res. Lett.*, 37, L24105. doi:10.1029/2010GL045148.
- Cao, H., C. T. Russell, U. R. Christensen, M. K. Dougherty, and M. E. Burton (2011). Saturn's very axisymmetric magnetic field: No detectable secular variation or tilt. *Earth and Planetary Science Letters*, 304(1-2), 22 – 28. doi:10.1016/j.epsl.2011.02.035.
- Carbary, J. F., D. C. Hamilton, S. P. Christon, D. G. Mitchell, and S. M. Krimigis (2010a). Longitude dependences of energetic H⁺ and O⁺ at Saturn. *J. Geophys. Res.*, 115, A07226. doi:10.1029/2009JA015133.
- Carbary, J. F. and S. M. Krimigis (1982). Charged particle periodicity in the Saturnian magnetosphere. *Geophys. Res. Lett.*, 9(9), 1073–1076.

- Carbary, J. F., S. M. Krimigis, D. G. Mitchell, C. Paranicas, and P. Brandt (2009a). Energetic neutral atom (ENA) and charged particle periodicities in Saturn's magnetosphere. *Adv. Space Res.*, 44, 483–493. doi:10.1016/j.asr.2009.04.019.
- Carbary, J. F., D. G. Mitchell, P. Brandt, C. Paranicas, and S. M. Krimigis (2008a). ENA periodicities at Saturn. *Geophys. Res. Lett.*, 35, L07102. doi:10.1029/2008GL033230.
- Carbary, J. F., D. G. Mitchell, P. Brandt, E. C. Roelof, and S. M. Krimigis (2008b). Periodic tilting of Saturn's plasma sheet. *Geophys. Res. Lett.*, 35, L24101. doi:10.1029/2008GL036339.
- Carbary, J. F., D. G. Mitchell, S. M. Krimigis, D. A. Gurnett, and W. S. Kurth (2010b). Phase relations between energetic neutral atom intensities and kilometric radio emissions at Saturn. *J. Geophys. Res.*, 115, A01203. doi:10.1029/2009JA014519.
- Carbary, J. F., D. G. Mitchell, S. M. Krimigis, D. C. Hamilton, and N. Krupp (2007a). Spin-period effects in magnetospheres with no axial tilt. *Geophys. Res. Lett.*, 34, L18107. doi:10.1029/2007GL030483.
- Carbary, J. F., D. G. Mitchell, S. M. Krimigis, and N. Krupp (2007b). Electron periodicities in Saturn's outer magnetosphere. *J. Geophys. Res.*, 112, A03206. doi:10.1029/2006JA012077.
- Carbary, J. F., D. G. Mitchell, S. M. Krimigis, and N. Krupp (2007c). Evidence for spiral pattern in Saturn's magnetosphere using the new SKR longitudes. *Geophys. Res. Lett.*, 34, L13105. doi:10.1029/2007GL030167.
- Carbary, J. F., D. G. Mitchell, S. M. Krimigis, and N. Krupp (2009b). Dual periodicities in energetic electrons at Saturn. *Geophys. Res. Lett.*, 36, L20103. doi:10.1029/2009GL040517.
- Cecconi, B., L. Lamy, P. Zarka, R. Prangé, W. S. Kurth, and P. Louarn (2009). Goniopolarimetric study of the revolution 29 perikrone using the Cassini Radio and Plasma Wave Science instrument high-frequency radio receiver. *J. Geophys. Res.*, 114, A03215. doi:10.1029/2008JA013830.
- Cecconi, B. and P. Zarka (2005). Model of a variable radio period for Saturn. *J. Geophys. Res.*, 110, A12203. doi:10.1029/2005JA011085.
- Chapman, S. and V. C. A. Ferraro (1930). A New Theory of Magnetic Storms. *Nature*, 126, 129–130. doi:10.1038/126129a0.
- Choi, D. S., A. P. Showman, and R. H. Brown (2009). Cloud features and zonal wind measurements of Saturn's atmosphere as observed by Cassini/VIMS. *J. Geophys. Res.*, 114, E04007. doi:10.1029/2008JE003254.
- Clarke, J. T., J.-C. Gérard, D. Grodent, S. Wannawichian, J. Gustin, J. Connerney, F. Crary, M. Dougherty, W. Kurth, S. W. H. Cowley, E. J. Bunce, T. Hill, and J. Kim (2005). Morphological differences between Saturn's ultraviolet aurorae and those of Earth and Jupiter. *Nature*, 433, 717–719.

- Clarke, K. E., N. André, D. J. Andrews, A. J. Coates, S. W. H. Cowley, M. K. Dougherty, G. R. Lewis, H. J. McAndrews, J. D. Nichols, T. R. Robinson, and D. M. Wright (2006). Cassini observations of planetary-period oscillations of Saturn's magnetopause. *Geophys. Res. Lett.*, 33, L23104,. doi:10.1029/2006GL027821.
- Clarke, K. E., D. J. Andrews, C. S. Arridge, A. J. Coates, and S. W. H. Cowley (2010a). Magnetopause oscillations near the planetary period at Saturn: occurrence, phase and amplitude. *J. Geophys. Res.*, 115, A08209. doi:10.1029/2009JA014745.
- Clarke, K. E., D. J. Andrews, A. J. Coates, S. W. H. Cowley, and A. Masters (2010b). Magnetospheric period oscillations of Saturn's bow shock. *J. Geophys. Res.*, 115, A05202. doi:10.1029/2009JA015164.
- Coates, A. J., F. J. Crary, G. R. Lewis, D. T. Young, J. H. W. Jr., and E. C. S. Jr. (2007). Discovery of heavy negative ions in Titans's ionosphere. *Geophys. Res. Lett.*, 34, L22103. doi:10.1029/2007GL030978.
- Connerney, J., M. Acuña, and N. Ness (1983). Currents in saturns magnetosphere. *J. Geophys. Res.*, 88(A11), 8779–8789.
- Connerney, J., M. Acuña, and N. Ness (1984). The Z3 Model of Saturn's Magnetic Field and the Pioneer 11 Vector Helium Magnetometer Observations. *J. Geophys. Res.*, 89(A9), 7541–7544.
- Connerney, J. E. P., N. F. Ness, and M. H. Acuña (1982). Zonal harmonic model of Saturn's magnetic field from Voyager 1 and 2 observations. *Nature*, 298, 44–46. doi: 10.1038/298044a0.
- Cowley, S. W. H. (1991). The plasma environment of the Earth. *Contemporary Physics*, 32, 235–250. doi:10.1080/00107519108223698.
- Cowley, S. W. H. (2006). Current-voltage and kinetic energy flux relations for relativistic field-aligned acceleration of auroral electrons. *Ann. Geophys.*, 24, 325–338.
- Cowley, S. W. H., C. S. Arridge, E. J. Bunce, J. T. Clarke, A. J. Coates, M. K. Dougherty, J.-C. Gérard, D. Grodent, J. D. Nichols, and D. L. Talboys (2008). Auroral current systems in Saturn's magnetosphere: comparison of theoretical models with Cassini and HST observations. *Ann. Geophys.*, 26, 2613–2630.
- Cowley, S. W. H. and E. J. Bunce (2001). Origin of the main auroral oval in Jupiter's coupled magnetosphere-ionosphere system. *Planet. Space Sci.*, 49(10-11), 1067–1088.
- Cowley, S. W. H. and E. J. Bunce (2003). Corotation-driven magnetosphere-ionosphere coupling currents in Saturn's magnetosphere and their relation to the auroras. *Ann. Geophys.*, 21, 1691–1707.
- Cowley, S. W. H., E. J. Bunce, and J. M. O'Rourke (2004). A simple quantitative model of plasma flows and currents in Saturn's polar ionosphere. *J. Geophys. Res.*, 109, A05212. doi:10.1029/2003JA010375.

- Cowley, S. W. H., D. M. Wright, E. J. Bunce, A. C. Carter, M. K. Dougherty, G. Giampieri, J. D. Nichols, and T. R. Robinson (2006). Cassini observations of planetary-period magnetic field oscillations in Saturn's magnetosphere: Doppler shifts and phase motion. *Geophys. Res. Lett.*, 33, L07104. doi:10.1029/2005GL025522.
- Cowling, T. (1933). The magnetic field of sunspots. *Mon. Not. R Astro. Soc.*, 94(39-48).
- Cuzzi, J., R. Clark, G. Filacchione, R. French, R. Johnson, E. Marouf, and L. Spilker (2009). Ring particle composition and size distribution. In *Saturn from Cassini-Huygens*, edited by M. K. Dougherty, S. M. Krimigis, and L. W. Esposito, chapter 15, 459–509. Springer. doi:10.1007/978-1-4020-9217-6_15.
- de Keyser, J., M. W. Dunlop, C. J. Owen, B. U. Ö. Sonnerup, S. E. Haaland, A. Vaivads, G. Paschmann, R. Lundin, and L. Rezeau (2005). Magnetopause and Boundary Layer. *Space Sci. Rev.*, 118, 231–320. doi:10.1007/s11214-005-3834-1.
- DeJong, A., J. Burch, J. Goldstein, A. Coates, and D. Young (2010). Low-energy electrons in saturn's inner magnetosphere and their role in interchange injections. *J. Geophys. Res.*, 115, A10229. doi:10.1029/2010JA015510.
- Desch, M. D. and M. L. Kaiser (1981). Voyager measurement of the rotation period of Saturn's magnetic field. *Geophys. Res. Lett.*, 8, 253–256.
- Dougherty, M. K., N. Achilleos, N. André, C. S. Arridge, A. Balogh, C. L. Bertucci, M. E. Burton, S. W. H. Cowley, G. Erdos, G. Giampieri, K.-H. Glassmeier, K. K. Khurana, J. Leisner, F. M. Neubauer, C. T. Russell, E. J. Smith, D. J. Southwood, and B. T. Tsurutani (2005). Cassini magnetometer observations during Saturn orbit insertion. *Science*, 307, 1266–1270. doi:10.1126/science.1106098.
- Dougherty, M. K., S. Kellock, D. J. Southwood, A. Balogh, E. J. Smith, B. T. Tsurutani, B. Gerlach, K. H. Glassmeier, F. Gleim, C. T. Russell, G. Erdos, F. M. Neubauer, and S. W. H. Cowley (2004). The Cassini magnetic field investigation. *Space Sci. Rev.*, 114(1-4), 331–383.
- Dougherty, M. K., K. K. Khurana, F. M. Neubauer, C. T. Russell, J. Saur, J. S. Leisner, and M. E. Burton (2006). Identification of a Dynamic Atmosphere at Enceladus with the Cassini Magnetometer. *Science*, 311(5766), 1406–1409. doi:10.1126/science.1120985.
- Dungey, J. (1961). Interplanetary magnetic field and the auroral zones. *Physical Review Letters*, 6(2), 47–48.
- Espinosa, S. A. and M. K. Dougherty (2000). Periodic perturbations in Saturn's magnetic field. *Geophys. Res. Lett.*, 27(17), 2785–2788.
- Espinosa, S. A., D. J. Southwood, and M. K. Dougherty (2003a). How can Saturn impose its rotation period in a noncorotating magnetosphere? *J. Geophys. Res.*, 108(A2), 1086. doi:10.1029/2001JA005084.
- Espinosa, S. A., D. J. Southwood, and M. K. Dougherty (2003b). Reanalysis of Saturn's magnetospheric field data in view of spin-periodic perturbations. *J. Geophys. Res.*, 108(A2), 1085. doi:10.1029/2001JA005083.

- Farrell, W. M., M. D. Desch, M. L. Kaiser, A. Lecacheux, W. S. Kurth, D. A. Gurnett, B. Cecconi, and P. Zarka (2005). A nightside source of Saturn kilometric radiation: Evidence for an inner magnetosphere energy driver. *Geophys. Res. Lett.*, 32, L18107. doi:10.1029/2005GL023449.
- Fischler, M. A. and R. C. Bolles (1981). Random sample consensus: a paradigm for model fitting with applications to image analysis and automated cartography. *Commun. ACM*, 24(6), 381–395. doi:10.1145/358669.358692.
- Fouchet, T., J. I. Moses, and B. J. Conrath (2009). Saturn: Composition and Chemistry. In *Saturn from Cassini-Huygens*, edited by M. K. Dougherty, S. M. Krimigis, and L. W. Esposito, chapter 5, 83–112. Springer. doi:10.1007/978-1-4020-9217-6_5.
- Galopeau, P. H. M. and A. Lecacheux (2000). Variations of Saturn's radio rotation period measured at kilometer wavelengths. *J. Geophys. Res.*, 105(A6), 13,089–13,101.
- Galopeau, P. H. M., P. Zarka, and D. Le Quéau (1995). Source location of Saturn's kilometric radiation: The Kelvin-Helmholtz instability hypothesis. *J. Geophys. Res.*, 100(E12), 26,397–26,410.
- Gérard, J., D. Grodent, S. W. H. Cowley, D. G. Mitchell, W. S. Kurth, J. T. Clarke, E. J. Bunce, J. D. Nichols, M. K. Dougherty, F. J. Crary, and A. J. Coates (2006). Saturn's auroral morphology and activity during quiet magnetospheric conditions. *J. Geophys. Res.*, 111(A12), A12,210. doi:10.1029/2006JA011965.
- Giampieri, G. and M. K. Dougherty (2004). Rotation rate of saturn's interior from magnetic field observations. *Geophys. Res. Lett.*, 31, L16701. doi:10.1029/2004GL020194.
- Giampieri, G., M. K. Dougherty, E. J. Smith, and C. T. Russell (2006). A regular rotation period for Saturn's magnetic field that may track its internal rotation. *Nature*, 441, 62–64. doi:10.1038/nature04750.
- Goldreich, P. and A. J. Farmer (2007). Spontaneous axisymmetry breaking of the external magnetic field at Saturn. *J. Geophys. Res.*, 112, A05225. doi:10.1029/2006JA012163.
- Gombosi, T. I., T. P. Armstrong, C. S. Arridge, K. K. Khurana, S. M. Krimigis, N. Krupp, A. M. Persoon, and M. F. Thomsen (2009). Saturn's magnetospheric configuration. In *Saturn from Cassini-Huygens*, edited by M. K. Dougherty, S. M. Krimigis, and L. W. Esposito, chapter 9, 203–255. Springer. doi:10.1007/978-1-4020-9217-6_9.
- Gomes, R., H. Levison, K. Tsiganis, and A. Morbidelli (2005). Origin of the cataclysmic late heavy bombardment period of the terrestrial planets. *Nature*, 435(7041), 466–469. doi:10.1038/nature03676.
- Grodent, D., J.-C. Gérard, S. W. H. Cowley, E. J. Bunce, and J. T. Clarke (2005). Variable morphology of Saturn's southern ultraviolet aurora. *J. Geophys. Res.*, 110, A07215. doi:10.1029/2004JA010983.
- Gurnett, D., A. Persoon, A. Kopf, W. Kurth, M. Morooka, J. Wahlund, K. Khurana, M. Dougherty, D. Mitchell, S. Krimigis, et al. (2010a). A plasmapause-like density boundary at high latitudes in Saturn's magnetosphere. *Geophys. Res. Lett.*, 37(16), L16806. doi:10.1029/2010GL044466.

- Gurnett, D. A., J. B. Groene, A. M. Persoon, J. D. Menietti, S.-Y. Ye, W. S. Kurth, R. J. MacDowall, and A. Lecacheux (2010b). The reversal of the rotational modulation rates of the north and south components of Saturn kilometric radiation near equinox. *Geophys. Res. Lett.*, 37, L24101. doi:10.1029/2010GL045796.
- Gurnett, D. A., W. S. Kurth, G. B. Hospodarsky, A. M. Persoon, T. F. Averkamp, B. Cecconi, A. Lecacheux, P. Zarka, P. Canu, N. Cornilleau-Werhlin, P. Galopeau, A. Roux, C. Harvey, P. Louarn, R. Bostrum, G. Gustafsson, J.-E. Wahlund, M. D. Desch, W. M. Farrell, M. L. Kaiser, K. Goetz, P. J. Kellogg, G. Fischer, H.-P. Ladreiter, H. Rucker, H. Alleyne, and A. Pedersen (2005). Radio and plasma wave observations at Saturn from Cassini's approach and first orbit. *Science*, 307, 1255–1259. doi:10.1126/science.1105356.
- Gurnett, D. A., W. S. Kurth, D. L. Kirchner, G. B. Hospodarsky, T. F. Averkamp, P. Zarka, A. Lecacheux, R. Manning, A. Roux, P. Canu, N. Cornilleau-Wehrlin, P. Galopeau, A. Meyer, R. Bostrom, G. Gustafsson, J. E. Wahlund, L. Ahlen, H. O. Rucker, H. P. Ladreiter, W. Macher, L. J. C. Woolliscroft, H. Alleyne, M. L. Kaiser, M. D. Desch, W. M. Farrell, C. C. Harvey, P. Louarn, P. J. Kellogg, K. Goetz, and A. Pedersen (2004). The Cassini radio and plasma wave investigation. *Space Sci. Rev.*, 114(1-4), 395–463.
- Gurnett, D. A., W. S. Kurth, and F. L. Scarf (1981). Plasma waves near Saturn: Initial results from Voyager 1. *Science*, 212, 235–239.
- Gurnett, D. A., A. Lecacheux, W. S. Kurth, A. M. Persoon, J. B. Groene, L. Lamy, P. Zarka, and J. F. Carbary (2009a). Discovery of a north-south asymmetry in Saturn's radio rotation period. *Geophys. Res. Lett.*, 36, L16102. doi:10.1029/2009GL039621.
- Gurnett, D. A., A. M. Persoon, J. B. Groene, A. J. Kopf, G. B. Hospodarsky, and W. S. Kurth (2009b). A north-south difference in the rotation rate of auroral hiss at Saturn: Comparison to Saturn's kilometric radio emission. *Geophys. Res. Lett.*, 36, L21108. doi:10.1029/2009GL040774.
- Gurnett, D. A., A. M. Persoon, W. S. Kurth, J. B. Groene, T. F. Averkamp, M. K. Dougherty, and D. J. Southwood (2007). The variable rotation period of the inner region of Saturn's plasma disk. *Science*, 316(5823), 442–445. doi:10.1126/science.1138562.
- Hansen, C. J., L. W. Esposito, A. I. F. Stewart, B. Meinke, B. Wallis, J. E. Colwell, A. R. Hendrix, K. Larsen, W. Pryor, and F. Tian (2008). Water vapour jets inside the plume of gas leaving Enceladus. *Nature*, 456(7221), 477–479. doi:10.1038/nature07542.
- Horne, J. H. and S. L. Baliunas (1986). A prescription for period analysis of unevenly sampled time series. *Astrophys. J.*, 302, 757–763. doi:10.1086/164037.
- Hughes, W. J. (1995). The magnetopause, magnetotail and magnetic reconnection. In *Introduction to space physics*, edited by M. G. Kivelson and C. T. Russell, 227–287. Cambridge University Press.
- Jacobson, R. A., P. G. Antreasian, J. J. Bordi, K. E. Criddle, R. Ionasescu, J. B. Jones, R. A. Mackenzie, M. C. Meek, D. Parcher, F. J. Pelletier, J. W. M. Owen, D. C. Roth, I. M. Roundhill, and J. R. Stauch (2006). The gravity field of the saturnian system from satellite observations and spacecraft tracking data. *The Astronomical Journal*, 132(6), 2520.

- Johnson, T. V. and P. R. Estrada (2009). Origin of the Saturn System. In *Saturn from Cassini-Huygens*, edited by M. K. Dougherty, S. M. Krimigis, and L. W. Esposito, chapter 3, 55–74. Springer. doi:10.1007/978-1-4020-9217-6_5.
- Kaiser, M. L. and M. D. Desch (1982). Saturn kilometric radiation: source locations. *J. Geophys. Res.*, 87(A6), 4555–4559.
- Kaiser, M. L., M. D. Desch, and A. Lecacheux (1981). Saturn kilometric radiation: Statistical properties and beam geometry. *Nature*, 292, 731–733.
- Kaiser, M. L., M. D. Desch, J. W. Warwick, and J. B. Pearce (1980). Voyager detection of nonthermal radio emission from Saturn. *Science*, 209, 1238–1240. doi:10.1126/science.209.4462.1238.
- Kellett, S., C. S. Arridge, E. J. Bunce, A. J. Coates, S. W. H. Cowley, M. K. Dougherty, A. M. Persoon, N. Sergis, and R. J. Wilson (2010). Nature of the ring current in saturn's dayside magnetosphere. *J. Geophys. Res.*, 115, A08201. doi:10.1029/2009JA015146.
- Kellett, S., C. S. Arridge, E. J. Bunce, A. J. Coates, S. W. H. Cowley, M. K. Dougherty, A. M. Persoon, N. Sergis, and R. J. Wilson (2011). Saturn's ring current: Local time dependence and temporal variability. *J. Geophys. Res.*, 116, A05220. doi:10.1029/2010JA016216.
- Kellett, S., E. J. Bunce, A. J. Coates, and S. W. H. Cowley (2009). Thickness of Saturn's ring current determined from north-south Cassini passes through the current layer. *J. Geophys. Res.*, 114, A04209. doi:10.1029/2008JA013942.
- Khurana, K. K., D. G. Mitchell, C. S. Arridge, M. K. Dougherty, C. T. Russell, C. Paranicas, N. Krupp, and A. J. Coates (2009). Sources of rotational signals in Saturn's magnetosphere. *J. Geophys. Res.*, 114, A02211. doi:10.1029/2008JA013312.
- Kivelson, M. G. (1995). The physics of space plasmas. In *Introduction to space physics*, edited by M. G. Kivelson and C. T. Russell, 27–57. Cambridge University Press.
- Krupp, N., A. Lagg, J. Woch, S. M. Krimigis, S. Livi, D. G. Mitchell, E. C. Roelof, C. Paranicas, B. H. Mauk, D. C. Hamilton, and M. K. Dougherty (2005). The Saturnian plasma sheet as revealed by energetic particle measurements. *Geophys. Res. Lett.*, 32, L20S03. doi:10.1029/2005GL022829.
- Kurth, W. S., T. F. Averkamp, D. A. Gurnett, J. B. Groene, and A. Lecacheux (2008). An update to a Saturnian longitude system based on kilometric radio emissions. *J. Geophys. Res.*, 113, A05222. doi:10.1029/2007JA012861.
- Kurth, W. S., A. Lecacheux, T. F. Averkamp, J. B. Groene, and D. A. Gurnett (2007). A Saturnian longitude system based on a variable kilometric radiation period. *Geophys. Res. Lett.*, 34, L02201. doi:10.1029/2006GL028336.
- Lamy, L. (2011). Variability of southern and northern SKR periodicities. In *Proc. VII Internat. Workshop on Planetary, Solar, and Heliospheric Radio Emissions, Graz, Austria*, edited by H. O. Rucker, W. S. Kurth, P. Louarn, and G. Fischer. Austrian Acad. Sci. Press, in press.

- Lamy, L., B. Cecconi, R. Prangé, P. Zarka, J. D. Nichols, and J. T. Clarke (2009). An auroral oval at the footprint of Saturn's kilometric radio sources, colocated with the UV aurorae. *J. Geophys. Res.*, 114, A10212. doi:10.1029/2009JA014401.
- Lamy, L., P. Schippers, P. Zarka, B. Cecconi, C. S. Arridge, M. K. Dougherty, P. Louarn, N. André, W. S. Kurth, R. L. Mutel, D. A. Gurnett, and A. J. Coates (2010). Properties of Saturn kilometric radiation measured within its source region. *Geophys. Res. Lett.*, 37, L12104. doi:10.1029/2010GL043415.
- Lamy, L., P. Zarka, B. Cecconi, S. Hess, and R. Prangé (2008a). Modeling of Saturn kilometric radiation arcs and equatorial shadow zone. *J. Geophys. Res.*, 113, A10213. doi:10.1029/2008JA013464.
- Lamy, L., P. Zarka, B. Cecconi, R. Prangé, W. S. Kurth, and D. A. Gurnett (2008b). Saturn kilometric radiation: Average and statistical properties. *J. Geophys. Res.*, 113, A07201. doi:10.1029/2007JA012900.
- Lecacheux, A. and F. Genova (1983). Source localization of Saturn kilometric radio emission. *J. Geophys. Res.*, 88(A11), 8993–8998.
- Lomb, N. R. (1976). Least-squares frequency analysis of unequally spaced data. *Astrophys. Space Sci.*, 39, 447–462. doi:10.1007/BF00648343.
- Mardia, K. V. and P. E. Jupp (2000). *Directional Statistics*. John Wiley and Sons, Ltd., Chichester, UK.
- Masters, A., N. Achilleos, C. Bertrucci, M. K. Dougherty, S. J. Kanani, C. S. Arridge, H. J. McAndrews, and A. J. Coates (2009). Surface waves on Saturn's dawn flank magnetopause driven by the Kelvin-Helmholtz instability. *Planet. Space Sci.* doi: 10.1016/j.pss.2009.02.010.
- Masters, A., N. Achilleos, M. K. Dougherty, J. A. Slavin, G. B. Hospodarsky, C. S. Arridge, and A. J. Coates (2008). An empirical model of Saturn's bow shock: Cassini observations of shock location and shape. *J. Geophys. Res.*, 113, A10210. doi: 10.1029/2008JA013276.
- Masters, A., N. Achilleos, M. G. Kivelson, N. Sergis, M. K. Dougherty, M. F. Thomsen, C. S. Arridge, S. M. Krimigis, H. J. McAndrews, S. J. Kanani, N. Krupp, and A. J. Coates (2010). Cassini observations of a Kelvin-Helmholtz vortex in Saturn's outer magnetosphere. *J. Geophys. Res.*, 115, A07225. doi:10.1029/2010JA015351.
- McAndrews, H. J., M. F. Thomsen, C. S. Arridge, C. M. Jackman, R. J. Wilson, M. G. Henderson, R. L. Tokar, K. K. Khurana, E. C. Sittler, A. J. Coates, and M. K. Dougherty (2009). Plasma in Saturn's nightside magnetosphere and the implications for global circulation. *Planet. Space Sci.*, 57, 1714–1722. doi:10.1016/j.pss.2009.03.003.
- Moore, L. E., M. Mendillo, I. C. F. Müller-Wodarg, and D. L. Murr (2004). Modelling of global variations and ring shadowing in Saturn's ionosphere. *Icarus*, 172, 503–520. doi:10.1016/j.icarus.2004.07.007.
- Morooka, M. W., R. Modolo, J.-E. Wahlund, M. André, A. I. Eriksson, A. M. Persoon, D. A. Gurnett, W. S. Kurth, A. J. Coates, G. R. Lewis, K. K. Khurana, and M. K. Dougherty (2009). The electron density of saturn's magnetosphere. *Ann. Geophys.*, 27, 2971–2991.

- Mutel, R. L., J. D. Menietti, D. A. Gurnett, W. Kurth, P. Schippers, C. Lynch, L. Lamy, C. S. Arridge, and B. Cecconi (2010). CMI growth rates for Saturnian kilometric radiation. *Geophys. Res. Lett.*, 37, L19105. doi:10.1029/2010GL044940.
- Nagy, A. F., A. J. Kliore, M. Mendillo, S. Miller, L. Moore, J. I. Moses, I. C. F. Müller-Wodarg, and D. Shemansky (2009). Upper atmosphere and ionosphere of Saturn. In *Saturn from Cassini-Huygens*, edited by M. K. Dougherty, S. M. Krimigis, and L. W. Esposito, chapter 8, 181–201. Springer. doi:10.1007/978-1-4020-9217-6_8.
- Narvaez, P. (2004). The magnetostatic cleanliness program for the Cassini Spacecraft. *Space Sci. Rev.*, 114, 385–394.
- Nichols, J. D., B. Cecconi, J. T. Clarke, S. W. H. Cowley, J.-C. Gérard, A. Grocott, D. Grodent, L. Lamy, and P. Zarka (2010a). Variation of Saturn's UV aurora with SKR phase. *Geophys. Res. Lett.*, 37, L15102. doi:10.1029/2010GL044057.
- Nichols, J. D., J. T. Clarke, S. W. H. Cowley, J. Duval, A. J. Farmer, J.-C. Gérard, D. Grodent, and S. Wannawichian (2008). Oscillation of Saturn's southern auroral oval. *J. Geophys. Res.*, 113, A110205. doi:10.1029/2008JA013444.
- Nichols, J. D., S. W. H. Cowley, and L. Lamy (2010b). Dawn-dusk oscillation of Saturn's conjugate auroral ovals. *Geophys. Res. Lett.*, 37, L24102. doi:10.1029/2010GL045818.
- Parker, E. N. (1958). Dynamics of the interplanetary gas and magnetic fields. *Astrophys. J.*, 128, 664. doi:10.1086/146579.
- Persoon, A. M., D. A. Gurnett, O. Santolik, W. S. Kurth, J. B. Faden, J. B. Groene, G. R. Lewis, A. J. Coates, R. J. Wilson, R. L. Tokar, J.-E. Wahlund, and M. Moncuquet (2009). A diffusive equilibrium model for the plasma density in Saturn's magnetosphere. *J. Geophys. Res.*, 114, A04211. doi:10.1029/2008JA013912.
- Porco, C., P. Helfenstein, P. Thomas, A. Ingersoll, J. Wisdom, R. West, G. Neukum, T. Denk, R. Wagner, T. Roatsch, et al. (2006). Cassini observes the active south pole of enceladus. *Science*, 311(5766), 1393.
- Provan, G., D. J. Andrews, C. S. Arridge, S. W. H. Cowley, S. E. Milan, M. K. Dougherty, and D. M. Wright (2009a). Polarization and phase of planetary period oscillations on high latitude field lines in Saturn's magnetosphere. *J. Geophys. Res.*, 114, A02225. doi:10.1029/2008JA013782.
- Provan, G., D. J. Andrews, B. Cecconi, S. W. H. Cowley, M. K. Dougherty, L. Lamy, and P. M. Zarka (2011). Magnetospheric period magnetic field oscillations at Saturn: Equatorial phase ‘jitter’ produced by superposition of southern- and northern-period oscillations. *J. Geophys. Res.*, 116, A04225. doi:10.1029/2010JA016213.
- Provan, G., S. W. H. Cowley, and J. D. Nichols (2009b). Phase relation of oscillations near the planetary period of Saturn's auroral oval and the equatorial magnetospheric magnetic field. *J. Geophys. Res.*, 114, A04205. doi:10.1029/2008JA013988.
- Saur, J., B. H. Mauk, A. Käßner, and F. M. Neubauer (2004). A model for the azimuthal plasma velocity in Saturn's magnetosphere. *Journal of Geophysical Research (Space Physics)*, 109, A05,217. doi:10.1029/2003JA010207.

- Scargle, J. D. (1982). Studies in astronomical time series analysis. II - Statistical aspects of spectral analysis of unevenly spaced data. *Astrophys. J.*, 263, 835–853. doi:10.1086/160554.
- Schippers, P., M. Blanc, N. André, I. Dandouras, G. R. Lewis, L. K. Gilbert, D. A. Gurnett, A. J. Coates, S. M. Krimigis, and M. K. Dougherty (2008). Multi-instrument analysis of electron populations in Saturn's magnetosphere. *J. Geophys. Res.*, 113, A07208. doi:10.1029/2008JA013098.
- Seidelmann, P. K., B. A. Archinal, M. F. A'hearn, A. Conrad, G. J. Consolmagno, D. Hestroffer, J. L. Hilton, G. A. Krasinsky, G. Neumann, J. Oberst, P. Stooke, E. F. Tedesco, D. J. Tholen, P. C. Thomas, and I. P. Williams (2007). Report of the IAU/IAG Working Group on cartographic coordinates and rotational elements: 2006. *Celestial Mech. Dyn. Astr.*, 98, 155–180. doi:10.1007/s10569-007-9072-y.
- Sergis, N., S. M. Krimigis, E. C. Roelof, C. S. Arridge, A. M. Rymer, D. G. Mitchell, D. C. Hamilton, N. Krupp, M. F. Thomsen, M. K. Dougherty, A. J. Coates, and D. T. Young (2010). Particle pressure, inertial force, and ring current density profiles in the magnetosphere of Saturn, based on Cassini measurements. *Geophys. Res. Lett.*, 37, L02102. doi:10.1029/2009GL041920.
- Slavin, J., E. Smith, J. Spreiter, and S. Stahara (1985). Solar wind flow about the outer planets: Gas dynamic modeling of the Jupiter and Saturn bow shocks. *J. Geophys. Res.*, 90(A7), 6275–6286.
- Smith, C. G. A. (2011). A saturnian cam current system driven by asymmetric thermospheric heating. *Mon. Not. R. Astro. Soc.*, 410(4), 2315–2328. doi:10.1111/j.1365-2966.2010.17602.x.
- Smith, E. J., L. Davis, D. E. Jones, P. J. Coleman, D. S. Colburn, P. Dyal, and C. P. Sonett (1980). Saturn's magnetic field and magnetosphere. *Science*, 207, 407–410.
- Smith, H. T., R. E. Johnson, E. C. Sittler, M. Shappirio, D. Reisenfeld, O. J. Tucker, M. Burger, F. J. Crary, D. J. McComas, and D. T. Young (2007). Enceladus: The likely dominant nitrogen source in Saturn's magnetosphere. *Icarus*, 188, 356–366. doi:10.1016/j.icarus.2006.12.007.
- Southwood, D. (2011). Direct evidence of differences in magnetic rotation rate between Saturn's northern and southern polar regions. *J. Geophys. Res.*, 116, A01201. doi:10.1029/2010JA016070.
- Southwood, D. J. and M. G. Kivelson (2007). Saturn magnetospheric dynamics: Elucidation of a camshaft model. *J. Geophys. Res.*, 112, A12222. doi:10.1029/2007JA012254.
- Southwood, D. J. and M. G. Kivelson (2009). The source of Saturn's periodic radio emission. *J. Geophys. Res.*, 114, A09201. doi:10.1029/2008JA013800.
- Spencer, J. R., A. C. Barr, L. W. Esposito, P. Helfenstein, A. P. Ingersoll, R. Jaumann, C. P. McKay, F. Nimmo, and J. H. Waite (2009). Enceladus: An active cryovolcanic satellite. In *Saturn from Cassini-Huygens*, edited by M. K. Dougherty, S. M. Krimigis, and L. W. Esposito, chapter 21, 683–724. Springer. doi:10.1007/978-1-4020-9217-6_5.

- Stanley, S. (2010). A dynamo model for axisymmetrizing saturn's magnetic field. *Geophys. Res. Lett.*, 37, L05201. doi:10.1029/2009GL041752.
- Stevenson, D. (1980). Saturn's luminosity and magnetism. *Science*, 208, 746–748.
- Strobel, D. F., S. K. Atreya, B. Bézard, F. Ferri, M. Flasar, M. Fulchignoni, E. Lellouch, and I. C. F. Müller-Wodarg (2009). Atmospheric structure and composition. In *Titan from Cassini-Huygens*, edited by R. H. Brown, J. P. Lebreton, and J. H. Waite, chapter 10, 235–257. Springer, 1 edition. doi:10.1007/978-1-4020-9215-2.
- Talboys, D. L., C. S. Arridge, E. J. Bunce, A. J. Coates, S. W. H. Cowley, and M. K. Dougherty (2009a). Characterization of auroral current systems in Saturn's magnetosphere: High-latitude Cassini observations. *J. Geophys. Res.*, 114, A06220. doi:10.1029/2008JA013846.
- Talboys, D. L., C. S. Arridge, E. J. Bunce, A. J. Coates, S. W. H. Cowley, M. K. Dougherty, and K. K. Khurana (2009b). Signatures of field-aligned currents in Saturn's nightside magnetosphere. *Geophys. Res. Lett.*, 36, L19107. doi:10.1029/2009GL039867.
- Trauger, J. T., J. T. Clarke, G. E. Ballester, R. W. Evans, C. J. Burrows, D. Crisp, J. S. G. III, R. E. Griffiths, J. J. Hester, J. G. Hoessel, J. A. Holtzman, J. E. Krist, J. R. Mould, R. Sahai, P. A. Scowen, K. R. Stapelfeldt, and A. M. Watson (1998). Saturn's hydrogen aurora: Wide field and planetary camera 2 imaging from the Hubble Space Telescope. *J. Geophys. Res.*, 103, 20,237–20,244.
- Vasyliūnas, V. M. (1983). Plasma distribution and flow. In *Physics of the Jovian magnetosphere*, edited by A. J. Dessler, 395–453. Cambridge University Press, N. Y.
- Wang, Z., D. A. Gurnett, G. Fischer, S.-Y. Ye, W. S. Kurth, D. G. Mitchell, J. S. Leisner, and C. T. Russell (2010). Cassini observations of narrowband radio emissions in Saturn's magnetosphere. *J. Geophys. Res.*, 115, A06213. doi:10.1029/2009JA014847.
- Warwick, J. W., D. S. Evans, J. H. Romig, J. K. Alexander, M. D. Desch, M. L. Kaiser, M. Aubier, Y. Leblanc, A. Lecacheux, and B. M. Pedersen (1982). Planetary radio astronomy observations from Voyager-2 near Saturn. *Science*, 215, 582–587.
- Warwick, J. W., J. B. Pearce, D. R. Evans, T. D. Carr, J. J. Schauble, J. K. Alexander, M. L. Kaiser, M. D. Desch, M. Pedersen, A. Lecacheux, G. Daigne, A. Boischot, and C. H. Barrow (1981). Planetary radio astronomy observations from Voyager-1 near Saturn. *Science*, 212(4491), 239–243.
- Wilson, R. J., R. L. Tokar, M. G. Henderson, T. W. Hill, M. F. Thomsen, and D. H. Pontius, Jr (2008). Cassini plasma spectrometer thermal ion measurements in Saturn's inner magnetosphere. *J. Geophys. Res.*, 113, A12,218. doi:10.1029/2008JA013486.
- Wu, C. S. and L. C. Lee (1979). A theory of the terrestrial kilometric radiation. *Astrophys. J.*, 230, 621–626. doi:10.1086/157120.
- Ye, S., J. Menietti, G. Fischer, Z. Wang, B. Cecconi, D. Gurnett, and W. Kurth (2010). Z mode waves as the source of Saturn narrowband radio emissions. *J. Geophys. Res.*, 115(A8), A08228. doi:10.1029/2009JA015167.

- Young, D., J. Berthelier, M. Blanc, J. Burch, A. Coates, R. Goldstein, M. Grande, T. Hill, R. Johnson, V. Kelha, D. McComas, E. Sittler, K. Svenes, K. Szego, P. Tanskanen, K. Ahola, D. Anderson, S. Bakshi, R. Baragiola, L. Barracough, R. Black, S. Bolton, T. Booker, R. Bowman, P. Casey, F. Crary, D. Delapp, G. Dirks, N. Eaker, H. Funsten, J. Furman, J. Gosling, H. Hannula, C. Holmlund, H. Huomo, J. Illiano, P. Jensen, M. Johnson, D. Linder, T. Luntama, S. Maurice, K. McCabe, K. Mursula, B. Narheim, J. Nordholt, A. Preece, J. Rudzki, A. Ruitberg, K. Smith, S. Szalai, M. Thomsen, K. Viherkanto, J. Vilppola, T. Vollmer, T. Wahl, M. Wuest, T. Ylikorpi, and C. Zinsmeyer (2004). Cassini Plasma Spectrometer investigation. *Space Sci. Rev.*, 114(1-4), 1–112.
- Young, D. T., J. J. Berthelier, M. Blanc, J. L. Burch, S. Bolton, A. J. Coates, F. J. Crary, R. Goldstein, M. Grande, T. W. Hill, R. E. Johnson, R. A. Baragiola, V. Kelha, D. J. McComas, K. Mursula, E. C. Sittler, K. R. Svenes, K. Szego, P. Tanskanen, M. F. Thomsen, S. Bakshi, B. L. Barracough, Z. Bebesi, D. Delapp, M. W. Dunlop, J. T. Gosling, J. D. Furman, L. K. Gilbert, D. Glenn, C. Holmlund, J. M. Illiano, G. R. Lewis, D. R. Linder, S. Maurice, H. J. McAndrews, B. T. Narheim, E. Pallier, D. Reisenfeld, A. M. Rymer, H. T. Smith, R. L. Tokar, J. Vilppola, and C. Zinsmeyer (2005). Composition and dynamics of plasma in Saturn's magnetosphere. *Science*, 307(5713), 1262–1266. doi:10.1126/science.1106151.
- Zarka, P. (1998). Auroral radio emissions at the outer planets: Observations and theories. *J. Geophys. Res.*, 103(E9), 20,159–20,194.
- Zarka, P., L. Lamy, B. Cecconi, R. Prangé, and H. O. Rucker (2007). Modulation of Saturn's radio clock by solar wind speed. *Nature*, 450, 265–267.

Colophon

Typeset in 12 pt Fourier (a licensed derivative of Adobe Utopia), with X_ET_EX (<http://scripts.sil.org/xetex>) using the L_AT_EX memoir, hyperref, xunicode, xltxtra, color, graphicx, amsmath, bm, url, acronym, rotating and natbib packages.

BibTex bibliography managed in BibDesk (<http://bibdesk.sourceforge.net/>).

Original vector graphics produced using InkScape (<http://inkscape.org/>).

The majority of the data used in this thesis was processed in IDL, using D. Fanning's 'coyote' library, S. E. Milan's 'holly' library, and M. Craig's 'TeXtoIDL' library.

NASA/JPL CSPICE software was used to calculate spacecraft and planetary ephemerides.

Git is damn useful too (<http://git-scm.com/>).

This work is licensed under the Creative Commons Attribution-NonCommercial-NoDerivs 3.0 Unported License. To view a copy of this license, visit <http://creativecommons.org/licenses/by-nc-nd/3.0/> or send a letter to Creative Commons, 444 Castro Street, Suite 900, Mountain View, California, 94041, USA.

*Shakedown 1979
Cool kids never have the time
On a live wire right up off the street
You and I should meet
Junebug skipping like a stone
With the headlights pointed at the dawn
We were sure we'd never see an end to it all*